2020

Sympathy for the Microbiota: How Changes in Gut Microbial Composition Influence the Immune System and Basic Physiology by Way of the Sympathetic Nervous System

Paul Andrew Muller

Sympathy for the Microbiota: How Changes in Gut Microbial Composition Influence the Immune System and Basic Physiology by Way of the Sympathetic Nervous System

A Thesis Presented to the Faculty of

The Rockefeller University

in Partial Fulfillment of the Requirements for

the degree of Doctor of Philosophy

by

Paul Andrew Muller

June 2020

Sympathy for the Microbiota: How Changes in Gut Microbial Composition Influence the Immune System and Basic Physiology by Way of the Sympathetic Nervous System

Paul Andrew Muller, Ph.D.

The Rockefeller University 2020

The gastro-intestinal tract is the most extensive mucosal surface in mammals and harbors the most numerous immune cell reservoir as well as a complex and autonomous nervous system. The GI tract is continuously exposed to foreign antigen and potentially toxic chemicals through the ingestion of food. In addition, the lumen of the human GI tract is populated with approximately 10^{13} bacteria, which is equivalent to the number of cells in the entire human body (Sender et al., 2016). The intestinal microbiome, which aids in host metabolism, represents a diverse population of microorganisms separated from the inside of the body by only a single layer of epithelial cells. Thus, in this highly inflammatory and ever-changing environment, the intestine must be able to balance tolerance to dietary antigens and microbes, while remaining vigilant when exposed to potentially toxic substances or pathogens. Sensing of the microbiota has been previously shown to impact the intestinal immune and nervous systems, including crosstalk between the two. However, how microbes influence the enteric associated nervous system and whether these effects play a role in mediating host physiology, inclusive of immune responses, remains unanswered.

We previously uncovered neuro-immune cross-talk in the intestine (Muller et al., 2014), whereby *muscularis* macrophages (MM) that reside in the muscle layers of the

intestine express bone morphogenetic protein 2 (BMP2) that can directly impact intrinsic enteric associated neurons (iEAN) and intestinal motility. Reciprocally, iEAN express colony-stimulating factor 1 (CSF1), which may play a role in the local maintenance and differentiation of MM. Both axes of this crosstalk occur during normal, steady-state conditions and are dependent upon the commensal microbiota.

To determine whether these macrophages played a role during the course of an intestinal infection, we first aimed to better characterize how MM differed from their counterparts that reside in the intestinal lamina propria, in close proximity to the microbial-rich lumen. Through two-photon intravital microscopy, cleared tissue light-sheet imaging, and RNA-sequencing of purified macrophage populations, we found that MM are morphologically, anatomically, dynamically, and transcriptionally distinct from LpM. These MM were skewed towards a more anti-inflammatory transcriptional profile and were in close apposition to actively firing iEAN. Utilizing an attenuated form of *Salmonella* typhimurium, *spiB*, we found that although MM are not in direct contact with luminal contents, they were rapidly polarized towards an enhanced anti-inflammatory profile in response to pathogenic infection. Furthermore, polarization was dependent upon sympathetic neuronal activation in the celiac-superior mesenteric ganglion (CG-SMG), which enabled communication from the lumen to MM through adrenergic receptor beta 2 (ADBR2) engagement (Gabanyi & Muller et al., 2016). Together, these results established that neurotransmitter signaling can swiftly coordinate a response to infection through anatomically-associated immune cells.

To gain insights into how sympathetic neurons, and more broadly, all extrinsic enteric associated neurons (eEAN) might detect and/or be influenced by changes in the microbiota, we performed unbiased RNA translational profiling comparing eEAN sensory and effector nodes from germ free and specific pathogen free mice. RNA sequencing revealed changes in activity-dependent transcripts in afferent sensory neurons in the nodose ganglion and efferent sympathetic neurons in the CG-SMG. These results served as an entry point to identify which microbial signals and neuronal populations transmit microbial information to the central nervous system (CNS), and which CNS populations integrate this information to control gut physiology. We identified a subset of distal intestine-projecting vagal neurons positioned to play an afferent role in luminal detection through chemogenetic manipulation, translational profiling and anterograde tracing. Using retrograde polysynaptic neuronal tracing from the intestinal wall, we identified brainstem sensory nuclei activated by specific bacterial metabolites, including short chain fatty acids. Finally, chemogenetic modulation demonstrated that activation of sympathetic premotor glutamatergic neurons is sufficient to regulate gastrointestinal transit. In sum, we established an anatomical, molecular, and functional framework for the complex circuit(s) monitoring microbial content (Muller et al., 2019a).

Equipped with a more complete understanding of how the gut sympathetic nervous system functions, we then asked whether pathogen-induced adrenergic changes in MM are important for a proper tissue-protective response. Infection with multiple pathogens, including *spiB*, led to a significant and persistent loss in iEAN numbers and chronic dysmotility. Intersectional genetics, pharmacological intervention, and chemogenetic

sympathetic activation was used to demonstrate that MM-specific B2AR signaling is required to confer neuronal protection during the course of infection and prevent further pathogen-induced damage. Furthermore, translational profiling of iEAN led to the discovery that these neurons express a unique combination of inflammasome pathway components as compared to other peripheral neuronal sub-populations. These inflammasome components are activated in iEAN during infection, and neuron-specific gene targeting was sufficient to prevent pathogen-induced neuronal loss. Thus, we found that MM-adrenergic signaling can mitigate EAN inflammasome-dependent cell-death during enteric infection (Matheis & Muller et al., 2019).

Based upon our discovery of iEAN dysbiosis detection via the inflammasome, we next probed how changes in the microbiota might further impact these neurons. Using translational profiling, we found that distinct regions of the intestine have unique gene expression programs in the presence of the microbiome. By comparing this profile to germ free mice, we found that the microbiota is a principal driving force in establishing these regional differences and that specific neuropeptides populations are decreased in the distal intestine in the absence of a microbiota. Chemogenetic characterization of microbiota-influenced iEAN identified a subset of viscerofugal CART+ neurons that modulate feeding behavior through insulin-glucose levels independent of the central nervous system. We discovered that CART+ iEAN numbers decrease in the absence of the microbiota through the same iEAN inflammasome pathway we previously identified. Finally, genetic ablation of this inflammasome pathway was sufficient to prevent insulin-glucose level changes normally seen in antibiotic-treated conditions (Muller et al., 2019b).

Through these studies we found that multiple signals generated by changes in the gut microbial composition are integrated by the sympathetic nervous system to control gastrointestinal motility, enteric immunity, and blood glucose. Cumulatively, these findings have increased our understanding of how the enteric associated nervous system responds to changes in the microbiota and consequently regulates local tissue and overall mammalian homeostasis.

To my father, Robert,

for his gruff love, wisdom, and for teaching me how to ask the right questions

To my mother, Deirdre,

for her resolute love and whose passion for learning is infectious

To my partner, Veronica,

for her endless support, love, and intellectual prowess

that has made a lasting impact on my work

Acknowledgements

Despite the solitary nature of academic science, I would have never made it to this point without a seemingly endless list of people in my life.

First and foremost, thank you to my mentor Daniel Mucida, who I met several years before I made my way to his lab at Rockefeller. It was in Daniel's lab that I was given the tools I needed to not only have a successful PhD, but to make my mark on basic science in general. The lab and the environment he has fostered are a testament to his strengths as a scientist. I have grown by leaps and bounds during my time in Daniel's lab, and so I am incredibly grateful to have been a part of his group.

It goes without saying that the entire Mucida lab has been an immense part of my life all these years. To the former lab members Virginia, Daria, Tomiko, and Tomo it was a great honor to have been able to work and learn from all of them. To Ilana, it was a distinct pleasure to work with her from the outset in the lab, and her friendship has been vital even from across the Atlantic. To Aneta, I have to thank for providing her perspective on anything from mountain climbing to baking, I certainly learned a lot of outside information over these years and I will miss having the best baked bread as my "birthday cake". To Angelina, I have to thank her for laughing at my terrible jokes and for being such a great scientific mentor. To Bernardo, who is both an amazing scientist and human being, his general joy helped to make life a little more tolerable when things were down. To Ainsley, whose dark sense of humor never ceases to horrify me, but her kindness in the end is unparalleled. To David, whose passion for science is unparalleled and perhaps only matched by his fanaticism for Netherlands football, I thank for his

friendship and brainstorming sessions. To Mariya, I have to thank for her friendship and hiccups all this time, she has always given me something to smile about. To Fanny, I was lucky to make a great friend and scientific partner without whom I could not have made it to this point, truly.

Thank you to the Victora lab for being such great scientific neighbors and friends since they joined Rockefeller. It has been a pleasure to work with the entire group through the years, particularly Luka, Arien, Johanne, and Carla. The same goes for the Nussenzweig lab, who have provided a haven of sorts for immunology since I started in the lab. Thank you to Lillie for her friendship during her time at Rockefeller, that started with a confusing email. I also would like to thank Zoran, who made both labs run without a hitch. I still cannot enter the lab without looking towards his desk for both his reassuring presence and a smiling wave, you are missed. Thank you to Gabriel Victora and Michel Nussenzweig for the help during my tenure here.

Thank you to my committee members Leslie Vosshall and again to Gabriel Victora. They were both an integral part of my development as a scientist, and I am indebted to their help in advancing what at first seemed like an insurmountable task. I am appreciative of their honesty and support in my next steps as a scientist. To Marcelo Dietrich, my external examiner, thank you for taking the time to be a part of this work as well as for our great scientific conversations past and hopefully future.

I have to thank my first true scientific mentor, Alexander Rotenberg, for giving me the chance to embark on this journey. At one point I was the only member of the lab, and it was amazing to watch things grow from a small closet in Frances Jensen's lab to

our own space in a new biomedical building. Alex gave me complete freedom as a scientist which, from what I have seen, is extremely rare. While I was and still am fascinated by the medicine I was exposed to under Alex's guidance, I quickly realized that I had the most to gain on the basic science portion of my work. It is with that independence and creative mentorship in Alex's lab that I knew I could make an impact on the academic world.

Thank you to Miriam Merad, in whose lab I was exposed to world class immunology. It was truly an honor to be able to spend my days with such an amazing group of students and scientists. Miriam has also stayed in touch over these years and her mentorship has been a key to my success during this time.

An incredible thank you to Milena Bogunovich, the post-doc (now PI at UMass) who decided to hire me as a technician in Miriam's lab. Just as with Alex, I was given an incredible amount of latitude to develop as a scientist. It was under Milena's guidance that I established my passion for the mucosal immune system and how the nervous system could be integrated into biology in unexpected ways. I consider her a great friend and mentor since leaving the lab, someone who has always advocated for my career no matter the circumstance. Milena taught me how to do great and rigorous science without the need to please anyone but your own curiosity, a trait she shares with my father.

Thank you to Joel Oppenheim, the former Dean at NYU Sackler, for taking a chance on me when many likely would not have. My time at NYU was instrumental to my progress as a scientist and an individual, and Joel made that possible. In leaving

NYU, it was a reflection of my need to pursue a particular path but my couple of years in the program changed me forever.

Both Juan Lafaille and Hernandez Moura Silva were mentors at NYU, who helped to hone my immunology expertise. They have continued their presence and friendship during my time at Rockefeller, which has been a vital part of my success.

I am forever indebted to the David Rockefeller Graduate program and members of The Rockefeller University Dean's Office: Sidney Strickland, Emily Harms, Andrea Morris, Kristen Cullen, Marta Delgado, Stephanie Fernandez, and in particular Cristian Rosario for being there at every step to make my life as a graduate student as painless as possible.

Thank you to the Dead Poet and family, particularly Kevin, John, Matt, Tim, and Jimmy. Without this outlet in my life and the bonus of being with friends, I would have failed long ago.

Great friends are key to surviving any ordeal in life and so I have to say a special thank you to the life-long friends I made when I started my graduate school career at NYU. Specifically, to Korey, Anthony, Vangel, Simon, and Jessie, words cannot express how their friendship has buoyed me all these years. These are five friends who, no matter the time or distance between us, make it feel as if we never missed a beat.

My friends at Rockefeller have also been a key to my years in graduate school. I have to say thank you to Ed, Jakob, Luka, Elisabeth, and Amy for their friendship. I hope that Ed has finally gotten over the scar of eating lox-spread when he thought he was getting strawberry cream cheese that first day we met. I was fortunate to have a

fantastic roommate and dear friend, Jaime, when I started at Rockefeller. His sense of humor was a refreshing way to arrive home each day. Thank you to Marc for his incredible friendship and many conversations both scientific and personal that have kept me afloat. I could not have done this without him. Thank you to Maria-Jose, for putting up with the distractions I may have introduced for Marc, but also for her friendship and warmth that have made me feel like family.

To Stacey, I have to thank being such an amazing sister-in-law who always knows how to laugh and cry at the right moments. To Miguel, I thank for teaching me what a titmouse is as well as being an overall fantastic human being and friend.

To my brother David, whose friendship and sense of humor have kept me sane during this time. To my incredibly talented sister Alex, her passion for life and kindness have helped to keep a light on during some dark times. It is not every day that you can truly count your siblings as best friends, but I am blessed to be able to say so. I love both of you dearly.

Thank you to my nephews Alexander and Samuel. I don't think it is possible to love two little human beings more than I love both of them. Visiting and seeing them both grow up has been a constant joy in my life.

To my mother Deirdre, there is no one who exudes more excitement for every activity than her and I am the man I am because of her unwavering love and support. Unconditional love is hard to come by, but she has certainly demonstrated that throughout my life. I love you immensely and always.

To Veronica, she has quite literally changed my life forever and I would not have been able to do this work without her love and support. Given the amazing things she is destined to do, I am lucky to have commanded just a small part of her attention all these years. I love you steadfastly.

To my father Robert, I cannot find the words to express how much I have missed him these past seven years. I feel his absence every day, but particularly in these moments. He showed me what it means to be true to yourself both in life and in science. I learned to never be afraid to work at something until it is right, even if that means tearing everything down in the process. I hope that I can instill in my children some of the same values that he taught me. I love you Dad.

Disclaimer

Portions of text and figures from Chapters 1-5 are adapted from manuscripts written with Dr. Daniel Mucida. Some figures contained within this thesis use images and graphics created with Biorender.com.

Table of Contents

List of Figures

Chapter 1:

Chapter 2:

Chapter 3:

List of Tables

Chapter 3:

List of Abbreviations

5-HT	5-hydroxytryptamine (serotonin)
AAV	Adeno-associated virus
ADRB2	Adrenergic receptor beta 2
Adx	Adrenalectomy
AGRP	Agouti related peptide
AP	Area postrema
ARC	Arcuate nucleus
ARG1	Arginase 1
ASC	Apoptosis-associated speck-like protein containing a CARD
ASF	Altered Schaedler flora
Avil	Advillin
β_2AR	Adrenergic receptor beta 2
BBB	Blood brain barrier
CART	Cocaine- and amphetamine- related transcript
CASP1	Caspase 1
CASP4	Caspase 4
CASP11	Caspase 11 (mouse homolog of Caspase 4)
CCK	Cholestocystokinin
CG-SMG	Celiac-ganglion superior mesenteric ganglion
ChAT	Choline acetyltransferase
CNS	Central nervous system
CTB	Cholera toxin subunit B
CVLM	Caudal ventrolateral medulla
CX3CR1	Fractalkine receptor
DBH	Dopamine beta-hydroxylase
DFMO	Difluoromethylornithine,
DIO	Double floxed inverse orf
DMV	Dorsal motor nucleus of the vagus
DREADD	Designer receptor exclusively activated by designer drugs
DRG	Dorsal root ganglion
DTA	Diptheria toxin fragment A
DTR	Diptheria toxin receptor
EAN	Enteric associated neuron
eEAN	Extrinsic enteric associated neuron
EEC	Enteroendocrine cell
ELAVL4	Embryonic Lethal, Abnormal Vision, Drosophila-Like 4
ENS	Enteric nervous system
FLEX	Flip-excision switch
FFAR2	Free fatty acid receptor 2
FFAR3	Free fatty acid receptor 3
FST	Follistatin
GCaMP	GFP-calmodulin-myosin peptide fusion protein

GCaMP3	High signal-to-noise Ca2+ probe based on a single GFP protein 3
GCaMP6s	High signal-to-noise Ca2+ probe based on a single GFP protein 6s
GF	Germ-free
GFP	Green fluorescent protein
GLP-1	Glucagon-like peptide 1
GLP1r	Glucagon-like peptide 1 receptor
GPCR	G protein coupled receptor
GPR41	Free fatty acid receptor 2
GPR43	Free fatty acid receptor 3
HA	Hemagglutinin
HAND2	Heart- and neural crest derivatives-expressed protein 2
hM3Dq	Human muscarinic 3 receptor [$Y149C^{3.33}$/$A239G^{5.46}$]
hM4Di	Human muscarinic 4 receptor [$Y113C^{3.33}$/$A203G^{5.46}$]
HPA	Hypothalamic-pituitary-adrenal
i.c.v.	Intracerebroventricular
ICC	Interstitial cell of Cajal
iDISCO	Immunolabeling-enabled 3D imaging of solvent-cleared organs
iEAN	Intrinsic enteric associated neuron
IL-1β	Interleukin 1 beta
IL-18	Interleukin 18
ILC2/3	Innate lymphoid cell 2/3
IML	Interomediolateral column
invA	*Salmonella typhimurium* Δ*invA*
i.p.	Intraperitoneal
IPAN	Intrinsic primary afferent neuron
log_2FC	Log_2 fold change
LpM	Lamina propria macrophage
LysM	Lysozyme M (*Lyz2*)
MC4R	melanocortin receptor 4
MHCII	Major histocompatibility protein II
MM	Muscularis macrophage
NA	Noradrenaline
Nav1.8	Sodium voltage-gated channel alpha subunit 10
NE	Norepinephrine
NG	Nodose ganglion
NLRP6	NOD-like receptor family pyrin domain containing 6
NMU	Neuromedin U
nNOS	Neuronal nitric oxide synthase
NPY	Neuropeptide Y
NTS	Nucleus tractus solitarius
ODC1	Ornithine decarboxylase 1
POI	Post-operative ileus
POMC	Pro-opionmelanocortin-alpha
PRV	Pseudo-rabies virus

PVH	Paraventricular hypothalamus
PYCARD	Apoptosis-associated speck-like protein containing a CARD
PYY	Peptide YY
RFP	Red fluorescent protein
RPa	Raphe pallidus
RVLM	Rostral ventrolateral medulla
SCN5a	Sodium voltage-gated channel alpha subunit 5
SCN10a	Sodium voltage-gated channel alpha subunit 10
sdVx	Subdiaphragmatic vagotomy
SNS	Sympathetic nervous system
SPF	Specific pathogen free
spiB	*Salmonella typhimurium* Δ*spiB*
SST	Somatostatin
tdTomato	Tandem dimer tomato protein
TH	Tyosine hydroxylase
TLR	Toll like receptor
TPH1	Tryptophan hydroxylase 1
TPH2	Tryptophan hydroxylase 2
TRAP	Translating ribosome affinity purification
TTX	Tetrodotoxin
VGLUT2	Vesicular glutamate transport 2
VGAT	Vesicular GABA transporter
VIP	Vasoactive intestinal peptide
zDC	Zinc finger and BTB domain containing 46

Chapter 1: Introduction

> "For several years during discussions with young scientists in my laboratory, I have spoken of an interest in feeding a young animal (rabbit, guinea pig, dog or chicken) from birth with pure nutritive material. By this expression I mean nutritive products that have been artificially and totally deprived of the common microorganisms. …
>
> Without affirming anything, I do not conceal the fact that if I had the time, I would undertake such a study, with the preconceived idea that under these conditions, life would be impossible. …
>
> Whether the result would be positive and confirm my preconceived view, or whether it would be negative, in other words that life would be easier and more active, it would be most interesting to perform the experiment."
>
> -Pasteur, L., C. R. *Acad. Sci.*, *Paris*, 100, 68 (1885).

In his remarks to the Académie des Sciences, Louis Pasteur posed the question as to how mammals would fare if they were devoid of all microorganisms from birth, thereby living in a germ-free state (Pasteur, 1885). The first germ-free mammal, a guinea pig, was generated by Nuttal and colleagues in 1897 (Nuttall and Thierfelder., 1896). Several other germ-free animal models were subsequently generated, including additional rodents and mammals (Reyniers et al., 1946), which has allowed for the study of how commensal microbes impact mammalian physiology. With a particular focus on the gastro-intestinal tract, where on the order of 10^{13} bacteria reside in humans (Sender et al., 2016), the broad morphologic, metabolic, and physiologic changes that accompany a lack of commensal microbes have been well-documented (Gordon and Pesti, 1971). The immune system of the intestine is particularly tuned to respond to microbiota, and its function is significantly impacted in cases of microbial depletion (Belkaid and Hand, 2014). However, despite the fact that the small and large intestine contain an extensive autonomous nervous system, the impact of the microbiota on these components has only

recently been appreciated. Our initial findings identified distinct microbiota-dependent signals from innate immune cells and neurons in the muscle layer of the intestine, both of which are far from the microbe-rich lumen. We additionally uncovered a direct connection between these two cell populations, whereby microbial-dependent signals from each population was essential for the other, and critical for normal gut motility. These results suggest that microbes can directly affect the nervous system, and that microbe-dependent changes in the nervous system can influence the immune system and homeostatic function (Gabanyi et al., 2016; Muller et al., 2014). Given the rapid expansion of molecular tools in the field of neuroscience (Veiga-Fernandes and Mucida, 2016), we sought to apply these techniques to understand how the enteric associated nervous system is influenced by the microbiota and, in turn, how modulation of the nervous system impacts host physiology, including, but not limited to, immune function.

Due to the number of anatomically and functionally distinct cell populations I will discuss during the course of this thesis, I will first succinctly lay out their organization and function. I will begin with a brief overview of the anatomy of the small and large intestine, including their respective microbiota. I will then transition into a description of the enteric associated nervous and immune systems, highlighting the impact of the intestinal microbiota on each. I will then delineate potential neuro-immune interactions and emphasize the importance of macrophage-neuron crosstalk. Finally, I will lay out the aims of this thesis and the approaches taken to reach those goals.

1.1 Functional anatomy of the small and large intestine

The gastrointestinal (GI) tract has evolved as a crucial interface at which nutrients are absorbed and potentially harmful substances are excluded from organisms (Montgomery et al., 1999) (Figure 1.1). In mammals, once food has been ingested it moves from the mouth via pharynx and esophagus into the stomach, where stomach

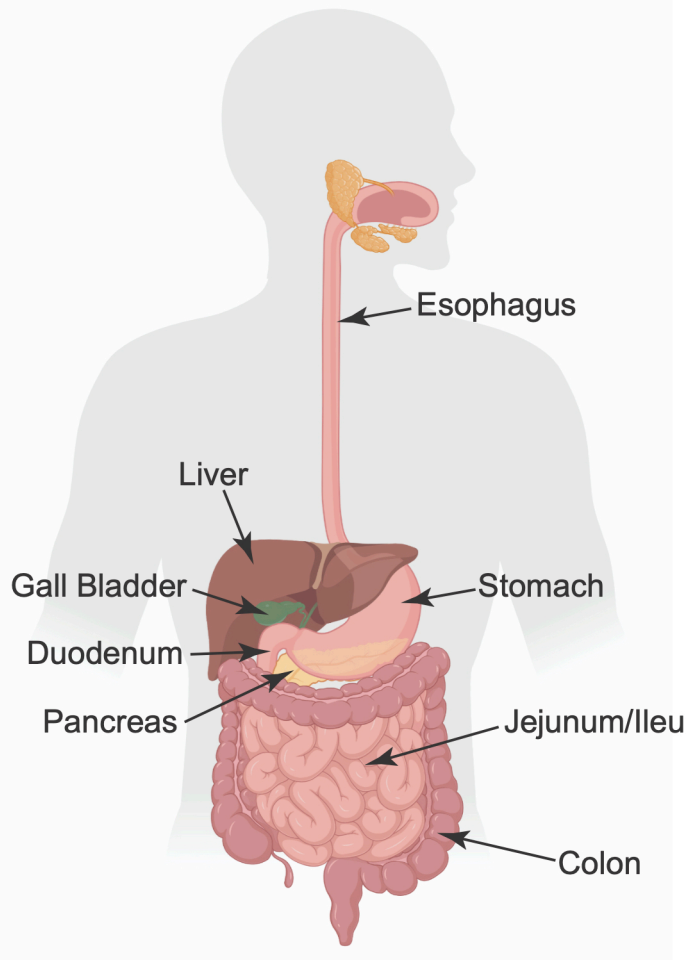

Figure 1.1. Organization of human gastrointestinal tract. Schematic showing the route by which food progresses through the GI tract and highlighting some of the tissues discussed in this thesis.

acids, enzymes, and physical churning aid in the initial processing of the bolus. The contents of the stomach are then moved into the first segment of the small intestine, the

duodenum, which is the main absorptive site for carbohydrates, amino acids, and lipids in the GI tract –owing to its large epithelial surface area and high expression of fatty acid- and glucose transporters (Vertzoni et al., 2019). Propulsive, coordinated muscle contractions of the intestine circular and longitudinal muscle move luminal contents from the duodenum to the jejunum, ileum and colon, successively. The jejunum complements the duodenum in absorption of essential nutrients, while the ileum is tasked with absorption of electrolytes and bile salts, and the colon performs absorption of water, vitamins and essential microbial metabolites (Martinez-Guryn et al., 2019; Pawel R and Fayez K, 2016). The overall architecture of the intestinal tissue is preserved between the small and large intestine, although there are some key differences (Figure 1.2). Both the small and large intestine have a single layer of epithelial cells that separates the lumen of the intestine from the inside of the body. Below the epithelium lies the lamina propria, followed by the muscularis mucosae, submucosa, submucosal plexus, circular muscle, myenteric plexus, longitudinal muscle, and the serosa (Ødegaard et al., 2012). In the small intestine finger-like flexible structures, termed villi, extend into the lumen of the intestine and small

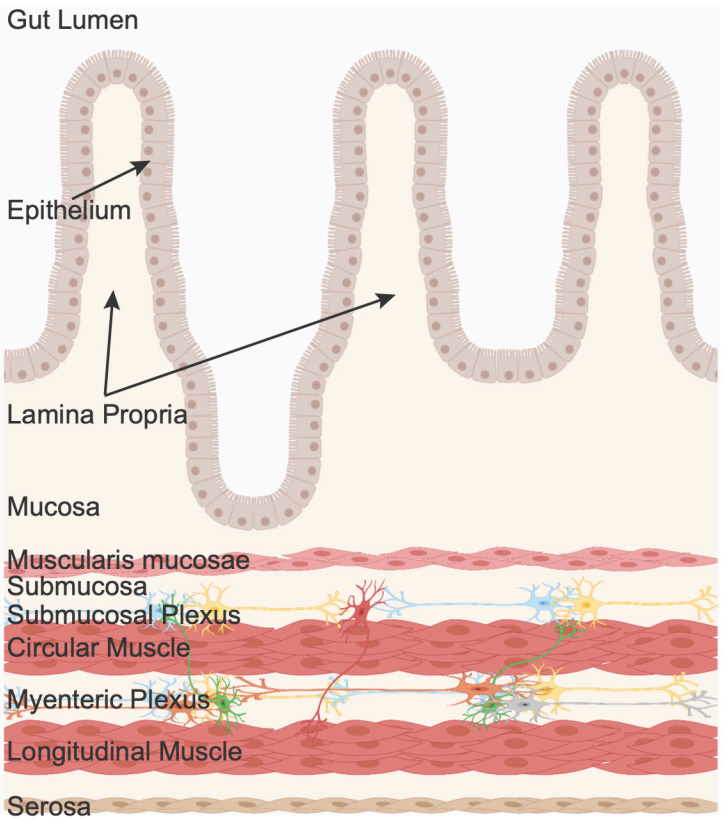

Figure 1.2. General organization of layers of the intestine. Schematic highlighting the different layers and compartments of the intestine that will be discussed in this thesis. Neurons are included to more clearly delineate the submucosal and myenteric plexuses.

invaginations, termed crypts, contain epithelial stem cells. In the cecum and colon, villi are absent and enlarged crypts are present instead (Spit et al., 2018) (Figure 1.3). As one moves from the duodenum to the colon, the bacterial density and diversity increases dramatically, which has a direct impact on intestinal segment function and cellular makeup (Martinez-Guryn et al., 2019; Thursby and Juge, 2017) (Figure 1.3).

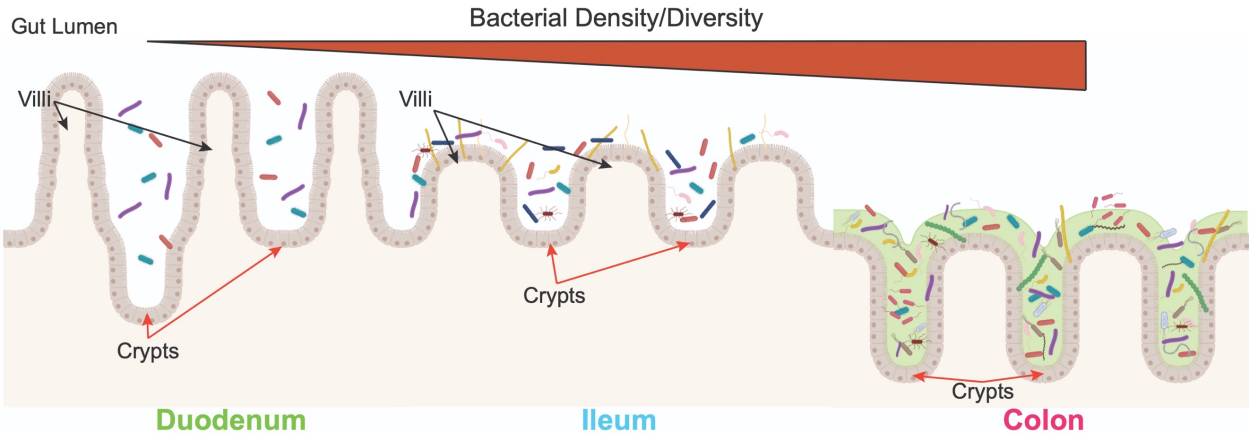

Figure 1.3. General structure and bacterial content in different segments of the intestine. Schematic showing the presence of villi and crypts in the duodenum and ileum, with only crypts present in the colon. In moving from the duodenum to the colon (proximal to distal intestine), the overall density and diversity of the microbiota increases.

1.2 The gut microbiota is a key component of GI function

The mammalian gut microbiota, which is interchangeably called the microbiome, refers to all gut-residing taxa constituting microbial communities, such as bacteria, archeae, fungi and protists (Cani, 2018). For the purposes of this thesis I will use the terms microbiota and microbiome, to indicate only the bacteria in the small and large intestine. The concept that the microbiome is a key component of organismal function has been attributed to Dr. Joshua Lederberg (Hooper and Gordon, 2001), although this credit may be somewhat controversial (Prescott, 2017). A microbiota is uniquely coupled to the GI tract, termed the commensal microbiota, and is present even in nematodes such as *Caenorhabditis elegans* (Zhang et al., 2017). While microbes also serve as a food source in organisms like *C. elegans* (Zhang et al., 2017), they also function to aid in the breakdown of other food sources and can in turn produce metabolites that are beneficial for the host (Martinez-Guryn et al., 2019; Rowland et al., 2018). The number of bacteria

in the human GI tract was originally estimated to be on the order of 10^{14}-10^{15}, however recent work has revised these estimates to bring the number closer to 10^{13} (Sender et al., 2016). Regardless, this still equates to an almost 1:1 ratio with the total number of cells in the human body. As such, we can consider this bacterial community, also known as the commensal microbiota, as a separate organ within the lumen of the intestine.

To reiterate what was stated earlier, the number and diversity of bacteria increases when moving from the proximal to distal direction in the intestine (Martinez-Guryn et al., 2019). The small intestine is high in acid, relatively oxygenated, enriched in antimicrobial peptides, and transports luminal contents at a faster rate than the large intestine. Thus, rapidly proliferating facultative anaerobe bacterial species dominate the small intestine (Martinez-Guryn et al., 2019; Thursby and Juge, 2017). The colon is mostly hypoxic, its epithelial surface hosts a thick mucus layer, and transit of luminal contents is considerably slower. As a result, mainly fermenting anaerobes dominate this area of the intestine (Martinez-Guryn et al., 2019; Thursby and Juge, 2017). The gut microbiota is mainly shaped by diet (Zmora et al., 2019) and host factors such as antimicrobial peptides, bile acids, and mucus (Thursby and Juge, 2017). While Pasteur was wrong in his overall hypothesis that without a microbiota “life would be impossible” (Pasteur, 1885), it has become clear that mammalian physiology is dependent upon the microbiota for ideal function. The gut microbiota in particular has been shown to impact host metabolism (Dabke et al., 2019; Fetissov, 2017), bone development (Zaiss et al., 2019), immunity (Spencer et al., 2019), and neurological function (Fung et al., 2017), all of which can simultaneously impact the development of numerous diseases (Blander et al., 2017; Fung

et al., 2017; Helmink et al., 2019). I will focus on the effects of microbiota as they relate to the ability of the enteric nervous and immune systems to maintain tissue and general host homeostasis.

1.2.1 Microbial metabolites

Beyond their ability to directly interact with host cells, the gut microbiota can produce a wide array of metabolites which in turn can impact host physiology (Levy et al., 2016; Nicholson et al., 2012; Rooks and Garrett, 2016). Combinatorial systems, composed of host-derived molecules that then feed into complementary bacterial strains, lead to the production of metabolites such as short chain fatty acids, secondary bile acids, and choline (Nicholson et al., 2012). The microbiota can also produce host-derived molecules, such as GABA (Strandwitz et al., 2019) or dopamine (Valles-Colomer et al., 2019), and chemicals that mimic host signaling molecules, like N-acyl amides (Cohen et al., 2017). The list of physiologically relevant microbial metabolites is expanding at a rapid pace, and underscore the extent to which the gut microbiota is tied to the regulation of host processes (Chen et al., 2019a). Because our studies led to the discovery that short chain fatty acids can affect gut-associated nervous system, I will provide a brief overview of these immunologically and metabolically relevant metabolites below.

1.2.1.1 Short chain fatty acids

Short chain fatty acids (SCFA) are among the most well-studied microbial metabolites produced in mammals. When fiber is ingested, it remains intact until reaching

the distal ileum, cecum, and colon. There, fermenting anaerobes begin to break down fiber into successively smaller subunits. Three main SCFAs are produced in the distal intestine: acetate, propionate, and butyrate, all saturated aliphatic organic acids containing 2, 3, and 4 carbon atoms respectively (Den Besten et al., 2013). Upon being released in the lumen, SCFAs are rapidly and efficiently absorbed by enterocytes and colonocytes. SCFAs are then released from the basolateral side of the epithelium, where they enter the circulation and eventually make their way to the liver.

The molar ratio of acetate, propionate, and butyrate is approximately 60:20:20 in the colon and stool (Den Besten et al., 2013). Butyrate is primarily utilized as an energy source for colonocytes, thus very little is present in either systemic or portal blood (Koh et al., 2016; Priyadarshini et al., 2018). Propionate is metabolized in the liver, and as such portal blood levels are much higher than in the peripheral circulation. Acetate, on the other hand, is high in both portal and systemic blood, and thus this SCFA is most likely to affect tissues beyond the gut and liver. Of interest, acetate has been demonstrated to cross the blood brain barrier (Frost et al., 2014).

How do SCFA interact with mammalian cells? There are four known receptors for SCFA; free fatty acid receptor 2 (FFAR2 or GPR43), free fatty acid receptor 3 (FFAR3 or GPR41), hydroxycarboxylic acid receptor 2 (GP109a or HCA2), and olfactory receptor 78 (OLFR78) (Koh et al., 2016; Priyadarshini et al., 2018). FFAR2 are $G_{i/o}/G_{\alpha/q,}$ while FFAR3 and GPR109a are $G_{i/o}$ G protein coupled receptors (GPCR). GPCR signaling in OLFR78 is less clear, as there is evidence for both $G_{\alpha/q}$ and $G_{\alpha/s}$ (Priyadarshini et al., 2018). Both FFAR2 and 3 respond to all three SCFA with varying levels of potency, whereas GPR109

only responds to butyrate, and OLFR78 responds to acetate and propionate. These receptors are all expressed in a wide range of tissues but, importantly, they are expressed in intestinal epithelial cells, immune cells, and some populations of peripheral neurons (Priyadarshini et al., 2018). Beyond their role as GPCR ligands, the SCFAs butyrate and propionate have been shown to act as inhibitors of histone deacetylases (HDACs), thus they can epigenetically change mammalian cells (Koh et al., 2016).

Finally, how do SCFA impact mammalian physiology? Thus far, they have been linked with control of host metabolism, gut immunity, cancer, asthma, and changes in the nervous system (Koh et al., 2016). The metabolic influence of SCFA has been attributed to their ability to stimulate production of feeding-related neuropeptides from enteroendocrine cells, activation of intestinal gluconeogenesis, and direct effects on the pancreas or adipose tissue (Priyadarshini et al., 2018). Gut immune cells respond to SCFA to change their cytokine production, inflammatory programming, and can lead to changes in cell-type differentiation such as with CD4 T cells (Koh et al., 2016; Priyadarshini et al., 2018). Effects on the nervous system range from changes in microglia (Erny et al., 2015; Sampson et al., 2016), suppression of feeding (Frost et al., 2014), activation of sympathetic neurons (Samuel et al., 2008), changes in vagal afferent activity (Cuche et al., 2001; Goswami et al., 2018), and modulation of intestinal motility (Priyadarshini et al., 2018). Despite attempts to link SCFA to intestinal physiology, such as control of the gut hormone glucagon-like peptide 1 and resultant effects on motility (Wichmann et al., 2013), the effects of these microbial metabolites on the enteric associated nervous system are still relatively unknown.

1.3 The enteric-associated nervous system

Because enteric nervous system refers to both neuronal and non-neuronal cellular components, and also that the peripheral nervous system contributes a significant proportion of intestinal innervation, we have chosen to use the term enteric-associated nervous system (EANS) to address solely its neuronal compartments. This vast and intricate set of neurons can be broadly divided into two categories: *intrinsic* (neurons that have their cell bodies within the intestinal wall) and *extrinsic* (neurons that innervate the intestine but the cell bodies of which are located outside of the intestine) enteric-associated neurons (EANs).

1.3.1 Intrinsic enteric-associated neurons

Intrinsic enteric-associated neurons are part of the intrinsic enteric nervous system, which is tasked with coordinating muscle movement, blood flow, and secretions within the small and large intestine (Furness, 2012). John Langley was the first to establish that the enteric nervous system was a separate arm of the autonomic nervous system, capable of autonomous operation when separated from the CNS (Langley, 1921). Several cell types comprise this complex network, including interstitial cells of Cajal, enteric glia, and intrinsic enteric-associated neurons (iEAN) (Wood, 2011). iEAN are assembled in ganglia within two distinct plexuses in the intestine; Auerbach's or myenteric plexus (Auerbach, 1864) and Meissner's or submucosal plexus (Meissner, 1857). The ganglia within the myenteric plexus are significantly larger in both size and number of cells per ganglion as compared to the submucosal plexus (Figure 1.4a).

Additionally, the number of iEAN increases when moving from the proximal to distal direction (Figure 1.4a). Both vagal and sacral neural crest cells, which seed the embryonic intestine, contribute to the development of adult iEAN networks (Obermayr et al., 2013). The intrinsic enteric nervous system is composed of a heterogeneous mix of motor neurons, secreto-motor neurons, interneurons, and intrinsic primary afferent neurons (IPANs) (Furness, 2000, 2012). Morphologically, iEAN have been classified into two types, Dogiel Type I and Type II. Type I neurons have a single axon and short club-like dendrites, whereas Type II neurons are typically larger in size and have a smooth cell body with two or more long axons (Qu et al., 2008). Functionally, the traditional method by which iEAN are classified, is termed the "neurochemical code" (Figure 1.4b), which is based on the neuropeptides/neurotransmitters expressed, and reveals that the two enteric plexuses differ in terms of the types of neurons present (Furness, 2000). Over 30 different neuropeptides and neurotransmitters are described to be expressed in iEAN, and in many cases multiple combinations thereof are expressed by a single iEAN. Despite prior key insights into iEAN morphology (Chan et al., 2017), neurochemical coding (Furness, 2000), regional organization (Li et al., 2019b), developmental regulation (Lasrado et al., 2017; Obermayr et al., 2013), single-cell transcriptional profiles (Zeisel et al., 2018), and electrophysiological properties (Carbone et al., 2014), our understanding of the specific roles for iEAN subtypes *in vivo* is particularly lacking. Additionally, the influence of the gut microbiota on iEAN has thus far only been superficially described.

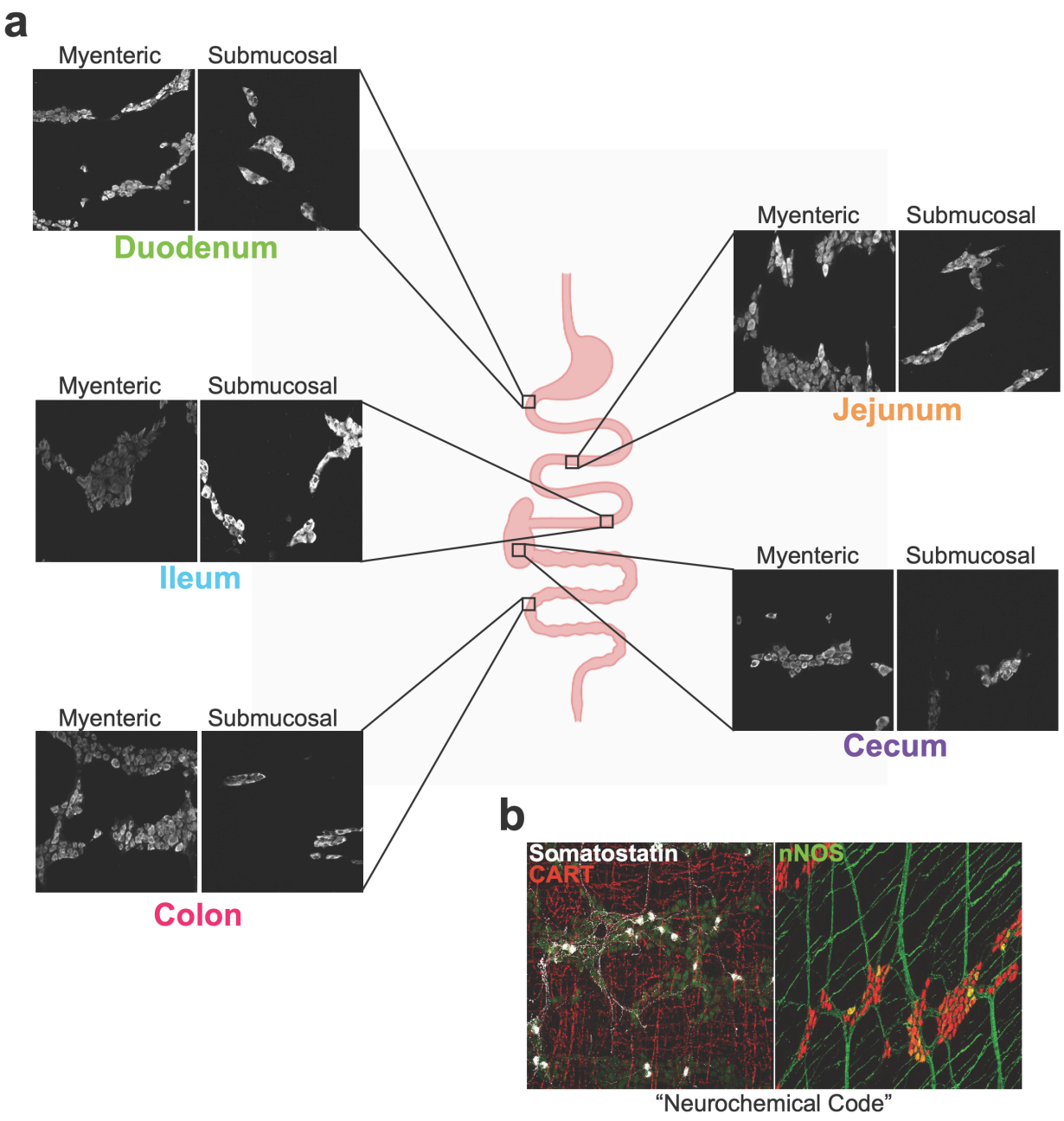

Figure 1.4. Distribution of iEAN within different segments of the intestine. (**a**) Schematic showing the structure of iEAN ganglia within the myenteric and submucosal plexuses of the duodenum, jejunum, ileum, cecum, and colon. (**b**) Representative immunofluorescent whole mount images of the myenteric plexus highlighting the presence of different neuropeptides (SST and CART) and neurotransmitters (NOS) which have been classically used to define subpopulations of iEAN.

1.3.1.1 iEAN neuropeptide populations

Because our findings concerning specific neuropeptides in the small and large intestine specifically relate to host metabolism, I chose to highlight a few of the relevant neuropeptides in the gut for clarity on what is known in the field.

SST

Somatostatin (SST) was first discovered in the ovine hypothalamus, during a screen for growth hormone releasing factor (Reichlin, 1983). It turned out that SST, produced by neuro-endocrine cells in the hypothalamus, was in fact capable of inhibiting growth hormone release as well as thyroid stimulating hormone. In neurons within the central nervous system (CNS), SST is expressed in a prominent population of inhibitory neurons (Yavorska and Wehr, 2016). The inhibitory action of SST is mediated by somatostatin receptors, SSTR1-5, which are $G_{i/o}$ G GPCRs (Theodoropoulou and Stalla, 2013). Peripheral expression of SST has been described in sensory ganglia (Usoskin et al., 2015), sympathetic ganglia (Furlan et al., 2016), the pancreas (Rorsman and Huising, 2018), enteroendocrine delta (D) cells (Lucey, 1986) and iEAN (Gonkowski and Rytel, 2019). While the role of SST in the ENS is thought to be inhibition of motility and secretions mediated through local effects on the myenteric and submucosal plexus iEAN (Gonkowski and Rytel, 2019), the precise function of SST itself or SST+ iEAN populations within the gut is largely unknown due to the lack of tools for cell-type specific modulation.

AGRP

Agouti related peptide (AGRP) is a neuropeptide located primarily in neurons in the arcuate nucleus (ARC) of the hypothalamus and was discovered in 1997 by Ollman and colleagues (Ilnytska and Argyropoulos, 2008). These neurons are responsible for regulating food intake and foraging in adults (Dietrich et al., 2015; Waterson and Horvath, 2015). Further, in neonatal mice they have been described to influence offspring-to-caregiver behavior (Zimmer et al., 2019). Hypothalamic AGRP neurons, which are potently activated by fasting and promote food seeking, are counter-balanced by pro-opionmelanocortin-alpha (POMC) neurons, which are inhibited by fasting and promote satiety (Chen et al., 2015). These populations of neurons release AGRP and melanocyte-stimulating hormones (αMSH) respectively to act on melanocortin receptor 4 (MC4R) (AGRP-antagonist; αMSH-agonist), a G_s-coupled GPCR (Gonçalves et al., 2018). However, the effects of AGRP and POMC neuronal populations on feeding is not solely dependent on melanocortin receptor signaling (Andermann and Lowell, 2017; Chen et al., 2019b; Wu et al., 2012). In the periphery expression of AGRP has been described in adrenal chromaffin cells (Gupta et al., 2017), however it is not known whether cells in the gut, including iEAN, express AGRP.

NPY

In searching for the presence of peptide YY (PYY) in the porcine brain, Tatemoto and colleagues discovered a novel peptide called neuropeptide Y (NPY) (Tatemoto et al., 1982). The receptors for NPY are NPYR (1,2,4,5), all $G_{i/o}$-coupled GPCRs (Li et al., 2019a). Within the CNS, NPY+ neurons are most prominent in the hippocampus, but

hypothalamic NPY neurons are perhaps the most well-studied population, where AGRP is co-expressed in the same population (Li et al., 2019a). As I highlighted above, this population of hypothalamic neurons drives food intake and foraging behavior in adult mice. The specific role for NPY in the hypothalamus is proposed to be the immediate prolongation of stimulatory, or orexigenic, feeding behavior, while AGRP may be involved in driving food intake over longer time-scales (Chen et al., 2019b). In the periphery, NPY is sparsely expressed in the nodose and dorsal root ganglia (NG and DRG, respectively), with significant expression in sympathetic neurons as well as in iEAN in the myenteric and submucosal plexuses of all segments of the intestine (Holzer et al., 2012). NPY released from iEAN and sympathetic neurons can inhibit gastrointestinal motility, as well as electrolyte and water secretion (Holzer et al., 2012). While global manipulations through peripheral administration of NPY and related receptor knockouts have led to key insights into NPY function in the intestine, similar to SST, there is a conspicuous lack of tools to perform organ-specific manipulation to make definitive claims.

CART

The neuropeptide cocaine- and amphetamine- regulated transcript (CART, encoded by *Cartpt*), was first described as part of a screen to identify brain mRNA transcripts that changed after administration of the stimulants cocaine and amphetamine (Douglass et al., 1995). Its role as a key player in metabolism was uncovered when researchers studied expression levels of *Cartpt* in the hypothalamus during fasting or feeding. A marked decrease in hypothalamic *Cartpt* mRNA was noted during fasting, and

further investigation led to the discovery that CART is a potent CNS anorexigenic neuropeptide the expression of which is partly controlled by leptin (Kristensen et al., 1998). In the hypothalamus, CART is co-expressed with POMC in neurons in the ARC, which are potently inhibited by fasting (Chen et al., 2015). Although leptin has been shown to modulate CART+ hypothalamic neurons (Baver et al., 2014), the effects of leptin on glucose and energy homeostasis is through AGRP neurons only (Xu et al., 2018). Despite significant effort to deorphanize the receptor for CART, researchers have only been able to confirm that it likely is a GPCR coupled to $G_{i/o}$ signaling pathways (Lau and Herzog, 2014). Beyond the predominant metabolic role of CART in the ARC, CART protein has also been described in additional brain areas, such as the Edinger-Westphal nucleus, and is widely expressed in the periphery including in the pancreas, NG, and intestine (Lau and Herzog, 2014; Yuan et al., 2016). Expression of CART in iEAN has been reported in both the myenteric and submucosal plexuses in all segments of the intestine (Ekblad, 2006; Ellis and Mawe, 2003). The exact role of CART in the EANS remains unclear, as it appears to not have an effect on motility when applied locally (Ekblad, 2006). Changes in gastric secretion and colonic motility were reported only when CART was delivered by i.c.v. administration, thus the effects of CART on the gut have mostly been shown to be mediated by the CNS (Ekblad, 2006; Lau and Herzog, 2014). While there is some evidence that CART can play a neuro-protective role in the gut (Ekblad, 2006), further work needs to be done to solidify these claims. The widespread expression of CART along the length of the intestine is suggestive of a role in basic intestinal physiology, but

due to a previous lack of tools to properly interrogate this neuronal population in a tissue-specific manner, its role remains thus far unclear.

1.3.1.2 Microbial effects on iEAN

Excitability

The first description of microbial-dependent changes in iEAN was reported by Dupont and colleagues in 1965 (Dupont et al., 1965). They observed that iEAN in the cecum of GF animals were larger in size and displayed lower metabolic activity based upon decreased NADPH diaphorase staining. Similar findings of decreased metabolic activity in iEAN of GF mice have been reported in recent years (Anitha et al., 2012). Altered iEAN excitability in GF mice has also been corroborated by recent literature indicating that IPANs have lower resting membrane potential and prolonged after-hyperpolarization (McVey Neufeld et al., 2013, 2015). These effects could be reversed by conventionalization of adult GF mice with SPF feces. To establish possible causation of these changes in excitability, a recent study found that reduced numbers of serotonin-producing enterochromaffin cells in GF mice, otherwise linked to the presence of spore-forming bacterial strains, could decrease the levels of the immediate early gene cFos, in iEAN in the colon (Yano et al., 2015). They concluded that this decrease in an indirect marker of neuronal activity, coupled with a decrease in serotonin (5-HT), may be a possible explanation for gastro-intestinal motility delays observed in GF mice. Another possible explanation for decreased iEAN activity and delayed motility has been proposed in a recent preprint publication, where bulk nuclei RNA-sequencing of iEAN pointed to a

microbial-influence on aryl hydrocarbon receptor (*Ahr*) expression (Obata et al., 2019). Using viral methods to either remove *Ahr* or modulate its activity in neurons, the authors found they could phenocopy GI transit delays or reverse dysmotility. Despite significant evidence indicating that iEAN are hypoactive and hypoexcitable when the microbiota is absent or significantly reduced, a truly mechanistic explanation has not yet been established.

Development and maintenance

The lack of a microbiota in GF mice has been described to lead to reductions in neuronal number, neurochemical code, and fiber density in the jejunum, ileum, and colon (Anitha et al., 2012; Collins et al., 2014). In contrast, no difference in either parameter was observed in the microbial-sparse duodenum. Neonatal colonization with a consortium of bacteria proposed to recapitulate many properties of the full microbiome, the “altered-Schaedler flora” (ASF), normalized proximal intestine iEAN alterations observed in GF animals (Collins et al., 2014). In line with the findings in GF mice, microbial depletion with antibiotics results in reduced iEAN numbers and alter their neurochemical distribution (Hung et al., 2019). While it had been previously thought that iEAN numbers were set during development, recent work has challenged this notion by demonstrating continuous turnover of iEAN during adulthood in mice (Kulkarni et al., 2017). There are conflicting findings regarding iEAN numbers in GF versus antibiotic-treated mice. For example, a recent study found that GF exhibit no difference in neuronal density in the colon but antibiotic treatment causes a significant reduction (De Vadder et al., 2018). In another study, the authors found no significant changes in the numbers of iEAN in mice kept on

antibiotics from birth (Touré et al., 2019). It is not clear whether these discrepancies result from experimental design or possibly due to differences in microbiota between institutions (Franklin and Ericsson, 2017). Yet, despite varying findings, it is evident that the microbiota can impact the development and ultimate phenotype of iEAN.

How does the microbiota control iEAN development and maintenance? The presence of a tonic bacterial signal acting through neuronal-specific toll-like receptors (TLRs) has been proposed by some groups to control iEAN development (Anitha et al., 2012; Brun et al., 2013). TLRs are a class of innate immune receptors that recognize both pathogen-associated molecular patterns (PAMPs), such as lipopolysaccharide (LPS), or damage associated molecular patterns (DAMPs) from the host, such as heat shock protein or fibrinogen (Satoh and Akira, 2016). Despite the prominent role of TLRs in innate immunity, there is also evidence for TLR signaling in neuronal development (Anthoney et al., 2018). It remains unclear whether TLR detection of microbial products or its intrinsic role in neuronal development is driving the observed changes in iEAN number and cell fate.

Serotonin, or 5-hydroxytryptoptamine (5-HT), is also thought to be a significant player in the development and maintenance of iEAN (Hung et al., 2019; Li et al., 2011; Terry and Margolis, 2017; De Vadder et al., 2018). Gut-derived serotonin accounts for almost 95% of mammalian serotonin levels, the source of which is proposed to be primarily enterochromaffin cells with a minor contribution from iEAN, the production of which is mediated by the enzymes tryptophan hydroxylase 1 (TPH1) and 2 (TPH2) respectively (Terry and Margolis, 2017). A reduction in gut 5-HT is well-documented in

GF or antibiotic treated mice (Hung et al., 2019; De Vadder et al., 2018; Yano et al., 2015), and supplementation with 5-HT or agonists of the serotonin receptor HTR4 can impact neuronal numbers in cases of microbial depletion or in SPF mice (Hung et al., 2019; Liu et al., 2009; De Vadder et al., 2018). However, the use of whole-body knockouts of *Tph1* and *Tph2*, as well as systemic administration of compounds to modulate serotonergic signaling complicate the interpretation of these data. Additionally, a recent preprint documenting single nuclei RNA-sequencing of mouse colon iEAN found no expression of *Tph2* in this tissue-site (Drokhlyansky et al., 2019). These results call into question whether iEAN can actually produce 5-HT as previously thought. Thus, while there appears to be considerable effects of 5-HT on iEAN development and maintenance, it is not yet clear through what mechanism – epithelial or neuronal – this occurs.

Another set of possible iEAN developmental factors could be through the action of muscularis macrophages (MM), which can produce BMP2 (Muller et al., 2014), or enteric glia, iEAN-supportive cells whose numbers are significantly reduced in the absence of a microbiota (Kabouridis et al., 2015). In *Csf1*$^{op/op}$ mice, which lack macrophages, we have previously found that the number of iEAN is significantly increased. However, antibiotic treatment of wild type (WT) mice leads to a significant reduction in MM numbers (Muller et al., 2014). Similarly, GF mice also display reduced numbers of MM (Kang et al., 2020; Mikkelsen et al., 2004). In light of the fact that iEAN numbers are reduced in both GF and antibiotic-treated mice, MM are likely indispensable for microbiota-iEAN effects. With regards to enteric glia, glial-specific diphtheria toxin ablation does not lead to any appreciable impact on iEAN numbers (Rao et al., 2017). We can conclude that these two

iEAN-associated cell types do not appear to be essential mediators of microbiota-effects on steady-state development or maintenance of iEAN. In summary, how the microbiota control iEAN maintenance and survival during development and in adulthood is still an open question in the field.

1.3.2 Extrinsic enteric-associated neurons

Neurons that innervate the intestine, yet have their cell bodies outside of the intestinal wall are termed extrinsic enteric-associated neurons (eEAN) (Uesaka et al., 2016). These gut-connected neurons can be categorized as either sensory (afferent) or

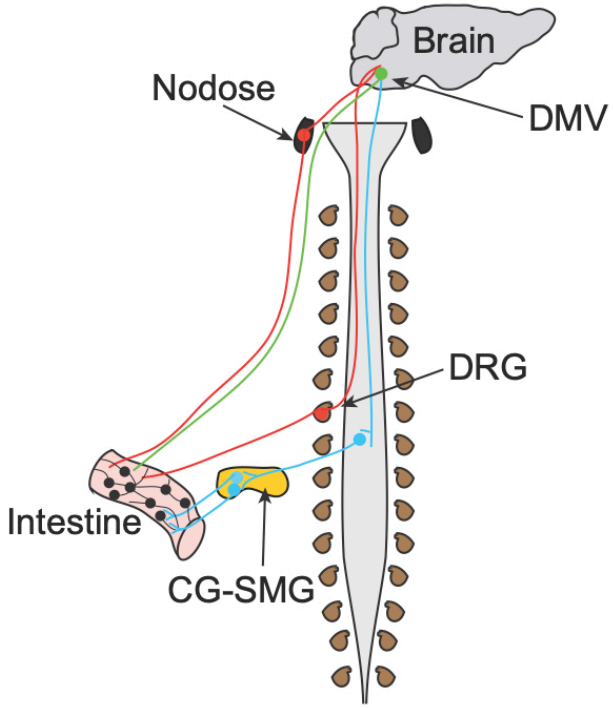

Figure 1.5. eEAN that connect to the intestine. Schematic highlighting the eEAN nodes that are connected to the intestine including the nodose ganglion, dorsal root ganglion (DRG), celiac-superior mesenteric ganglion (CG-SMG), and dorsal motor nucleus of the vagus (DMV).

effector/motor (efferent). Below, I highlight the four major populations of eEAN: the dorsal root ganglion (DRG) (afferent), nodose-jugular ganglion (NG) (afferent), the sympathetic celiac-superior mesenteric ganglion (CG-SMG) (efferent), and parasympathetic neurons of the dorsal motor nucleus of the vagus (DMV) (efferent) (Brookes et al., 2013; Gonella et al., 1987) (Figure 1.5).

1.3.2.1 Afferent Innervation

Dorsal Root Ganglion

The primary source of sensory innervation in mammals are derived from DRG, located on the dorsal side of the spinal column (Usoskin et al., 2015). DRG located in the thoracic, lumbar, and sacral vertebral levels innervate the length of the small and large intestine (Brookes et al., 2013; Costa et al., 2004). A broad array of mechanosensitive, chemosensitive, and nociceptive DRG neurons monitor information from the intestinal epithelium, mucosa, vasculature, lymphatics, muscle, and iEAN (Brookes et al., 2013; Hockley et al., 2019). Gut bacteria or bacterial products can modulate DRG neurons to influence visceral pain, motor function, and immune responses (Lai et al., 2019; Lomax et al., 2019). Bacterial effects on DRG neurons can occur through TLR activation or indirectly by way of inflammatory molecules produced by the host (Lomax et al., 2019). Direct effects of bacterial products have also been reported, such as the insertion of the *Staphylococcus aureus* pore forming toxin α-hemolysin into the membrane of DRG neurons to induce calcium influx (Chiu et al., 2013) or activation of PAR-4 on DRG neurons by serine proteases that are largely derived from a single human commensal

bacterium which leads to neuronal inhibition (Sessenwein et al., 2017a). Based on the anatomical distribution of afferents and their inherent capacity to detect bacteria, further physiological or immune-related roles for bacterial interactions with gut-specific DRG afferents are likely.

Nodose-Jugular Ganglion

The vagal nerve serves as a conduit for sensory information from the periphery to the CNS and parasympathetic instructions from the CNS. In composition, the vagus is approximately 90% afferent and only 10% efferent indicating an overwhelming sensory capacity (Chang et al., 2015). The ganglion that contains vagal sensory neurons is known as the nodose-jugular ganglion in mice. Despite its fusion in mice, the molecular identity of nodose and jugular sensory neurons is clearly delineated by their expression of the transcription factors *Phox2b* and *Prdm12* respectively (Kupari et al., 2019). Nodose sensory afferents from all organs project to the nucleus tractus solitarius (NTS) and area postrema (AP) in the brainstem (Chang et al., 2015; Han et al., 2018; Williams et al., 2016). In the intestine, vagal afferent fibers are present in the *muscularis*, mucosa, and villi where they are positioned next to epithelial cells at the interface of the gut and the lumen (Han et al., 2018; Kaelberer et al., 2018; Williams et al., 2016). Reports are conflicting regarding the distribution of vagal afferents along the length of the intestine, with some studies claiming overwhelming proximal distribution (Berthoud, 1990; Williams et al., 2016) and others indicating that the distal intestine also receives significant vagal afferent innervation (Wang and Powley, 2007, 2000). These conflicting observations may

simply be the result of different neuronal tracing methods used, but further efforts are needed to clarify these discrepancies.

While concepts of gut-brain communication have been proposed since the 19th century (Mathias, 2018; Miller, 2018), significant interest in the impact of the microbiota on the CNS was sparked by a study in 2004, by Sudo and colleagues, which described an exaggerated hypothalamic-pituitary-adrenal response to stress in GF mice that could be modulated by gnotobiotic manipulation (Sudo et al., 2004). The field of gut-brain research has since expanded dramatically, but the mechanisms by which the microbiota can influence behavior and other CNS-driven physiological effects remain elusive (Mayer et al., 2015; Rhee et al., 2009). Due to its ability to transmit intestine-specific sensory information to the CNS, the vagus nerve and its associated afferent neurons are proposed as one route by which microbes can influence the brain (Bonaz et al., 2018). Gut-projecting nodose afferents are capable of detecting mechanical, hormonal, and nutrient derived intestinal stimuli (Han et al., 2018; Kaelberer et al., 2018; Williams et al., 2016). Thus, the ability of microbes to signal through the vagus are proposed to be mediated by the effects of the microbiota on intestinal motility, neuropeptide/neurotransmitter release from enteroendocrine cells (such as glucagon-like peptide 1, GLP-1), and changes in host metabolism (Cryan et al., 2019). It is also possible that gut-resident microbes can have a direct effect on vagal afferents through metabolites, as microbial SCFAs can modulate vagal nerve activity (Cuche et al., 2001; Goswami et al., 2018; Lal et al., 2001; Perez-Burgos et al., 2014). A large proportion of gut-brain research has been devoted to understanding how the microbiota impacts the CNS and related disorders, however

whether effects on the CNS and the role of the vagus play any part in regulating gut physiology is not clear.

1.3.2.2 Efferent Innervation

DMV (Parasympathetic nervous system)

Vagal motor neurons, the parasympathetic arm of the autonomic nervous system, are contained within the dorsal motor nucleus of the vagus (DMV) in the brainstem (Travagli and Anselmi, 2016). Retrograde tracing from the intestine shows that innervation to different intestinal segments are organized into rostro-caudal columns within the DMV (Browning et al., 2017). These neurons are cholinergic in nature and they form dense intra-muscular and intra-ganglionic axonal arrays in the intestine (Browning and Travagli, 2019; Powley, 2000). In synapsing on iEAN, vagal efferents can exert either an excitatory or inhibitory effect on the intestine. These diverging effects are due to either direct cholinergic innervation of the smooth muscle or activation of cholinergic (excitatory) and non-adrenergic non-cholinergic (inhibitory: adenosine triphosphate or neuronal nitric oxide) post-synaptic iEAN (Travagli et al., 2006). Due to significant connections between the NTS/AP and the DMV, it is likely that vagal sensing of the microbiota can also impact parasympathetic input to the periphery including the intestine (Browning and Travagli, 2019; Travagli et al., 2006).

CG-SMG (sympathetic nervous system)

The sympathetic nervous system (SNS) is composed of the sympathetic chain, or prevertebral ganglia, and paravertebral ganglia, such as the celiac-superior mesenteric

and inferior mesenteric ganglia. Recent work has also determined that what was long presumed to be spinal cord derived parasympathetic efferent input to visceral organs, such as the intestine, is in fact sympathetic in nature (Espinosa-Medina et al., 2016). This redefinition of sacral innervation has broad implications, as it may be that certain organs receive only sympathetic autonomic control (Adameyko, 2016).

The catecholamine, norepinephrine (NE) also termed noradrenaline (NA), is the primary neurotransmitter utilized by the SNS (Ernsberger and Rohrer, 2018). Key enzymes for the production of NE are tyrosine hydroxylase (TH) and dopamine beta hydroxylase (DBH) (Ernsberger and Rohrer, 2018). Its effects are mediated by binding to α- and β-adrenergic receptors on post-synaptic neurons and other cells. Sympathetic ganglia have traditionally been regarded as homogenous in terms of neuronal subtype, but recent single-cell sequencing of sympathetic ganglia has established significant diversity of neuronal subtypes with respect to their relevant neurotransmitters, neuropeptides, and motor output in the periphery (Furlan et al., 2016).

The small and large intestines both receive sympathetic input from the celiac ganglion (CG) and superior mesenteric ganglion (SMG). In rodents the CG and SMG are fused to form a large complex, the celiac-superior mesenteric ganglion (CG-SMG), although in rats the right CG can be found as a separate entity (Berthoud and Powley, 1993). The neuronal makeup of the CG-SMG is less diverse than the sympathetic chain, and is predominantly comprised of TH+ and NPY+ neurons (Kaestner et al., 2019).

The effects of sympathetic innervation to the intestine are thought to be primarily inhibitory, slowing GI motility and secretory function (Browning and Travagli, 2014;

Gonella et al., 1987; Straub et al., 2006) foremost through direct inhibition of iEAN networks, although there is sparse innervation of the longitudinal and smooth muscle (Burnstock and Costa, 1973; Furness and Costa, 1974; Tack and Wood, 1992; Womack et al., 1988).

The effect of the microbiota on the gut SNS has not been studied, although dysbiosis has been correlated with increased sympathetic activity in rodent models of hypertension (Zubcevic et al., 2019) and microbiota-derived SCFA can interact with their cognate receptors on sympathetic neurons to modulate activity (Kimura et al., 2011). The control of gut-projecting sympathetic ganglia can come from several proposed inputs: spinal cord (sympathetic preganglionic), end-organ (viscerofugal or intestinofugal), or parasympathetic (vagal). I will further describe these sympathetic inputs in the following sections. While the effect of NE on gut motility and secretions has been well established, the extensive sympathetic innervation of the GI tract is suggestive of additional effects on basic gut physiology and perhaps the large immune cell reservoir within the intestine. It is also unclear what signals can drive gut-specific or other CG-SMG sympathetic activation and if the microbiota plays a role especially in light of prior work highlighting the effects of SCFA on other sympathetic neuronal populations (Samuel et al., 2008).

Sympathetic Preganglionic Neurons

Sympathetic preganglionic neurons are monosynpatically connected to paravertebral sympathetic neurons, cholinergic in nature, and are located primarily in the interomediolateral (IML) column of the spinal cord (Deuchars and Lall, 2015). These IML neurons in turn can receive input from visceral sensory DRG neurons or from descending

brainstem premotor neurons (Ueno et al., 2016). Work on high spinal cord injury has demonstrated the sympatho-excitatory nature of visceral sensory input, while highlighting the presence of tonic top-down sympathetic inhibition (Duale et al., 2017; Prüss et al., 2017; Ueno et al., 2016).

Viscerofugal Neurons

A small percentage of iEAN are proposed to be viscerofugal (also termed intestinofugal), and are defined as neurons with cell bodies within the wall of the intestine that send axons to extra-intestinal targets, including the CG-SMG (Messenger and Furness, 1992). The existence of viscerofugal neurons was first suggested by the work of Bayliss and Starling in 1899, who noted that manipulation of the canine intestine in one location could induce a potent reflexive inhibition in a distal segment of the intestine (Bayliss and Starling, 1899). Control of this intestino-intestinal inhibitory reflex was linked to the CG-SMG, as its removal abolished reflex inhibition but interfering with CNS-derived signals had no effect (Semba, 1954). Identification of viscerofugal neurons was first achieved by back-filling of damaged mesenteric nerves, which revealed a sparse population of neurons in the myenteric plexus (Hibberd et al., 2012). The density increases moving from the proximal small intestine (low density) to the distal large intestine (highly concentrated) (Luckensmeyer and Keast, 1995). Prior work also highlighted the mechanosensitive properties of viscerofugal neurons in *ex vivo* preparations (Brookes et al., 2013; Hibberd et al., 2012, 2014; Palmer et al., 2016). Based upon their anatomical projection to the CG-SMG and mechanosensitive properties, it was proposed that viscerofugal neurons are responsible for stretch-mediated relaxation that

would explain the original observations of Bayliss and Starling (Hibberd et al., 2014). Despite this hypothesis, experimental evidence for this reflex is lacking *in vivo* and the possibility of other viscerofugal-sympathetic controlled reflexes beyond the intestine has not been suggested.

Parasympathetic

Anterograde labeling of neurons in the DMV revealed vagal efferent innervation of CG-SMG of the rat, suggesting possible vagal control of sympathetic neurons (Berthoud and Powley, 1993, 1996). Indeed, this anatomical tracing was later adopted to explain the anti-inflammatory effects of vagal nerve stimulation, termed the cholinergic anti-inflammatory pathway, which is proposed to indirectly modulate splenic macrophages and T-cells via the CG-SMG (Rosas-Ballina et al., 2008). Although this anatomical connection has been demonstrated, whether DMV neurons can drive sympathetic activity has never been formally tested.

1.4 Enteroendocrine cells, neuropods, and tuft cells

Although there is dense mucosal and epithelial innervation of the intestine, nerve fibers do not extend between epithelial cells to directly sense the lumen (Hao et al., 2019). Thus, some luminal signals detected by the EANS, including from microbes, are derived indirectly through sensing by a particular a set of sensory epithelial cells (Gribble and Reimann, 2016). Enteroendocrine cells (EECs) and the newly termed neuropod cells (Kaelberer et al., 2018; Worthington et al., 2017), are specialized epithelial cells that line the GI tract and are tuned to detect a large number of luminal stimuli. The stomach has

an array of EECs that allow for fine-tuned release of gastric enzymes and acid, such as G cells that produce gastrin (Worthington et al., 2017). In the upper intestine there are I, K, and S cells (releasing cholestocystokinin (CCK), gastric inhibitory peptide, and secretin respectively), which are primarily tasked with detection of nutrients and subsequent release of hormones. The distal small intestine and large intestine contain D, L and enterochromaffin (releasing somatostatin, GLP-1, and 5-HT respectively) cells that respond to luminal signals such as bile acids, glucose, and microbial metabolites like short chain fatty acids (SCFA) (Worthington et al., 2017). While much of the research on EEC has focused on local paracrine or humoral neuropeptide or neurotransmitter effects, recent work on enterochromaffin cells and CCK+/PYY+ EECs has demonstrated that specific subsets of EECs are electrically excitable and in some cases are synaptically connected to sensory afferent neurons (Bellono et al., 2017; Kaelberer et al., 2018). Based on the synaptic connectivity of some EECs, Bohorquez and colleagues have proposed a new term to describe these cells, neuropod cells. EECs also have a role in modulating the immune system and intestinal inflammation through release of not only neuro-modulatory molecules, but cytokines as well (Worthington et al., 2017). Another type of epithelial secretory sensory cell, termed tuft cells, has received recent attention due to its capacity to control type 2 immune responses to intestinal helminth infections (Ting and von Moltke, 2019). Due to their direct exposure to luminal microbes and associated metabolites, EECs, neuropod cells, and tuft cells are critical microbial sensors whose effects on the EANS are only beginning to be appreciated.

1.5 Diversity and breadth of the GI immune system

The intestine is continuously exposed to foreign antigen derived from ingested food, the commensal microbiota, and potential pathogens. The vast innate and adaptive immune cell repertoire in the intestine is necessary to properly balance tolerance to commensal microbes and food antigens, with resistance to potentially harmful microbes or toxins (Faria et al., 2017) (Figure 1.6). The epithelium is patrolled by intraepithelial lymphocytes, dendritic cells, and macrophages. The lamina propria is populated by macrophages, dendritic cells, innate lymphoid cells (ILCs), CD8 T cells, B cells, and multiple populations of CD4 T cells. Further specialization of the intestinal immune system is evident with the presence of organized gut associated lymphoid tissues such as Peyer's Patches and tertiary lymphoid follicles, which allow for local germinal center formation

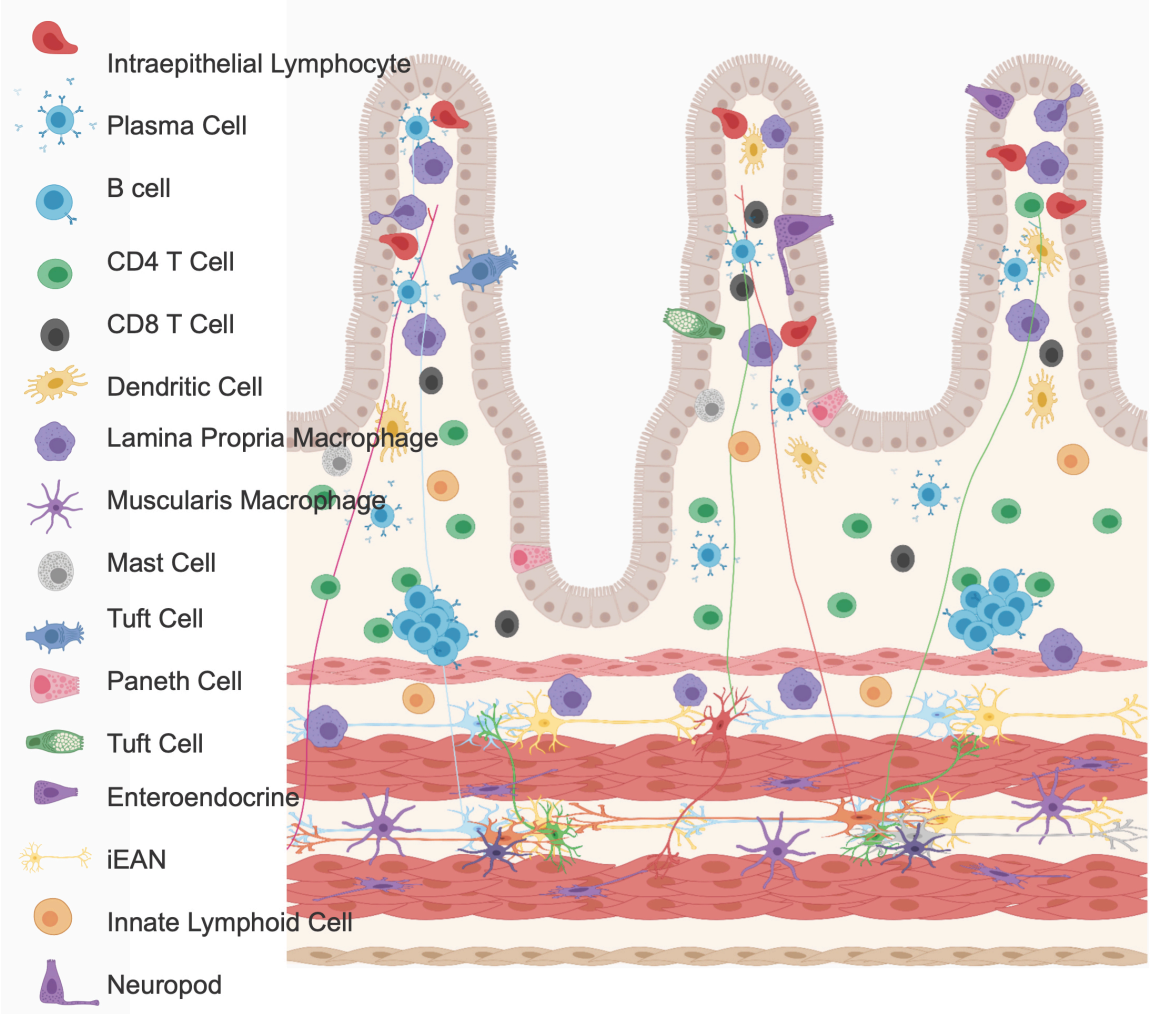

Figure 1.6. Breadth of the mucosal immune system. Schematic showing the relative organization of the layers of the intestine and the immune cells that inhabit each of these compartments.

and resultant antibody secretion (Perez-Lopez et al., 2016). Both the microbiota and EANS can have a significant impact on the mucosal immune system (Yoo and Mazmanian, 2017), however the cellular heterogeneity and complex anatomy of the lamina propria complicates the study of microbiota-neuro-immune interactions. The myenteric plexus, in contrast is primarily populated by macrophages and only sparsely by other immune cells. Thus, these macrophages in the *muscularis* of the intestine, which we will define later in this chapter, present an ideal model in which to study potential

interactions with the EANS, based upon their proximity and almost exclusive access to neurons. Before delving into intestinal macrophages, we will briefly highlight an important sensory component of intestinal immunity, the inflammasome, which we will find plays an unexpected role in the gut in a later chapter.

1.5.1 Inflammasome

The initial description of the inflammasome was put forth by Tschopp and colleagues (Martinon et al., 2002), when they described a high molecular weight protein complex that was capable of generating the pro-inflammatory cytokine, interleukin 1β (IL-1β) through cleavage of its proform. Activation of the inflammasome is dependent on receptors, such as nucleotide binding oligomerization domain (NOD), leucine-rich repeat (LRR)-containing protein (NLRP) family members (Broz and Dixit, 2016). These proteins bind to specific bacterial components, such as lipopolysaccharide, or respond to damage signals in the cell, whereupon they recruit other components of the inflammasome to trigger the production of IL-1β and interleukin 18 (IL-18). The production of these cytokines may also be accompanied by the cleavage of gasdermin D (GSDMD), which forms pore-like structures that insert into the cell membrane to initiate a form of cell death known as pyroptosis (Broz and Dixit, 2016; Tsuchiya et al., 2019).

We can broadly define inflammasome pathways as either canonical or non-canonical. In the canonical inflammasome pathway, caspase-1 cleaves pro-IL-1β, pro-IL-18, and GSDMD, leading to the release of cytokines and in some cases pyroptosis. In the non-canonical inflammasome pathway, which utilizes caspase-11, cleavage of interleukin

cytokine proforms is not thought to take place, while GSDMD cleavage is possible (Broz and Dixit, 2016). While the predominant NLR receptor, acting through the canonical inflammasome, is NLRP3 in the intestine, a recently described member, NLRP6, has gained attention in the gut (Levy et al., 2017; Wlodarska et al., 2014). NLRP6 is highly expressed in intestinal epithelial cells, where it is proposed to have an effect on IL-18 and mucus production, which ultimately impact the commensal microbiota (Levy et al., 2017). These findings have recently been challenged, as several groups have shown that NLRP6 does not actively shape the microbiota (Lemire et al., 2017; Mamantopoulos et al., 2017). Activation of the NLRP6 inflammasome can be controlled by microbial metabolites such as the polyamine spermine, or by host derived factors like histamine (Levy et al., 2015). Despite insights into how NLRP6 is shaped by the local environment, including the microbiota, the exact ligands that activate this inflammasome are still under investigation. Salmonella can directly active NLRP6 in macrophages, and it was recently suggested that lipoteichoic acid, a component of gram-positive bacteria, may also be an activating ligand (Hara et al., 2018). Although there has been intense interest in this inflammasome component, the true function of NLRP6 in the intestine is still an open question.

1.5.2 Intestine macrophage populations

Tissue-resident macrophages represent a highly heterogeneous cell population able to sense and quickly adapt to environmental cues (Hine and Loke, 2019). Initial descriptions of intestinal macrophages were the result of whole tissue preparations where

physical, or phenotypical, separation between macrophage populations residing in the different layers of the intestinal wall was not routinely performed. Recent work has shown that within the human and murine intestine, macrophages can be defined by their anatomical location, broadly divided into mucosal or lamina propria macrophages (LpM) and muscularis macrophages (MM) (Bujko et al., 2018; Muller et al., 2014; De Schepper et al., 2018) – although functionally distinct populations likely exist in the epithelium, submucosal and serosal regions (Bujko et al., 2018; De Schepper et al., 2018). We will highlight recent work concerning the origin, phenotype and function of macrophages residing in the different layers of the intestine.

Origin and maintenance of intestinal macrophages

Intestinal macrophages, in contrast to other murine tissue-resident macrophages, are thought to be continuously replaced by circulating monocytes through a process known as the “monocyte waterfall”, and evidence has recently emerged that this step-wise differentiation is also present in humans (Bain and Schridde, 2018; Bain et al., 2014; Bernardo et al., 2018). As an early population of embryo-derived macrophages are turned over during development, monocytes, defined as Ly6C^{hi} CD64- CX3CR1^{int} MHCII- (P1), enter the gut where they begin to transition through three subsequent stages of differentiation, P2-P4, becoming mature CD64+ CX3CR1^{hi} MHCII^{hi} macrophages (Bain and Schridde, 2018; Bain et al., 2014). Although fractalkine receptor (CX3CR1) is a critical mediator of murine intestinal macrophage function, macrophages in the intestine of humans do not express significant levels of this receptor during homeostasis (Bernardo

et al., 2018). Recent work by two different groups has challenged the concept of continuous replenishment by identifying a population of early-seeded, long-lived tissue-resident intestinal macrophages not replaced by circulating monocytes (De Schepper et al., 2018; Shaw et al., 2018). Flow cytometric phenotyping and fate mapping experiments in mice indicated the existence of macrophages that were present at birth and displayed little to no turnover as the animals aged (De Schepper et al., 2018; Shaw et al., 2018). Observations from human patients receiving intestinal transplants also identified a population of long-lived macrophages that differ from those readily replaced by circulating monocytes (Bujko et al., 2018).

Macrophages in the intestine express high levels of colony stimulating factor receptor (CSF1R), and targeting of CSF1 or CSF1R by genetic or pharmacologic approaches results in a complete lack of macrophages in the gut (Avetisyan et al., 2018; Cipriani et al., 2018; Muller et al., 2014). Sources of CSF1 are thought to include nestin+ stem cells in the bone marrow systemically (Lavin et al., 2015), or non-hematopoietic compartments within the intestine, including endothelial cells and interstitial cells of Cajal in developing mice, or intestinal crypts and enteric neurons in the adult, the latter postulated to be age- and partially microbiota-dependent (Avetisyan et al., 2018; Muller et al., 2014). Although CSF1 is the major driver of macrophage recruitment and maintenance, additional factors have been reported, including CD11c-cell intrinsic Notch signaling in the small intestine, macrophage-secreted monocyte chemoattractants, and TGF-β signaling in the colon (Ishifune et al., 2014; Schridde et al., 2017). Beyond the role for local growth factors and recruitment cytokines, the presence of the microbiota is a

critical mediator of intestinal macrophage recruitment and differentiation. Both monocyte-derived and tissue-resident macrophages are decreased in number in mice that lack a microbiota, or in mice that that are acutely depleted of a microbiota with antibiotics (Bain et al., 2014; Muller et al., 2014; Shaw et al., 2018).

The basic mechanisms by which LpM and MM seed the tissue are likely similar, however there appears to be a clear difference in the balance of macrophage composition, as MM were recently described to primarily originate from a long-lived subset rather than being monocyte-derived (De Schepper et al., 2018). This, coupled with the fact that the lamina propria and muscularis comprise very distinct niches, has led to the recategorization of intestinal macrophages based upon their location within the tissue. It remains to be seen whether this anatomical segregation within the intestine can further impact not only how macrophages can regulate tissue physiology, but their immune function as well.

1.5.2.1 Lamina propria macrophages

In the initial description of the intestinal villus as a unit in 1959 by electron microscopy, Karlin and colleagues first described the presence of LpM (Palay, 1959). These macrophages line the intestinal epithelium where they are ideally positioned to sample luminal antigens, phagocytose dead cells, and eliminate pathogens that succeed in crossing the epithelial layer. LpM are mostly composed of macrophages derived from the monocyte waterfall, with a smaller contribution of long-lived macrophages compared to deeper layers of the intestine (De Schepper et al., 2018). They are classically defined

as CD64+ CD11c+ MHCII^{hi}, and in mice are CX3CR1^{hi}. Intravital imaging from our work has shown that these sessile macrophages have rapid and dynamic membrane ruffling and pseudopod extension (Gabanyi & Muller et al., 2016). LpM pseudopods can form transepithelial dendrites (TEDs) that efficiently cross the epithelium to sample the intestinal lumen and capture potential pathogens, a process that is dependent on CX3CR1 expression in mice, but may be antigen-dependent (Chieppa et al., 2006; Niess et al., 2005; Vallon-Eberhard et al., 2006). Due to their unique positioning in a tissue continuously exposed to foreign antigen, we found that LpM possess a more pro-inflammatory transcriptional profile than their muscularis counterparts (Gabanyi & Muller et al., 2016). Regardless, LpM are also precisely equipped to be tolerogenic in nature, endowing the balance between pathogen clearance and the maintenance of tissue integrity.

Recent work has illustrated that interactions with resident microbial species play a key role in balancing proinflammatory and tolerogenic responses in LpM (Danne et al., 2017; Hayashi et al., 2013; Kim et al., 2018). Additional input may also come from neuronal interactions, as LpM are in close apposition with nerve fibers in the intestinal villi and mucosa (Palay, 1959; De Schepper et al., 2018), and they have been shown to express receptors for neurotransmitters or neuropeptides, such as vasoactive intestinal peptide (VIP) (Buckinx et al., 2017; Gabanyi & Muller et al., 2016). A recent report showed that in the context of experimental food allergy, stimulation of the vagus nerve significantly improved intestinal inflammation, and this was associated with an increase in allergen uptake by CX3CR1^{hi} LpM, suggesting a role for a neuron-macrophage axis to dampen

tissue damage during food allergy (Bosmans et al., 2019). Despite these descriptions and literature suggesting a role for neuropeptides in general modulation of macrophage inflammatory responses (Carrión et al., 2016a; Nijhuis et al., 2010; Ran et al., 2015), a specific function for neuron-LpM interactions is largely lacking in experimental evidence, as opposed to their muscularis counterparts.

1.5.2.2 Muscularis macrophages

Macrophage-like cells were first observed in the muscularis externa of the intestine by Mikkelsen and colleagues in 1982 through analysis of electron microscopy images (Mikkelsen et al., 1985; Rumessen et al., 1982). Following this initial observation, these cells were defined to be macrophages present in the serosal, circular, and longitudinal muscle layers with a significant proportion in the myenteric or Auerbach's plexus containing iEAN. Through our studies we find that MM display two distinct morphologies, bipolar and stellate, and are intimately associated with cell bodies and processes of both glia and neurons (Gabanyi & Muller et al., 2016; Mikkelsen et al., 1985). Phenotypically, they can be defined by their high expression of MHCII, CD163, and CX3CR1 (Muller et al., 2014). In the steady state, we observed that they do not migrate through the tissue and display slow continuous remodeling of their dendritic-like pseudopod processes (Gabanyi & Muller et al., 2016). In comparison to LpM, a large proportion of MM are composed of early-seeded macrophages of both bone marrow and embryonic origin (De Schepper et al., 2018). Despite their description close to four decades ago, the function of MM remained relatively unknown until recent work that has established these

macrophages as key players in gut function and tissue homeostasis, with a particular emphasis on gut motility. As stated earlier, the only known impact of the microbiota on MM is a significant decrease in number and a change in the production of BMP2, whose effects we will highlight in the following section (Bain et al., 2014; Muller et al., 2014; Shaw et al., 2018).

1.6 Neuro-immune interactions in the gut

The enteric nervous system and immune systems are the primary sensory units that can detect, integrate, and respond to changes in the intestinal tissue. Both systems have an innate capacity to rapidly respond to signals and store information for subsequent recall (Veiga-Fernandes and Mucida, 2016). Modulation of the nervous system, specifically the vagal nerve, has been shown to dampen inflammation in the context of colitis (Payne et al., 2019). Thus, it is not surprising that interactions between the nervous and immune systems are key to the maintenance of GI homeostasis. Recent work in the intestine has shown that neurotransmitters and their receptors are expressed by immune cells, and that neurons can sense and influence immune pathways.

1.6.1 Innate lymphoid cells

Innate lymphoid cells (ILCs) are emerging as a population of gut-resident immune cells with significant interactions with the immune system. Veiga-Fernandes and colleagues expanded on their initial findings of the impact of rearranged during transfection proto-oncogene (RET) on hematopoetic stem cells, to show that RET

signaling was necessary for the development of gut ILC3s that produce interleukin-22 (IL-22) (Ibiza et al., 2016). Enteric glial cells that express RET ligands such as glial derived neurotrophic factor (GDNF), were found to be critical for the maintenance of ILC3s in the intestine and their production of IL22. Following this seminal finding, subsequent work in gut ILCs has shown that the neuropeptide neuromedin U (NMU) and NE are critical to activate and dampen ILC2 immune responses respectively during helminth infection (Cardoso et al., 2017; Klose et al., 2017; Moriyama et al., 2018; Wallrapp et al., 2017).

1.6.2 Muscularis macrophages

1.6.2.1 Steady State

Motility

The original concept of macrophage contribution to GI motility was put forth by groups studying models of sepsis and POI. Possible neuro-immune contributions to motility were suggested by work in which high resolution light-microscopy at steady state depicted the extent to which MM are positioned within the smooth muscle and in close apposition to EAN (Phillips and Powley, 2012). Additional studies have since established that MM are in close contact with enteric neurons within the myenteric and submucosal plexuses (De Schepper et al., 2018). We demonstrated a direct role for MM in steady state peristalsis through an antibody-mediated MM-preferential depletion, which led to significant changes in colonic motility (Muller et al., 2014). In comparing transcriptional profiles of LpM to MM, among the most differentially expressed genes, bone morphogenetic protein 2 (BMP2) was found to be one of the main drivers of steady state

MM control of GI motility (Muller et al., 2014). BMP2 was shown to impact the generation of colonic migrating motor complexes in the large intestine, an effect that was mediated by BMP2 signaling through intrinsic EANs expressing BMPRIIα. In conjunction with observations of inflammation-associated dysmotility, these studies established a steady state role for MM in the regulation of peristaltic activity.

Neuronal development and maintenance

In mice lacking all macrophages, such as *Csf1*$^{op/op}$ mice, we have previously observed an increase in numbers of enteric neurons, possibly due to a reduction in MM-derived BMP2 (Cipriani et al., 2019; Muller et al., 2014). MM developmental control of neuronal numbers also appears specific to subpopulations of enteric neurons. For example, in the case of the stomach, the number of nNOS-expressing neurons are preferentially controlled by MM (Cipriani et al., 2018). Recent work has challenged the idea that enteric neuronal numbers are set developmentally. Instead, enteric neurons may be continuously turned over during adulthood. MM were shown to continuously phagocytose dying neurons, a process that may be necessary to maintain appropriate numbers of enteric neurons (Kulkarni et al., 2017). During aging, MM upregulate pro-inflammatory markers and this phenotypic change in MM during aging was linked to a macrophage-intrinsic decrease in the immune-regulatory forkhead transcription factor FOXO3, resulting in a decline in enteric neural stem cell populations (Becker et al., 2017). However, the exact nature of MM contribution to neuronal numbers in the adult remains unclear, although one group has recently found that MM ablation can lead to rapid neuronal degeneration (De Schepper et al., 2018). These findings may be particularly

relevant in clinical cases of hypo-, hyper-, or agangliosis, where large changes in enteric neuronal numbers can lead to intestinal pathology, as observed in pseudo-obstruction or even irritable bowel syndrome (Heuckeroth, 2018). Although further work is needed to link the above-mentioned studies that span a wide range of experimental contexts, a multifaceted role for MM in enteric neuronal differentiation and support is becoming evident, a subject that we will return to in further detail later in this thesis.

1.6.2.2 Inflammation

Bauer and colleagues in the late 1990s focused on clinical conditions associated with GI dysmotility, to better understand possible functions of MM. They found that release of LPS in sepsis resulted in MM activation and upregulation of lymphocyte activation marker 1 (LFA-1), and correlated with a profound decrease in intestinal motility (Kalff et al., 2019). An increase in LFA-1+ MM was also characterized by a large influx of immune cells, predominantly neutrophils (Farro et al., 2017; Pohl et al., 2017). In turn, a recent study suggested that the immune infiltrate in post-operative ileus (POI), a condition where intestine manipulation during surgery leads to a temporary cessation in peristalsis, is driven by activation of MM. The study found that depletion of macrophages improved the symptoms of POI in murine models (Farro et al., 2017). Additionally, cholinergic stimulation of macrophages, in part derived from vagal efferent input to enteric neurons, has been described to reduce neutrophil and additional macrophage recruitment, ameliorating symptoms in POI (Costes et al., 2014; de Jonge et al., 2005; Kimura et al., 2019). The understanding of possible effects of MM activation on gut motility is not limited

to POI. In the context of diabetes induced gastroparesis, MM-derived inflammatory cytokines, including IL-6, TNF-α and IL-1β, seem to contribute to the loss of the pacemaker cells in the muscularis, the interstitial cells of Cajal (ICC) (Cipriani et al., 2018). These findings clearly implicate the pro-inflammatory potential of MM in dictating subsequent inflammation-induced dysmotility. What remains unaddressed in these studies is whether MM-EAN interactions play any role in the response to an enteric infection.

1.7 Defining the impact of gut microbial composition on intestinal nervous and immune systems.

The work laid out in this thesis aims to define how changes in the gut microbiota can influence the enteric associated nervous system, immune system, and potential interactions between the two. We first investigated how MM respond to enteric pathogens, and the potential for neuro-immune interactions to coordinate this response (**Chapter 2**). Upon discovering that the gut-sympathetic nervous system is critical in the response to *Salmonella*, we sought to understand how the entire EANS is impacted by changes in the microbiota through the application of modern transcriptional, imaging, and neuromodulatory techniques. We found that the microbiota tonically suppresses gut sympathetic activity and identified brainstem regions that are activated by distinct bacterial metabolites (**Chapter 3**). This work also enabled tool development to manipulate EANs and address whether signaling from the SNS to MM play a role in response to infection (**Chapter 4**). We discovered that MM are essential to prevent excessive iEAN loss upon enteric infection, leading us to ask how specific iEAN sub-populations

contribute to tissue homeostasis. We found that surprisingly, an iEAN population that is drastically modulated by changes in the microbiota can also control blood glucose levels through activation of the SNS (**Chapter 5**). These studies provide a new perspective into how the microbiota, through the SNS, can influence homeostatic processes across multiple cell types and tissues. We conclude (**Chapter 6**) with discussions as to how these effects on gut physiology, extra-intestinal physiology, and immune function relate to the field, along with future directions.

Chapter 2: Macrophage-Sympathetic Interactions during Infection

2.1 Distinct morphological features and cell dynamics inherent to lamina propria and muscularis macrophages

To obtain a deep-tissue, 3D view of gut-resident macrophage distribution within the intact intestinal tissue, we performed whole-mount immunolabeling, utilizing a novel tool referred to as immunolabeling-enabled three-dimensional imaging of solvent-cleared organs (iDISCO) (Renier et al., 2014). Small intestine sections from *Cx3cr1*$^{GFP/+}$ macrophage reporter mice (Niess et al., 2005) were stained with anti-GFP antibodies and visualized using light-sheet microscopy. Resulting images revealed dense macrophage networks throughout the tissue layers and particularly concentrated in the lamina propria (LpM) and muscularis (MM) regions, suggesting compartmentalization of gut macrophage populations (Figure 2.1a). To gain insight into cell dynamics in these two distinct layers of the intestinal wall of live animals, we utilized intravital multi-photon microscopy (Farache et al., 2013). We analyzed *Itgax*^{eYFP} (CD11c^{YFP}) and *Cx3cr1*$^{GFP/+}$ reporter mice side-by-side, which allow for the visualization of intestinal antigen-presenting cells (APCs) and macrophage populations, respectively (Farache et al., 2013; Niess et al., 2005). Comparison between macrophages (CD11c+ and/or CX3CR1+) residing in the lamina propria and muscularis compartments revealed distinct morphologies inherent to these populations, including varied displacement and dendrite extension patterns. LpM exhibited slow displacement, while MM were primarily static, and MM possessed greater dendrite ramifications than LpM but reduced dendritic extension movements (Figure

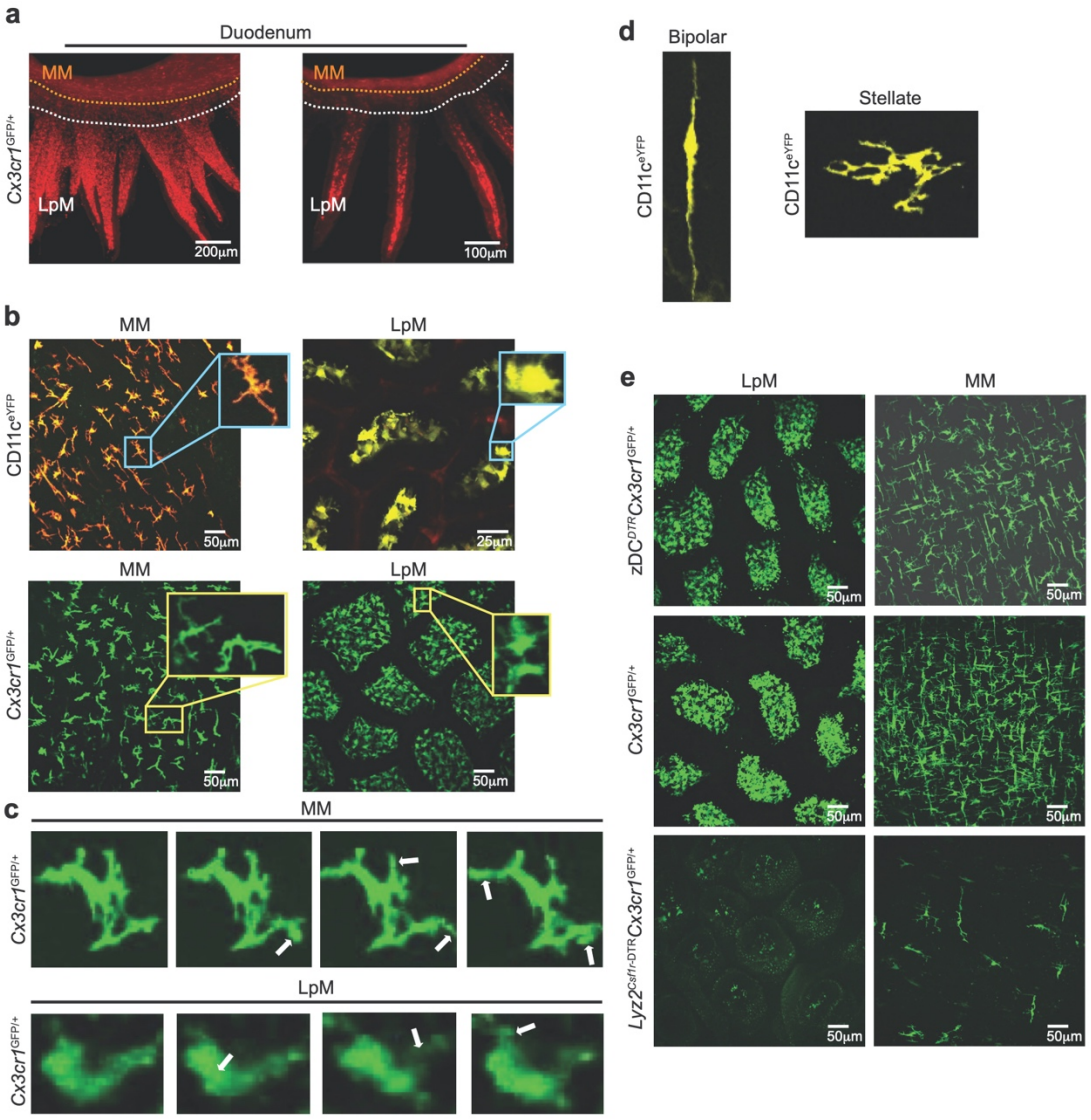

Figure 2.1. MM differ from LpM in morphology and cell dynamics. (**a**) Whole-mount imaging (iDISCO) of gut macrophages in the duodenum isolated from *Cx3cr1*$^{GFP/+}$ reporter mouse and stained with anti-GFP. Left, still image from a 3-D reconstruction. Right, *Imaris*-generated orthogonal slice. (**b**) Images from IVM of the ileum *muscularis* (left panels) and *lamina propria* (right panels) of live CD11c^{eYFP} (upper panels) and *Cx3cr1*$^{GFP/+}$ (lower panels) mice. Insets depict different morphological features of APCs in each region. (**c**) Images from IVM of the ileum *muscularis* (upper panels) and *lamina propria* (lower panels) of live *Cx3cr1*$^{GFP/+}$ mice. White arrows indicate morphologic changes over 15-20 min. (**d**) Confocal images from the ileum *muscularis* isolated from CD11c^{eYFP} mice depicting different morphological features of MMs: bipolar cell (left panel) and stellate cell (right panel). (**e**) Images from IVM of the *ileum lamina propria* (left column) and *muscularis* (right column) of *Cx3cr1*$^{GFP/+}$ (middle row), zDC^{DTR}*Cx3cr1*$^{GFP/+}$ (upper row) and *Lyz2*$^{Csf1r\text{-}DTR}$*Cx3cr1*$^{GFP/+}$ (lower row) mice 12h post final DT administration. (**a**), Image is representative of 2 similar experiments with sections obtained from duodenum, jejunum, and ileum; (**b**-**d**), images are representative of at least 5 similar experiments; (**e**), images are representative of 3 similar experiments. Scale bars = 50, 100, or 200μm.

2.1b,c). Among the MM population, we observed at least two morphologically distinct sub-populations: bipolar and stellate cells (Phillips and Powley, 2012) (Figure 2.1d). In general, bipolar cells produced small pseudopodia along the length of the cell body, approximately 0.2-0.8µm in size. Stellate cells also exhibited these pseudopodia, but they also displayed constant extensions and retractions of their dendritiform processes. These observations suggest that macrophages within distinct compartments of the gut display different morphologies and cellular dynamics.

Since, in addition to macrophages, the gut wall also contains several DC subpopulations (Bogunovic et al., 2009; Schreiber et al., 2013), we complemented this cell surface marker-based lineage classification with complementary ontogeny strategies. We targeted the macrophage/monocyte lineage using *Lyz2*^{Cre} x *Csf1r*$^{lsl\text{-}DTR}$ (*Lyz2*$^{Csf1r\text{-}DTR}$) and the pre-DC derived lineage using *Zbtb46*^{DTR} (zDC^{DTR}) mice (Schreiber et al., 2013). Administration of diphtheria toxin (DT) to *Lyz2*$^{Csf1r\text{-}DTR}$ mice leads to broad, rapid depletion of monocytes, monocyte– and yolk sac–derived tissue macrophages and inflammatory DCs that lasts for at least 36h. Complementarily, DT-injected zDC^{DTR} mice show rapid and virtually complete loss of classical DCs (cDCs) (Schreiber et al., 2013). We generated bone marrow chimeras (BMC) from *Cx3cr1*$^{GFP/+}$ reporter mice crossed to *Lyz2*$^{Csf1r\text{-}DTR}$, zDC^{DTR} or WT controls to allow CX3CR1+ APCs not targeted by DT to be visualized by the expression of GFP. At 12h post final DT injection, we observed a drastic reduction in GFP+ cells in the muscularis and lamina propria of *Lyz2*$^{Csf1r\text{-}DTR}$ when compared to WT

controls or zDC^{DTR} mice, indicating that the great majority of CX3CR1+ cells in these layers belongs to the monocyte/macrophage lineage (Figure 2.1e). In contrast, DT administration to CD11c^{YFP}*Lyz2*$^{Csf1r\text{-}DTR}$ BMC resulted in a drastic reduction in YFP+ cells in the muscularis, but only mild reduction in YFP+ in the lamina propria (Figure 2.2a). These data indicate that CX3CR1-based strategies faithfully label macrophages throughout the gut tissue, while CD11c also labels non-monocyte/macrophages in the lamina propria and can therefore only be used to visualize MM.

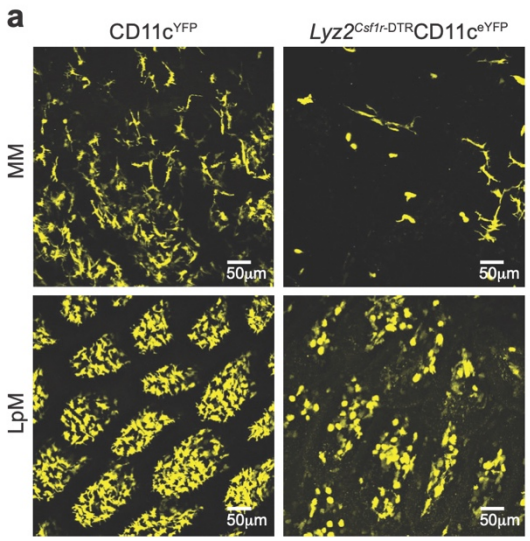

Figure 2.2. A proportion of MM are CD11c+. (**a**) Images from IVM of the ileum *muscularis* (upper panels) and *lamina propria* (lower panels) of live CD11c^{eYFP} (left panels) and *Lyz2*$^{Csf1r\text{-}DTR}$CD11c^{eYFP} (right panels) mice 12h post final DT administration. Images are representative of 3 similar experiments. Scale bars = 50μm.

By combining novel methods to visualize deep-tissue structures with intersectional genetics and live imaging, these experiments establish tissue segregation, distinct morphology and cell dynamics of macrophages residing within distinct microenvironments in the intestinal tissue.

2.2 Intra-tissue specialization of lamina propria and muscularis macrophages

To address whether the morphological and cell dynamics characteristics of gut macrophages correspond to divergent tissue-specific adaptation, we analyzed the transcriptomes of LpM and MM. RNA-seq analysis of sorted (live, CD45^{+}Lineage^{-} MHCII^{+}CD11b^{+}CD11cintCD103^{-}) cells at steady state revealed significant differences between LpM and MM cells in genes related to immune- and metabolic-processes (Figure 2.3a,b and 2.4a,e). MM preferentially expressed

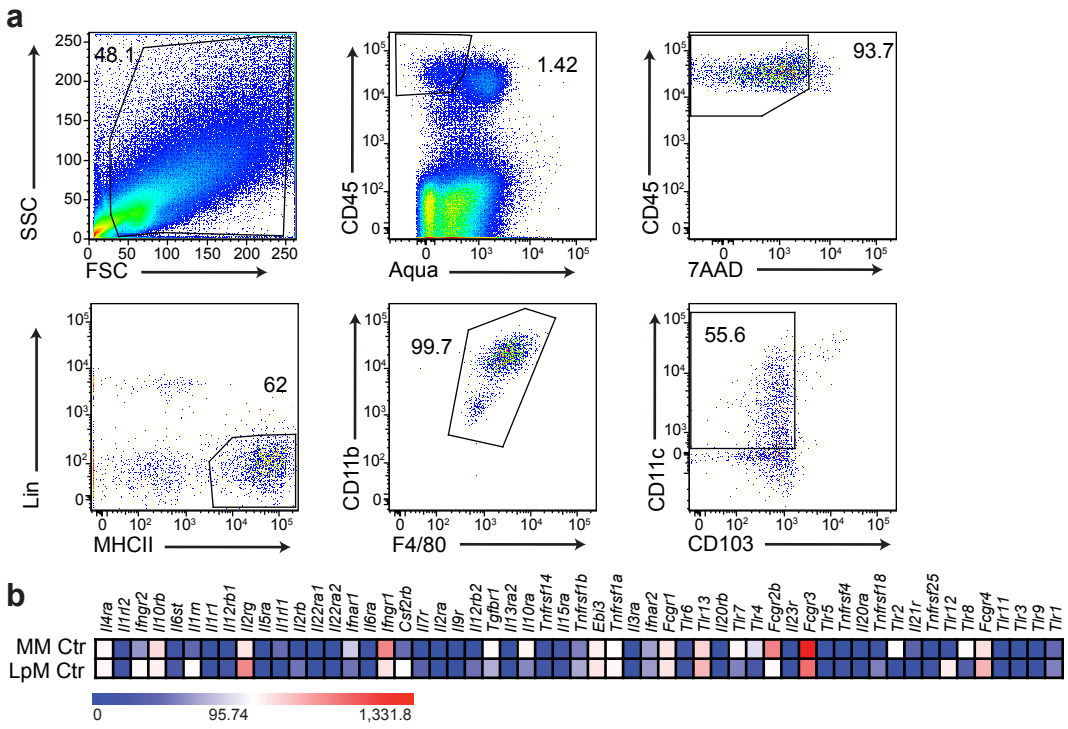

Figure 2.3. Gating strategy for gut macrophages and macrophage polarization genes from RNA-seq. (**a**) Representative flow cytometry pseudo-color plots showing gating strategy for intestinal macrophage sorting (example of *muscularis* macrophage strategy is shown). MMs and LpMs were isolated from the small intestine *muscularis externa* and mucosal layers, respectively, of WT mice and sorted as live (Aqua^{-}, 7AAD^{-}) CD45^{+}Lin^{-}(CD3^{-}B220^{-}SiglecF^{-}LY6G^{-}) MHCII^{+} F4/80^{+}CD11B^{+}CD11C^{+}CD103^{-}. (**b**) Heat map of genes for most common receptors associated with macrophage polarization expressed by sorted small intestine MM and LpM isolated from naïve WT mice under steady state conditions, determined by RNA-seq.

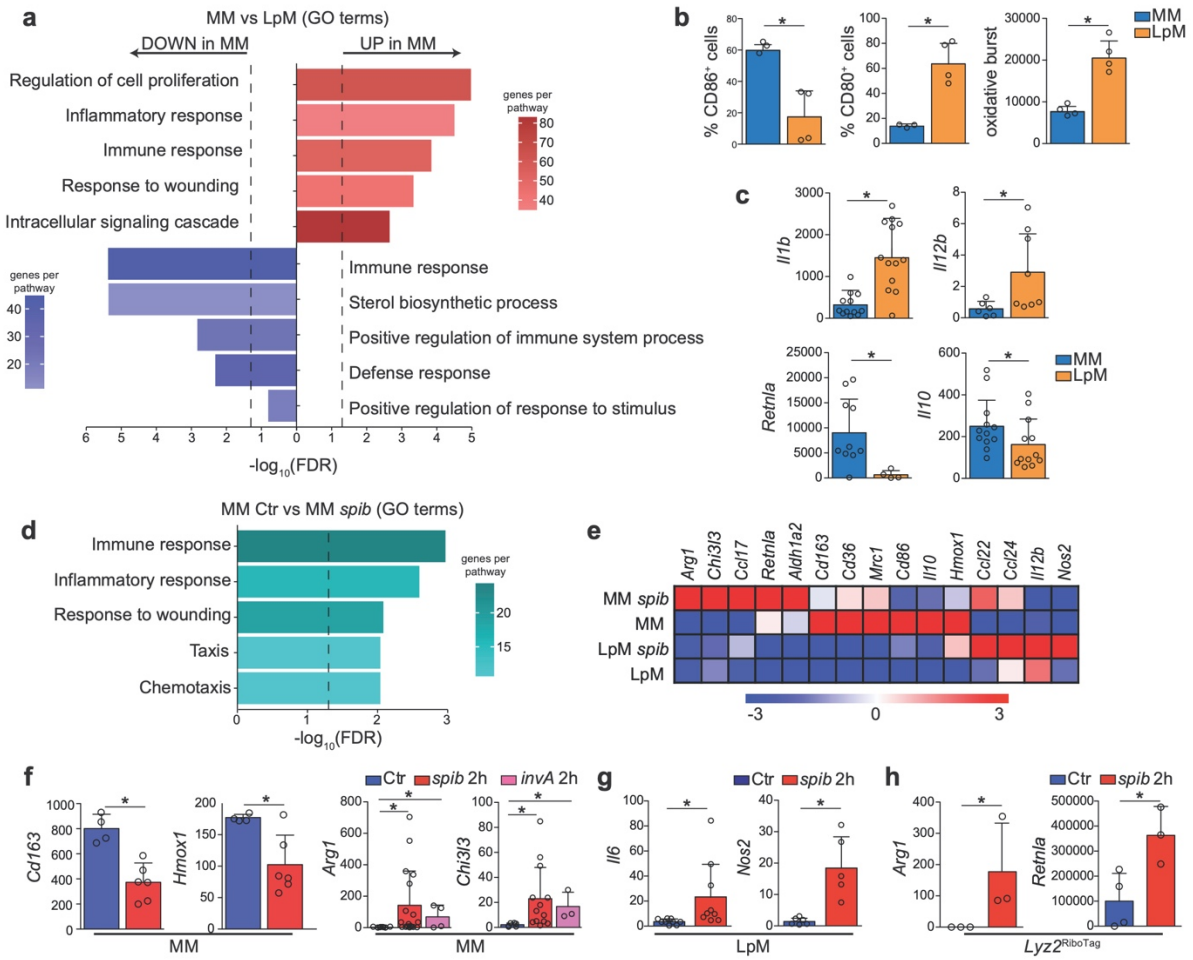

Figure 2.4. MM and LpM exhibit distinct gene expression signatures. (**a**-**g**) MM and LpM were isolated from the small intestine *muscularis externa* and mucosal layers, respectively, of WT mice and sorted as live (Aqua$^-$) CD45$^+$Lin$^-$MHCII$^+$F4/80$^+$CD11B$^+$ CD11C$^+$CD103$^-$. (**a**) Annotated gene ontology (GO) biological processes were assigned to genes differentially expressed by MMs when compared to LpMs, determined by RNA-seq. (**b**) Flow cytometry analysis of CD80 and CD86 expression and oxidative burst by MM and LpM. (**c**) Expression of mRNA for *Il1b*, *Il12b*, *Retnla*, and *Il10* by MM and LpM determined by qPCR, presented relative to housekeeping gene *Rpl32* expression. (**d**) Annotated GO biological processes were assigned to genes differentially expressed by MMs 2 h post intragastric exposure to *spib* when compared to MMs isolated from naïve mice, determined by RNA-seq. (**e**) Heat map of representative M1- and M2-related gene were assigned to genes differentially expressed by MMs and LpMs 2 hr post intragastric exposure to *spib*, determined by RNA-seq. (f,g) Expression of mRNA for various genes by (**f**) MMs and (**g**) LpMs 2 hr post intragastric exposure to *spib* or *invA Salmonella typhimurium* mutant strains determined by qPCR, presented relative to *Rpl32* expression. (**h**) Expression of polysome-associated mRNA from small intestine *muscularis* of *Lyz2*$^{\text{RiboTag}}$ mice 2 hr post intragastric exposure to *spib* determined by qPCR, presented relative to *Gapdh*. (**a**,**d**,**e**), n = 2 per condition; (**b**), data are representative of at least 2 independent experiments, n = 4; (**c**), n = 6-12, pooled data; (**f** , **g**), n = 4-13; pooled data; (**h**), n= 3 per condition. Data were analyzed by unpaired t-test and are shown as mean±s.d.,* $P < 0.05$.

tissue-protective and wound healing genes, such as *Retnla* (encoding Fizz1), *Mrc1*, *Cd163* and *Il10* and increased levels of the co-stimulatory molecule CD86 when compared to macrophages isolated from the lamina propria (Figure 2.4a-c,e). Thus, MM overall resemble alternatively activated (M2) macrophages (Van Dyken and Locksley, 2013). Analysis of the ImmGen database (Gautier et al., 2012), as well as flow cytometry and qPCR further confirmed this trend, also indicating that LpM preferentially expressed pro-inflammatory, or M1, genes with increased oxidative burst and increased CD80 expression when compared to MM (Figure 2.4b,c).

The above data demonstrate an intra-tissue specialization among intestinal macrophages with potential for modified responses in specific microenvironments. To determine whether the basal differences between intestinal macrophages are maintained during responses to a pathogen, we sorted LpM and MM 2 hr post intra-gastric exposure to mutant strains of *Salmonella typhimurium*, *spib* and *invA*, which exhibit impaired proliferation or invasiveness, respectively, due to mutations in the type-III secretion system (Tsolis et al., 1999). We chose to study non-pathogenic or non-invasive bacteria strains since wild-type (WT) *Salmonella typhimurium* quickly invades and damages the intestinal epithelium, hindering our objective to compare macrophages located in different regions of intact intestinal tissue. A 2-hr time-point was chosen to represent the earliest detection point for immediate early gene (IEG) responses in macrophages (Ghisletti et

al., 2010). Following gavage with the *spib*-mutant, we observed significant further upregulation in some M2-associated genes in MM, particularly *Arg1* and *Chi3l3* (encoding YM1). While *Cd163* and *Hmox1* were downregulated, they were still expressed at higher levels than in LpM's (Figure 2.4d-f). Of note, whereas we observed variability in the expression of some IEG's, particularly *Arg1*, among different animals, MM from non-infected mice consistently did not express these genes (Figure 2.4f). In contrast, very few changes in gene expression were observed in LpM upon intragastric exposure to *spib*, and these changes were mostly restricted to M1-associated genes, including *Nos2* and *Il6* (Figure 2.4e, g).

To corroborate observed changes in MM gene expression profile using an independent approach, we conducted cell type-specific ribosomal profiling. This approach eliminates the need for cell sorting to purify sub-populations, thus reducing processing time and variability. We chose to specifically focus on actively translated mRNAs by interbreeding mice expressing *Cre* under the *Lyz2* promoter with mice carrying a targeted knockin into the ribosomal protein L22 gene (RiboTag). *Cre*-mediated activation in this system creates an HA-tagged ribosomal protein, enabling affinity-tagged purification and identification of actively translated ribosome-bound mRNAs in macrophages from intact tissues (Sanz et al., 2009). Analysis of intestinal muscularis from *Lyz2*$^{\text{RiboTag}}$ mice confirmed high levels of active translation of M2-related genes in steady state in MM's, particularly *Retnla*. Importantly, intragastric inoculation of mice with *spib* rapidly led to upregulation of *Arg1* as well as *Retnla* (Figure 2.4h). These results suggest that unique

microenvironmental cues influence the specialization of gut-resident macrophages and that this specialization is reinforced upon infection.

2.3 β_2AR-positive muscularis macrophages reside in close proximity to firing neurons

We next asked whether specific environmental signals, particularly soluble factors, were responsible for the distinct gene expression profiles and responses to luminal insults by LpM and MM populations. Gene expression profiling of LpM and MM cells indicated that pro- or anti-inflammatory cytokine-, TLR- or FcR-mediated signaling did not segregate these populations, especially considering the canonical M1 (IFN-γR, IFN-αR, IL-1R, TLR4) or M2 (FcγRIIb, IL-4Rα, IL-10Rα, ST2 (encoded by *Il1rl1*)) polarizing receptors (Figure 2.3b) (Gautier et al., 2012). Given their distinct locations near the lumen (LpM) or near neuronal networks (MM) (Kinoshita et al., 2007; Muller et al., 2014; Phillips and Powley, 2012), we next asked whether these macrophage populations differentially expressed neurotransmitter or neuropeptide receptors. MM's expressed high levels of *Adrb2* (encoding β_2 adrenergic receptors, [AR]), and this was also among the most significantly differentially-expressed genes between MM and LpM populations in the ImmGen database (Figure 2.5a) (Gautier et al., 2012). We confirmed these results by performing qPCR on sorted cells isolated from WT mice and on HA-bound polysomes of intestinal muscularis tissue isolated from *Lyz2*$^{\text{RiboTag}}$ mice (Figure 2.5b,c). Furthermore, flow-cytometric expression analysis of LpM's and MM's isolated from the small intestine

of WT mice revealed high levels of membrane β_2AR expression in MM and lower, albeit detectable, expression of β_2ARs by LpM (Figure 2.5d).

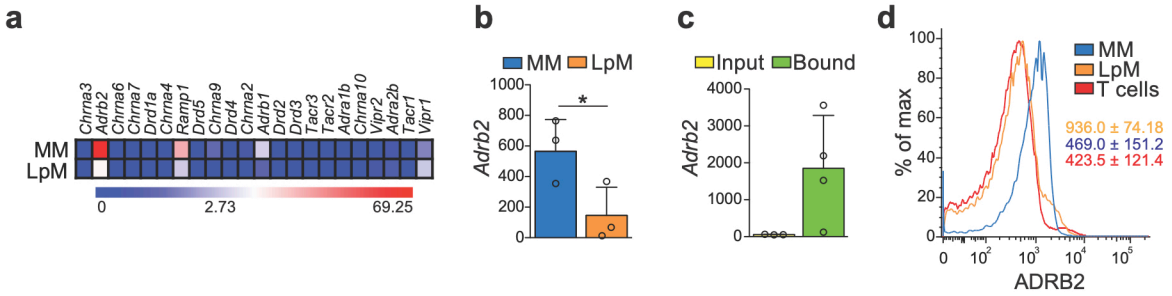

Figure 2.5. MM preferentially express *Adrb2*. (**a**) Heat maps of genes for neurotransmitter receptors expressed by sorted small intestine MMs and LpMs isolated from naïve WT mice under steady state conditions, determined by RNA-seq. (**b**) Expression of mRNA for *Adrb2* by sorted small intestine MMs and LpMs isolated from naïve WT mice, determined by qPCR, presented relative to *Rpl32* expression. (**c**) Expression of polysome-associated mRNA from small intestine *muscularis* of *Lyz2*$^{\text{RiboTag}}$ mice, determined by qPCR, presented relative to *Gapdh* expression. (**d**) Representative flow cytometry histogram for β2-AR expression by small intestine MMs, LpMs, and peripheral T cells isolated from naïve WT mice. (**a**), n=2 per condition; (**b**), data are representative of 2 independent experiments, n=3; (**c**), Input n = 3, Bound n=4; (**d**), histograms are representative of 2 independent experiments, n=3. Data were analyzed by unpaired t-test and are shown as mean±s.d.,* $P < 0.05$

The near immediate gene-expression response of MM to distal luminal stimuli, along with their selective expression of neurotransmitter receptors, suggested that their specific location in close proximity to neuronal networks could be influencing their activity. We therefore chose to characterize this neuron-rich microenvironment and how it interacts with gut macrophages. To that end, we developed multiple genetic labeling tools, allowing for concomitant and dynamic visualization of these cell types. To gain insight into neuron-macrophage interactions in live animals, we first generated a more specific enteric neuronal-associated reporter by interbreeding *Rosa26*$^{\text{lsl-tdTomato}}$ with *Hand2*$^{\text{Cre}}$ (*Hand2*$^{\text{Tomato}}$) mice (Hendershot et al., 2007). These mice express

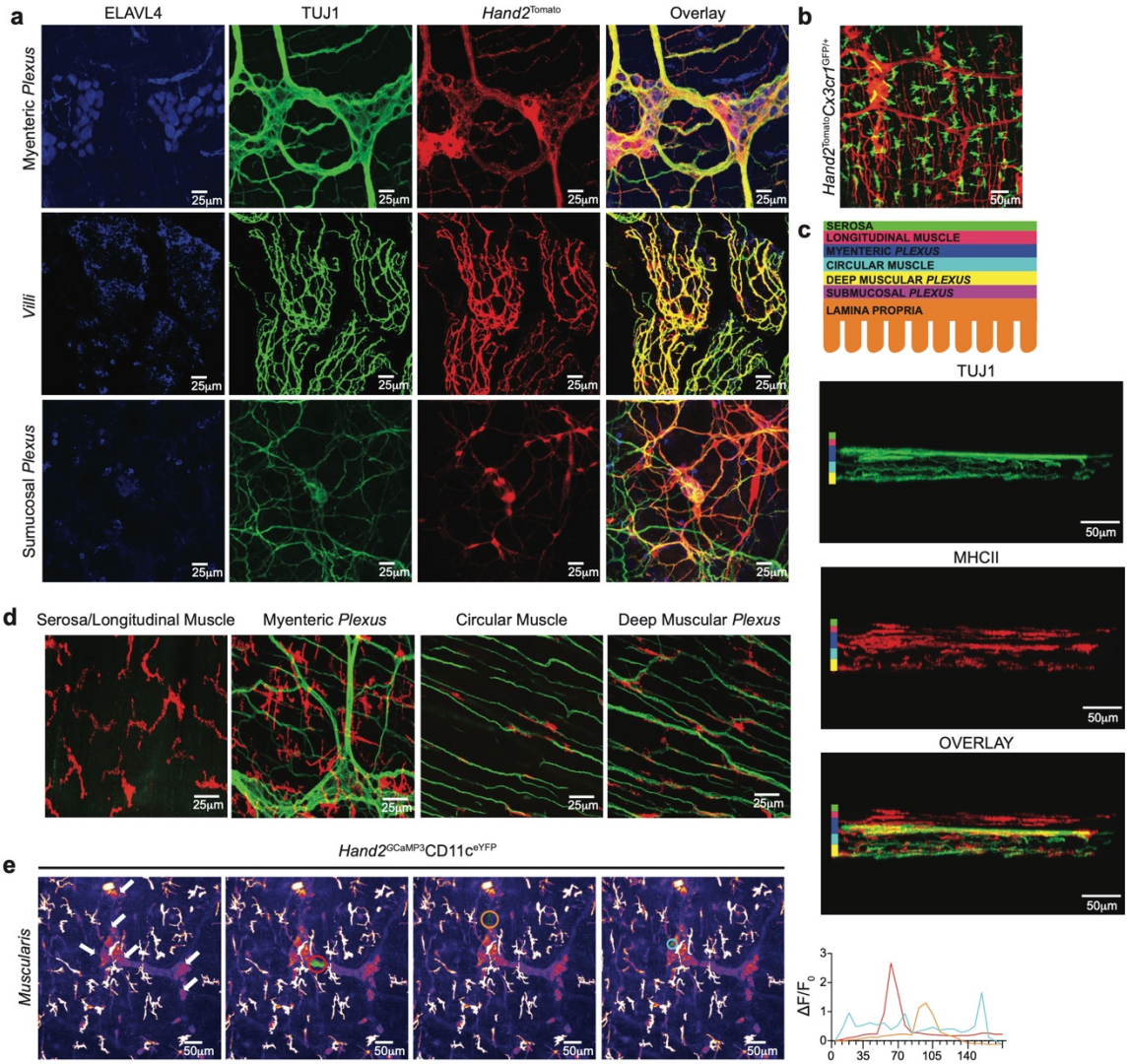

Figure 2.6. MMs are closely associated with active neurons. (**a**) Confocal images from the myenteric *plexus* (upper panels), *villi* (middle panels) and submucosal *plexus* (lower panels) isolated from naïve *Hand2*^{Tomato} mice and stained using anti-ELAVL4 (HuC/D) and anti-TUJ1 (βIII-tubulin) antibodies. (**b**) Image from IVM of the *ileum muscularis* of live *Hand2*^{Tomato}*Cx3cr1*$^{GFP/+}$ mice. (**c**, **d**) Confocal images from the *ileum* isolated from naïve WT mice stained using anti-TUJ1 (βIII-tubulin) and anti-MHCII antibodies. (**c**, upper panel) Schematic of layers of different small intestine *muscularis*. (**c**, lower panel) Four layers of *muscularis* orthogonal slices are depicted according to the color scheme. (**d**) Images depict macrophages occupying each of the four layers: serosal/longitudinal muscle, *myenteric plexus*, circular muscle, and deep muscular *plexus*. (**e**) Images from IVM of the ileum *muscularis* of live *Hand2*^{GCaMP3}CD11c^{eYFP} mice over 3 min. White arrows indicate neurons labeled with GCaMP3, and colored regions of interest (ROI) highlight neural activity. Corresponding colored traces plot changes in fluorescence (ΔF) of ROI per time frame (in seconds), with an increase in fluorescence indicative of Ca^{2+} influx and depolarization (right panel). (**a**), images are representative of 2 similar experiments with sections obtained from duodenum, jejunum, and ileum; (**b**), image is representative of at least 10 similar experiments; (**c**-**e**), images are representative of at least 3 independent experiments. Scale bars = 25 or 50μm

Cre recombinase under the promoter of *Hand2*, a helix-loop-helix transcription factor with an established role in development of intrinsic enteric-associated neurons (iEAN) (Barron et al., 2011). *Cre*-mediated removal of the stop cassette generated bright red fluorescence that allowed the visualization and tracking of *Hand2*-expressing cells, mostly restricted to iEAN (Figure 2.6a). These mice were crossed with *Cx3cr1*$^{GFP/+}$ reporter mice for tracking intestinal macrophages, and the resulting offspring were used for concomitant EAN-macrophage visualization. We observed that most of the CX3CR1+ cells in the muscular region were in close proximity to neuronal cell bodies or processes of the myenteric ganglia (Figure 2.6b). We distinguished four layers of muscularis macrophages: serosal/longitudinal, myenteric plexus, circular muscle, and deep muscular plexus (Figure 2.6c,d). Serosal macrophages do not appear to be associated with enteric neurons and tend to be larger in size when compared to the other layers (Figure 2.6d). Myenteric plexus MM are in close proximity to neuronal cell bodies and some nerve fibers, while MM within the circular muscle and deep muscular plexus have their cell bodies running in parallel to the nerve fibers (Figure 2.6d).

To complement our cell dynamics analysis, we assessed neuronal activation in areas where MM's were co-localized with EAN utilizing a mouse strain containing a genetically-encoded, *Cre*-dependent calcium indicator (GCaMP3) (Zariwala et al., 2012). Analysis of *Hand2*^{Cre} x *Rosa26*$^{lsl\text{-}GCaMP3}$ (*Hand2*^{GCaMP3}) x CD11c^{eYFP} mice revealed neuronal activity in very close proximity to MM's in the myenteric plexus (Figure 2.6e).

Taken together, these data indicate that MM that express β_2AR reside in close proximity to active neurons in the intestine.

2.4 Rapid activation of catecholaminergic neurons occurs upon luminal infection

We next sought to characterize the specific neurochemical pathway involved in the activation of β_2AR+ MM by defining the source of norepinephrine (NE) in the gut muscularis. Although neurons are the most studied sources for catecholamines, controversial studies have claimed that myeloid cells, including macrophages, can also produce these neurotransmitters. Specifically, alternatively-activated macrophages involved in the regulation of thermogenesis were shown to express tyrosine hydroxylase (TH) and produce NE (Nguyen et al., 2011), although this claim has been recently refuted by groups seeking to reproduce these results (Fischer et al., 2017). To better characterize possible neuronal and non-neuronal sources for NE in the gut, we first interbred *Rosa26*$^{lsl\text{-}tdTomato}$ with *Th*^{Cre} mice (*Th*^{Tomato}) as a fate-mapping strategy to visualize cells that express TH at any point during development. Fate-mapping analysis suggested that myeloid cells were not the main source of NE within intestinal tissue, and immunofluorescence microscopy of intestinal muscularis revealed extensive tomato-expressing neuronal processes but no expression in myeloid cells (Figure 2.7a,b). To visualize cells actively expressing TH, we also performed ex vivo staining for TH and additional neuronal or myeloid markers. Again, TH staining was restricted to the neuronal compartment, particularly the fibers near MM's (Figure 2.7b). To visualize catecholaminergic innervation throughout the intestinal tissue and how it might interact with gut macrophages, we performed iDISCO in small intestinal samples from *Cx3cr1*$^{GFP/+}$ reporter mice, co-stained

with anti-GFP and anti-TH antibodies. Light-sheet microscopy analysis revealed intense TH+ innervation in the gut muscularis, but sparse labeling in the lamina propria (Figure 2.8a,b). We also observed TH+ processes extending from the muscularis region (Figure 2.8c), suggesting an extrinsic nature for this innervation.

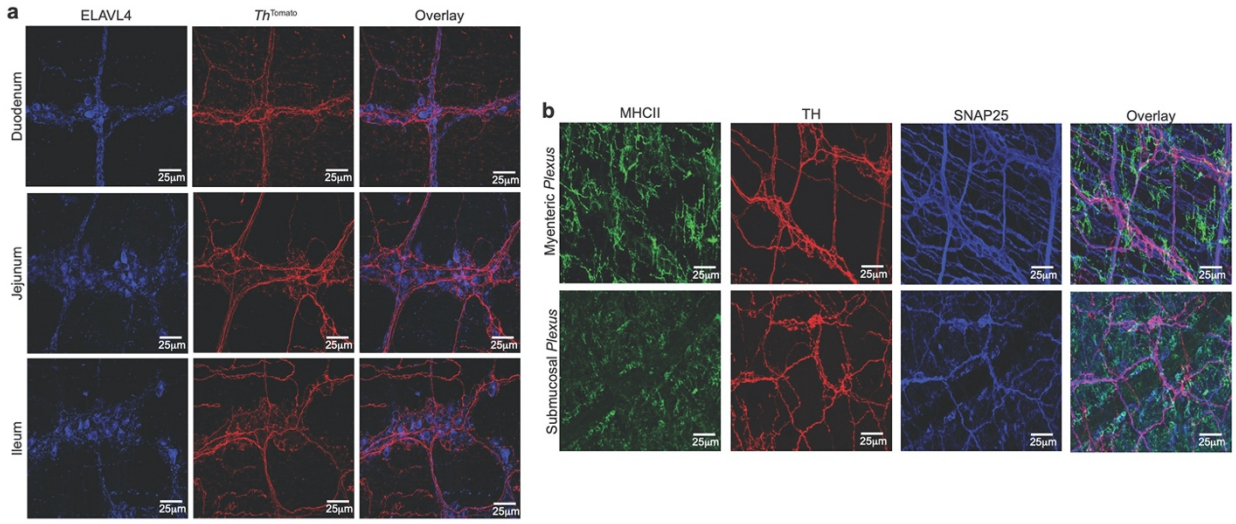

Figure 2.7. Confocal analysis of catecholaminergic innervation of the intestinal *muscularis.* (**a**) Confocal images from the *duodenum* (upper panels), *jejunum* (middle panels) and *ileum* (lower panels) isolated from naïve *Th*^{Tomato} mice and stained using anti-ELAVL4 (HuC/D) antibodies. (**b**) Confocal images from the myenteric (upper panels) and submucosal plexuses (lower panels) isolated from naïve WT mice and stained using anti-MHCII, anti-SNAP25 and anti-TH antibodies. (**a**,**b**) Images are representative of at least 2 independent experiments with sections obtained from duodenum, jejunum, and ileum. Scale bars = 25µm

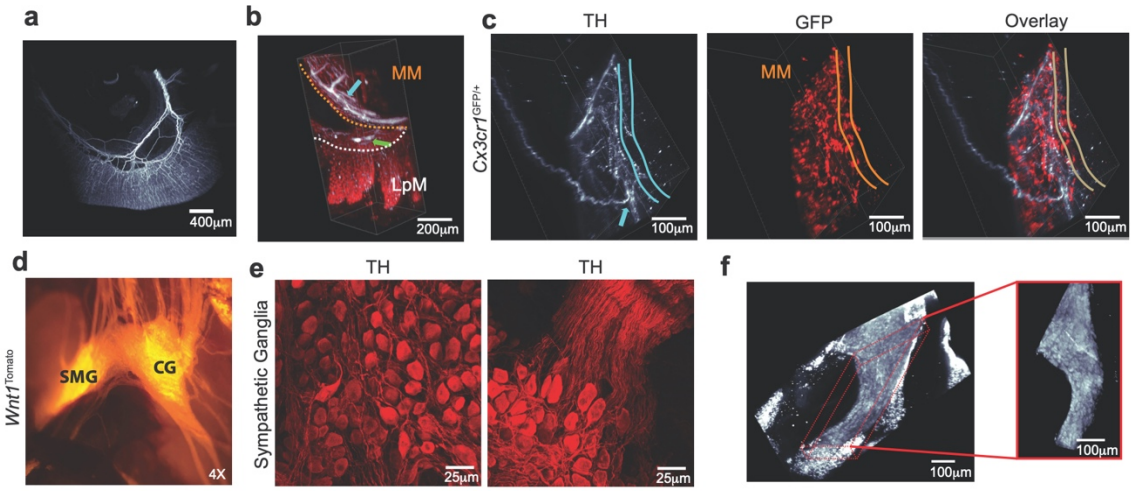

Figure 2.8. Light sheet and whole mount analysis of catecholaminergic innervation of the intestinal *muscularis.* (**a**) Whole-mount imaging (iDISCO) from the ileum isolated from naïve WT mouse stained using anti-TH (white) antibodies. (**b**,**c**) iDISCO from the ileum isolated from *Cx3cr1*$^{GFP/+}$ reporter mouse stained using anti-GFP (red) and anti-TH (white) antibodies. (**b**) Arrows indicate TH^{+} processes in the myenteric (light blue) and submucosal (green) plexuses. (**c**) Light blue arrow indicates TH^{+} processes innervating the myenteric plexus. (**d**) Epifluorescent imaging from the CG-SMG of *Wnt1*^{Tomato} mice. (**e**) Confocal images from the CG isolated from naïve WT mice and stained using anti-TH antibodies. Left panel, TH^{+} cell bodies; right panel, TH^{+} cell bodies and processes. (**f**) iDISCO from the CG-SMG isolated from WT mouse stained using anti-ELAVL4 antibody, showing the entire ganglia and the surrounding fat tissue. (**a-f**) Images representative of at least n=3. Scale bars = 25μm

After defining catecholaminergic innervation as the probable source of NE in the MM's microenvironment, we next characterized the intrinsic versus extrinsic nature of these neuronal processes. In order to identify and visualize the sympathetic innervation of the intestine, we developed general fate-mapping strategies for neurons or peripheral (neural crest-derived) neurons by crossing *Rosa26*$^{lsl\text{-}tdTomato}$ with *Wnt1*^{Cre} mice, which revealed the celiac-superior mesenteric ganglion (CG-SMG) (Figure 2.8d). Immunolabeling of the CG-SMG showed a dense network of TH+ neurons extending processes towards the gut (Figure 2.8e,f). Consistent with this, staining for dopamine β-hydroxylase (DBH), which converts dopamine into norepinephrine, revealed punctate

labeling restricted to ganglia and nerve fibers in the myenteric and submucosal plexuses, while extrinsic sympathetic neurons displayed signal in their cytoplasm (Figure 2.9a). This observation indicates that at least part of the TH staining observed in the muscularis was of an extrinsic nature, as previously suggested (Li et al., 2010).

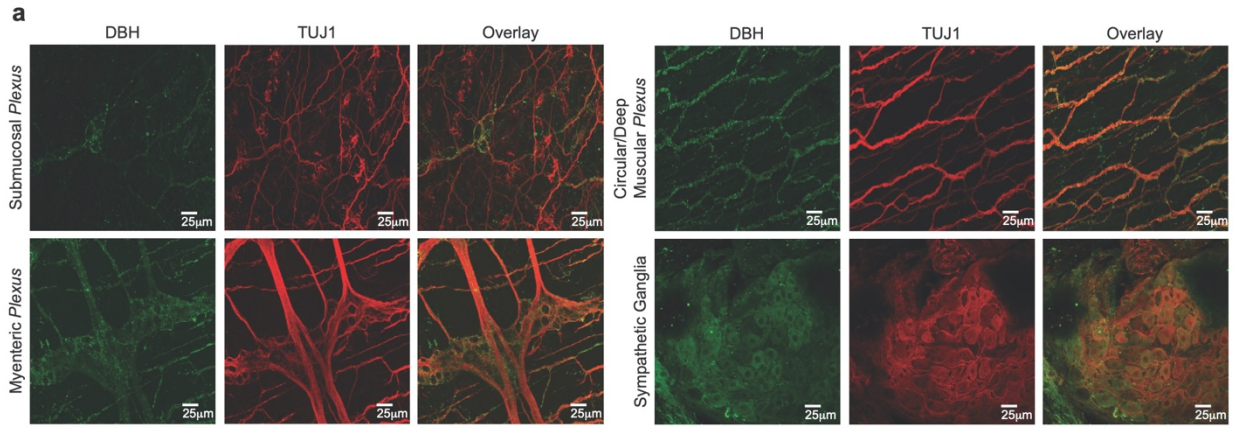

Figure 2.9. Catecholaminergic innervation of the intestinal *muscularis*. (**a**) Confocal images from the ileum submucosal, myenteric, circular/deep muscular plexuses, and the sympathetic ganglion (CG-SMG) isolated from naïve WT mice and stained using anti-DBH and anti-TUJ1 antibodies. Images are representative of at least n=3. Scale bars = 25µm

To address whether intrinsic innervation also contributed to the catecholaminergic response in the muscle, we generated a broad neuronal RiboTag strain by crossing *Rpl22*^{HA} with *Snap25*^{Cre} (*Snap25*^{RiboTag}) mice. Analysis of HA-bound fractions from the muscularis and the CG-SMG revealed high expression of both *Th* and *Dbh* by SMG-CG but very little expression in comparison in the myenteric plexus (Figure 2.10a). We therefore concluded that a majority of the NE release in the gut muscularis microenvironment is derived from extrinsic sympathetic innervation.

One of the consequences of NE release in the muscularis region is the relaxation of intestinal smooth muscle. Consistent with this effect, we observed a significant

impairment of gastrointestinal motility following oral gavage with *spib* (Figure 2.10b). Additionally, quantification of NE in the cecal contents also indicated increased, but non-significant, NE release in the intestinal tissue upon *spib* infection (Figure 2.10c). Finally, to confirm catecholaminergic neuronal activation after luminal infection, we measured c-Fos activation using *Fos*^{GFP} reporter mice. Oral administration of *spib* resulted in pronounced activation of SMG-CG ganglia neurons and undetectable (or non-neuronal) c-Fos expression in the intestinal muscularis (Figure 2.10d-f). Collectively, these data suggest that enteric infections activate gut extrinsic sympathetic innervation resulting in NE release within the muscular region and signaling through β2AR in MM.

2.5 β_2AR mediates alternative activation of intestinal macrophages

To investigate whether interaction with neurons is sufficient to directly modulate gene expression in macrophages, we first developed an in vitro co-culture system using neurosphere-derived primary enteric neurons and either peritoneal macrophages or a macrophage cell line (RAW 264). Co-culture of RAW 264 macrophages or WT peritoneal macrophages with primary enteric neurons resulted in increased levels of *Arg1* and *Chi3l3* expression with no change in

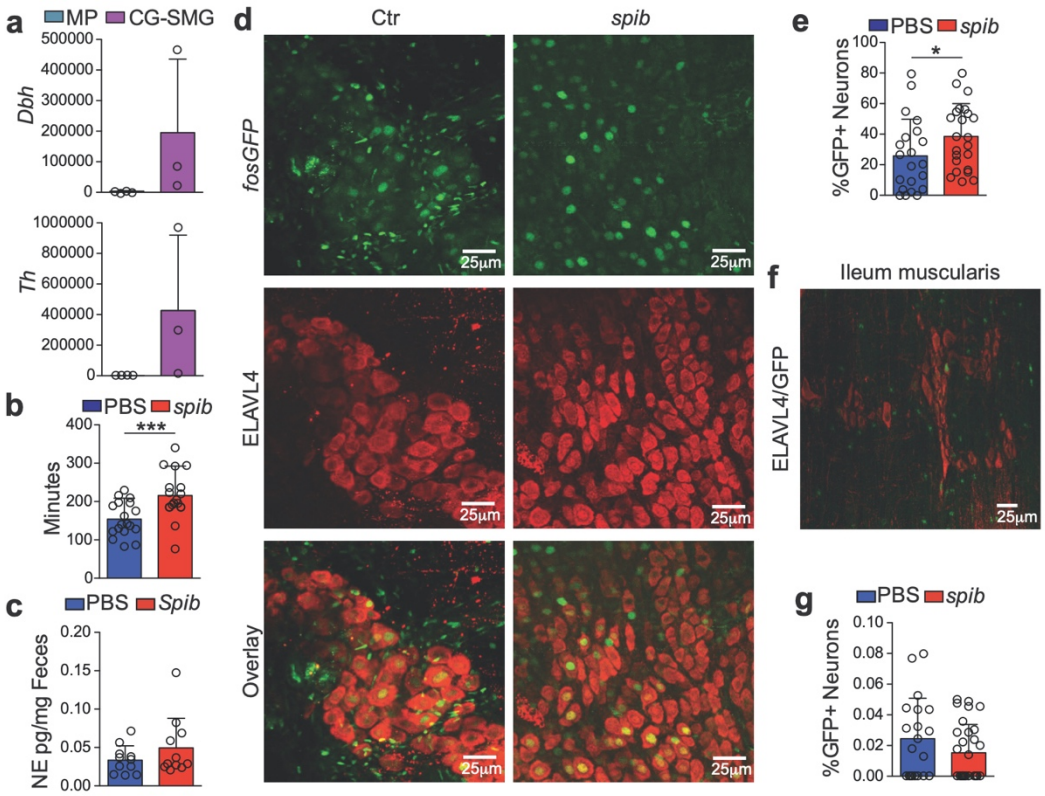

Figure 2.10. Extrinsic sympathetic innervation is activated during enteric infection. (**a**) Expression of polysome-associated mRNA from small intestine *muscularis* and SMG-CG of naïve *Snap25*$^{\text{RiboTag}}$ mice determined by qPCR, presented relative to *Hprt*. (**b**) Total GI transit time (time required to expel feces containing carmine red dye) in mice 30 min post intragastric exposure to *spib* or PBS (control). (**c**) Quantification of norepinephrine by ELISA in the cecal contents of WT mice 2 hr post intragastric exposure to *spib*. (**d**) Confocal images from the SMG-CG isolated from *Fos*$^{\text{GFP}}$ mice 2 hr post *spib* intragastric exposure and stained using anti-GFP (upper panels) and anti-ELAVL4 (middle panels) antibodies. (**e**) Quantification of the number of GFP+ nuclei amongst ELAVL4+-TH+ neurons in the CG-SMG. (**f**) Confocal image from the myenteric *plexus* isolated from *Fos*$^{\text{GFP}}$ mice 2 hr post intragastric exposure to *spib* and stained using anti-GFP and anti-ELAVL4 antibodies. (**g**) Quantification of the number of GFP+ nuclei amongst ELAVL4+ neurons within the myenteric *plexus*. (**a**) Pooled data shown are from 3 independent experiments, n = 3; (**b**), pooled data shown are from 4 independent experiments, n = 18; (**d**), images are representative of 2 independent experiments, n=6; (**e**), pooled data shown are from 2 independent experiments, n = 6 (each dot represents one image of sympathetic ganglion neurons); (**f**,**g**) pooled data from 2 independent experiments, n = 6 (each dot represents one image of myenteric *plexus* neurons). Scale bars = 25μm. Data were analyzed by unpaired t-test and are shown as e shown as mean±s.d., * $P < 0.05$, *** $P < 0.001$.

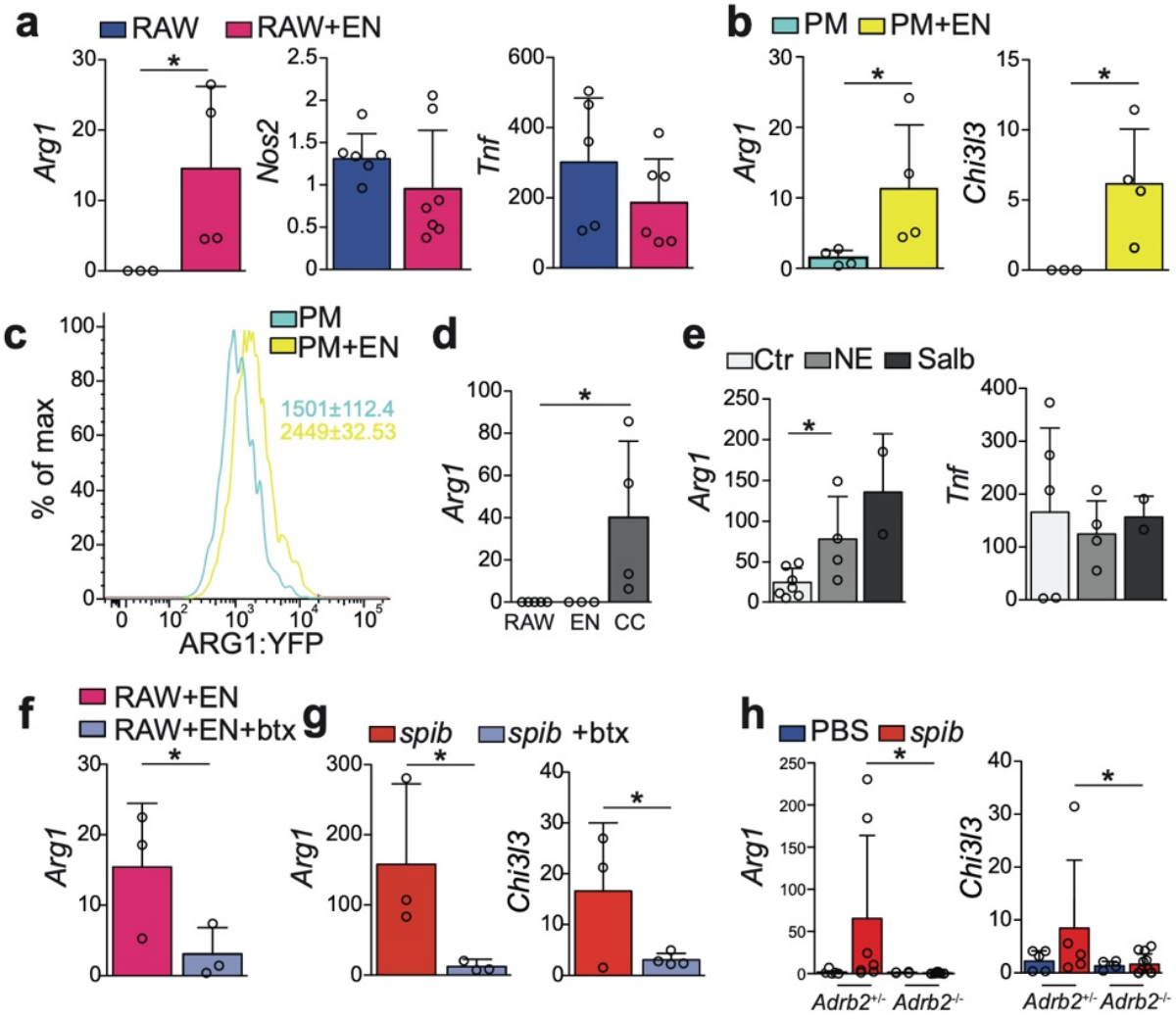

Figure 2.11. β2ARs-mediate polarization of macrophages. (**a-f**) WT mice neurosphere–derived primary enteric-associated neurons (EANs) were co-cultured with RAW or peritoneal macrophages (PM) from WT mice. (**a**,**b**) Expression of mRNA for *Arg1*, *Nos2*, *Tnf* and *Chi3l3* by sorted (**a**) RAW or (**b**) PM 18 hrs post co-culture with EANs. (**c**) Representative flow cytometry histogram for YFP expression by sorted PM isolated from *Arg1*^{YFP} mice cultured with EANs as in (**b**). (**d**) Expression of mRNA for *Arg1* by sorted RM 18 h post exposure to conditioned media from RM, EANs or RM-EANs co-cultures (CC). (**e**) Expression of mRNA for *Arg1* and *Tnf* by sorted PM 1 h post exposure to NE or Salbutamol (β2AR agonists). (**f**) Expression of mRNA for *Arg1* by sorted RM 18 hr post co-culture with EANs with or without butaxamine (β2AR-selective blocker). (**g**) Expression of mRNA for *Arg1* and *Chi3l3* by sorted small intestine MMs isolated 2 hr post intragastric exposure to *spib* in mice treated with vehicle or butoxamine. (**h**) Expression of mRNA for *Arg1* and *Chi3l3* by sorted small intestine MM isolated from *Adrb1*$^{+/-}$*Adrb2*$^{-/-}$ and *Adrb1*$^{+/-}$ *Adrb2*$^{+/-}$ littermate control mice 2 hr post intragastric exposure to *spib*. qPCR results are presented relative to *Rpl32* expression. (**a-h**), pooled data of at least 2 independent experiments (**a**, n = 3-7; **b-d**, n = 3–4; **e**, n = 2-4; **f**,**g**, n = 3-4;**h**, n = 4-11. Data were analyzed by unpaired t-test and are shown as mean±s.d., * $P < 0.05$.

Nos2 or *Tnf* expression (Figure 2.11a,b). We also observed a shift in YFP signal in PM from *Arg1*^{YFP} reporter mice (Reese et al., 2007) that were cultured with iEAN (Figure 2.11c). The supernatant of EAN-macrophage co-cultures (conditioned media), but not EAN or macrophage media alone, was also able to induce *Arg1* in macrophages, further suggesting that a soluble factor was responsible for macrophage specialization, termed polarization (Figure 2.11d). Aptly, both NE and salbutamol, a specific β_2AR agonist, directly induced Arg1 upregulation but did not change Tnf expression in peritoneal macrophages (Figure 2.11e). Furthermore, addition of butaxamine, a selective β_2AR blocker, prevented *Arg1* upregulation in macrophages co-cultured with EAN (Figure 2.11f). In these settings, however, we were unable to detect gene changes in additional M2-genes associated with the MM profile (data not shown). These findings reveal that enteric neurons and β_2AR ligands can induce macrophage polarization in vitro resembling MM.

We next asked whether β_2AR-mediated signaling contributes to in vivo MM polarization after intestinal infection. Previous studies have reported anti-inflammatory effects of β_2AR signaling on macrophages, possibly mediated by upregulation of M2-related genes upon exposure to β_2AR agonists (Spengler et al., 1994). In vivo administration of butoxamine significantly impaired upregulation of *Arg1* and *Chi3l3* (Figure 2.11g). To further address the role of β2AR in this pathway, we also analyzed β-adrenergic receptor null mice. MM isolated from *Adrb1*$^{+/-}$ *Adrb2*$^{-/-}$ mice exhibited markedly reduced expression of *Arg1* and *Chi3l3* relative to MM isolated from *Adrb1*$^{+/-}$ *Adrb2*$^{+/-}$ littermate controls upon *spib* infection (Figure 2.11h). The above in vivo and in vitro data provide evidence that enteric infection triggers changes in MM gene expression via neuron-derived adrenergic signaling.

2.6 Conclusions

Through the use of confocal, light-sheet, and intravital imaging we found that MM are morphologically and dynamically distinct from LpM. Flow cytometry-assisted cell sorting coupled with bulk RNA-sequencing showed that MM are transcriptionally different from LpM, and that infection with an attenuated form of *Salmonella*-induced transcriptional reinforcement of an anti-inflammatory gene program in MM. We used whole mount tissue imaging and intravital microscopy to uncover that MM are in close apposition to EAN, including sympathetic neuronal processes that we found are activated in the presence of a luminal pathogen. Analysis of our MM transcriptional profiling led to the discovery that MM express higher levels of β_2AR as compared to LpM, a finding we further confirmed through the use of translating ribosomal affinity purification. Finally, we used a combination of in vitro and in vivo pharmacologic and genetic manipulation of MM to demonstrate that adrenergic signaling through B2AR was required for the rapid increase in an anti-inflammatory transcriptional program. Together these results clearly demonstrate that neuronal pathogen sensing enables fast and long-range communication from the gut lumen to intestinal immune populations that are not directly exposed to infection.

Chapter 3: Microbes Modulate Sympathetic Neurons

3.1 The microbiota modulate gut–projecting extrinsic sympathetic neurons

We sought to better characterize the connections of eEAN and whether their activity or gene expression is influenced by the gut microbiota. To identify the location of eEAN cell bodies, we injected a fluorescent retrograde tracer, cholera toxin beta subunit (CTB), into the wall of different intestinal segments, and dissected extrinsic ganglia that project to the gut, specifically the sensory nodose ganglion (NG) and dorsal root ganglia (DRG), as well as the sympathetic celiac–superior mesenteric (CG-SMG) ganglion (Figure 3.1a-g). The number of NG retrograde traced neurons was highest in the duodenum with the majority of neurons labeled in the left NG (Figure 3.1b), while in the more sparsely innervated distal small intestine and colon we noted a bias towards right NG labeling (Figure 3.1b,d). Retrograde tracing to the CG-SMG revealed an increase in CTB+ neurons in moving from the duodenum to the colon (Figure 3.1c,e). Lastly, the representation of retrograde traced neurons in the DRG was similar for all areas of the intestine in the thoracic DRG, however the mid-distal colon also received innervation derived from lumbar DRG (Figure 3.1f,g). Tracing specificity was confirmed by multiple approaches including

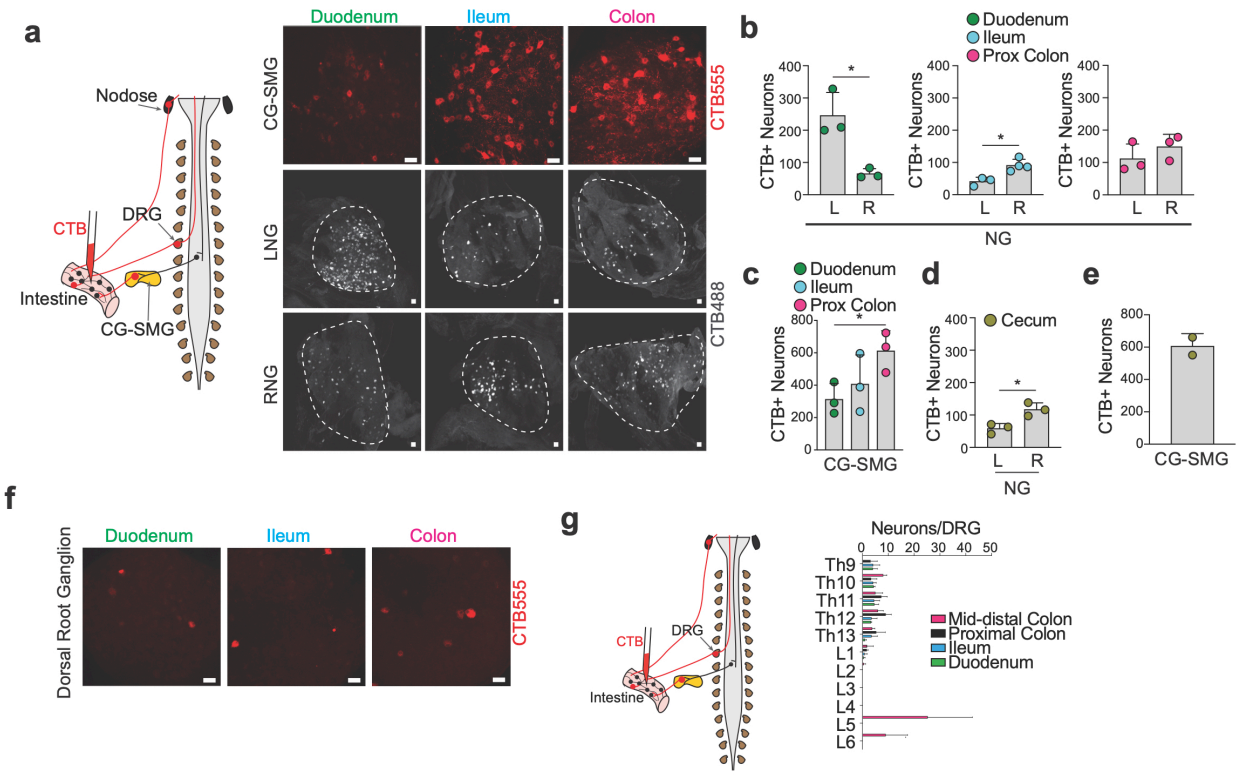

Figure 3.1. Distribution of eEAN innervation to the small and large intestine. (**a**) (left) Scheme depicting retrograde CTB AF555 (CTB555) or AF488 (CTB488) tracing from the duodenum, ileum, and colon to the CG-SMG, left (L) and right (R) nodose ganglion (NG) of C57BL/6J SPF mice. Images representative of duodenum (n=5), ileum (n=6), and colon (n=5). (**b**) Quantification of the number of neurons in the L-NG and R-NG retrograde labeled from the duodenum, ileum, and proximal colon. (**c**) Number of CTB+ neurons per CG-SMG retrograde labeled from the duodenum, ileum, and proximal colon. (n=3 per condition) (d) Quantification of the number of neurons in the left (L) and right (R) nodose ganglion (NG) retrograde labeled from the cecum (n=3). (**e**) Number of CTB+ neurons per CG-SMG retrograde labeled from the cecum (n=2). (**f**) Retrograde CTB Alexafluor555 (CTB555) tracing from the duodenum, ileum, and colon to the thoracic 10 DRG of C57BL/6J SPF mice. Images representative of duodenum (n=3), ileum (n=3), proximal colon (n=3), and distal colon (n=2). (**g**) (Left) Schematic showing retrograde tracing of DRG. (Right) Distribution of CTB555 retrograde traced neurons in the DRG from injections in the duodenum (n=3), ileum (n=3), proximal colon (n=3), and distal colon (n=2). (**a**,**f**) Scale bars = 50μm; (**b**,**c**,**d**) data represented as mean ± s.d. * $P < 0.05$ as calculated by unpaired t-test.

subdiaphragmatic vagotomy (sdVx), tracing from unrelated organs, and selective intestinal denervation (Figure 3.2a-k). All three of these approaches definitively establish

that retrograde labeled neurons we observed from the intestine are not the result of tracer leakage, which could potentially confound interpretation. Individual CTB tracing of the duodenum, ileum, and colon indicated that sensory and sympathetic innervation of these anatomically distinct intestinal regions is mediated by non-overlapping neuronal cell populations (Figure 3.2l,m). However, in areas that are closely linked, such as the stomach and the proximal duodenum, we did find some overlap in retrograde traced populations (Figure 3.2g). This small overlap may reflect the need to integrate common signals and instruct coordinated motor patterns between the duodenum and stomach in moving chyme through the pylorus for example. These results highlight the distinct compartmentalization of both sensory and effector eEAN projecting to the intestine.

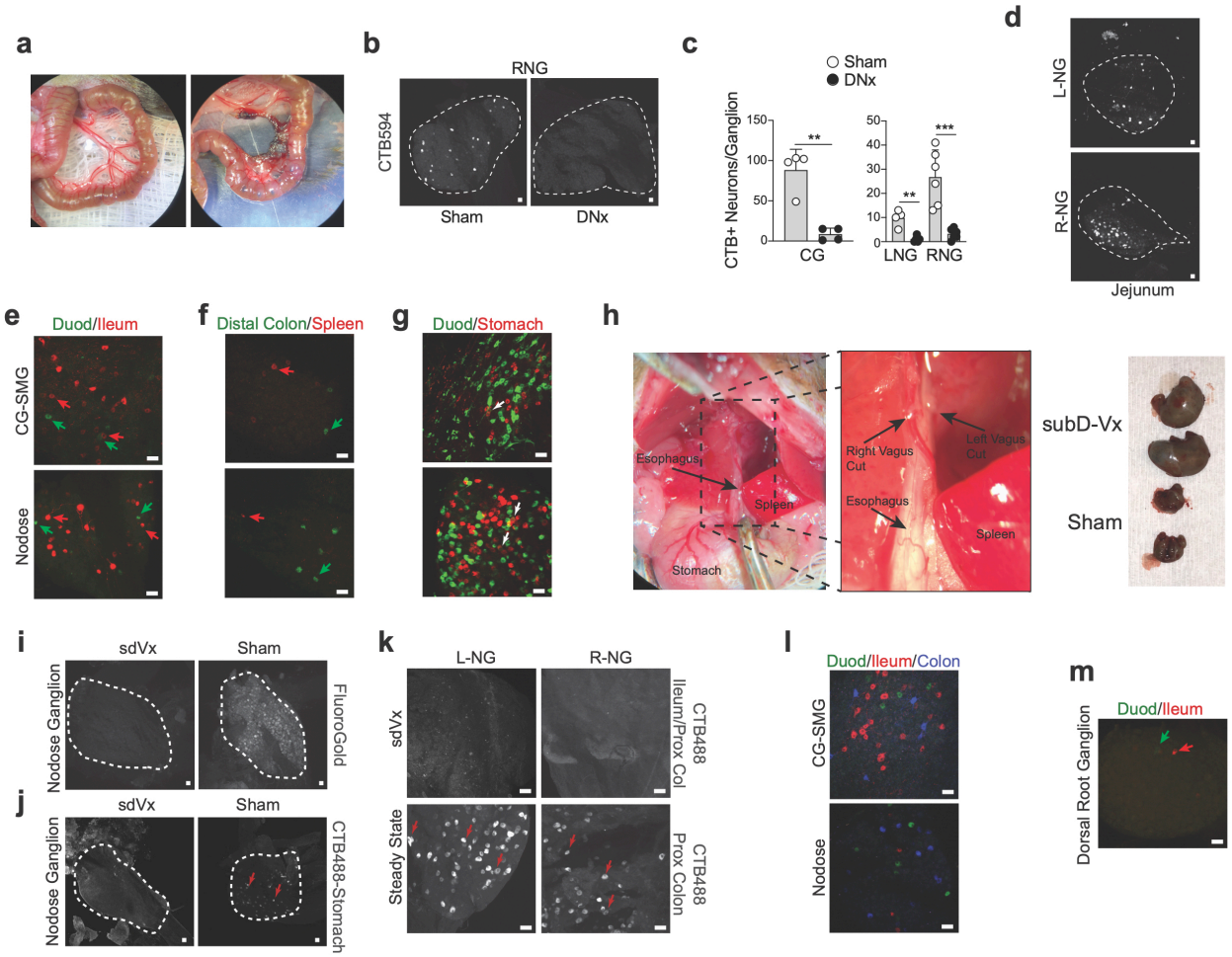

Figure 3.2. Specificity of intestine retrograde tracing. (**a**) Loop of distal sham (left panel) and denervated (right panel) ileum, with CTB594 injected into the wall of the intestine. (**b**) Representative R-NG of mice injected with CTB594 into the distal ileum of sham or denervated mice. Images representative of n=6. Scale bars = 50mm. (**c**) Number of CTB594+ neurons in the CG-SMG and NG of sham or distal ileum-denervated mice (for both conditions: n=4 CG, n=4 (L-NG), n=6 (R-NG)). (**d**) Image of NG of mice injected with CTB488 into the jejunum. Images representative of n=2. (**e**) Dual CTB tracing in the NG and CG-SMG with CTB488 from the duodenum and CTB555 from the ileum. Green arrows show duodenum-traced neurons and red arrows show ileum-traced neurons. Image representative of n=3. (**f**) Dual CTB tracing in the NG and CG-SMG with CTB488 from the spleen and CTB555 from the colon. Green arrows show colon-traced neurons and red arrows show spleen-traced neurons. Image representative of n=3. (**g**) Dual CTB tracing in the NG and CG-SMG with CTB488 from the duodenum and AlexaFluor594 from the stomach. White arrows indicate neurons labeled with both AF488/AF555. Image representative of n=3. (**h**) Anatomical verification of subdiaphragmatic vagotomy (sdVx) showing enlarged stomach and successful severing of the vagal nerves below the diaphragm. Images representative of n= 10. (**i**) Confocal whole-mount image of the NG with FluoroGold injected i.p. in mice with sdVx and sham surgery. Dashed lines highlight the NG. Images representative of n= 5. (**j**) Immunofluorescence whole-mount image of the NG with CTB injected into the stomach in mice with sdVx and sham surgery. Arrows indicate CTB+ cells. Dashed lines highlight the NG. Images representative of n= 5. (**k**) Immunofluorescence NG whole mount images of CTB injected into the ileum/proximal colon in mice with sdVx and into the proximal colon in mice without surgery. Arrows indicate CTB+ cells. Dashed lines highlight the NG. Images representative of n=2. (**b**,**d-g**,**i-m**) Scale bars = 50μm; (**c**) Data represented as mean ± s.d. ** $P < 0.01$, *** $P < 0.001$ as calculated by unpaired t-test.

We characterized microbial-mediated EAN gene expression changes by transcriptionally profiling eEAN ganglia identified by CTB-tracing using cell sorting-independent translating ribosomal affinity purification (TRAP) (Heiman et al., 2014). We interbred pan–neuronal *Snap25*^{Cre} with *Rpl22*$^{lsl\text{-}HA}$ (RiboTag) mice (Sanz et al., 2009), which express a hemagglutinin (HA)–tagged ribosomal subunit 22, allowing for neuronal-specific immunoprecipitation of actively translated polysome-bound mRNA from whole tissue homogenates, avoiding possible confounding effects of neuronal dissociation on gene expression. Specific expression of HA–tagged ribosomes in neurons was confirmed in different eEAN ganglia isolated from *Snap25*^{RiboTag} mice (Figure 3.3a,b). We performed TRAP-seq of the NG, thoracic 9 DRG, and CG-SMG isolated from specific pathogen free (SPF) mice and *Snap25*^{RiboTag} mice re-derived into germ-free (GF) conditions (Figure 3.3c-e). Comparisons of eEAN nodes revealed significant enrichment of transcripts associated with both sensory and sympathetic neurons (Zeisel et al., 2018), validating our TRAP approach (Figure 3.3c-h). We did not observe significant changes in expression of actively translated genes in the DRG between SPF and GF groups (Figure 3.3i). However, gene ontology (GO) analysis of the NG suggested an enrichment for genes associated with synaptic signaling and neuronal activation in GF mice (Figure 3.3j,k). Additionally, the CG-SMG from GF animals displayed enriched GO pathways for plasticity and signaling with significantly higher transcript levels of *Fos* (Figure 3.3l,m), a classic neuronal immediate–early gene and indirect marker for neuronal activity, or plasticity (used thereof interchangeably (Mei et al., 2001)). Immunofluorescence analysis

Figure 3.3. Gene expression changes in eEAN of GF mice. (**a**) Whole-mount immunofluorescence of the nodose ganglion (NG), celiac-superior mesenteric (CG-SMG), and dorsal root ganglion (DRG) from *Snap25*^{RiboTag} mice SPF mice using anti-hemagluttinin (HA, in green) antibody and NeuroTrace (red). Image representative of n=5. (**b**) Whole-mount immunofluorescence of the NG, CG-SMG, and DRG from Snap25RiboTag mice GF mice using anti-HA (HA, in green) antibody and NeuroTrace (red). Image representative of n=2. (**c**) Volcano plot of differentially-expressed genes compared between the NG and Th9 DRG of *Snap25*^{RiboTag} SPF mice. Grey dots indicate all genes analyzed by differential expression analysis. Red dots indicate genes enriched in the NG ($log_2FC > 3$). Blue dots highlight genes enriched in DRG ($log_2FC > 3$). Number of samples analyzed are indicated in parentheses at top. (**d**) Volcano plot of differentially-expressed genes between the Th9 DRG and CG-SMG of *Snap25*^{RiboTag} SPF mice. Grey dots indicate all genes analyzed by differential expression analysis. Red dots indicate genes enriched in the Th9 DRG ($log_2FC > 3$). Blue dots indicate genes enriched in CG-SMG ($log_2FC > 3$). Number of samples analyzed are indicated in parentheses at top. (**e**) Volcano plot of differentially-expressed genes compared between the NG and CG-SMG of *Snap25*^{RiboTag} SPF mice. Grey dots indicate all genes analyzed by differential expression analysis. Red dots indicate genes enriched in the NG ($log_2FC > 3$). Blue dots indicate genes enriched in CG-SMG ($log_2FC > 3$). Number of samples analyzed are indicated in parentheses at top. (**f**) Immunofluorescence whole-mount staining of the CG-SMG with anti-TH (green) and anti-NPY (red) antibodies. Image representative of n=3. (**g**) Immunofluorescence whole-mount staining of the CG-SMG with anti-TH (green) and anti-SST (red) antibodies. Image representative of n=2. (**h**) Immunofluorescence whole-mount staining of the CG-SMG with anti-cFos (red) antibody and native tdTomato fluorescnce (green). Image representative of n=3. (**i**) Volcano plots of differentially-expressed genes of thoracic 9 DRG from GF and SPF *Snap25*^{RiboTag} mice. Grey dots indicate all genes analyzed by differential expression analysis. Black dots indicate specific genes. Red dots and number ($log_2FC > 0.5$) indicate genes higher in GF. Blue dots and number ($log_2FC > 0.5$) indicate genes significantly higher in SPF. Parentheses indicate

$log_2FC > 1$. Number of samples analyzed are indicated in parentheses at top. (**j**) Volcano plots of differentially expressed genes compared between the NG of *Snap25*^{RiboTag} germ-free (GF) or specific pathogen-free (SPF) mice. Grey dots indicate all genes analyzed by differential expression analysis. Black dots indicate select genes. Red dots and number ($log_2FC > 0.5$) indicate genes higher in GF samples. Blue dots and number ($log_2FC > 0.5$) indicate genes significantly higher in SPF samples. Parentheses indicate $log_2FC > 1$ genes. Number of samples analyzed are indicated in parentheses at top. (**k**) Gene ontology pathways, identified by TopGO analysis of differentially expressed genes (log_2FC Change > 0.5, $p_{adj} < 0.05$), enriched in the GF NG (red) vs SPF NG (blue). Dashed lines represent threshold of significance (1.3) as calculated by Fisher's test with an elimination algorithm. (**l**) Volcano plots of differentially expressed genes compared between the CG-SMG of Snap25RiboTag GF or SPF mice. Grey dots indicate all genes analyzed by differential expression analysis. Black dots indicate select genes. Red dots and number ($log_2FC > 0.5$) indicate genes higher in GF samples. Blue dots and number ($log_2FC > 0.5$) indicate genes significantly higher in SPF samples. Parentheses indicate log2Fold Change > 1 genes. (**m**) Gene ontology pathways, identified by TopGO analysis of differentially expressed genes ($log_2FC > 0.5$, $p_{adj} < 0.05$), enriched in the GF CG-SMG (red) vs SPF CG-SMG (blue). Dashed lines represent threshold of significance (1.3) as calculated by Fisher's test with an elimination algorithm. Scale bars = 50μm

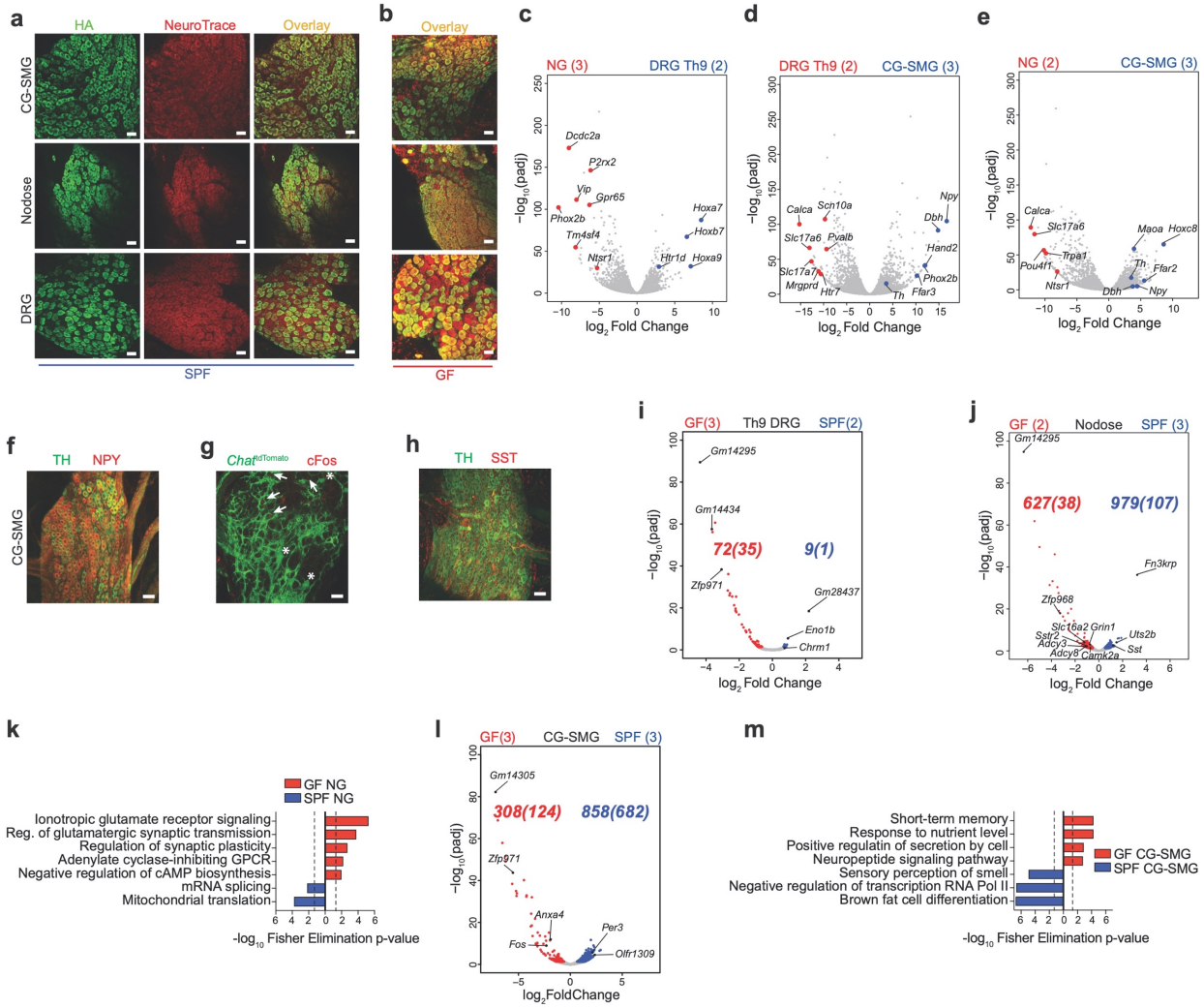
a
HA
NeuroTrace
Overlay
CG-SMG
Nodose
DRG
SPF
b
Overlay
GF
c
NG (3)
DRG Th9 (2)
Dcdc2a
P2rx2
Vip
Gpr65
Phox2b
Tm4sf4
Ntsr1
Hoxa7
Hoxb7
Ftr1d
Hoxa9
−log10(padj)
log2 Fold Change
d
DRG Th9 (2)
CG-SMG (3)
Calca
Scn10a
Slc17a6
Pvalb
Slc17a7
Mrgprd
Htr1
Th
Npy
Dbh
Hand2
Phox2b
Ffar3
e
NG (2)
CG-SMG (3)
Calca
Slc17a6
Pou4f1
Ntsr1
Maoa
Hoxc8
Tnpa1
Th
Ffar2
Dbh
Npy
f
TH
NPY
CG-SMG
g
ChatRdTomato
cFos
h
TH
SST
i
GF(3)
Th9 DRG
SPF(2)
Gm14295
Gm14434
72(35)
9(1)
Zfp971
Gm28437
Eno1b
Chrm1
j
GF (2)
Nodose
SPF (3)
Gm14295
627(38)
979(107)
Fn3krp
Zfp968
Slc16a2
Grin1
Sstr2
Adcy3
Adcy8
Camk2a
Uts2b
Sst
k
GF NG
SPF NG
Ionotropic glutamate receptor signaling
Reg. of glutamatergic synaptic transmission
Regulation of synaptic plasticity
Adenylate cyclase-inhibiting GPCR
Negative regulation of cAMP biosynthesis
mRNA splicing
Mitochondrial translation
-log10 Fisher Elimination p-value
l
GF(3)
CG-SMG
SPF (3)
Gm14305
308(124)
858(682)
Zfp971
Anxa4
Fos
Per3
Olfr1309
log2FoldChange
m
Short-term memory
Response to nutrient level
Positive regulatin of secretion by cell
Neuropeptide signaling pathway
Sensory perception of smell
Negative regulation of transcription RNA Pol II
Brown fat cell differentiation
GF CG-SMG
SPF CG-SMG
-log10 Fisher Elimination p-value

confirmed that CG-SMG isolated from GF mice displayed significantly more cFos+ neuronal nuclei than their SPF mice counterparts (Figure 3.4a-e). Altogether these results show that absence of a microbiota results in elevated levels of gut–extrinsic sympathetic activity.

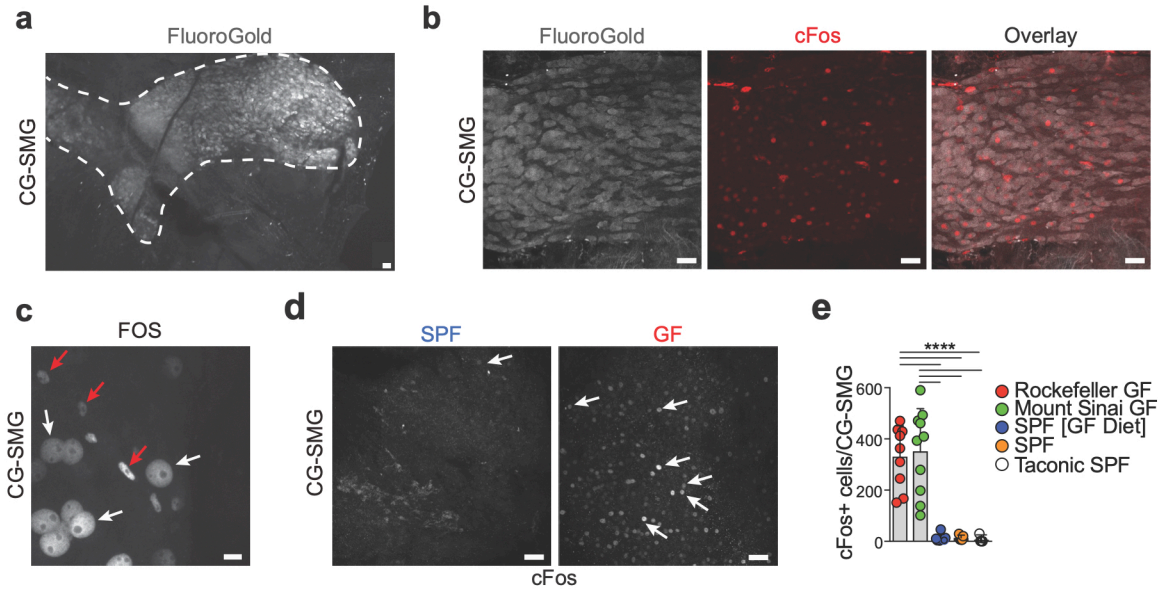

Figure 3.4. GF mice have increased cFos in viscera-projecting sympathetic neurons. (**a**) Native fluorescence of FluoroGold in a whole-mount preparation of the CG-SMG from C57BL/6J SPF mice 3 days after i.p. injection. Dotted line outlines the CG-SMG FluoroGold+ signal. Image representative of n=4. (**b**) Immunofluorescence whole-mount of CG-SMG from an acutely stressed C57BL/6J SPF mouse, stained with anti-cFos (red) antibody and native fluorescence of FluoroGold. Image representative of at least n=4. (**c**) Immunofluorescence whole-mount of CG-SMG from an acutely stressed mouse. Stained for cFos (white). White arrows indicate neuronal cFos+ nuclei, red arrows indicate non-neuronal cFos+ nuclei. (**d**) CG-SMG whole-mount immunostaining of C57BL/6J GF and SPF mice using anti-cFos antibody. White arrows indicate cFos+ nuclei. Images representative of GF (n=9) and SPF kept in germ-free diet (n=7). (**e**) Numbers of cFos+ neurons in the CG-SMG of C57BL/6J GF mice from Rockefeller (n=9) or Mount Sinai (n=10) animal facilities as compared to SPF kept in germ-free diet (n=7), SPF normal chow (n=5), and Taconic SPF normal chow (n=5) controls. (**a**,**b**,**d**) Scale bars = 50μm; (**c**) Scale bar = 10μm; (**e**) Data represented as mean ± s.d., **** $P < 0.0001$ as calculated by one-way ANOVA with Tukey multiple comparisons.

3.2 Short-chain fatty acid producing bacteria suppress gut extrinsic sympathetic activation

To address whether specific microbes could mediate tonic suppression of CG-SMG neurons, we utilized multiple microbial manipulation strategies. Fecal transfer from age-, sex-, strain-, and diet–matched SPF donors into GF mice restored CG-SMG neuronal cFos to levels comparable to SPF conditions, suggesting that microbiota can suppress gut–extrinsic sympathetic neurons (Figure 3.5a). The mere presence of live bacteria was not enough to suppress CG-SMG neuronal activation, as evidenced by the comparable cFos levels observed in GF mice mono-colonized with segmented filamentous bacteria and GF mice (Figure 3.5b). However, colonization of GF mice with

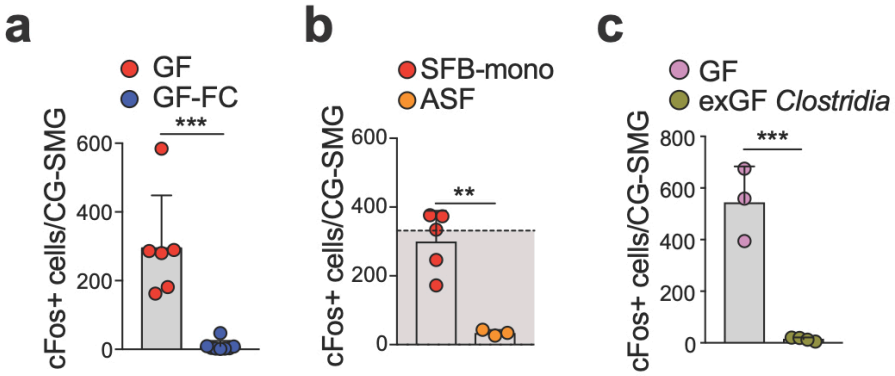

Figure 3.5. **GF sympathetic activation can be suppressed by specific microbes.** (**a**) Number cFos+ neurons in the CG-SMG of C57BL/6J GF mice (n=6) and GF mice (n=8) colonized with feces from SPF mice 2 weeks prior to analysis. (**b**) Number of cFos+ neurons in the CG-SMG of C57BL/6J SFB monocolonized mice (n=5) and ASF colonized mice (n=3). Dashed line and shaded area below indicate the average number (334) of cFos+ neurons in GF mice. (**c**) Number of cFos+ neurons in the CG-SMG of Germ Free C57BL/6J mice from Weill Cornell with (n = 4) or without (n = 3) *Clostridium* colonization. (**a-c**) Data represented as mean ± s.d. , ** $P < 0.01$, *** $P < 0.001$ as measured by unpaired t-test.

the defined altered–Schaedler–flora consortium (ASF) (Dewhirst et al., 1999) or a defined *Clostridia.* consortium (Atarashi et al., 2013), was sufficient to suppress cFos expression in the CG-SMG (Figure 3.5b,c). These results demonstrate that sympathetic activation is

reversible both at birth and in adulthood, where a diverse microbiota can suppress CG-SMG cFos.

We next treated SPF mice with broad-spectrum antibiotics to address whether microbial effects on sympathetic neurons were a specific phenotype of GF mice. Microbiota depletion of SPF mice for 2 weeks using broad-spectrum antibiotics resulted in increased cFos+ neurons in the CG-SMG when compared to control mice (Figure 3.6a,b). Treatment with either ampicillin or vancomycin, but not with metronidazole or neomycin, was sufficient to drive sympathetic cFos expression, suggesting that specific subsets of bacteria were able to suppress cFos activation (Figure 3.6c). Additionally, a single oral gavage of streptomycin to SPF C57BL/6, BALB/c, or CBA/J mice resulted in CG-SMG neuronal activation as early as 24 h post-gavage, as well as decrease in microbiota diversity. Five days post streptomycin treatment, cFos levels in the CG-SMG returned to SPF levels, indicating that gut–sympathetic activity is rapidly tuned to changes in the gut microbiota (Figure 3.6d-f). Finally, to address whether activated CG-SMG sympathetic neurons project to the intestine, we injected fluorescent CTB in the ileum of broad-spectrum antibiotic–treated *Fos*^{GFP} mice (Barth et al., 2004). We observed extensive colocalization between CTB+ (red) and cFos+ (green) neurons in the CG-SMG (Figure 3.6g), confirming that sympathetic neurons activated upon microbial depletion project to the intestine, although we cannot exclude projections to other visceral tissue connected to the CG-SMG. Activation of sympathetic neurons leads to inhibition of iEAN which in turn mediate smooth muscle tone and pacemaker activity of ICC. Thus, we hypothesized that changes in gut-sympathetic activity could impact the activity of iEAN

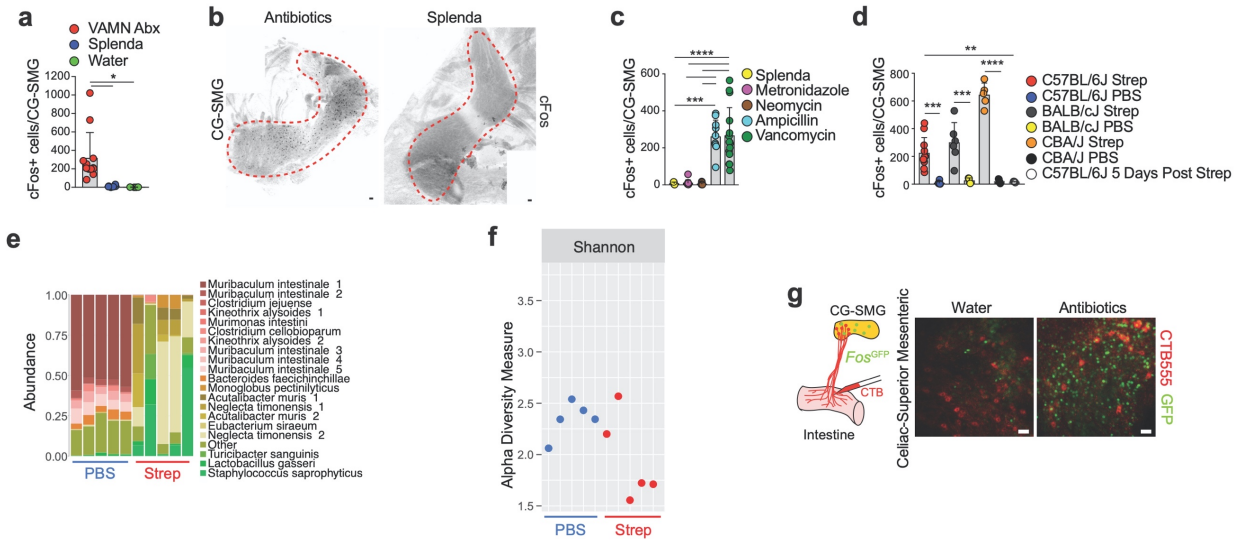

Figure 3.6. **Microbial depletion leads to activation of gut-projecting sympathetic neurons.** (**a**) Number of cFos+ neurons in the CG-SMG of C57BL/6J SPF mice treated for 2 weeks with vancomycin, ampicillin, metronidazole, and neomycin (n=12) in drinking water as compared to Splenda (n=6) and water (n=5) treated controls. (**b**) Whole-mount stitched images of cFos staining in the CG-SMG from of C57BL/6J SPF mice treated with VAMN or Splenda. Images representative of at least n=6. (**c**) Number of cFos+ neurons in the CG-SMG following 2 weeks of single antibiotic (metronidazole: n=10, neomycin: n=10, ampicillin: n=10, vancomycin: n=15) or Splenda (n = 5) treatment. (**d**) cFos+ neurons in the CG-SMG of C57BL/6J (streptomycin: n=11, PBS: n=6), BALBc/J (streptomycin: n = 6, PBS: n = 4), and CBA/J (streptomycin: n = 5, PBS: n = 5) mice 24 hours post oral gavage of streptomycin or PBS and 5 days post streptomycin in C57BL/6J mice (n=4). (**e**) Most abundant bacterial genera in 16S sequencing of cecal samples from PBS- and streptomycin-treated C57BL6/J mice as determined by the phyloseq R package. (**f**) Shannon diversity index of 16S sequencing of cecal samples in PBS- or streptomycin-treated C57BL6/J mice as determined by the phyloseq R package. (**g**) Whole-mount of CG-SMG of FosGFP SPF mice treated with VAMN or water for 2 weeks, with AlexaFluor555 conjugated CTB injected into the ileum. (**b**,**g**) Scale bars = 50μm; (**a**,**c**,**d**) Data represented as mean ± s.d., * $P < 0.05$, ** $P < 0.01$, *** $P < 0.001$, **** $P < 0.0001$ as calculated by one-way ANOVA with Tukey's multiple comparisons.

and other electrically excitable cells. Through intravital multiphoton imaging, we observed a significant increase in the frequency of ICC calcium transients of antibiotic treated germline genetically encoded calcium indicator GFP-calmodulin-myosin peptide fusion protein version 6s (GCaMP6s) mice as compared to Splenda-treated controls, suggesting

a change in the tone of iEAN networks (Figure 3.7a). The above results indicate that a defined microbial consortium is sufficient to suppress cFos expression in gut sympathetic neurons, and that sympathetic activity can reflect shifts in the gut microbial community.

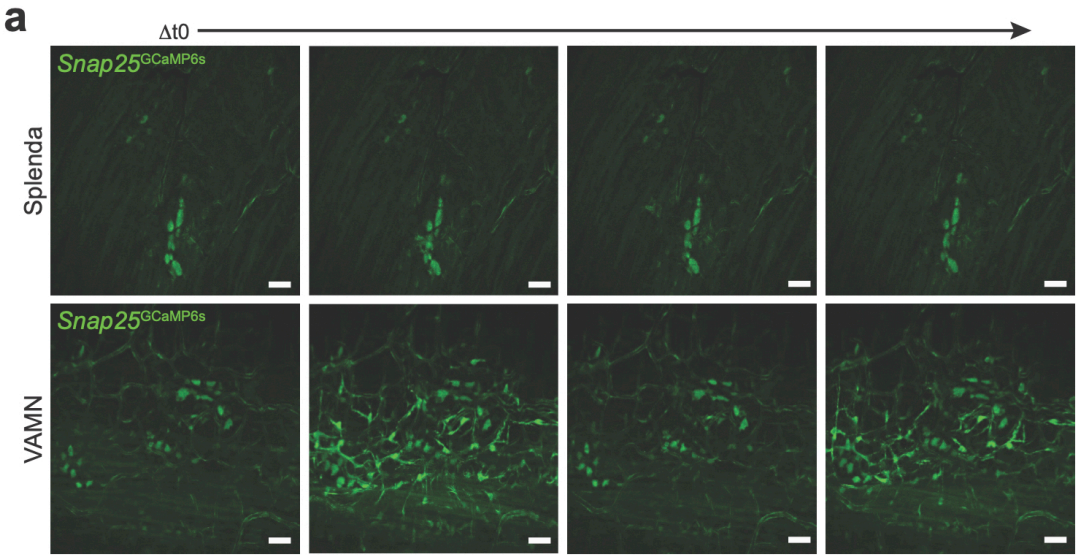

Figure 3.7. **Increase in ICC GCaMP6s activity with antibiotics.** (**a**) Intravital two-photon microscopy time lapse of the myenteric plexus of *Snap25*^{GCaMP6s} mice (germline recombined) treated with Splenda- (top) or VAMN antibiotic- (bottom) supplemented water for 2 weeks. Each panel is representative of 1 second. Scale bars = 50μm

We observed that gnotobiotic manipulations resulted in suppression of CG-SMG neurons when defined microbial consortia, known to restore levels of SCFAs, were introduced (Atarashi et al., 2013; Biggs et al., 2017; Dewhirst et al., 1999). Mass spectrometric quantification of SCFAs confirmed that GF mice lacked detectable levels of butyrate, propionate, and acetate in their cecal contents (Figure 3.8a).

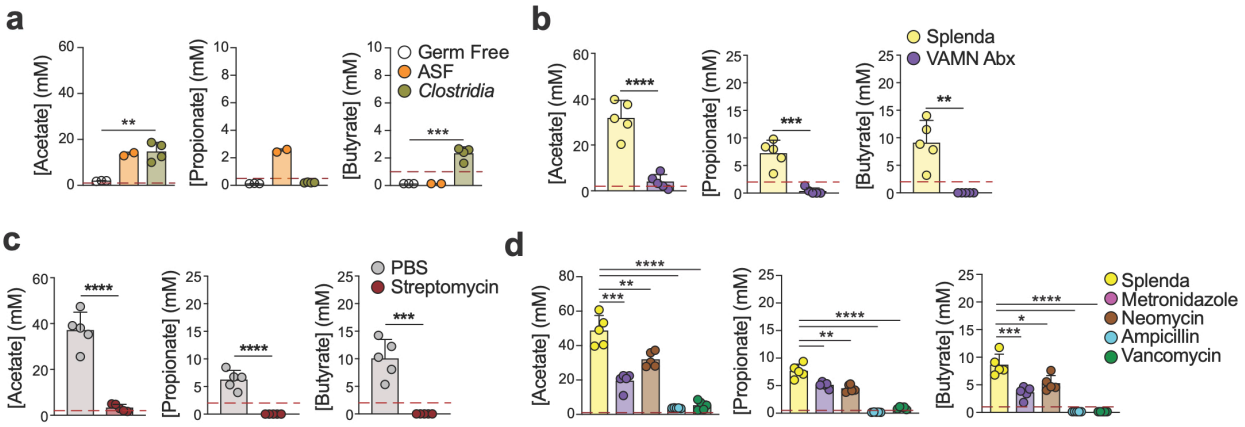

Figure 3.8. **Microbial depletion results in a significant reduction in SCFA.** (**a**) Quantification of SCFA in the cecal contents of GF mice colonized with ASF or *Clostridia* consortium. (**b**) Quantification of SCFA in the cecal contents of VAMN- and Splenda-treated C57BL6/J mice. (**c**) Quantification of SCFA in the cecal contents of PBS- and streptomycin-treated C57BL6/J mice. (**d**) Quantification of SCFA in the cecal contents of single antibiotic- and Splenda-treated C57BL6/J mice. (**a-d**) Data represented as mean ± s.d. Dashed line indicates lowest limit of detection; (**a**,**d**) * $P < 0.05$, ** $P < 0.01$, *** $P < 0.001$, **** $P < 0.0001$ as calculated by one-way ANOVA with Tukey's multiple comparisons; (**b**,**c**) ** $P < 0.01$, *** $P < 0.001$, *** $P < 0.0001$ as measured by unpaired t-test.

GF mice colonized with ASF displayed a significant increase in the levels of propionate and acetate in their ceca, while the *Clostridia* consortium led to a significant boost in butyrate and acetate levels (Figure 3.8a). Furthermore, treatment with broad-spectrum antibiotics, streptomycin, ampicillin or vancomycin alone recapitulated SCFA depletion to below detection threshold (Figure 3.8b-d). In each of these cases, the presence or absence of luminal SCFAs correlated with the number of cFos+ neurons in the CG-SMG. Cecum size, known to increase upon treatment with broad-spectrum antibiotics (Muller et al., 2014; Savage and McAllister, 1971), did not correlate with sympathetic activation, suggesting that mechanosensation likely does not play a role in sympathetic activation (Figure 3.9a). In contrast, in the context of *Salmonella* Typhimurium infection, which we

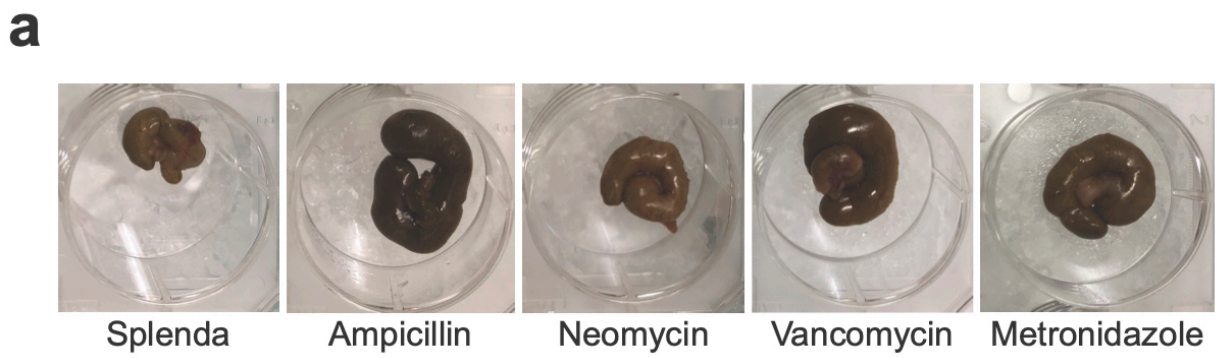

Figure 3.9. **Change in cecal size with antibiotics.** (**a**) Dissected cecum (in 6 well cell culture plate) images from mice treated with Splenda, ampicillin, neomycin, vancomycin, or metronidazole for 2 weeks. Images representative of at least n=5.

previously reported to induce CG-SMG activation (Gabanyi & Muller et al., 2016), we did not detect significant changes in SCFAs at early stages of infection (Rivera-Chávez et al., 2016a), suggesting that additional signals contribute to CG-SMG activation upon infection or in inflammatory contexts (Figure 3.10a-c). Next, we tested whether supplementation of

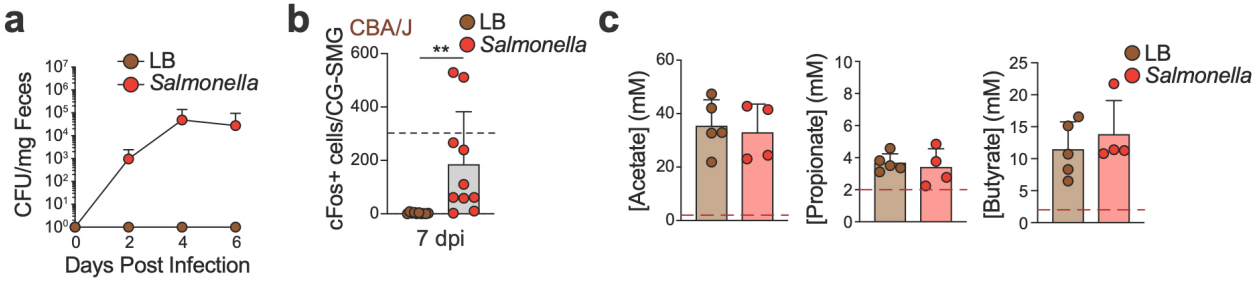

Figure 3.10. *Salmonella* induces sympathetic cFos without SCFA changes. (**a**) Number of colony forming units (CFU) of Salmonella per mg of feces in infected CBA/J mice (n=5), compared to luria broth (LB)-gavaged controls (n=5) at the indicated days post infection. (**b**) Number of cFos+ neurons in the CG-SMG of CBA/J mice given an oral gavage of luria broth (n=10) or Salmonella (n=10). Dashed line indicates average number of cFos+ neurons for antibiotic treated mice (320). ** $P < 0.01$ as calculated by unpaired t-test. (**c**) Quantification of SCFAs in the cecal contents of CBA/J mice given an oral gavage of luria broth (LB) (n=5) or Salmonella (n=4). Dashed line indicates lowest limit of detection. (**a-c**) Data represented as mean ± s.d.

SCFAs in microbiota–depleted mice could restore cFos levels in the CG-SMG. Administration of exogenous butyrate, acetate, and propionate in the drinking water

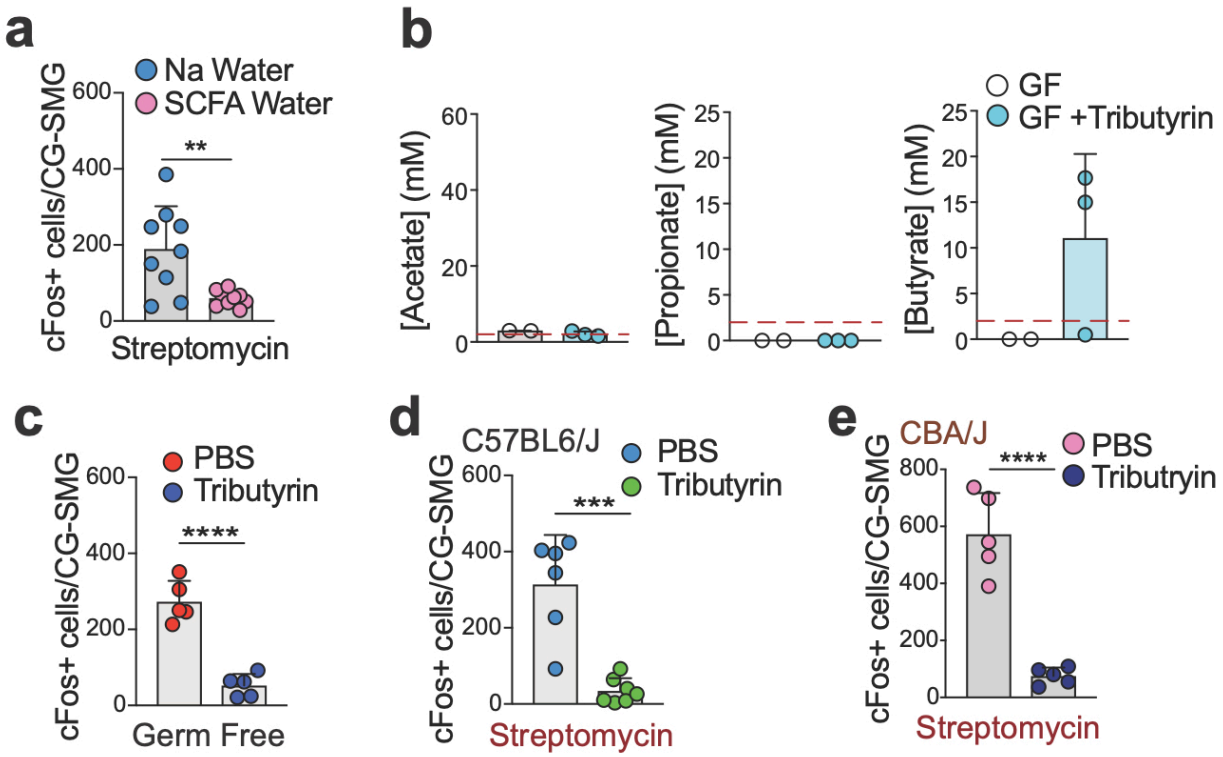

Figure 3.11. Supplementation with exogenous SCFA can suppress sympathetic cFos. (**a**) Number of cFos+ neurons in the CG-SMG of C57BL/6J SPF mice 24 hours post oral gavage with streptomycin in mice treated with SCFA-supplemented or sodium-containing water. (**b**) Quantification of SCFAs in cecal samples of Germ-Free mice given consecutive oral gavage of PBS (n=2) or Tributyrin (n=3). Dashed line indicates lowest limit of detection. (**c**) Number of cFos+ neurons in CG-SMG of C57BL/6J GF mice 24 hours post-treatment with tributyrin (n=5) or PBS (n=5). (**d**) Number of cFos+ neurons in CG-SMG of C57BL/6J SPF mice treated with tributyrin (n=7) or PBS (n=6) 24 hours post oral gavage of streptomycin. (**e**) Number of cFos+ neurons in CG-SMG of CBA/J SPF mice treated with tributyrin (n=5) or PBS (n=5) 24 hours post oral gavage of streptomycin. (**a**,**c**-**e**) Data represented as mean ± s.d., ** $P < 0.01$, *** $P < 0.001$, **** $P < 0.0001$ as calculated by unpaired t-test.

suppressed streptomycin–induced cFos (Figure 3.11a). Moreover, administration of tributyrin, a butyrate pro-drug containing three acetylated butyrate molecules that are readily hydrolyzed in the intestine (Rivera-Chávez et al., 2016a; Wichmann et al., 2013),

was sufficient to suppress cFos expression in CG-SMG neurons of both GF mice and SPF mice treated with streptomycin (Figure 3.11b-e). Butyrate, and additional SCFAs, can modulate gene expression in target cells via activation of G protein-coupled receptors GPR41, 43 or 109A, inhibition of histone deacetylases or act as an energy substrate (Koh et al., 2016). We evaluated cFos+ neurons in the CG-SMG in mice deficient for GPR41, GPR109A or double-deficient for GPR43 and GPR109A, all maintained under SPF conditions. While Gpr109a$^{-/-}$ and double Gpr43$^{-/-}$ Gpr109a$^{-/-}$ mice did not show differences when compared to wild-type controls, Gpr41$^{-/-}$ mice showed a mild yet significant increase in the number of cFos+ neurons in the CG-SMG (Figure 3.12a-c).

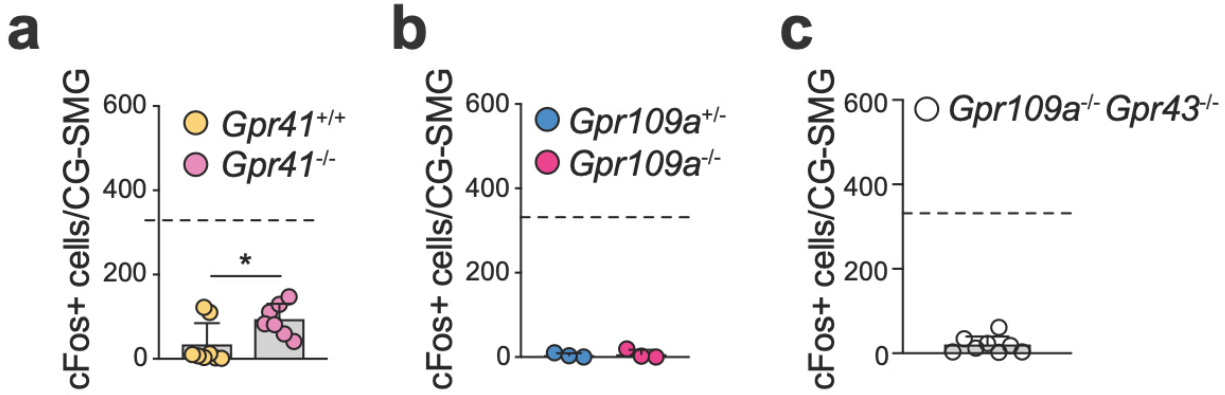

Figure 3.12. Sympathetic activation in different SCFA receptor knockout mice. (**a**) Number of cFos+ neurons per CG-SMG in Gpr41$^{-/-}$ (n=7) or Gpr41$^{+/+}$ control (n=8) mice. (**b**) Number of cFos+ neurons in the CG-SMG of Gpr109a$^{-/-}$ (n=3), compared to Gpr109a+/- control mice (n=3). (**c**) Number of cFos+ neurons in the CG-SMG of Gpr109a$^{-/-}$Gpr43$^{-/-}$ mice (n=8). (**a**-**c**) Dashed line indicates average number of cFos+ neurons for GF mice (334). Data represented as mean ± s.d. * $P < 0.05$ as calculated by unpaired t-test.

These data suggest a potential role for signaling via GPR41, which is expressed by intestinal epithelial cells, iEAN, and eEAN (Nøhr et al., 2015), as an upstream pathway

modulating gut sympathetic ganglia. Overall, the above results identify SCFAs as physiological modulators of gut sympathetic neuronal activation.

3.3 Microbe-modulated epithelial cell factors modulate gut sympathetic activity

Epithelial cell subsets, particularly enteroendocrine cells, are directly exposed to microbial signals and are capable of sensing and transmitting luminal input to EANs via synaptic transmission (Kaelberer et al., 2018) and/or via secretion of neuropeptides and neurotransmitters (Gribble and Reimann, 2016). Recent evidence pointed to a crucial role for the microbiota in modulating three major pathways: upregulation of serotonin (Yano et al., 2015), downregulation of L cell–derived glucagon-like peptide 1 (GLP-1) (Wichmann et al., 2013), and up or downregulation of peptide YY (PYY) (Browning and Lees, 2000; Newman et al., 2017; Samuel et al., 2008). Because secretion of these molecules is particularly enriched in the distal small intestine and colon, locations also enriched for SCFA production, we examined their role in the microbial modulation of sympathetic neurons. We addressed a possible suppressive role for epithelial–derived serotonin by crossing *Tph1*$^{fl/fl}$ mice (Yadav et al., 2008) with mice expressing inducible Cre^{ER} under the villin promoter (El Marjou et al., 2004) (Villin$^{\Delta Tph1}$). Conditional depletion of the key enzyme for serotonin production in gut epithelial cells upon tamoxifen administration did not result in changes in cFos+ neurons in the CG-SMG (Figure 3.13a-c). In contrast, administration of the GLP-1R agonist Exendin-4 increased cFos+ neurons in the CG-SMG, as well as the total gastrointestinal transit time (Figure 3.13d-f). To assess whether this pathway was required for microbial regulation of gut sympathetic

neurons, we treated *Glp1r*$^{-/-}$ mice (Scrocchi et al., 1996) with broad-spectrum antibiotics or Splenda. We observed similar numbers of cFos+ neurons in the CG-SMG isolated from

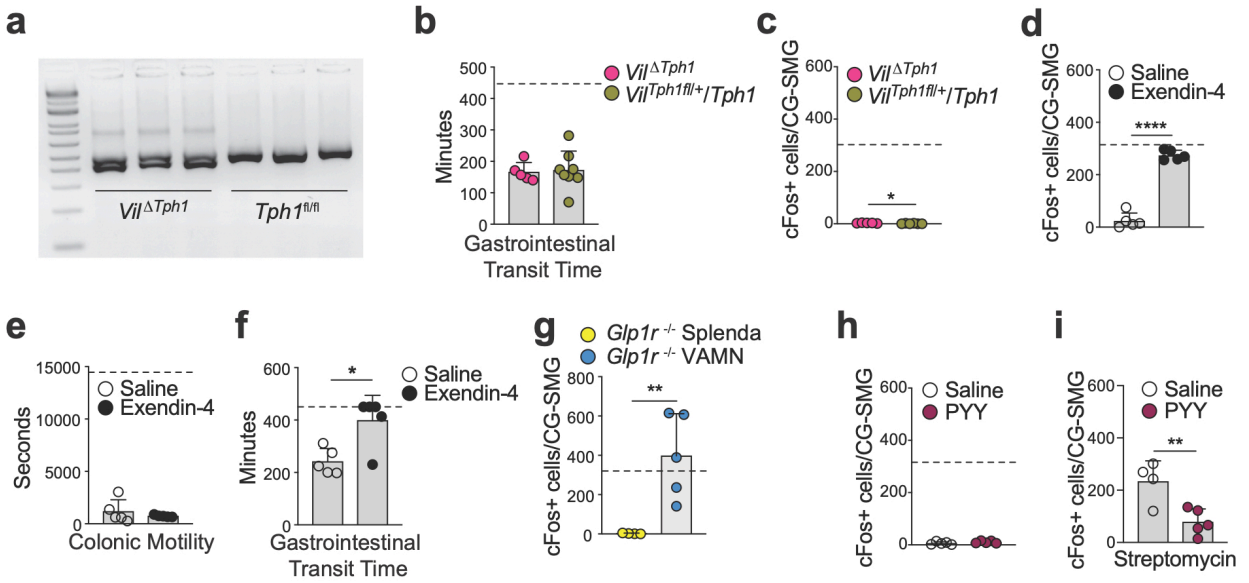

Figure 3.13. Effects of gut neuropeptides and neurotransmitters on sympathetic activation and gut motility. (**a**) Agarose gel image of recombination PCR analysis of colon samples. Lower band depcits the recombined allele in tamoxifen-treated *Vil*$^{\Delta Tph1}$, compared to Cre- control mice. (**b**) Gastrointestinal transit time of *Vil*$^{\Delta Tph1}$ mice (n=5) or control mice (n=8) 2 weeks post-tamoxifen injection. (**c**) Number of cFos+ neurons in the CG-SMG of *Vil*$^{\Delta Tph1}$ mice (n=5) or control mice (n=8) 2 weeks post-tamoxifen injection. (**d**) Number of cFos+ neurons in the CG-SMG of C57BL/6J mice 4 hours post i.p. injection of Exendin-4 (10mg/kg) (n=5) or saline (n=5). (**e** and **f**) Colonic motility (**e**) and gastrointestinal transit time (**f**) in C57Bl6/J mice post i.p. injection of Exendin-4 (10mg/kg) (n=5) or saline (n=5). (**g**) Number of cFos+ neurons in the CG-SMG of Glp1r-/- mice treated for 2 weeks with broad spectrum antibiotics (n=5) in drinking water as compared to Splenda (n=4) treated controls. (**h**) Number of cFos+ neurons in the CG-SMG of C57BL6/J mice 4 hours post i.p. injection of saline (n=5) or PYY (50mg/kg) (n=5). (**i**) Number of cFos+ neurons in the CG-SMG 4 hours post i.p. injection of PYY (50mg/kg) (n=5) or saline (n=5) in C57BL6/J mice that were given an oral gavage of streptomycin 24 hours prior. (**b**,**e**,**f**) Data represented as mean ± s.d. Dashed line indicates maximum time allowed per animal for each motility measurement. * $P < 0.05$ as calculated by unpaired t-test; (**c**,**d**,**g-i**) Data represented as mean ± s.d. Dashed line indicates average number of cFos+ neurons for antibiotic treated mice (320). ** $P < 0.01$, **** $P < 0.0001$ as calculated by unpaired t-test.

the antibiotic-treated group as compared to wild-type mice, suggesting that GLP-1 is sufficient to drive sympathetic activity, albeit not required for microbial–dependent modulation of gut sympathetic neurons (Figure 3.13g). Finally, PYY administration did not activate the CG-SMG in naïve SPF animals, but efficiently prevented the increase in cFos+ CG-SMG neurons following treatment with streptomycin (Figure 3.13h,i). These data suggest that the neuropeptides GLP-1 and PYY can modulate activity of gut sympathetic neurons and, in the case of PYY, may contribute to microbial regulation of gut sympathetic activity.

3.4 The efferent arm of the microbe-modulated gut sympathetic neuronal circuit

We next investigated the neuronal population(s), or circuits, upstream of the CG-SMG that could be involved in driving sympathetic activity under conditions of microbial depletion. We evaluated three possible neuronal inputs that could result in microbiota–dependent modulation of gut sympathetic neurons: i) direct sensing of the intestinal environment by CG-SMG sympathetic neurons due to innervation of the GI tract (Gabanyi & Muller et al., 2016; Uesaka et al., 2016) and expression of Gpr41 by sympathetic neurons (Samuel et al., 2008); ii) changes in iEAN activity that could influence sensory afferents or sympathetic neurons directly (viscerofugal neurons) (Hibberd et al., 2012; Linden, 2012; Perez-Burgos et al., 2014); iii) CNS-driven sympathetic pre-motor areas that would feed into sympathetic pre-ganglionic neurons (Deuchars and Lall, 2015; Ueno et al., 2016).

i) To visualize the extent to which sympathetic innervation reaches the gut epithelium, we injected retrograde adeno-associated virus AAVrg-CAG-FLEX-tdTomato into the CG-SMG of *Snap25*^{Cre} mice, thereby restricting the expression of Tomato protein to neurons (Figure 3.14a). As an independent and complementary strategy, AAVrg-hSyn1-Cre was injected into the CG-SMG of *Rosa*$^{lsl\text{-}tdTomato}$ mice (Figure 3.44d). In both approaches, we observed restriction of viruses to the ganglion and the immediate surrounding tissue (Figure 3.14a,d). Whole mount immunofluorescence or cleared–tissue imaging of the distal intestine showed innervation of the two neuronal plexuses, with sparse fibers extending to the mucosa, but little evidence of direct epithelial contact (Figure 3.14b,c,e,f). These results indicate that sympathetic eEANs may not be positioned to directly detect signals from the epithelial layer. It remains plausible that signals such as butyrate diffuse through the gut tissue or act via the circulation to influence CG-SMG activity. However, systemic (intraperitoneal) administration of tributyrin instead led to robust activation of the CG-SMG (Figure 3.14g) a result we also observed with i.p. injection of sodium butyrate (*data not shown*), as previously suggested by expression of Gpr41 in sympathetic neurons (Kimura et al., 2011; Samuel et al., 2008) and confirmed by our TRAP-seq data (Figure 3.14h). Coupled with *Gpr41*$^{-/-}$ data, which showed CG-SMG activation, the above data *suggest* that direct detection by sympathetic neurons is not the primary mechanism of microbiota–mediated suppression of CG-SMG activation.

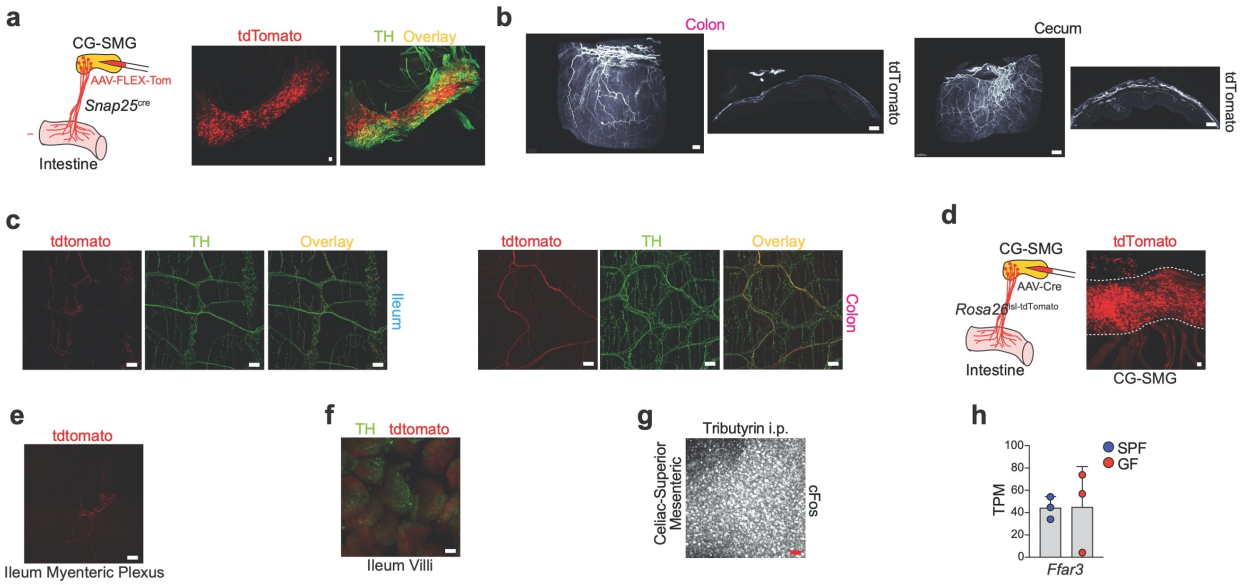

Figure 3.14. CG-SMG activation does not require direct sensing of microbes or metabolites. (**a**) (left) Scheme representing injection of AAVrg-CAG-FLEX-tdTomato into the CG-SMG of *Snap25*^{Cre} mice for tracing of fibers into the intestine. (right) Whole-mount immunofluorescence of the CG-SMG with native tdTomato fluorescence (red) and staining for tyrosine hydroxylase (green) antibody. Image representative of n=2. (**b**) (left) Light-sheet 3D reconstruction and optical section of the colon from (**a**). Image representative of n=2. (right) Light-sheet 3D reconstruction and optical section of the cecum from (**a**). Image representative of n=2. (**c**) Whole-mount immunofluorescence of the (left) ileum or (right) colon myenteric plexus from (**a**), with native tdTomato fluorescence (red) and staining for tyrosine hydroxylase (green) antibody. Scale bar = 50mm. Image representative of n=2. (**d**) (left) Scheme representing injection of AAVrg-hSyn1-Cre into the CG-SMG of *Rosa26*$^{lsl\text{-}tdTomato}$ mice for tracing of fibers in the intestine. (right) Whole-mount of the CG-SMG with native tdTomato fluorescence (red). Scale bar = 50mm. Image representative of n=2. (**e**) Whole-mount immunofluorescence of the ileum myenteric plexus with native tdTomato fluorescence (red) from (**d**). Scale bar = 50mm. Image representative of n=2. (**f**) Whole-mount immunofluorescence of the ileum villi with native Tomato fluorescence (red) and staining using anti-TH(green) antibody, from (**d**). Image representative of n=2. (**g**) Whole-mount immunofluorescence of the CG-SMG staining using anti-cFos antibody after i.p. injection of tributryin. Scale bar = 50mm. Image representative of n=4. (**h**) Transcripts per million (TPM) as calculated by Kallisto alignment for *Ffar3* expressed by CG-SMG neurons isolated from SPF and GF *Snap25*^{RiboTag} mice (TRAPseq analyses). (**a**,**c**-**g**) Scale bars = 50μm; (**b**) (left) Scale bar = 300μm (left image), scale bar = 200μm (right image). (right) Scale bar = 500μm (left image), scale bar = 200μm (right image); (**h**) Data represented as mean ± s.d.

ii) Viscerofugal neurons are thought to be activated by tissue distension and could provide excitatory or inhibitory inputs to CG-SMG neurons (Hibberd et al., 2012; Szurszewski et al., 2002). To address whether viscerofugal neurons directly regulate microbiota–dependent CG-SMG activation, we injected fluorescent CTB into the CG-SMG and identified a sparse population of CTB^{+} intrinsic EANs (iEANs), likely viscerofugal (Messenger and Furness, 1992), in the intestine muscularis (Figure 3.15a). To confirm that iEANs can make synaptic contacts with sympathetic neurons, we injected iEAN-tropic AAV6-CAG-FLEX-tdTomato (Benskey et al., 2015) into the ileum of *Snap25*^{cre} mice (Figure 3.15b). We detected tdTomato+ fibres within the CG-SMG, suggesting that viscerofugal neurons were capable of direct communication with sympathetic neurons (Figure 3.15b). To assess a possible link between activation of iEANs and the CG-SMG, we quantified the activation state of iEANs and viscerofugal neurons upon antibiotic treatment using cFos expression (Fung et al., 2018; Sharkey et al., 1999; Yano et al., 2015). We injected fluorescent CTB into the CG-SMG of wild-type mice to retrograde label viscerofugal neurons. Oral gavage of streptomycin did not result in a change in the total number of neurons or viscerofugal neurons, or in an increase of cFos+ viscerofugal neurons in the distal intestine (Figure 3.15c-l). We concluded that viscerofugal iEANs are likely not playing a direct role in modulation of CG-SMG neurons; however, because changes in the microbial load can rapidly affect the activation state of iEANs, it remains possible that iEANs could influence sensory neuronal pathways (Perez-Burgos et al., 2014).

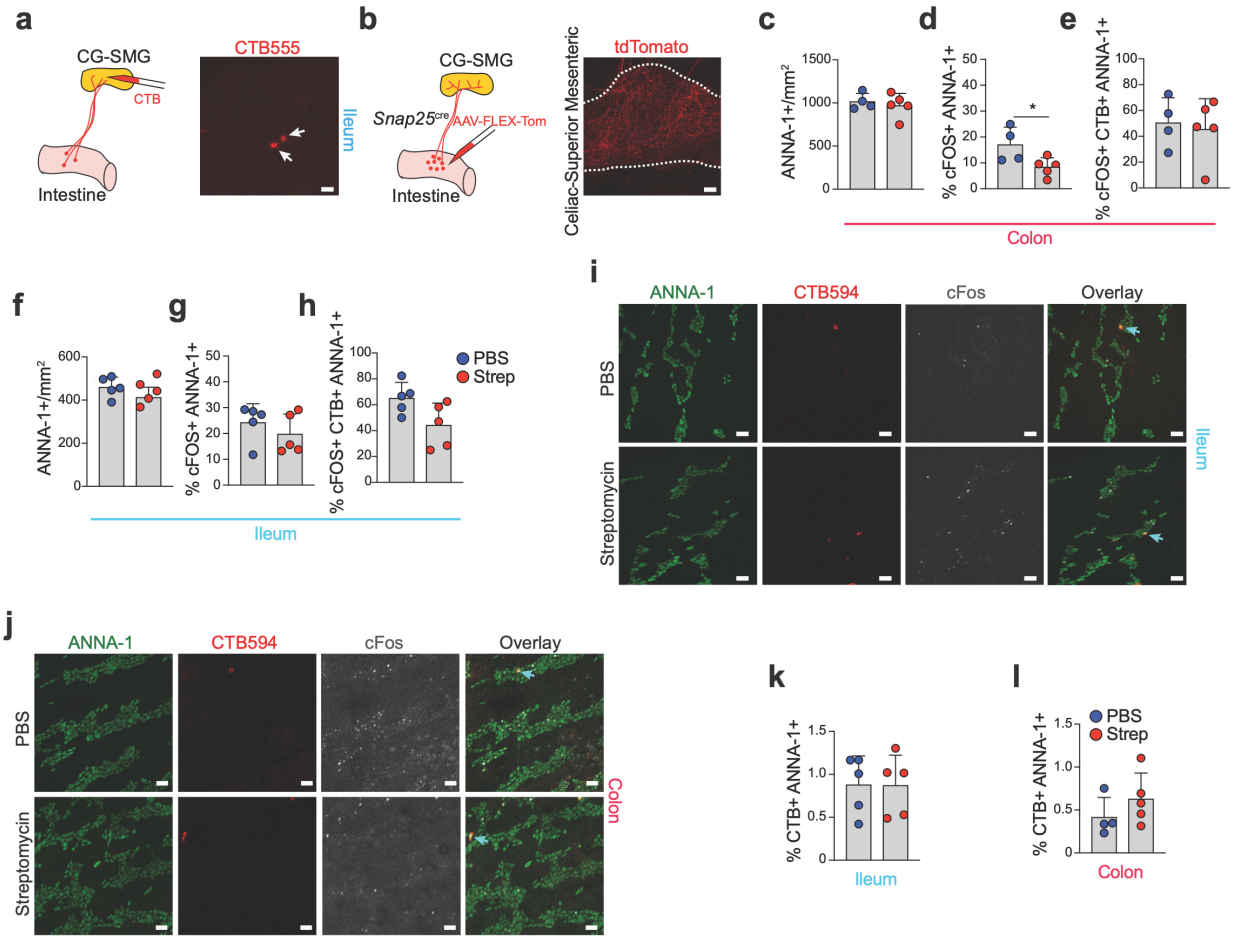

Figure 3.15. CG-SMG activation does not require viscerofugal input. (**a**) (left) Scheme representing injection of CT555 into the CG-SMG for visualization of viscerofugal neurons. (right) Whole-mount immunofluorescence of the ileum myenteric plexus with native CTB555 fluorescence. White arrows indicate CTB+ neurons. Image representative of n=3. (**b**) (left) Scheme representing injection of AAV6-CAG-FLEX-tdTomato into the intestine of *Snap25*^{Cre} mice for tracing of fibers. (right) Whole mount IF of CG-SMG showing tdTomato+ fibers originating, in part, from the intestine. CG-SMG is outlined with dashed lines. Image representative of n=2. (**c**) Total numbers of ANNA-1+ neurons in the colon in PBS (n=4) and streptomycin (n=5) treated C57BL6/J mice 24 hours post gavage. (**d**) Percent of ANNA-1+ neurons in the colon that are cFos+ in PBS (n=4) and streptomycin (n=5) treated C57BL6/J mice 24 hours post gavage. (**e**) Percent of CTB+ ANNA-1+ neurons in the colon cFos+ from retrograde injection into the CG-SMG in PBS- (n=4) and streptomycin- (n=5) treated C57BL6/J mice 24 hours post gavage. (**f**) Total numbers of ANNA-1+ neurons in the ileum in PBS- (n=5) and streptomycin- (n=5) treated C57BL/6J mice 24 hours post gavage. (**g**) Percent of ANNA-1+ neurons in the ileum cFos+ in PBS- (n=5) and streptomycin- (n=5) treated C57BL/6J mice 24 hours post gavage. (**h**) Percent of CTB+ ANNA-1+ neurons in the ileum cFos+ from retrograde injection into the CG-SMG in PBS- (n=5) and streptomycin- (n=5) treated C57BL/6jJ mice 24 hours post gavage. (**i** and **j**) Immunofluorescence staining of myenteric plexus neurons from the ileum (**i**) or colon (**j**) of C57BL6/J SPF mice treated with PBS or streptomycin using anti-neuronal nuclear (ANNA-1) (green) and anti-cFos (white) antibodies combined with CTB594 fluorescence. Images representative of at least n=5. Blue arrows indicate ANNA-1+ CTB+ cFos+ cells. (**k** and **l**) Percent of ANNA-1+ neurons in the ileum (**k**) or colon (**l**) CTB+ from retrograde injection into the CG-SMG in PBS- (n=5) and streptomycin- (n=5) treated C57BL6/J mice 24 hours post gavage. (**a**,**b**,**i**,**j**) Scale bars = 50μm; (**c**-**h**,**k**,**l**) Data represented as mean ± s.d. * $P < 0.05$ as calculated by unpaired t-test.

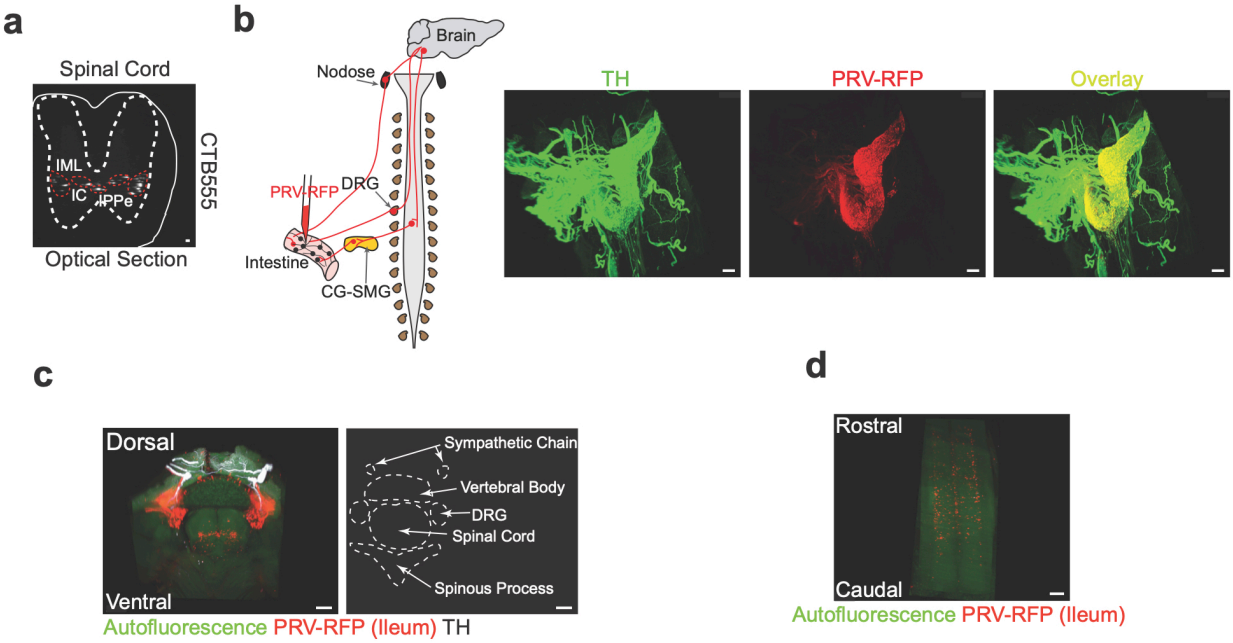

Figure 3.16. Gut injected PRV initially spreads to the CG-SMG and sympathetic preganglionic neurons. (**a**) Optical projection of 3DISCO-cleared spinal cord showing sympathetic preganglionic neurons labeled by retrograde transport of CTB555 injected into the CG-SMG of C57BL/6J SPF mice. Scale bar = 20μm. IML=intermediolateral cell column, IC: intercalated nucleus, IPPe: central autonomic area. Image representative of n= 3. (**b**) (left) Scheme representing injection of PRV into the intestine for multisynaptic tracing (for (B)-(L)). (right) 3D reconstruction of calAdipoClear-cleared CG-SMG with PRV-RFP (red) injected into the ileum 4 days post injection, stained with anti-TH (green) antibody. Scale bar = 300μm. Image representative of n= 3. (**c**) (left) 3D reconstruction of calAdipoClear-cleared intact spinal column with PRV-RFP (red) injected into the ileum 4 days post injection, stained with anti-TH (white) antibody. Autofluorescence in green. (right) outline of relevant spinal cord structures. Scale bars = 400μm. Image representative of n= 3. (**d**) 3D-cropped image of the spinal cord from (**c**), showing sympathetic preganglionic neurons labeled by PRV-RFP injected into the intestine. Scale bar = 300μm. Image representative of n= 3.

Our analyses did not support a role for either direct sensing of microbial depletion by CG-SMG sympathetic neurons, or for viscerofugal neurons modulating gut sympathetic activity. Thus, (iii) we investigated whether premotor neurons in the CNS could receive sensory input originating in the intestine to then modulate the sympathetic output. We focused on defining whether sympathetic premotor areas in the brainstem could modulate the CG-SMG through sympathetic preganglionic neurons in the spinal cord (SPN) (Deuchars and Lall, 2015). To define these premotor areas, we performed polysynaptic retrograde tracing by injecting mRFP1-expressing pseudorabies virus PRV-614 (Banfield et al., 2003) into the ileum or colon of SPF mice. We confirmed that viral spread moved back from the intestine to CG-SMG, then to SPN in the spinal cord (Figure 3.16a-d) (Ueno et al., 2016). Analysis of the brains at day 4 post-injection of PRV-RFP by AdipoClear tissue clearing (using a modification of ClearMap analysis (Renier et al., 2016)) identified the caudal raphe nuclei, involved in thermogenesis and various gastrointestinal functions (Browning and Travagli, 2014; Morrison and Nakamura, 2011); the gigantocellular reticular nucleus (Gi) and the lateral paragigantocellular nucleus (LPGi), both thought to be involved in locomotion and gastrointestinal function (Browning and Travagli, 2014; Capelli et al., 2017), and the rostroventrolateral medulla (RVLM), involved in autonomic regulation via C1 neurons (Abe et al., 2017) (Figure 3.17a-c). The specificity of this polysynaptic tracing was verified by comparison to intraperitoneal PRV injection or ileal PRV injection coupled with subdiaphragmatic vagotomy (sdVx), which eliminates brainstem areas labelled via vagal motor neurons (Figure 3.17d-f). Search of

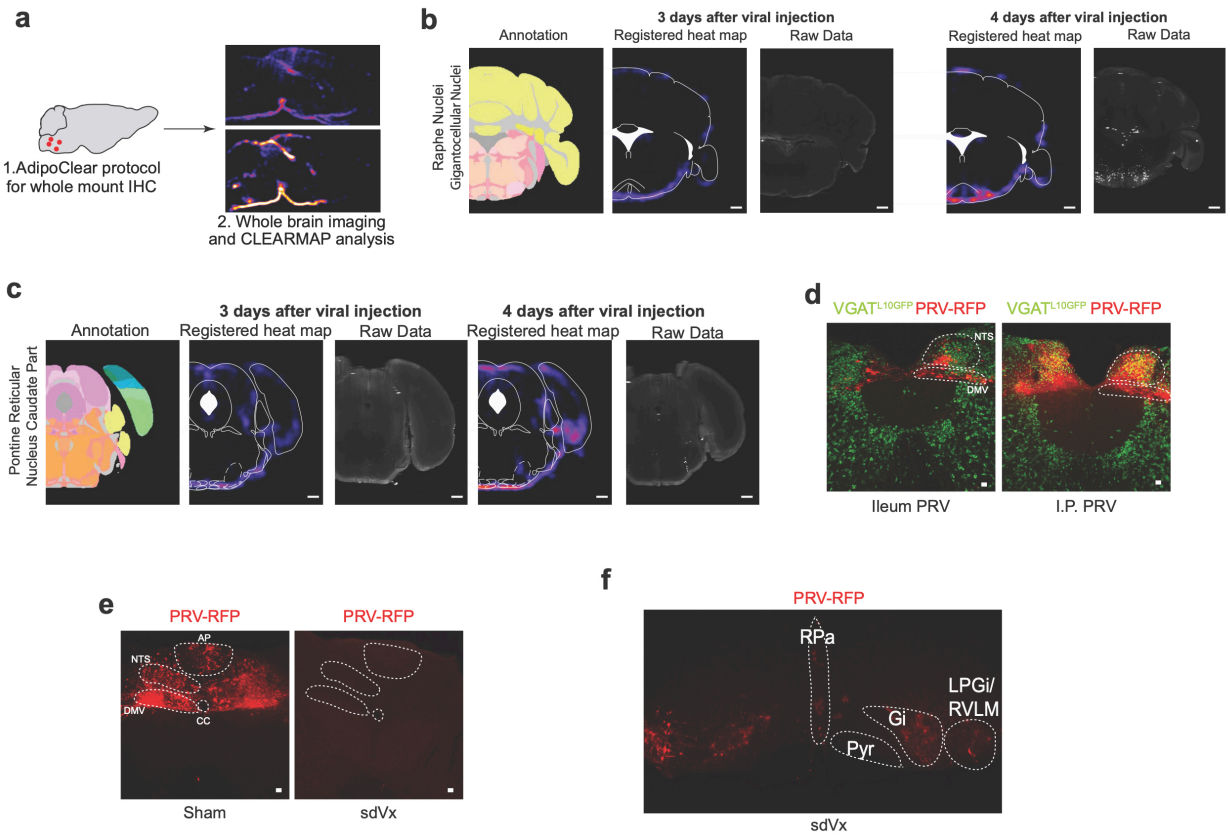

Figure 3.17. Mapping of gut sympathetic premotor neurons in the brainstem. (**a**) (right) Scheme representing tissue clearing followed by ClearMap analysis. (**b**) ClearMap analysis results of PRV-RFP injection into the ileum at days 3 and 4 post-injection showing raphe/gigantocellular nuclei. Scale bar = 1mm. Images representative of n= 3. (**c**) ClearMap analysis of PRV-RFP injection into the ileum of C57BL6/J mice at days 3 and 4 post-injection, showing the caudal pontine reticular nucleus (right). Scale bars = 1mm. Images representative of n= 3. (**d**) Immunofluorescence images of brainstem slices from VgatL10GFP mice injected with PRV-RFP in the ileum or peritoneum. Images from 4 days post injection. Dashed lines highlight relevant areas. Images representative of n=2. (**e**) Immunofluorescence images of the dorsal vagal complex in brainstem slices from C57BL6/J mice subjected to subdiaphragmatic vagotomy (sdVx) and injected with PRV-RFP in the ileum. Images from 4 days post injection. Dashed lines highlight relevant areas. Images representative of n=2. (**f**) Immunofluorescence images of medullary regions in a brainstem slice from C57BL6/J mice subjected to sudiaphragmatic vagotomy (sdVx) and injected with PRV-RFP in the ileum. Images from 4 days post injection. Dashed lines highlight relevant areas. Images representative of n=2. (**d-f**) Scale bars = 50μm.

the Allen Brain Atlas *in situ* hybridization database for potential neurotransmitter-defined populations in these sympathetic premotor areas pointed to inhibitory GABAergic neurons and excitatory glutamatergic neurons as possible populations involved in the modulation of downstream circuits polysynaptically connected to the intestine. Injection of PRV-RFP into the ileum of *Slc32a1*$^{L10\text{-}GFP}$ (VGAT: inhibitory) and *Slc17a6*$^{L10\text{-}GFP}$ (VGLUT2: excitatory) mice revealed extensive colocalization of RFP+/GFP+ neurons, with a majority of Gi neurons identified as VGAT+, and LPGi/RVLM neurons identified as VGLUT2+ respectively with a minor contribution from other neurotransmitters (Figure 3.18a-e). To address whether signals from different intestinal regions diverge from distinct or common neuronal populations in the brain, we injected PRV-RFP into the ileum and PRV-GFP into the colon or duodenum of wild-type SPF mice. A majority of neurons in each of these four brainstem areas were labelled with both fluorescent proteins (Figure 3.18f,g). These experiments define efferent premotor brainstem neurons polysynaptically connected to different regions of the intestine via preganglionic neurons in the spinal cord that, in turn, may control gut–sympathetic activity.

3.5 Glutamatergic brainstem neurons regulate gut sympathetic activity and motility

Gut sympathetic innervation is involved in the control of gut motility and secretion. Consistent with a possible role for the premotor brainstem nuclei identified above in the regulation of gut sympathetic activity, we observed elevated cFos in both RPa and LPGi/RVLM neurons in GF mice (Figure 3.19a), which are known to display gut

Figure 3.18. Characterization of sympathetic premotor populations that connect to the intestine. (**a**) Immunofluorescent images for neuronal subsets within the RPa and Gi in mice with PRV-RFP injected in the ileum. Native fluorescence for RFP (red) and stained with anti-5-HT (green), anti-VGLUT2 (green), and anti-TH (green) antibodies. Dashed lines highlight the RPa. White arrows indicate VGLUT2+ cells. Images representative of n=2-3. (**b**) Confocal image of native $VGAT^{L10GFP}$ and PRV-RFP fluorescence 4 days post-injection in a vibratome section of the brainstem. Relevant brainstem regions are highlighted. Arrows indicate GFP+ RFP+ cells and asterisks indicate RFP+ GFP- cells. Image representative of n = 5. (**c**) Confocal image of immunofluorescence staining with anti-GFP ($VGLUT2^{L10GFP}$) and anti-RFP (PRV-RFP) antibodies 4 days post-injection of PRV in a vibratome section of the brainstem. Relevant brainstem regions are highlighted. Arrows indicate GFP+ RFP+ cells and asterisks indicate RFP+ GFP- cells. Image representative of n= 5. (**d**) Percentage of PRV+ $VGAT^{L10GFP}$+ neurons in RPa, Gi, and LPGi/RVLM 4 days post injection. (n=5). (**e**) Percentage of PRV+ $VGLUT2^{L10GFP}$+ neurons in RPa, Gi, and LPGi/RVLM 4 days post injection. (n=5). (**f**) Immunofluorescent confocal image of PRV-GFP (duodenum) and PRV-RFP (ileum) fluorescence 4 days post-injection in a vibratome section of the brainstem. Arrows indicate GFP+ RFP+ cells and asterisks indicate RFP+ GFP- cells. Images representative of n=3. (**g**) Confocal image of native PRV-GFP (duodenum) and PRV-RFP (ileum) fluorescence 4 days post-injection in a vibratome section of the brainstem. Relevant brainstem regions are highlighted. Representative images of n=3. (**d**,**e**) Data represented as mean ± s.d., * $P < 0.05$, ** $P < 0.01$, *** $P < 0.001$, **** $P < 0.0001$ as calculated by by one way ANOVA with Tukey's multiple comparisons. (**a**-**c**,**f**,**g**) Scale bars = 50μm; AP = area postrema, NTS = nucleus tractus solitarius, DMV = dorsal motor nucleus of the vagus, pyr = pyramidal tract, RPa = raphe pallidus, Gi, gignantocellular nuclues, LPGi = lateral paragigantocellular nucleus, RVLM = rostral ventrolateral medulla.

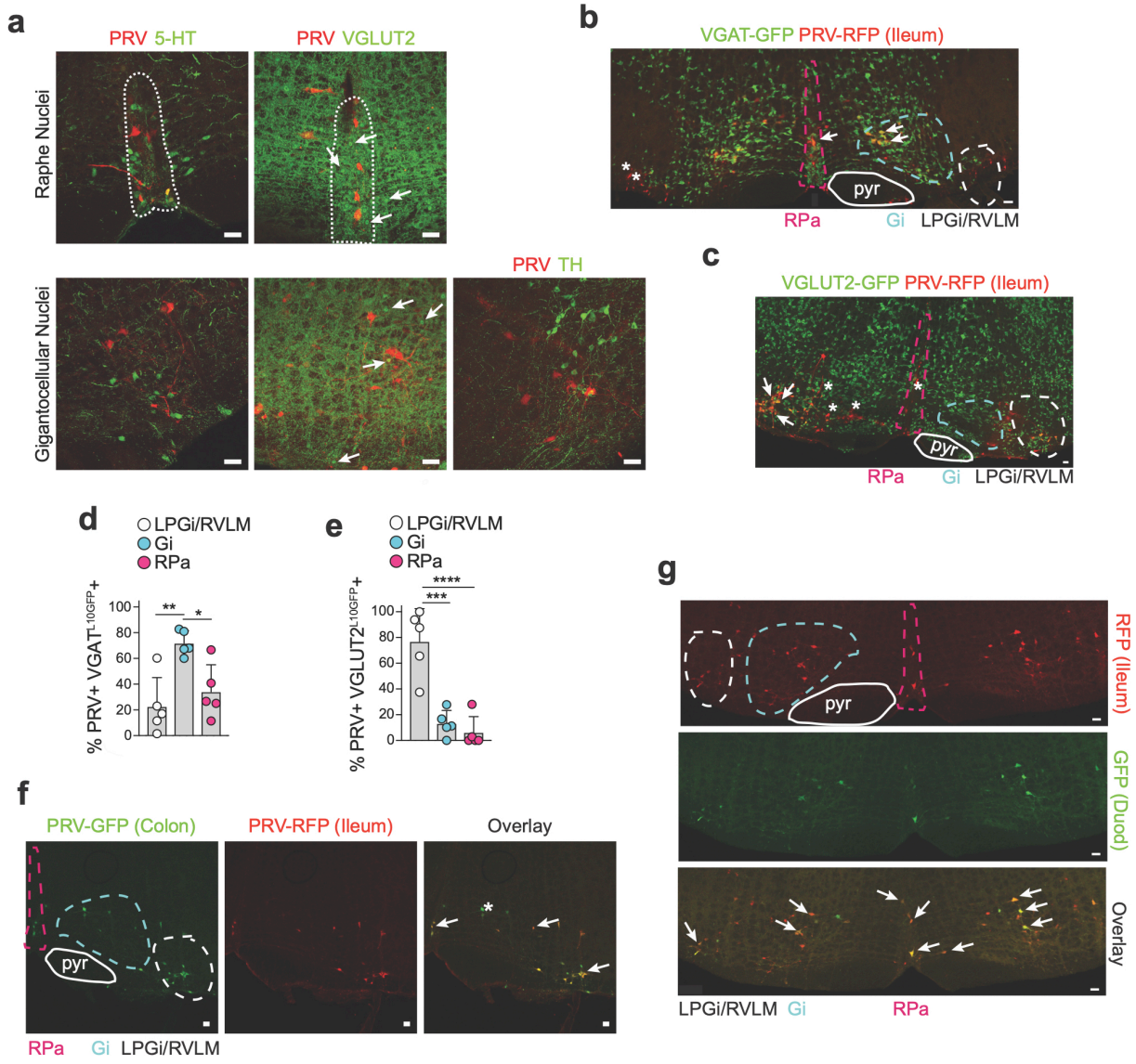
a
PRV 5-HT
PRV VGLUT2
Raphe Nuclei
PRV TH
Gigantocellular Nuclei
b
VGAT-GFP PRV-RFP (Ileum)
pyr
RPa
Gi
LPGi/RVLM
c
VGLUT2-GFP PRV-RFP (Ileum)
pyr
RPa
Gi
LPGi/RVLM
d
LPGi/RVLM
Gi
RPa
% PRV+ VGAT^10GFP+
100
80
60
40
20
0
**
*
e
LPGi/RVLM
Gi
RPa
% PRV+ VGLUT2^10GFP+
100
80
60
40
20
0
****
***
f
PRV-GFP (Colon)
PRV-RFP (Ileum)
Overlay
pyr
RPa
Gi
LPGi/RVLM
g
pyr
RFP (Ileum)
GFP (Duod)
Overlay
LPGi/RVLM
Gi
RPa

dysmotility (Barbara et al., 2005). To identify and permanently label recently-activated neurons following antibiotic treatment, we combined *Fos*$^{TRAP2:tdTomato}$ mouse plasticity mapping (Allen et al., 2017) and fluorescent PRV injection into the proximal colon, labelling gut–projecting neurons. Consistent with the increase in cFos, we observed an increase in the percentage of gut–connected (PRV+) TRAP+ cells in the LPGi/RVLM of these mice (Figure 3.19b). To directly determine whether these brainstem populations modulate gut–sympathetic activity, we bilaterally injected excitatory AAV5-DIO-hSyn-hM3Dq-mCherry into the Gi or the LPGi/RVLM of VGAT^{Cre} and VGLUT2^{Cre} mice, respectively (Figure 3.19c). Designer Receptors Exclusively Activated by Designer Drugs (DREADD) enable sustained chemogenetic modulation of neurons using the specific designer ligand compound 21 (C21) (Thompson et al., 2018). C21 administration to wild-type or (Gi)^{VGAT} mice did not affect baseline motility measurements, but it significantly slowed intestinal transit and fecal pellet output in (LPGi/RVLM)^{VGLUT2} mice (Figure 3.19d-m). As an additional control for the accurate targeting of these brain regions, C21 administration affected locomotion in both VGLUT2 and VGAT groups (Capelli et al., 2017) (Figure 3.19n,o). Finally, consistent with a role for the excitatory nuclei upstream of gut-sympathetic activation, chemogenetic activation of (LPGi/RVLM)^{VGLUT2} neurons, but not of (Gi)^{VGAT}, led to a significant increase in the number of cFos+ neurons in the CG-SMG (Figure 3.19p). These findings demonstrate that glutamatergic LPGi/RVLM brainstem neurons are capable of driving gut sympathetic activity, which in turn can slow gastrointestinal transit.

Figure 3.19. Sympathetic premotor neurons control gastro-intestinal motility. (**a**) Immunofluorescence images of brain slices from GF and SPF C57BL6/J mice stained with anti-cFos (black) and anti-tyrosine hydroxylase (red) antibodies. White-dashed lines outline RPa, Gi, LPGi, RVLM. Images representative of n=2. (**b**) (left) Percentage of TRAP+ cells among PRV GFP+ cells and (right) total number of TRAP+ cells in the LPGi/RVLM of *FosTRAP2*^{tdTomato} mice. Animals were treated with streptomycin (n=3) or PBS (n=3) and 4-OHT 24 hours later. (**c**) Immunofluorescence images of brain slices from VGAT:hM3Dq$^{Gi/RPa}$ and VGLUT2:hM3Dq$^{LPGi/RVLM}$ mice stained with anti-cFos (green) and anti-RFP (red) antibodies. White-dashed lines outline relevant areas. Arrows indicate mCherry+ cFos+ cells. Images representative of n=3. (**d** and **g**) Scheme representing the injection of AAV5-DIO-hSyn1-hM3Dq-mCherry into the LPGi/RVLM of VGLUT2^{Cre} mice (**d**) or into the Gi/RPa of VGAT^{Cre} mice (**g**). (**e**,**f**,**h**,**i**) Gastrointestinal transit time (**e** and **h**), colonic motility (**f** and **i**) of VGAT:hM3Dq$^{Gi/RPa}$ and VGLUT2:hM3Dq$^{LPGi/RVLM}$ mice and their relevant controls. (**j**) Gastrointestinal transit time of VGLUT2:hM3Dq$^{LPGi/RVLM}$ (n=14) or hM3Dq$^{LPGi/RVLM}$ (n=14) mice treated with saline. (**k**) Total fecal output of VGLUT2:hM3Dq$^{LPGi/RVLM}$ or (n=14) hM3Dq$^{LPGi/RVLM}$ (n=10) mice treated with 1mg/kg Compound 21. (**l**) (left) Colonic motility or (right) gastrointestinal transit time of C57BL6/J mice treated with 1 mg/kg Compound 21 (n=5) or saline (n=5). (**m** and **n**) Open-field test velocity of (left) VGLUT2:hM3Dq$^{LPGi/RVLM}$ (n=14) or hM3Dq$^{LPGi/RVLM}$ (n=8) mice and (right) VGAT:hM3Dq$^{Gi/RPa}$ (n=6) and hM3Dq$^{Gi/RPa}$ (n=6) treated with saline (**m**) or with 1 mg/kg Compound 21 (**n**). (**o**) Number of cFos+ neurons in the CG-SMG of VGAT:hM3Dq$^{Gi/RPa}$ or hM3Dq$^{Gi/RPa}$ mice 4 hours post treatment with 1mg/kg C21. (**p**) Number of cFos+ neurons in the CG-SMG of VGLUT2:hM3Dq$^{LPGi/RVLM}$ (n=14) or hM3Dq$^{LPGi/RVLM}$ (n=8) mice 4 hours post treatment with 1mg/kg C21. (**e**,**f**,**h**,**i**,**j**,**l**) Dashed-line indicates maximum time allowed per animal for motility measurement. Data represented as mean ± s.d., * $P < 0.05$, **** $P < 0.0001$ as calculated by unpaired t-test. (**b**,**m**,**n**-**p**) Data represented as mean ± s.d., * $P < 0.05$, ** $P < 0.01$ as calculated by unpaired t-test. (**a**,**c**) Scale bars = 50μm.

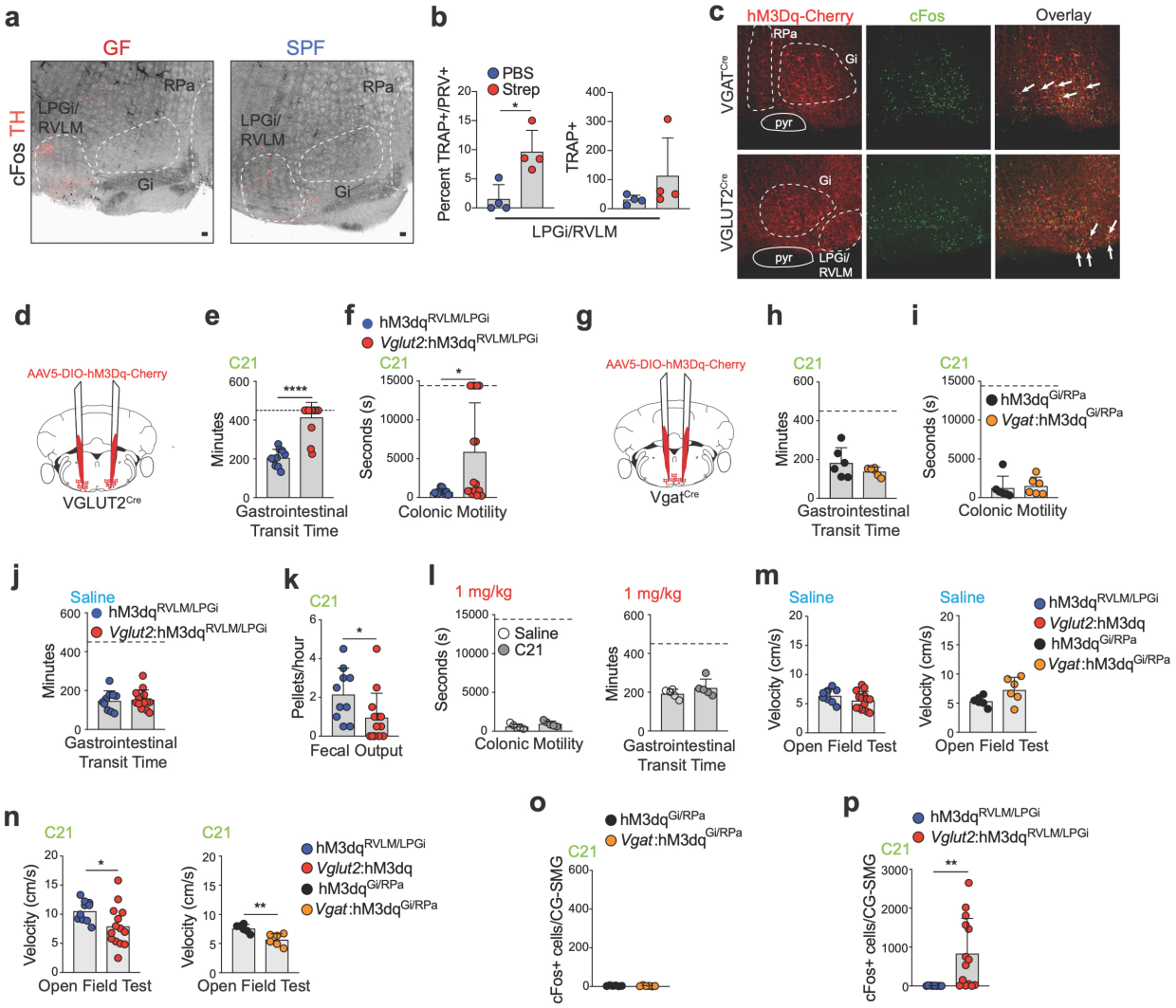
a
GF
SPF
cFos TH
RPa
LPGi/
RVLM
Gi
b
PBS
Strep
Percent TRAP+/PRV+
TRAP+
LPGi/RVLM
c
hM3Dq-Cherry
cFos
Overlay
VGAT^Cre
VGLUT2^Cre
pyr
d
AAV5-DIO-hM3Dq-Cherry
VGLUT2^Cre
e
C21
Minutes
Gastrointestinal
Transit Time
f
hM3dq^RVLM/LPGi
Vglut2:hM3dq^RVLM/LPGi
Seconds (s)
Colonic Motility
g
AAV5-DIO-hM3Dq-Cherry
Vgat^Cre
h
Gastrointestinal
Transit Time
i
hM3dq^Gi/RPa
Vgat:hM3dq^Gi/RPa
Colonic Motility
j
Saline
hM3dq^RVLM/LPGi
Vglut2:hM3dq^RVLM/LPGi
Gastrointestinal
Transit Time
k
Pellets/hour
Fecal Output
l
1 mg/kg
Saline
C21
Colonic Motility
Gastrointestinal
Transit Time
m
Velocity (cm/s)
Open Field Test
hM3dq^RVLM/LPGi
Vglut2:hM3dq
hM3dq^Gi/RPa
Vgat:hM3dq^Gi/RPa
n
o
cFos+ cells/CG-SMG
p

3.6 The afferent arm of microbe-modulated gut sympathetic neuronal circuit

We investigated further the ClearMap PRV-RFP analysis described above to identify additional brain areas synaptically connected to the gut, and possibly to the LPGi/RVLM. Examination of data four days post PRV infection revealed additional brainstem regions previously shown to connect to the stomach (Ye et al., 2014) and rectum (Li et al., 2018). Specifically, we observed significant PRV labelling in the dorso-vagal complex (Rinaman et al., 1999; Ye et al., 2014) including the dorsal motor nucleus of the vagus (DMV), nucleus tractus solitarius (NTS) and area postrema (AP) (Figure 3.20a-d). Previous studies demonstrated that the NTS and AP can directly integrate gut sensory information from vagal sensory neurons or circulating factors (Han et al., 2018; Williams et al., 2016) and that these nuclei connect to the LPGi/RVLM (Dampney, 1994; Young, 2012). To determine whether changes in microbial load could affect neuronal activity in the NTS and AP, we measured cFos in these areas after antibiotic treatment. Following streptomycin treatment, we observed a significant increase in cFos expression in both the NTS and AP (Figure 3.20e,f). These areas also displayed high levels of cFos in GF mice and *Fos*$^{TRAP2:tdTomato}$ treated with streptomycin, further suggesting a functional relevance of these areas (Figure 3.20g-i). To assess whether these sensory brainstem nuclei are involved in the detection of SCFAs, we analyzed their cFos levels post administration of tributyrin to streptomycin-treated mice. While cFos levels in the AP were suppressed, levels in the NTS remained elevated (Figure 3.20j,k), suggesting the AP as a distal sensory hub for intestinal SCFAs, although additional SCFA and unknown visceral signals might be sensed in the NTS during dysbiosis or microbial depletion. These results characterize a set of brainstem sensory nuclei tuned to detect changes in the gut microbiota or metabolites thereof.

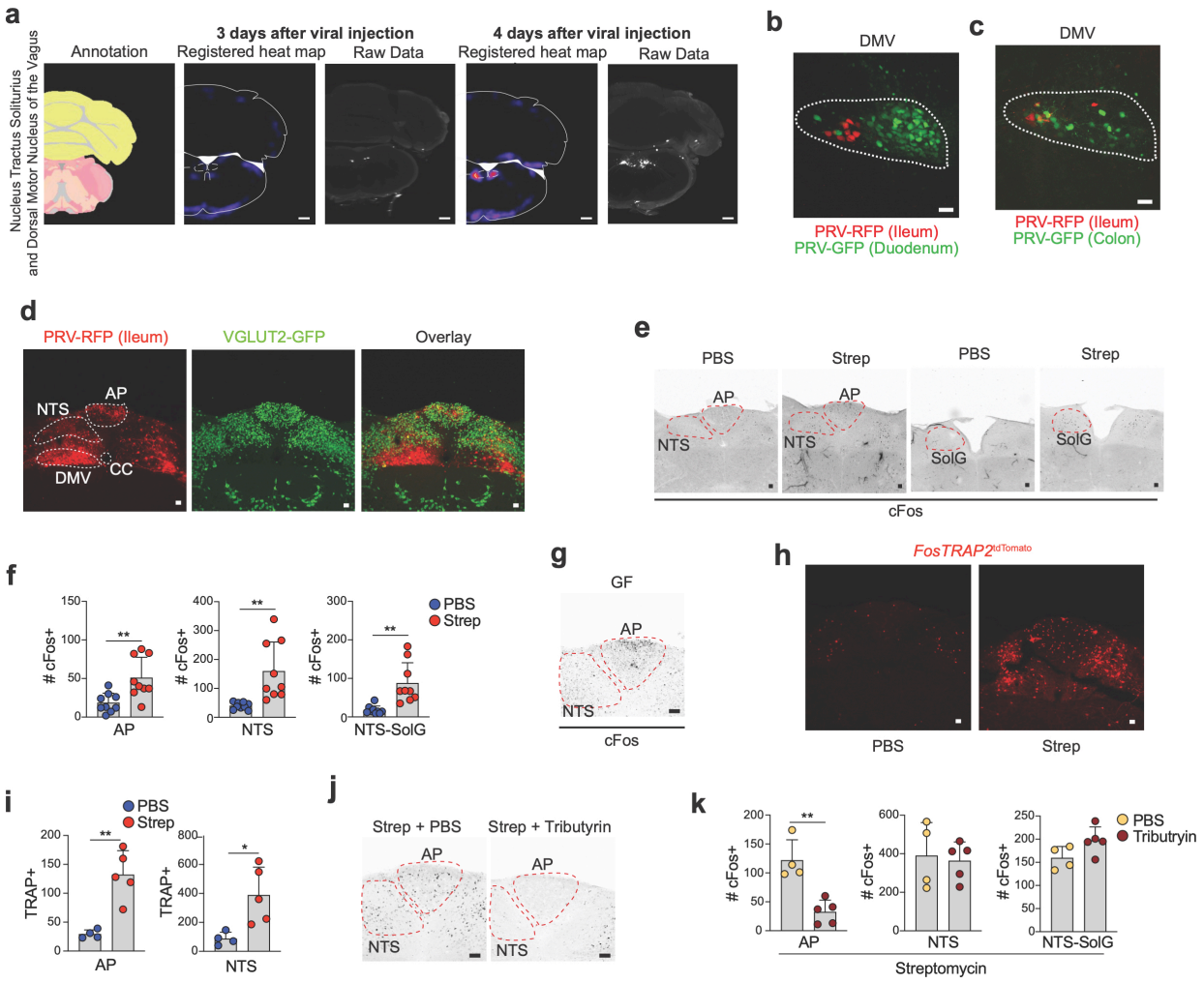

Figure 3.20. Brainstem sensory areas are modulated by the microbiota and SCFA. (**a**) ClearMap analysis of PRV-RFP injection into the ileum of C57BL6/J mice at days 3 and 4 post-injection, showing nucleus tractus solitarius (NTS)/dorsal motor nucleus of the vagus nerve (DMV)(left) and the caudal pontine reticular nucleus (right). Scale bars = 1mm. Images representative of n= 3. (**b** and **c**) Confocal image of the caudal brainstem. Dual PRV injection into the ileum (PRV-RFP) and duodenum (PRV-GFP) (**b**) or ileum (PRV-RFP) and colon (PRV-GFP) (**c**) at 4 days. Dashed line outlines the borders of the DMV. Scale bar = 50mm. Image representative of n=3. (**d**) Confocal image of immunofluorescence staining with anti-GFP (VGLUT2L10GFP) and anti-RFP (PRV-RFP) antibodies 4 days post-injection of PRV in a vibratome section depecting the brainstem sensory nuclei. (**e**) Immunofluorescence images of brains slices (left panels NTS and AP; right panels, SolG) of C57BL6/J mice treated with PBS or streptomycin. Images representative of n=10. (**f**) Number of cFos+ neurons in the AP, NTS-gelatinous (SolG), and NTS inclusive of SolG, 24 hours post oral gavage with PBS or streptomycin. (**g**) (NTS and AP magnified) from GF mice stained for cFos (black). Images representative of at least n=3. (**h**) Immunofluorescence images of brains slices showing TRAP+ cells in the AP and NTS of FosTRAP2:tdTomato mice treated with PBS (left) or streptomycin (right) given 4-OHT 24 hours later. Images representative of n=4. (**i**) Number of TRAP+ cells in the AP and NTS of FosTRAP2:tdTomato mice treated with streptomycin (n=4) or PBS (n=4) given 4-OHT 24 hours later. (**j**) (NTS and AP magnified) from C57BL6/J mice treated with streptomycin and concomitant PBS (left) or tributyring (right) stained for cFos (black). Images representative of at least n=3. (B) Number of cFos+ neurons in the AP, NTS, and SolG 24 hours post oral gavage streptomycin followed by treatment with PBS or Tributyrin. (**f**,**i**,**k**) Data represented as mean ± s.d., * $P < 0.05$, ** $P < 0.01$ as calculated by unpaired t-test. (**b**-**e**,**h**) Scale bars = 50μm.

The increased cFos expression in the NTS/AP upon microbial depletion suggests a functional role for afferent sensory neurons in the regulation of gut sympathetic activity. Extrinsic neuronal sensing at the intestinal epithelium, mucosa, and *muscularis* is primarily carried out by sensory afferents in the NG and DRG (Brookes et al., 2013), both also identified by our retrograde strategies described above. To target NG or DRG sensory activity we first crossed SNS^{Cre}, a BAC-transgenic mouse expressing Cre under the *Scn10a* (*Nav1.8*) promoter (Agarwal et al., 2004; Chiu et al., 2014), with inhibitory hM4Di ($Rosa26^{lsl\text{-}hM4Di}$) mice (Zhu et al., 2016). Therefore, if afferent eEAN were involved in this circuit, administration of C21 to SNS^{hM4Di} mice should result in the inhibition of afferent eEAN (Huang and Thathiah, 2015; Zhu et al., 2016), functionally phenocopying the loss of microbial signals and thus resulting in activation of gut sympathetic neuron activation. We confirmed that SNS^{Cre} recombination targets most DRG and NG neurons, in addition to robust labelling of nerve fibers spanning the width of the intestinal wall (Figure 3.21a,b and Table 3.1). Indeed, SNS^{hM4Di} mice displayed a significant activation of CG-SMG neurons upon administration of C21 (Figure 3.21c). To determine whether NG alone or combined NG/DRG inhibition was responsible for this phenotype, we crossed $Rosa26^{lsl\text{-}hM4Di}$ with $Phox2b^{Cre}$ mice (Scott et al., 2011), a Cre line that specifically targets the NG, and a small population of iEAN, while avoiding recombination of DRG neurons (Figure 3.21a,b and Table 3.1). Injection of C21 into $Phox2b^{hM4Di}$ mice also led to a marked increase in the number of cFos+ cells in the CG-SMG (Figure 3.21d).

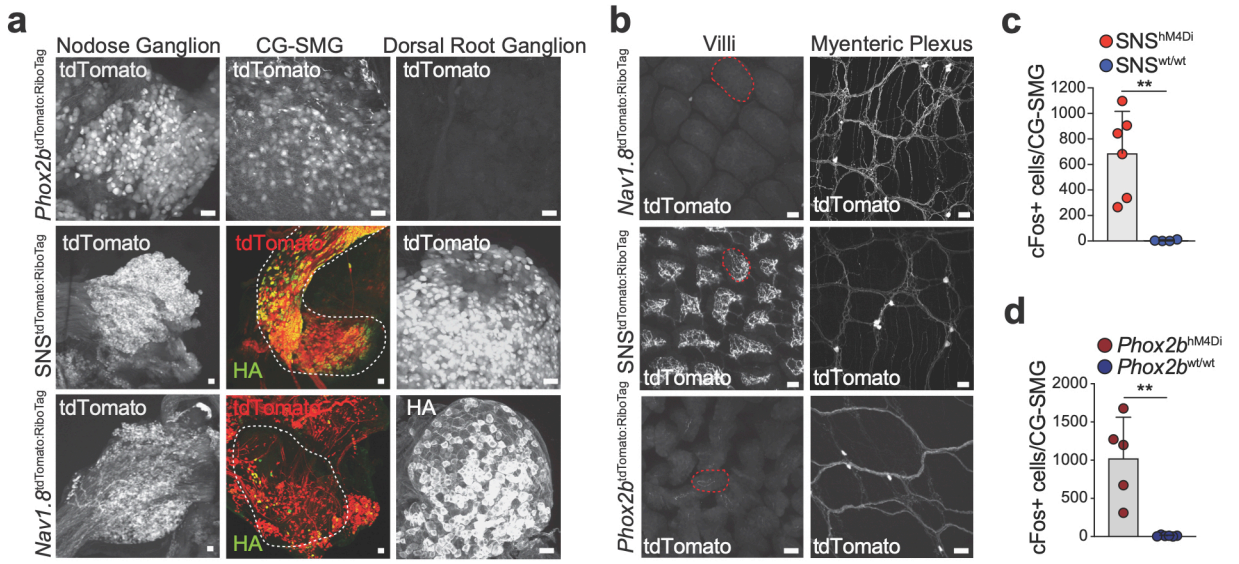

Figure 3.21. Chemogenetic modulation of peripheral neurons innervating the gut can activate gut-sympathetic neurons. (**a** and **b**) Immunofluorescence images of whole-mount NG, CG-SMG, and DRG (**a**) or myenteric plexus and villi in the ileum (**b**) from *Phox2b*$^{tdTomato:RiboTag}$, SNS$^{tdTomato:RiboTag}$, and *Nav1.8*$^{tdTomato:RiboTag}$ mice. Images representative of n=2-3. In (**b**), red-dashed lines highlight villi structure. (**c**) Number of cFos+ neurons in the CG-SMG of SNS^{hM4Di} (n=6) or control mice (n=4) 6 hours post Compound 21 (10mg/kg) injection. Data shown as mean +/- s.d. ** $P < 0.01$ as calculated by unpaired t-test. (**d**) Number of cFos+ neurons in the CG-SMG 4 hours post injection with 10mg/kg Compound 21 in *Phox2b*^{hM4Di} (n=5) and *Phox2b*$^{wt/wt}$ (n=6) mice. (**c**,**d**) Data represented as mean ± s.d. ** $P < 0.01$ as calculated by unpaired t-test; (**a**,**b**) Scale bars = 50μm.

We found that both SNS^{Cre} and *Phox2b*^{Cre} also targeted a subset of sympathetic neurons in the CG-SMG, raising the possibility that the effects observed in both mice could be due to direct effects in these ganglia (Figure 3.21a,b and Table 3.1). This is an unlikely possibility, since sympathetic neurons in the CG-SMG do not noticeably express

either *Girk2*, a key component of hM4Di-driven inhibition (Roth, 2016), or *Chrm4*, the endogenous cholinergic muscarinic receptor (*data not shown*). Nevertheless, to address this issue, we asked whether expression of excitatory hM3Dq or inhibitory hM4Di specifically in CG-SMG neurons could result in cFos expression following C21 administration. We injected AAV2-hSyn-hM4Di or hM3Dq into the CG-SMG of wild-type mice and administered either 1mg/kg or 10mg/kg of C21. We observed an increase in cFos expression by hM3Dq+ sympathetic neurons, but we failed to detect cFos+ hM4Di+ with either dose of C21 (Figure 3.22a-d). Extensive analyses of additional *Cre* lines

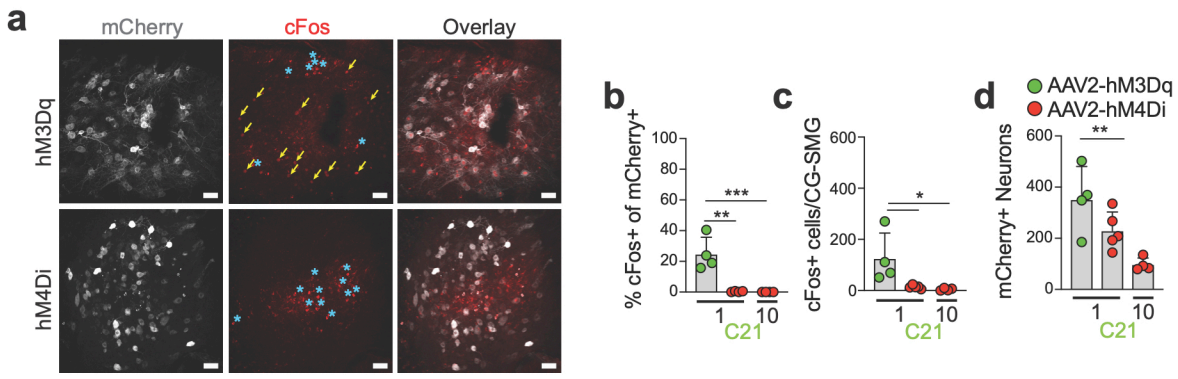

Figure 3.22. Chemogenetic inhibition of CG-SMG neurons does not result in increased cFos. (**a**) Immunofluorescence images of whole-mount of CG-SMG from C57BL6/J mice injected with AAV2-hSyn-hM3Dq-mCherry or AAV2-hSyn-hM3Dq-mCherry virus, after administration of 1mg/kg Compound 21. Arrows indicate cFos+ mCherry+ cells. Asterisks indicate other cFos+ cells (possibly hematopoietic cells). Scale bars = 50μm. (**b**) Percent of cFos+ neurons among mCherry+ in the CG-SMG of C57BL/6J mice injected with AAV2-hSyn-hM3Dq-mCherry (n=4) or AAV2-hSyn-hM4Di-mCherry (n=5 or n=4) virus after administration of 1mg/kg or 10mg/kg Compound 21. (**c**) Number of cFos+ neurons in the CG-SMG of C57BL6/J mice injected with AAV2-hSyn-hM3Dq-mCherry (n=4) or AAV2-hSyn-hM4Di-mCherry (n=5 or n=4) virus after administration of 1mg/kg or 10mg/kg Compound 21. (**d**) Number of mCherry+ neurons in the CG-SMG of C57BL6/J mice injected with AAV2-hSyn-hM3Dq-mCherry (n=4) or AAV2-hSyn-hM4di-mCherry (n=5 or n=4) virus. (**b-d**) Data represented as mean ± s.d. * $P < 0.05$, ** $P < 0.01$, *** $P < 0.001$ as calculated by one way ANOVA with Tukey's multiple comparisons.

revealed different patterns of NG targeting and CG-SMG activation with hM4Di, particularly with *Nav1.8*^{Cre} (Nassar et al., 2004; Stirling et al., 2005), which targets Scn10a, and with the pan-sensory *Advillin*^{CreERT2} (Lau et al., 2011) (Table 3.1). These chemogenetic experiments indicate that modulation of vagal afferents is sufficient to drive gut sympathetic activity.

Table 3.1. Description of Cre mouse lines used. +++++ = pan-neuronal or very high CG-SMG cFos, +++ = broad populations or significant CG-SMG cFos, + = small population or very little CG-SMG cFos, - = sparse population, X = not present, nc = not checked.

Driver Line	NG	CG	DRG	Intestine (MP)	Intestine (SMP)	Brain	CG-SMG Activation
Snap25	+++++	+++++	+++	+++++	+++++	+++++	nc
Nav1.8	+++	x	+++	+	x	nc	x
SNS	+++++	+++	+++++	+	+	x	+++++
Avil	+++++	+++++	+++++	+++	+++	nc	+
Npy	+	+++++	+	+++	+++	+	nc
Phox2b	+++++	+++	x	+	x	+	+++++
Th	+	-	+	x	x	+	x
Glp1r	+++	+++++	-	+	+	+	+++
Vglut2	+++++	x	nc	+	+	+++	nc
Vgat	x	x	x	x	x	+++	nc
Htr3a	+++++	+++++	+++++	+	+	+++	+++++

3.7 Nodose ganglia afferent neurons project fibers to sites of high microbial load

To narrow down the potential population of NG neurons targeted by these approaches, and their role in this gut-brain-gut loop, we first isolated the NG from

SNS^{RiboTag} mice, the *Cre* line in which DREADD modulation resulted in CG-SMG activation, or from *Avil*^{RiboTag} and *Nav1.8*^{RiboTag} mice, i.e. *Cre* lines that labelled subsets of NG neurons but were not affected by DREADD modulation (Figure 3.23a,b). We also observed that SNS^{Cre} targeted the majority retrograde traced neurons from the distal

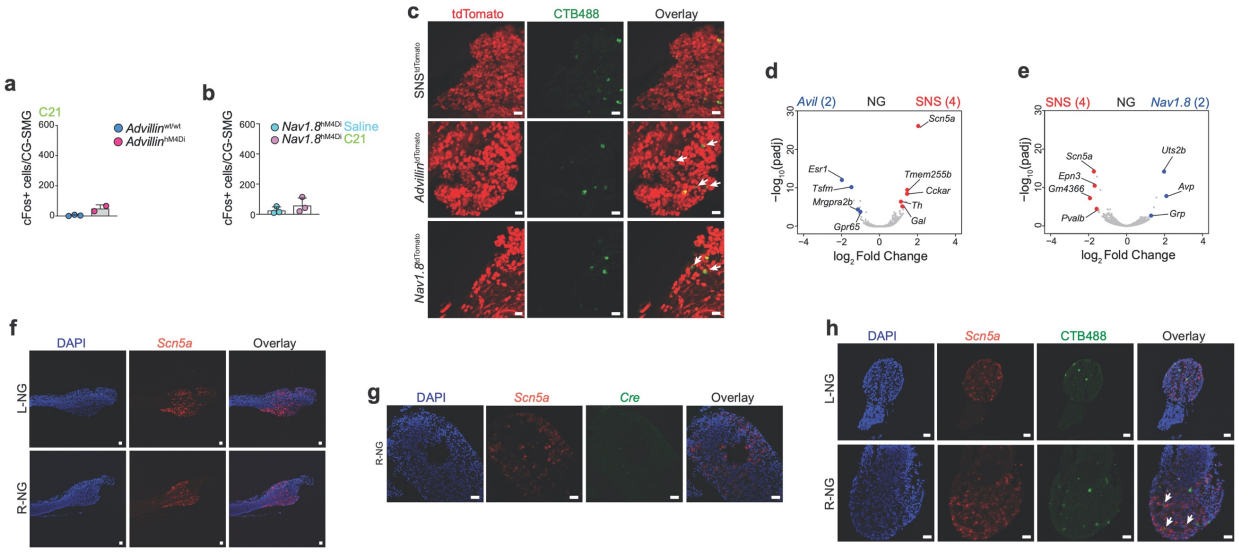

Figure 3.23. Distal gut-projecting NG neurons are Nav1.5+. (**a** and **b**) Number of cFos+ neurons in the CG-SMG of *Avil*$^{wt/wt}$ (n=3) or *Avil*^{hM4Di} (n=2) (**a**) or *Nav1.8*^{hM4Di} (n=3 per group) (**b**) mice 6 hours after treatment with 10mg/kg Compound 21 or saline. Data represented as mean ± s.d. (**c**) Immunofluorescence whole-mount images of CG-SMG from *Nav1.8*^{tdTomato}, *Avil*^{tdTomato}, and SNS^{tdTomato} mice injected with CTB488 in the proximal colon. Arrows indicate neurons that are CTB+ and tdTomato-. (**d**) Volcano plot of differentially expressed genes from the nodose ganglion of SNS^{RiboTag} and *Avil*^{RiboTag} mice. Blue dots indicate genes significantly enriched in the NG of *Avil*^{RiboTag} mice. Red dots indicate genes significantly enriched in the NG of SNS^{RiboTag} mice. Number of samples analyzed are indicated in parentheses at top. (**e**) Volcano plot of differentially expressed genes from the NG of SNS^{RiboTag} and *Nav1.8*^{RiboTag} mice. Blue dots indicate genes significantly enriched in the NG of *Nav1.8*^{RiboTag} mice. Red dots indicate genes significantly enriched in the NG of SNS^{RiboTag} mice. Number of samples analyzed are indicated in parentheses at top. (**f**) RNAscope *in situ* hybridization images of left (L-NG) and right nodose ganglion (R-NG) for *Scn5a* (*Nav1.5*) (red). Images representative of n=4. (**g**) RNAscope *in situ* hybridization images of the R-NG for *Scn5a* (Nav1.5) (red) and *Cre* from mice injected with AAVrg-pmSyn-Cre-EBFP into the proximal colon. Images representative of n=2. (**h**) RNAscope *in situ* hybridization images of the L-NG (top) and R-NG (bottom) for *Scn5a* (*Nav1.5*) (red) and immunofluorescence for CTB488 from mice with CTB488 injected into the proximal colon. Images representative of n=2. (**c**,**f-h**) Scale bars = 50μm.

intestine, when compared with less efficient targeting in *Avil*^{Cre} and *Nav1.8*^{Cre} mice (Figure 3.23c). We hypothesized that SNS^{Cre} targets a unique population of distal gut-projecting NG neurons. To compare targeting coverage we performed TRAP-seq analysis of the NG from these three *Cre* lines, which revealed a significant enrichment in the gene *Scn5a* (*Nav1.5*) in the NG of SNS^{RiboTag} mice when compared to either *Avil*^{RiboTag} or *Nav1.8*^{RiboTag} mice (Figure 3.23d,e). Moreover, *in situ* hybridization coupled with intestinal retrograde tracing confirmed that a proportion of gut-projecting NG are indeed Nav1.5+ (Figure 3.23f-h). To address whether vagal modulation can activate the sensory brainstem nuclei that we found to be modulated by microbiota manipulation, we examined the NTS and AP of SNS^{hM4Di} and *Phox2b*^{hM4Di} mice treated with C21, and observed significant increase in cFos (Figure 3.24a,b). We chose this indirect measure

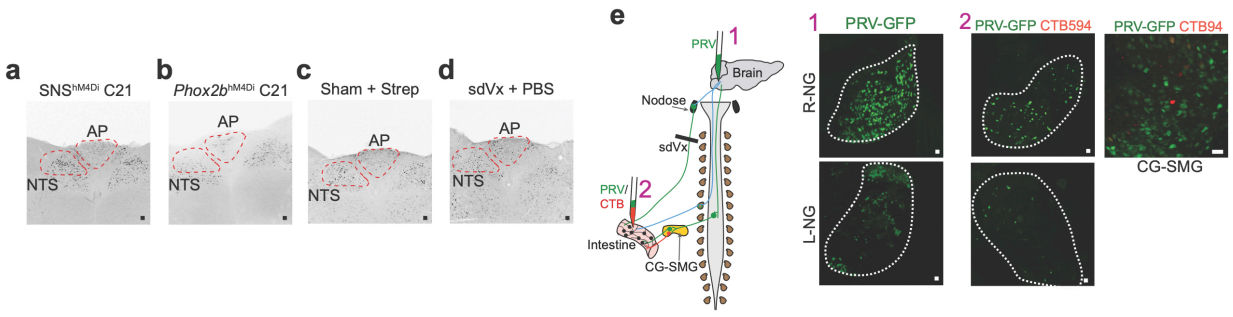

Figure 3.24. Distal-gut connected NG neurons modulate brainstem activity and are synaptically connected to gut sympathetic neurons. (**a** and **b**) Immunofluorescence images of brains slices highlighting the NTS/AP from (**a**) SPF SNS^{hM4Di} mice or (**b**) SPF *Phox2b*^{hM4Di} mice treated with C21 at 10 mg/kg. All stained for cFos (black). Images representative of at least n=3. (**c** and **d**) Immunofluorescence images of brains slices highlighting the NTS/AP from (**c**) sham operated C57Bl6/J mice given streptomycin or (**d**) sdVx C57Bl6/J mice given with PBS. All stained for cFos (black). Images representative of at least n=5. (**e**) Immunofluorescence whole-mount image of the NG and CG-SMG (right:2) after brainstem injection (left:1) or proximal colon with sdVx injection (right:2) of PRV-GFP. Images representative of n=3 (left:1) and n=2 (right:2). Outline highlights NG. (**a**-**e**) Scale bars = 50μm.

of vagal activity as reported markers of intrinsic NG activation in mice, such as phosphorylated ERK (Ayush et al., 2015; Campos et al., 2013), are not well characterized and vagal nerve recordings lack the resolution required to detect physiologic changes in afferent activity. We were not able to determine whether this increase in cFos is the result of hM4Di activation or simply disinhibition of NTS/AP neurons. Additionally, we were unable to surgically assess the requirement of vagal sensory input to these areas, as sdVx alone led to a significant increase in NTS/AP cFos (Figure 3.24c,d). However, bilateral injection of fluorescent PRV into the LPGi/RVLM confirmed that both connect to the NG (Figure 3.24e). Alternatively, injection of fluorescent PRV into the wall of the colon of sdVx mice resulted in significant labelling of the left and right NG after 5 days, with a bias towards right NG labelling, mirroring the trend observed with CTB tracing from the distal intestine. These results confirm the identification of a gut-vagal afferent sensing circuit that can potentially drive sympathetic activity and is distinct from the vagal parasympathetic circuitry (Figure 3.24e). Visualization of vagal afferents projections using Cre–dependent (SNS^{Cre} and $VGlut2^{Cre}$) and -independent (direct injection) AAV anterograde tracing methods, revealed dense labelling of neuronal processes particularly in the distal intestine(Berthoud, 1990; Wang and Powley, 2007, 2000), suggesting that NG sensory afferent neurons project fibers to sites of high microbial load or SCFA concentration

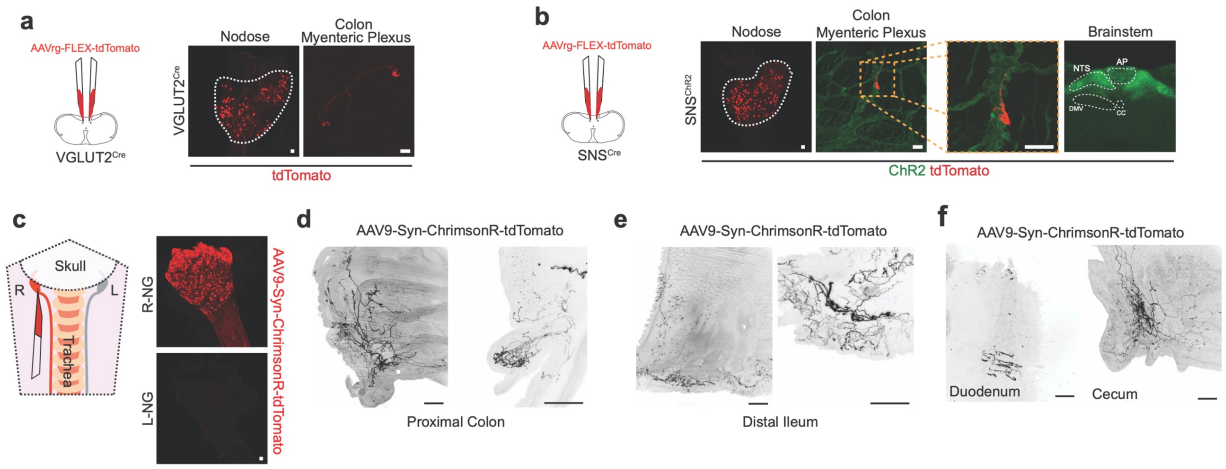

Figure 3.25. NG project to all layers of the distal intestine. (**a** and **b**) (left) Illustration of injection of AAVrg-FLEX-tdTomato into the NTS of (**a**) VGLUT2^{Cre} or (**b**) SNS^{ChR2} mice. (Right) Immunofluorescence whole-mount images of the NG and colonic myenteric plexus after AAVrg-FLEX-tdTomato injection into the NTS of (**a**) VGLUT2^{Cre} or (**b**) SNS^{ChR2} mice. Outline highlights NG. (**b**) Inset shows tdTomato+ fiber surrounding an intrinsic neuron. Brainstem slice shows absence of Cre activity in the dorsal motor nucleus of the vagus. Outline highlights relevant areas. (**c**) (left) Scheme of right NG injection. (right) Expression of AAV9-Syn-ChrimsonR-tdTomato in NG. (**d-f**) Whole-mount cleared-tissue immunofluorescence of the proximal colon (**d**), distal ileum (**e**), or duodenum/cecum (**f**) of mice injected with AAV9-Syn-ChrimsonR-tdTomato in the R-NG (left 1x and right 4x zoom: **d** and **e**). Scale bars = 500μm (left) and 250μm (right). Images representative of n=3. (**a-c**) Scale bars = 50μm. NG = nodose ganglion, RPa = raphe pallidus, Gi = gigantocellular nucleus, LPGi = lateral paragigantocellular nucleus, RVLM = rostral ventrolateral medulla, AP = area postrema, NTS = nucleus tractus solitarius.

(Figure 3.25a-f). Finally, calcium imaging of dissociated NG neurons from *Snap25*^{GCaMP6s} mice revealed reliable suppression of calcium signal upon addition of sodium butyrate, demonstrating that NG may have the capacity to respond to SCFA directly (Figure 3.26a-c). Overall, our results identify a gut-brain-gut circuit whereby distinct microbes and microbial metabolites modulate activation of gut sympathetic neurons and brainstem sensory nuclei capable of integrating gut-specific stimuli.

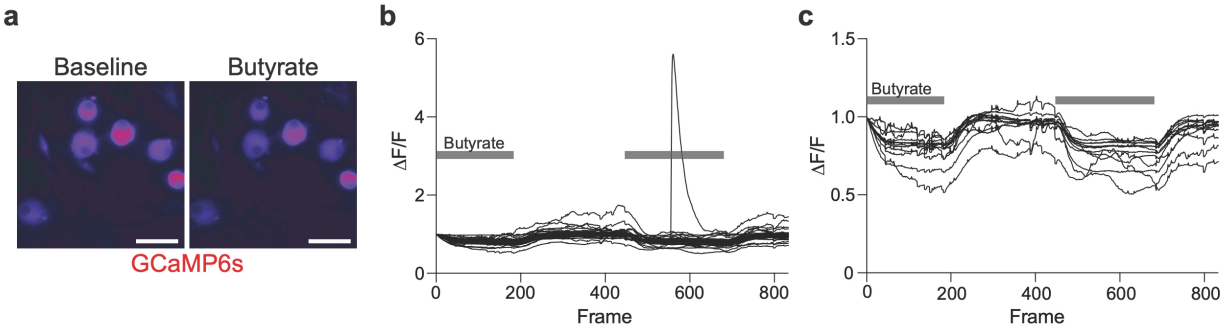

Figure 3.26. Calcium imaging of dissociated nodose neurons treated with sodium butyrate. (**a**) Representative magnified images of Snap25GCaMP6s nodose neurons at baseline and post-addition of 10mM sodium butyrate. Scale bars = 50μm.Images representative of n=4 separate replicates. (**b**) Representative GCaMP6s fluorescence traces from the entire field of view in a (calculated as change in fluorescence divided by the average baseline fluorescence) over time with the addition of 10mM sodium butyrate (osmolarity matched/not osmolarity matched are combined in the same grey bar). Representative of n=4 separate replicates. (**c**) Selected representative GCaMP6s fluorescence traces from (**b**) to demonstrate GCaMP6s decrease over time with the addition of 10mM sodium butyrate (osmolarity matched/not osmolarity matched are combined in the same grey bar). Representative of n=4 separate replicates.

3.8 Conclusions

We studied the influence of the microbiota on EAN by combining gnotobiotic mouse models with transcriptomics, circuit–tracing methods, and functional manipulation. Actively–translating ribosomal profiling comparing specific-pathogen free (SPF) and germ-free (GF) indicated that the gut microbiome played an overall suppressive role in the activity of gut–extrinsic sympathetic ganglia, the celiac–superior mesenteric ganglion (CG-SMG). While microbiota depletion led to increased cFos expression in the CG-SMG, colonization of germ-free mice with short-chain fatty acid–producing bacteria suppressed cFos expression in the gut sympathetic ganglia. Chemogenetic manipulations, translational profiling, and anterograde tracing identified a subset of distal intestine-projecting vagal neurons positioned to play an afferent role in microbiota–mediated

modulation of gut sympathetic neurons. Retrograde polysynaptic neuronal tracing from the intestinal wall identified brainstem sensory nuclei activated during microbial depletion, as well as efferent sympathetic premotor glutamatergic neurons that regulate gastrointestinal transit. These results reveal microbiota–dependent control of gut extrinsic sympathetic activation through a gut-brain circuit.

Chapter 4: Adrenergic signaling in muscularis macrophages limits neuronal death following enteric infection

4.1 Enteric pathogens trigger long-term impairment in GI physiology

Acute bacterial infections, including *Salmonella enterica* serovar Typhimurium*, Shigella dysenteriae, and Campylobacter spp*. have previously been linked to long-term GI dysfunction named post–infectious IBS (Ohman and Simrén, 2010). To characterize functional outcomes of acute intracellular bacterial infection in mice, we used an attenuated strain of *Salmonella* Typhimurium, *spiB* (Tsolis et al., 1999), which harbors a mutation in the type-III secretion system, impacting its intracellular replication. We chose to use the *spiB* strain due to the fact that wild-type *Salmonella* Typhimurium rapidly invades and damages the intestinal wall, ultimately resulting in mortality in wild-type C57BL/6 mice, interfering with our goal of studying long-term functional intestinal changes

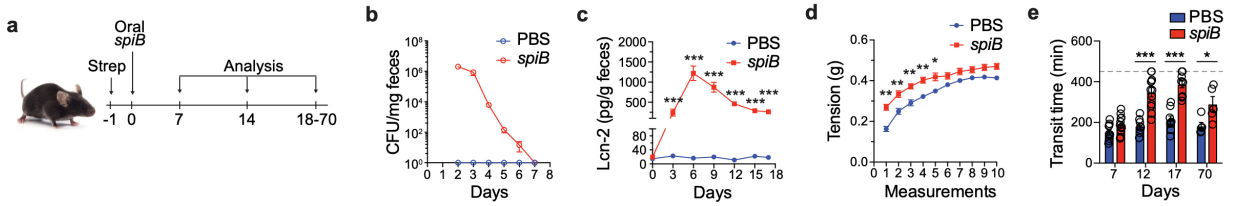

Figure 4.1. Enteric infection leads to iEAN loss and dysmotility. (**a**) Experimental design for (**b**-**e**). (**b**-**e**) C57BL/6J mice were orally gavaged with PBS or 10^9 colony forming units (CFU) of *Salmonella spiB*. (**b**) Quantification of fecal CFU. (**c**) Quantification of fecal lipocalin-2 (Lcn-2) levels as assessed by ELISA post infection. (**d**) Ileal ring myography assessed on day 18 post-infection. (**e**) Gastrointestinal motility as assessed by total gastrointestinal transit time evaluated on the indicated days post infection. Experiments were ended at 450 min (dashed line); Data are representative of at least 5 mice per condition. Data were analyzed by unpaired t-test or one-way ANOVA with Bonferroni correction and represented as mean ± s.d.; n.s. - not significant,* $P < 0.05$, ** $P < 0.01$, *** $P < 0.001$, **** $P < 0.001$.

post pathogen clearance. We observed that orally administered *spiB* was undetected in the feces by 7-10 days post infection (Figure 4.1a,b). Infection with *spiB* caused mild intestinal inflammation as evidenced by increased levels of fecal lipocalin-2 (Lcn-2), that peaked at 6 dpi, just before *spiB* clearance, but remained elevated following pathogen clearance (Figure 4.1c). This persistent inflammatory response was associated with lasting functional GI changes, including increased ileal ring contractility and a persistent delay in gastrointestinal transit time (GITT) (Figure 4.1d,e).

Changes in contractility and GITT can be associated with altered neuronal activity and nerve damage (Chalazonitis and Rao, 2018; Travagli and Anselmi, 2016; Wood, 2002, 2007). Intrinsic enteric-associated neurons (iEAN), commonly referred to as the enteric nervous system, are neural crest–derived and organized in two distinct networks, the submucosal or Meissner's plexus and myenteric or Auerbach's plexus (Furness et al., 2013). In order to determine the impact of intestinal infection on iEAN, we quantified enteric neurons along the GI tract, in both the submucosal and myenteric plexuses. Following *spiB* infection, we observed a 20-30% reduction in myenteric neuron numbers as early as 7 days post-infection in the ileum and colon, both of which are major sites of *Salmonella* invasion; reduced neuronal counts were observed up to 126 days post–infection (Figure 4.2a,b). In contrast, neuronal numbers were preserved in the sites where *Salmonella* invasion normally does not occur, namely the proximal small intestine (Figure 4.2c). We did not observe reduction in neuronal numbers in the submucosal plexus from mice infected with *spiB*; additionally, heat-killed *spiB* did not result in neuronal loss in the myenteric plexus (Figure 4.2d,e). Loss of enteric neurons was also observed after

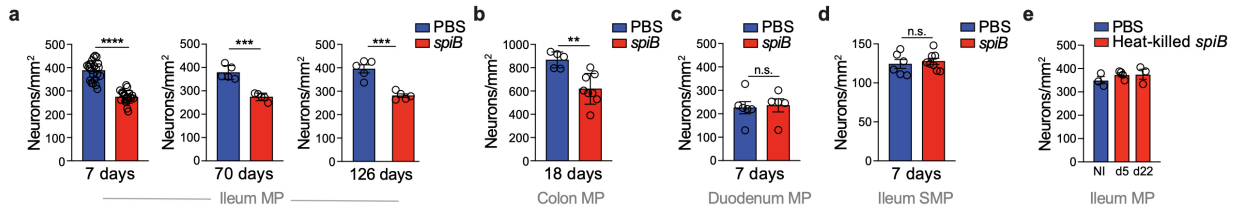

Figure 4.2. Enteric infection with attenuated *Salmonella* leads to iEAN loss. (**a-e**) Neuronal quantification as assessed by immunofluorescence staining (ANNA-1) on the indicated days post infection in the (**a**) myenteric plexus of ileal segments, (**b**) myenteric plexus of colonic segments, (**c**) myenteric plexus of duodenal segments; (**d**) submucosal plexus of ileal segments. (**e**) myenteric plexus of ileal segments from C57BL/6J mice on the indicated days post exposure to 10^9 CFU of heat-killed *Salmonella spiB*. MP – myenteric plexus; SMP – submucosal plexus; Data are representative of at least 5 mice per condition. At least 2 independent experiments were performed. Data were analyzed by unpaired t-test and represented as mean ± s.d.; n.s. - not significant,* $P < 0.05$, ** $P < 0.01$, *** $P < 0.001$, **** $P < 0.001$.

infection with another bacterial pathogen, *Yersinia pseudotuberculosis*, previously reported to cause long-term restructuring of gut lymphatics known as immunological scarring (Fonseca et al., 2015) (Figure 4.3a). We further interrogated whether we could recapitulate our findings in the context of the clinically relevant protozoan pathogens *Toxoplasma gondii* (*T. gondii*) and *Trypanosoma cruzi* (*T. cruzi*), which are known to induce various GI-related pathologies (Dutra et al., 2009; Wilhelm and Yarovinsky, 2014). These protozoans also induced intestinal inflammation, increased ileal ring contractility, delayed GITT and significant neuronal loss (Figure 4.3b-f and *data not shown*). By contrast, infection with the intestinal helminth *S. venezuelensis*, used as a rodent model for human *Strongyloides* infection that displays distinct duodenal tropism (Esterházy et al., 2019), did not lead to reduced neuronal numbers in either the duodenum or distal intestine (Figure 4.3g). These results suggest that parasites co-evolved with mammals do not induce damage in enteric neurons (Maizels et al., 2018). Together, these data

indicate that iEAN loss may be a conserved feature of many, though not all, enteric infections; we chose to continue with *spiB* as an infection model due to the inherent neurotropism of *T. gondii* and *T. cruzi*.

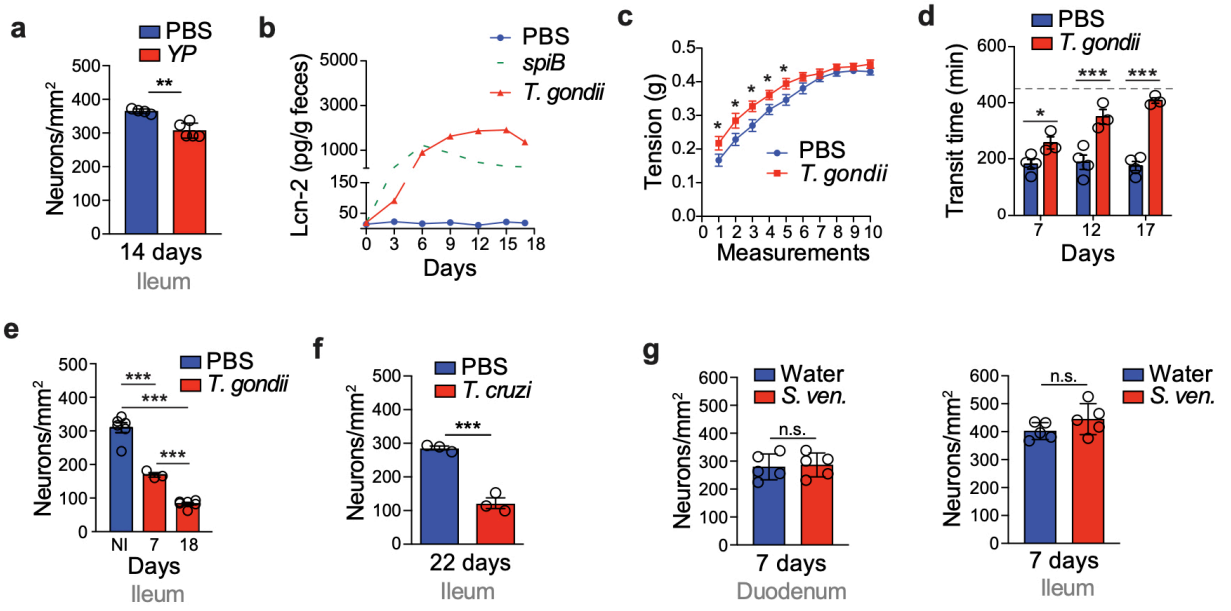

Figure 4.3. iEAN loss with other enteric pathogens. (**a**) Neuronal quantification (ANNA-1 staining) in the myenteric plexus of ileal segments from C57BL/6J mice orally infected with 10^8 CFU of *Y. pseudotuberculosis*. (**b-e**) C57BL/6J mice were orally infected with 5 cysts of *Toxoplasma gondii*. (**b**) Quantification of fecal Lcn-2 levels as assessed by ELISA on the depicted days; (**c**) Ileal ring myography assessed on day 18 post-infection; (**d**) Gastrointestinal motility as assessed by total gastrointestinal transit time on the indicated days post infection; experiments were ended at 450 min (dashed line); (**e**) Neuronal quantification as assessed by cuprolinic blue staining in the myenteric plexus of ileal segments on the indicated days post infection. NI = non-infected. (**f**) Neuronal quantification as assessed by cuprolinic blue staining in the myenteric plexus of ileal segments on the indicated days post infection of C57BL/6J mice with 10^4 parasites of *T. cruzi*. (**g**) Neuronal quantification (ANNA-1 staining) in the myenteric plexus of (left panel) duodenal and (right panel) ileal segments C57BL/6J mice subcutaneously injected with 700 L3 larvae of *S. venezulensis* (*S. ven.*), analyzed on day 8 post-infection. Data are representative of at least 5 mice per condition. At least 2 independent experiments were performed. Data were analyzed by unpaired t-test and represented as mean ± s.d.; n.s. - not significant,* $P < 0.05$, ** $P < 0.01$, *** $P < 0.001$, **** $P < 0.001$.

While it is generally accepted that enteric neurogenesis ceases in postnatal mammals, recent studies suggest continuous turnover of iEAN, for instance by

replenishment from Nestin+ stem cells (Kulkarni et al., 2017). However, in the present study, neither were we able to detect iEAN number recovery up to four months following *spiB* clearance, nor did we observe *Nestin*$^{GFP+}$ cell network changes within the myenteric plexus (Figure 4.4a). As an orthogonal approach, we also evaluated whether enteric glia

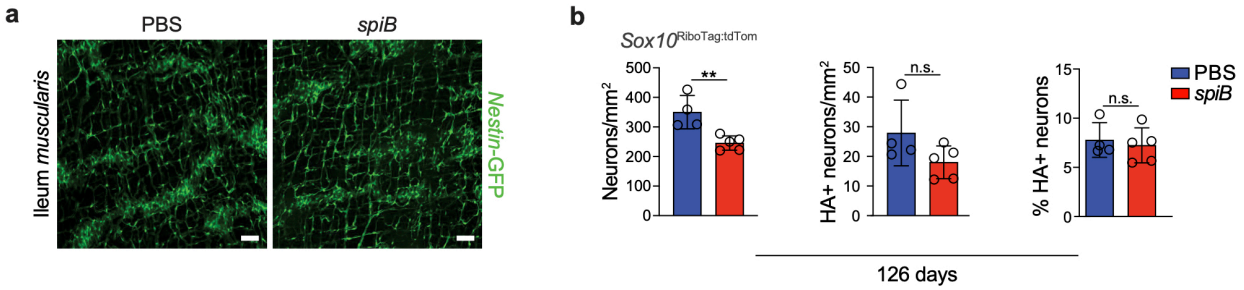

Figure 4.4. No change in potential iEAN precursor populations post-*spiB* infection. (**a**) Representative confocal immunofluorescence images of ileum muscularis from *Nestin*^{GFP} reporter mice 7 days post oral exposure to PBS or *spiB*. Scale bar = 50 μm. Images representative of at least n=5 animals per group. (**b**) Neuronal quantification (ANNA-1 staining, left panel), and quantification of HA+ neurons (*Sox10* reporter) per mm^2 (middle panel) and as percentage of ANNA-1+ neurons in the myenteric plexus of ileal segments from tamoxifen–treated *Sox10*^{RiboTag} reporter mice 126 days post oral infection with PBS or *spiB*. Scale bar = 50 μm. Images representative of at least n=5 animals per group.

cells or their precursors, which have been shown to replenish iEAN in response to injury (Laranjeira and Pachnis, 2009; Laranjeira et al., 2011), could be involved in neuronal maintenance after *spiB* infection. Using an inducible *Sox10*^{RiboTag}-fate mapping strategy, we found that approximately 10% of iEAN were HA+ four months following tamoxifen administration to adult *Sox10*^{RiboTag} control mice, suggesting a glial origin of these cells (Belkind-Gerson et al., 2017). However, we did not observe iEAN recovery nor changes in the frequency of HA+ in the ileum myenteric plexus of *Sox10*^{RiboTag} mice infected with *spiB* in the same period of time (Figure 4.4b). These results indicate that without further

manipulations, enteric neuronal loss is persistent in this model of infection.

Given the significant reduction in ileal and colonic myenteric neurons resulting from a single oral *spiB* infection, we asked whether subsequent pathogenic infection would result in exacerbated neuron loss. Following clearance of *spiB,* we infected mice with wild-type *Salmonella*, after which we observed no additional loss of enteric neurons, indicating a possible restructuring or adaptation of tissue cells preventing further damage (Figure 4.5a). To exclude the contribution of adaptive immunological memory, since both primary and secondary infections were with *Salmonella*, we next performed infection-challenge with different pathogens, *spiB* and *Y. pseudotuberculosis*, bacterial pathogens that resulted in EAN loss post primary infections. We observed that primary infection with *Y. pseudotuberculosis* resulted in iEAN protection against secondary challenge with *spiB*, and conversely, initial iEAN loss with primary *spiB* infection was not enhanced with heterologous *Y. pseudotuberculosis* exposure (Figure 4.5b). The prevention of infection–induced neuronal loss by previous exposure to heterologous pathogens suggests that a form of tissue “trained tolerance” may play a role in limiting enteric neuronal damage. The above results demonstrate that infections with enteric bacterial and protozoan pathogens have the capacity to induce prolonged low-grade inflammation and GI dysmotility, which are associated with a rapid and self-limiting, yet persistent loss of iEAN.

Human post-infectious IBS generally leads to long-term, yet reversible GI symptoms and neuropathy (Beatty et al., 2014; Ohman and Simrén, 2010). However, in the *spiB* model of infection, we did not observe recovery of neurons after a single pathogenic infection. Because of reported effects of microbiota, including recent work

from our group, on the development and maintenance of enteric neurons (Carabotti et al., 2009; Muller et al., 2019b; Obata and Pachnis, 2016; Obata et al., 2019), we assessed

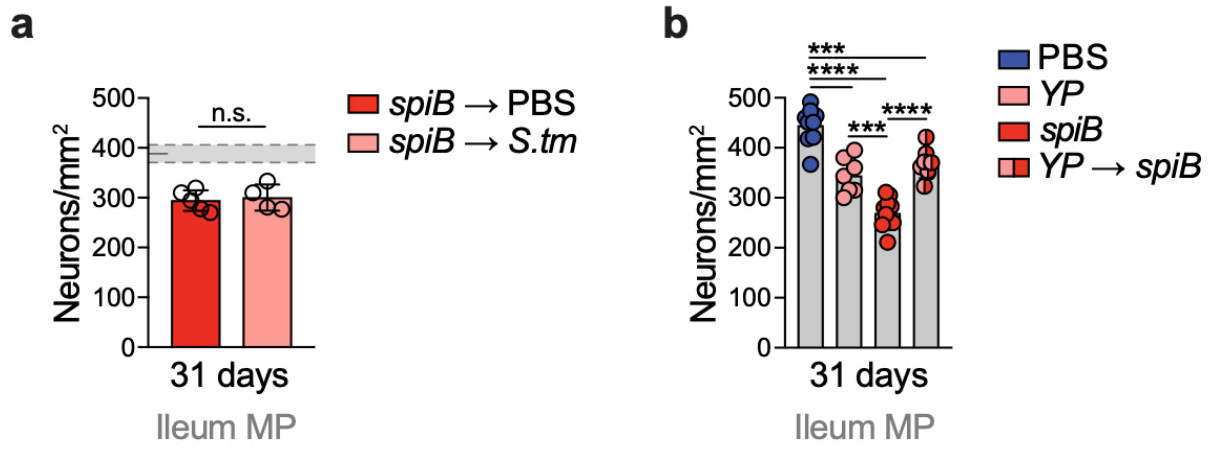

Figure 4.5. No iEAN loss upon subsequent enteric infection (**a**) Neuronal quantification (ANNA-1 staining) in the myenteric plexus of ileal segments of C57BL/6J mice orally gavaged PBS or 10^6 CFU of wild-type *Salmonella* Typhimurium (*S. tm*) 21 days post *spiB* infection, and sacrificed on day 10 post re-infection. Shaded area bounded by dashed lines indicates mean day 7 iEAN numbers ± SEM of all control C57BL6/J mice. (**b**) Neuronal quantification (ANNA-1 staining) in the myenteric plexus of ileal segments of C57BL/6J mice orally gavaged with PBS, 10^9 CFU *Yersinia pseudotuberculosis (Y.p.)*, *spiB,* or *Y.p.* followed by a secondary infection with *spiB* on day 21 post *Y.p.*, and sacrificed 10 days post *spiB* infection. Data are representative of at least 5 mice per condition. At least 2 independent experiments were performed. Data were analyzed by unpaired t-test and represented as mean ± s.d.; n.s. - not significant, *** $P < 0.001$, **** $P < 0.001$.

whether persistent changes in microbial composition (dysbiosis) could explain the lack of recovery of iEAN post infection. We infected SPF mice with *spiB* and administered a cocktail of broad-spectrum antibiotics after bacterial clearance, and subsequently re-colonized the animals

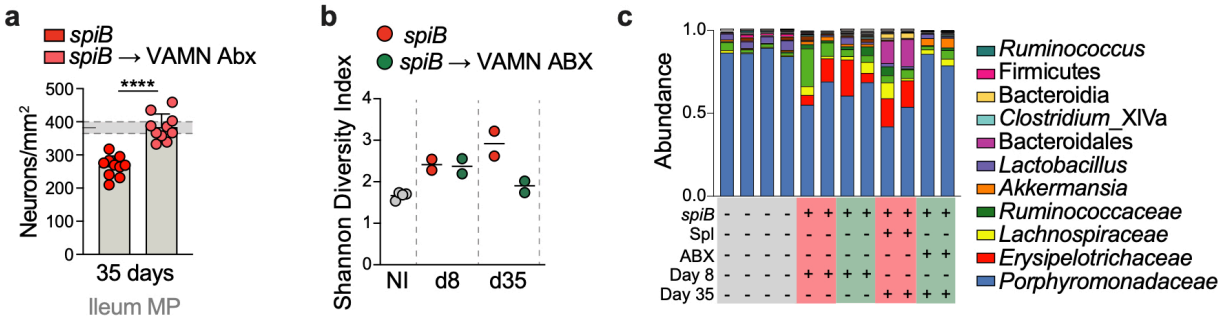

Figure 4.6: Restoration of the microbiome post-*spiB* infection leads to iEAN recovery. (**a**) Neuronal quantification (ANNA-1 staining) in the myenteric plexus of ileal segments of C57BL/6J mice reconstituted with a normal microbiota or not after *spiB* infection. Mice were orally gavaged with 10^9 CFU of *spiB*, followed by 2 weeks of broad-spectrum antibiotics in the drinking water supplemented with Splenda, or Splenda control drinking water, and a further 2 weeks on Splenda in cages containing C57BL/6J feces. Data are representative of at least 5 mice per condition. At least 2 independent experiments were performed. Data were analyzed by unpaired t-test and represented as mean ± s.d.; **** $P \leq 0.0001$. (**b**) Shannon diversity index of 16S sequencing from feces obtained from n=2 mice in representative groups in Figure 1L. (**c**) Top 11 most abundant genera from 16S sequencing of feces obtained from mice in representative groups in (**a**).

with “normal” microbiome from naïve SPF mice. Consistent with our hypothesis, we observed that reconstitution of a “normal” or pre-infection microbiota allowed for iEAN recovery (Figure 4.6a), effects that were correlated with a reduction in a member of the *Erysipelotrichaceae* family and Bacteriodales order when compared to untreated–infected mice (Figure 4.6b,c). These data point to a role for the gut microbiota in the recovery of iEAN post infection.

4.2 Enteric infection–induced neuronal loss is subtype-specific

iEAN comprise a numerous and heterogeneous population of neurons that monitor and respond to various environmental cues, including mechanical stretch and luminal metabolites (Furness et al., 2013; Mayer, 2011). We first asked whether the observed

loss of iEAN could be explained by a decrease of ELAVL3/4 protein expression. To address this question, we interbred a pan-neuronal Cre reporter mouse, *Snap25*^{Cre}, with *Rpl22*$^{lsl\text{-}HA}$ (RiboTag) mice (Sanz et al., 2009), which express a hemagglutinin (HA)–tagged ribosomal subunit 22. Immunofluorescence (IF) analysis of HA+ cells in the myenteric plexus confirmed the significant loss of iEAN as initially determined by ANNA-1 staining (Figure 4.7a,b and Appendix). It has been reported that in cases of overt intestinal

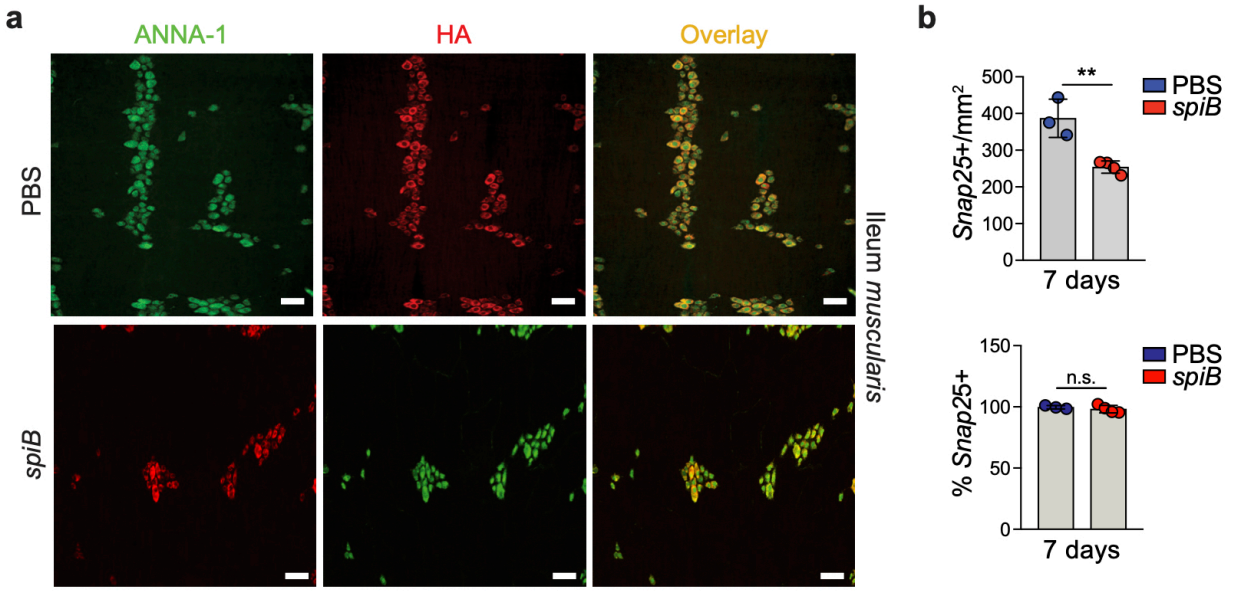

Figure 4.7. iEAN loss post-*spiB* is not due to decreased detection of neuronal-specific protein. (**a**, **b**) Mice were orally gavaged with PBS or 10^9 CFU of Salmonella *spiB*, and analyzed 7 days post infection. (**a**) Representative confocal immunofluorescence images of the ileum myenteric plexus stained with anti-ANNA-1 (red) and anti-HA (green) from *Snap25*^{RiboTag} mice treated with (top) PBS- or infected with (bottom) *spiB*. (**b**) Quantification of the (top) number of HA+ neurons per mm^2 or (bottom) percent HA and ANNA-1 overlap on day 7 post oral gavage with PBS or with 10^9 CFU of Salmonella *spiB*. Data are representative of at least 3 mice per condition. At least 2 independent experiments were performed. Data were analyzed by unpaired t-test and represented as mean ± s.d.; n.s. - not significant, ** $P \leq 0.01$.

inflammation, such as colitis, there is indiscriminate loss of iEAN (Linden et al., 2005; Mawe, 2015). To investigate whether specific neuronal subsets were preferentially lost after enteric infection, we used confocal IF imaging to evaluate the impact on excitatory and inhibitory neuronal cell populations (Zeisel et al., 2018). Imaging of the ileum myenteric plexus from infected and uninfected *Slc17a6*$^{td\text{-}Tomato}$ (VGLUT2) reporter mice revealed a significant reduction in total number and percentage of excitatory VGLUT2+ neurons (Figure 4.8a,b). In contrast, quantification of inhibitory NOS+ and somatostatin

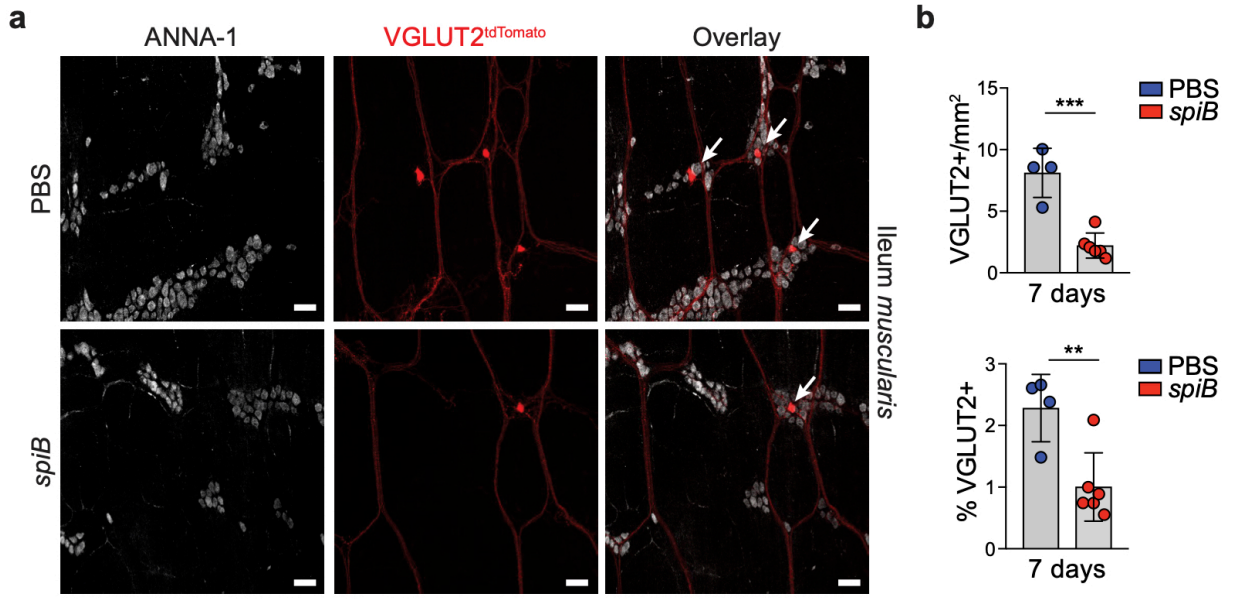

Figure 4.8. Infection with *spiB* leads to loss of VGLUT2+ iEAN. (**a**, **b**) Mice were orally gavaged with PBS or 10^9 CFU of Salmonella *spiB*, and analyzed 7 days post infection. (**a**) Representative confocal immunofluorescence image of the ileum myenteric plexus stained with anti-ANNA-1 (grey) from VGLUT2$^{td\text{-}Tomato}$ mice treated with (top) PBS or infected with (bottom) *spiB*. **(b)** Quantification of the number of VGLUT2+ neurons per mm^2 and as a percentage of ANNA-1+ neurons. Data are representative of at least 3 mice per condition. At least 2 independent experiments were performed. Data were analyzed by unpaired t-test and represented as mean ± s.d.; $^{**}P \leq 0.01$, $^{***}P \leq 0.001$.

(SST)+ iEAN populations revealed no changes (nNOS) (Figure 4.9a,b), and a subtle relative increase (SST) of these subtypes post infection (Figure 4.10a,b). These data

suggest a preferential loss of excitatory neuronal subsets post infection, resulting in changes in the neurochemical representation of iEAN, although the loss of VGLUT2+ neurons only represents a proportion of the total numbers of neurons lost during infection. These results may provide an explanation for functional changes in GI motility observed after infection.

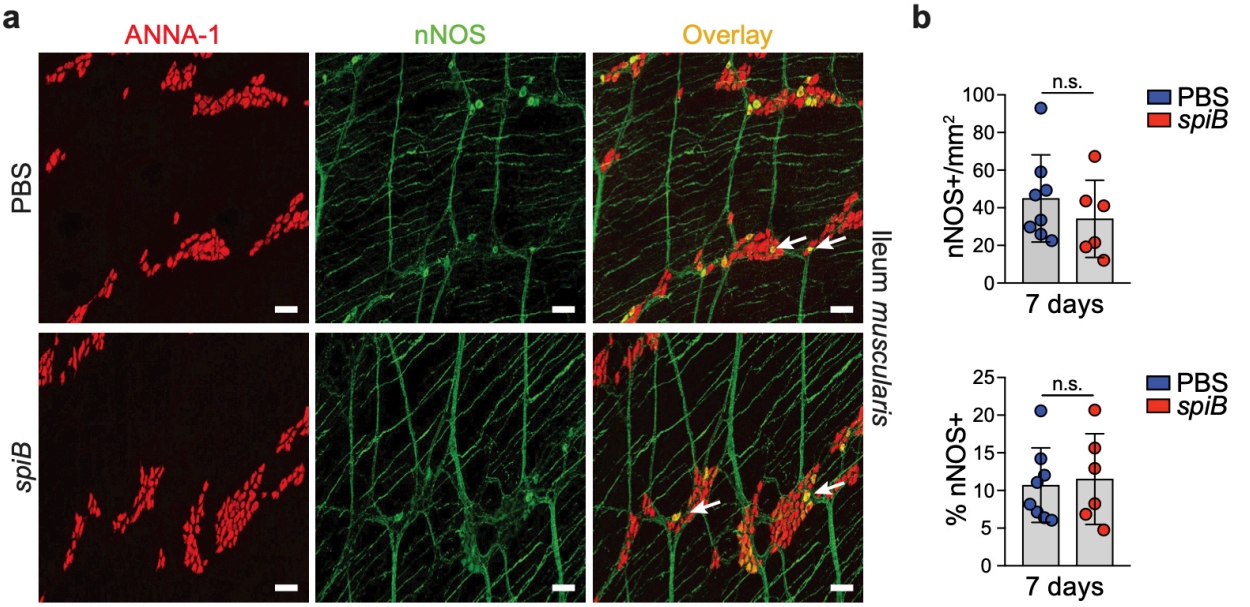

Figure 4.9. No change in nNOS+ iEAN post-*spiB* infection. (**a**, **b**) Mice were orally gavaged with PBS or 10^9 CFU of Salmonella *spiB*, and analyzed 7 days post infection. (**a**) Representative confocal immunofluorescence image of ileum myenteric plexus from C57BL/6J stained with anti-ANNA-1 (red) and anti-neuronal nitric oxide synthase (nNOS) (green) antibodies. (**b**) Quantification of the number of nNOS+ neurons per mm^2 and as a percentage of ANNA-1+ neurons. Data are representative of at least 3 mice per condition. At least 2 independent experiments were performed. Data were analyzed by unpaired t-test and represented as mean ± s.d.; n.s. - not significant.

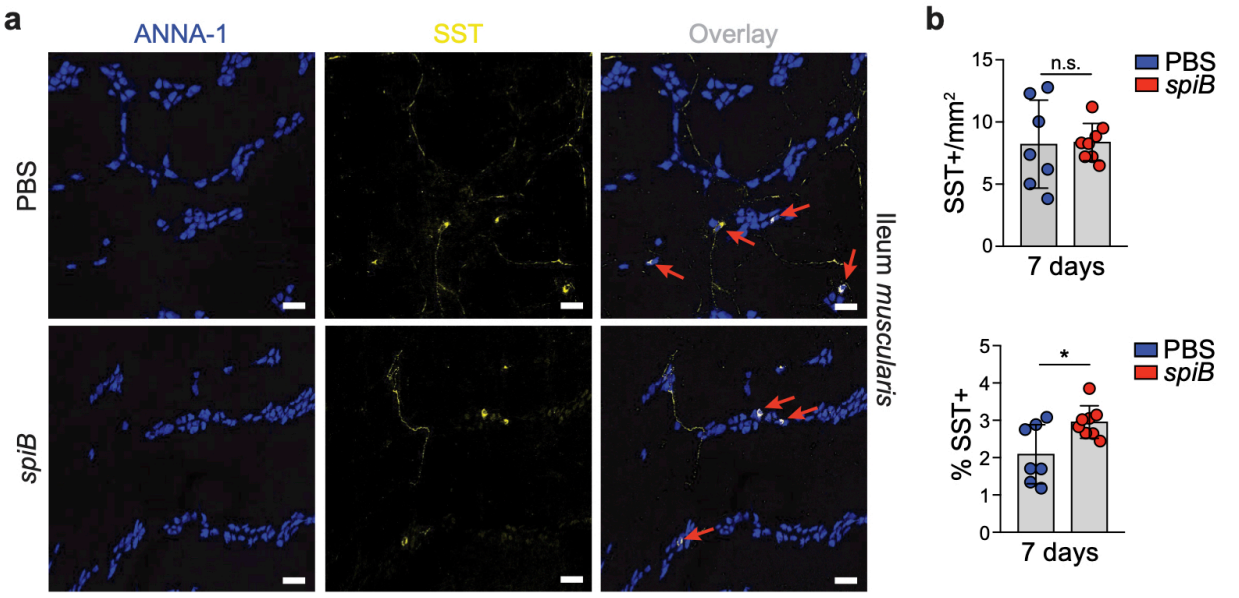

Figure 4.10. Small changes in SST+ iEAN post-*spiB* infection. (**a**, **b**) Mice were orally gavaged with PBS or 10^9 CFU of Salmonella *spiB*, and analyzed 7 days post infection. (**a**) Representative confocal immunofluorescence image of ileum myenteric plexus from C57BL/6J stained with anti-ANNA-1 (blue) and anti-somatostatin (SST) (yellow) antibodies. Scale bars = 50 μm. (**b**) Quantification of the number of SST+ neurons per mm^2 and as a percentage of ANNA-1+ neurons. Data are representative of at least 3 mice per condition. At least 2 independent experiments were performed. Data were analyzed by unpaired t-test and represented as mean ± s.d.; $^*P \leq 0.05$.

4.3 iEAN loss post–enteric infection is NLRP6- and caspase 11-dependent

To gain insights into a possible mechanism involved in infection-induced iEAN cell death, we used neuronal–specific cell–sorting independent translating ribosomal affinity purification (TRAP) using *Snap25*^{RiboTag} mice, described above, which allow neuronal-specific immunoprecipitation of actively translated mRNA (Heiman et al., 2014; Muller et al., 2019b; Sanz et al., 2009). We compared iEAN with extrinsic neurons in the nodose ganglia of *Snap25*^{RiboTag} mice; expression of HA–tagged ribosomes was confirmed in neurons of the myenteric plexus and nodose ganglion of *Snap25*^{RiboTag} mice (Figure 4.11a) (Muller et al., 2019b). RNA sequencing analysis of immunoprecipitated intact mRNA bound to HA–tagged ribosomes (TRAP-seq) revealed an iEAN–specific

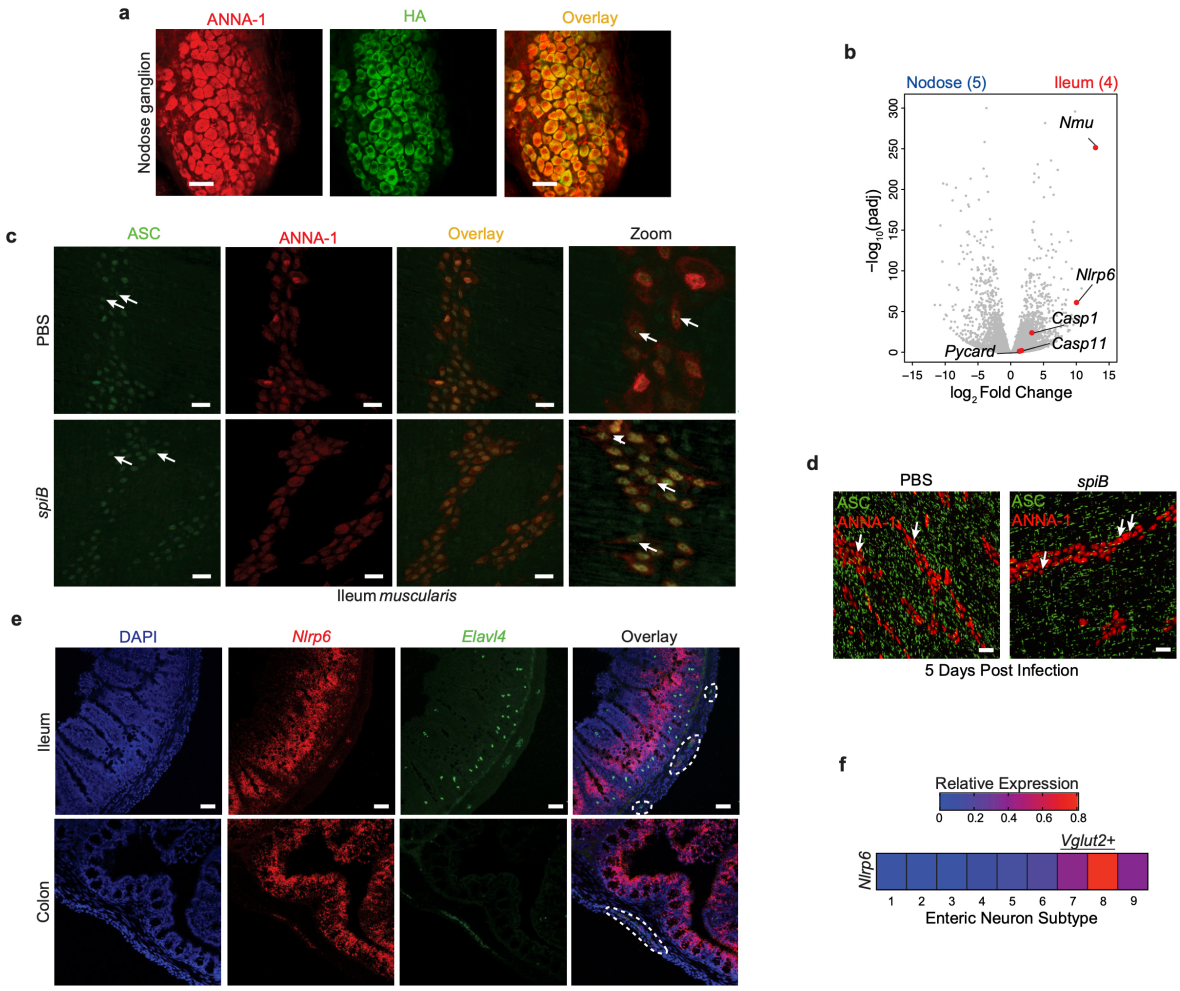

Figure 4.11. Translational profiling of iEAN reveals expression of inflammasome components. (**a**) Representative confocal immunofluorescence images of the nodose ganglia from *Snap25*$^{\text{RiboTag}}$ mice stained with anti-ANNA-1 (red) and anti-HA (green) antibodies. Scale bars = 50 μm. Images representative of n= 5 mice. (b) Volcano plot of differentially–expressed genes of ribosome-associated transcripts from neurons of the nodose ganglion (NG) and ileum myenteric iEAN isolated from *Snap25*$^{\text{RiboTag}}$ mice. Grey dots highlight all genes analyzed; red dots highlight genes that are significantly differentially expressed in ileum iEAN as compared to the NG. Number of samples are indicated in parentheses. (**c**) Immunofluorescence staining of the ileum myenteric plexus from C57BL/6J mice using anti-ANNA-1 (red) and anti-PYCARD (ASC, green) antibodies. Samples obtained 6 hours post oral gavage of PBS or 10^9 CFU of *Salmonella spiB*. Arrows indicate ASC "specks"; inset shows ImageJ zoom of the indicated panel in PBS-treated mice. Scale bars = 25 μm. Images representative of at least n=5 per group. (**d**) Immunofluorescence staining of ileum myenteric plexus from ASC$^{\text{mCitrine}}$ mice using anti-ANNA-1 (red) antibody and native mCitrine fluorescence. Samples obtained 5 days post oral gavage of PBS or 10^9 CFU of *Salmonella spiB*. Arrows indicate ASC "specks" within neurons. Scale bars = 50 μm. Images representative of at least n=3 per group. (**e**) Fluorescence *in situ* hybridization RNAScope® with probes for *Nlrp6* and *Elavl4* (pan-neuronal) in the ileum and colon from C57BL6/J mice. iEAN are outlined with a dashed line. Scale bars = 50 μm. Images representative of at least n=2 per group. (**f**) Heatmap representation of the relative expression of *Nlrp6* in iEAN subsets as defined by single-cell analysis from the published dataset mousebrain.org/genesearch.html (Zeisel et al., 2018). *Vglut2*+ subsets as defined by the same analysis are highlighted. Data are representative of 3-6 mice per condition. At least 2 independent experiments were performed.

enrichment in genes encoding neuropeptides, such as neuromedin (*Nmu*), as well as components of the inflammasome pathway including *Nlrp6*, *Pycard*, *Casp1*, and *Casp11* (Figure 4.11b). These data indicate that iEAN possess the machinery for engaging an inflammasome- and caspase 1/11-mediated cell death. Imaging analyses for the expression of the inflammasome adaptor ASC (PYCARD) using anti-ASC antibody in wild-type mice or the endogenous fluorescence of *Rosa26*$^{ASC:mCitrine}$ (ASC^{mCitrine}) mice confirmed the expression of this inflammasome component by iEAN of the ileum of both naïve and *spiB*–infected mice (Figure 4.11c,d). To visualize the pattern of *Nlrp6* expression by iEAN, we performed fluorescence *in situ* hybridization (FISH) on ileum and colon sections using RNAscope® probes specific to *Elavl4* (pan-neuronal) and *Nlrp6*. We observed dense localization of *Nlrp6* transcripts in the epithelium of both the ileum and colon, similar to what has previously been reported (Levy et al., 2015; Volk et al., 2019). In addition, we visualized *Nlrp6* transcripts in areas of *Elavl4*–expressing cells in the *muscularis* layer, supporting the expression of NLRP6 by myenteric neurons (Figure 4.11e). Analysis of data from single cell transcriptional profiling of iEAN (Zeisel et al., 2018) indicated that *Nlrp6* is highly enriched in excitatory enteric neurons compared with additional iEAN subsets (Figure 4.11f). These results may explain the preferential targeting of excitatory iEAN subsets during enteric infections.

To evaluate the role of caspase-mediated cell death in iEAN loss during infection, we systemically administered a pan caspase inhibitor (zVAD-FMK) to mice infected with *spiB*, which reduced infection-induced iEAN loss (Figure 4.12a,b). We directly addressed

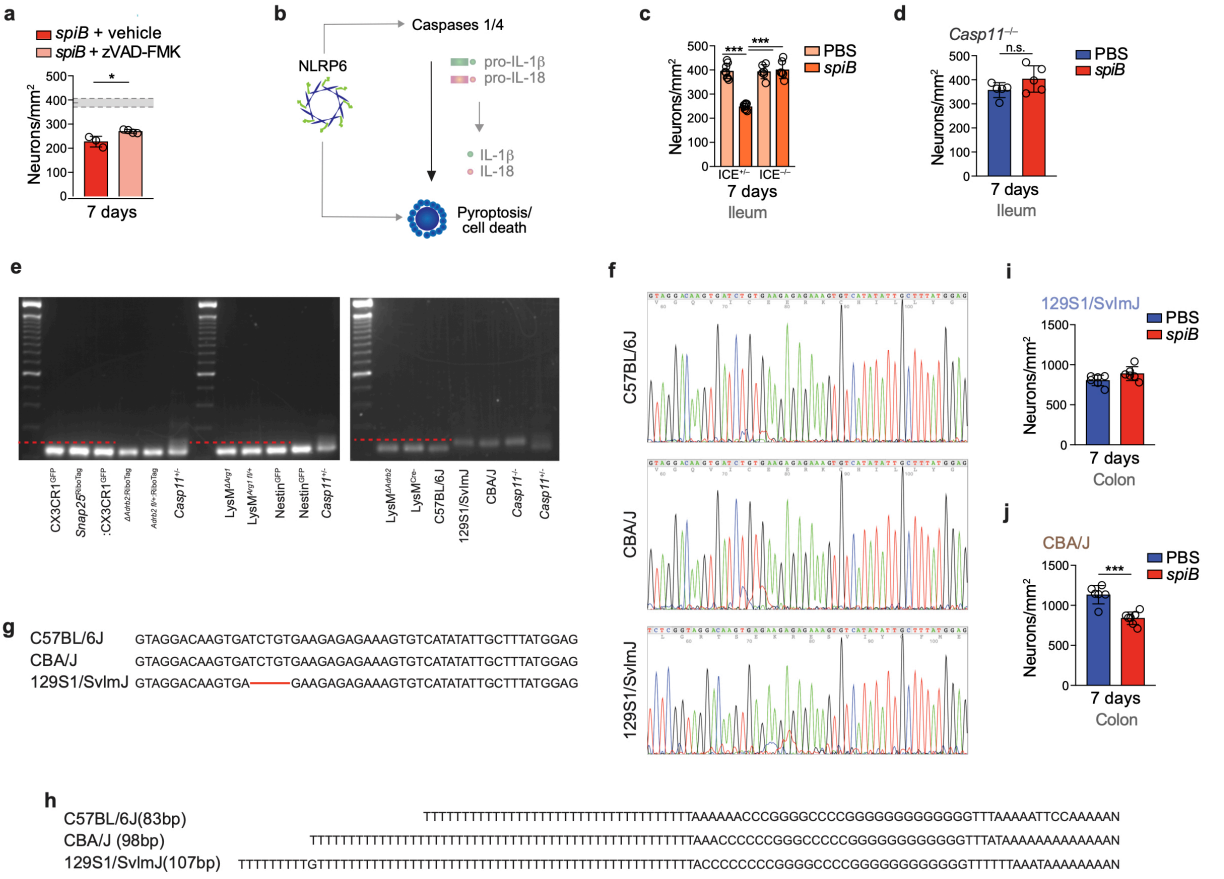

Figure 4.12. The inflammasome is necessary for iEAN loss post-*spiB* infection. (**a**) Neuronal quantification (ANNA-1 staining) in the myenteric plexus of ileal segments on day 7 post *spiB* infection of C57BL/6J mice receiving vehicle (dimethyl sulfoxide, DMSO) or zVAD-FMK (150 μg/day) by daily intraperitoneal injections over the course of infection. Shaded area bounded by dashed lines indicates mean day 7 iEAN numbers +/- SEM of all control C57BL6/J mice analyzed in Figure 4.1. (**b**) Scheme of the NLRP6 inflammasome pathway. (**c**) Neuronal quantification as assessed by immunofluorescence staining (ANNA-1) in the myenteric plexus of ileal segments on day 7 post gavage of PBS or *spiB* of *Casp1*$^{-/-}$ *Casp11*$^{-/-}$ (Interferon-converting enzyme, ICE) double-knockout (ICE$^{-/-}$) mice or heterozygous controls (ICE$^{+/-}$). (**d**) Neuronal quantification (ANNA-1 staining) in the myenteric plexus of ileal segments of *Casp11*$^{-/-}$ mice on day 7 post *spiB* infection or PBS treatment. (**e**) 3% agarose gel for *Casp11* 5bp deletion PCR product. Mouse strains used in this work are indicated below each lane. Red dashed line indicates the size at which a potential 5bp deletion PCR product will run; (**f**) Sanger sequencing of *Casp11* 5bp deletion PCR product in C57BL/6J, CBA/J, and 129S1/SvImJ mice; (**g**) Sequence surrounding *Casp11* 5bp deletion region in C57BL/6J, CBA/J, and 129S1/SvImJ mice. Red line indicates 5bp deletion in 129S1/SvImJ mice; (**h**) Comparison of the length of intron sequences obtained from *Casp11* 5bp deletion PCR product in C57BL/6J, CBA/J, and 129S1/SvImJ mice. (**i**, **j**) Neuronal quantification (ANNA-1 staining) in the myenteric plexus of colonic segments on day 7 post *spiB* infection of (**i**) 129S1/SvImJ mice and (**j**) CBA/J mice. Data are representative of 3-5 mice per condition. At least 2 independent experiments were performed. Data were analyzed by unpaired t-test and represented as mean ± s.d.; *$P \leq 0.05$, *** $P \leq 0.001$

the role of caspases 1 and 11 in infection–induced iEAN loss by infecting caspase 1/11 (ICE)–deficient or haplosufficient ($ICE^{+/-}$) mice (Kuida et al., 1995) with *spiB*. While $ICE^{+/-}$ mice exhibited pronounced iEAN loss in the ileal myenteric plexus 7 days post–infection, *spiB*-infected $ICE^{-/-}$ mice were completely protected from neuronal loss, despite similar bacterial clearance patterns (Figure 4.12c and Appendix). Infection with *spiB* also did not result in iEAN loss in single *Casp11*–deficient mice (Wang et al., 1998) (Figure 4.12d and Appendix). We further dissected the specific role caspases 1 and 11 in neuronal cell death by utilizing the 129S1/Sv mouse strain, which carries an inactivating mutation in the *Casp11* locus (human *Casp4*) (Vanden Berghe et al., 2015; Kenneth et al., 2012). 129 mice infected with *spiB* exhibited no loss of colonic iEAN numbers as compared to non-infected controls (Figure 4.12e-l and Appendix). This iEAN protection was independent of the ability of 129 mice to survive WT *Salmonella* infection due to expression of functional *Nramp*, as we found that CBA/J mice, which also express a functional *Nramp* (Brown et al., 2013), but do not carry a *Casp11* mutation, exhibited significant neuronal loss when infected with *spiB,* despite similar clearance of the bacteria (Figure 4.12e-h,j and Appendix). These data suggest a caspase 11–mediated cell death as a main mechanism involved in iEAN loss following *Salmonella* infection.

To define whether the NLRP6 inflammasome and caspase 11-mediated mechanisms proposed above were neuronal cell-intrinsic, we utilized two *in vivo* approaches of neuronal-specific gene deletion. Intravenous (i.v.) injection of AAV9 can target peripheral neurons, including iEAN, particularly upon the insertion of the neuronal-specific promoter hSyn (Gombash et al., 2014; Kügler et al., 2003; Obata et al., 2019).

Imaging analysis indicated that this strategy led to efficient virus targeting of iEAN (Figure 4.13a,b). To remove *Casp11* from iEAN, we i.v.-injected *Casp11*$^{flox/flox}$ mice with AAV9-hSyn-HI-eGFP-Cre-WPRE-SV40, which results in nuclear eGFP-Cre expression; AAV9-hSyn-eGFP-WPRE-bGH, which leads to eGFP expression mostly in the neuronal processes, was used as a control virus (Figure 4.13c,d). We detected Cre–expressing

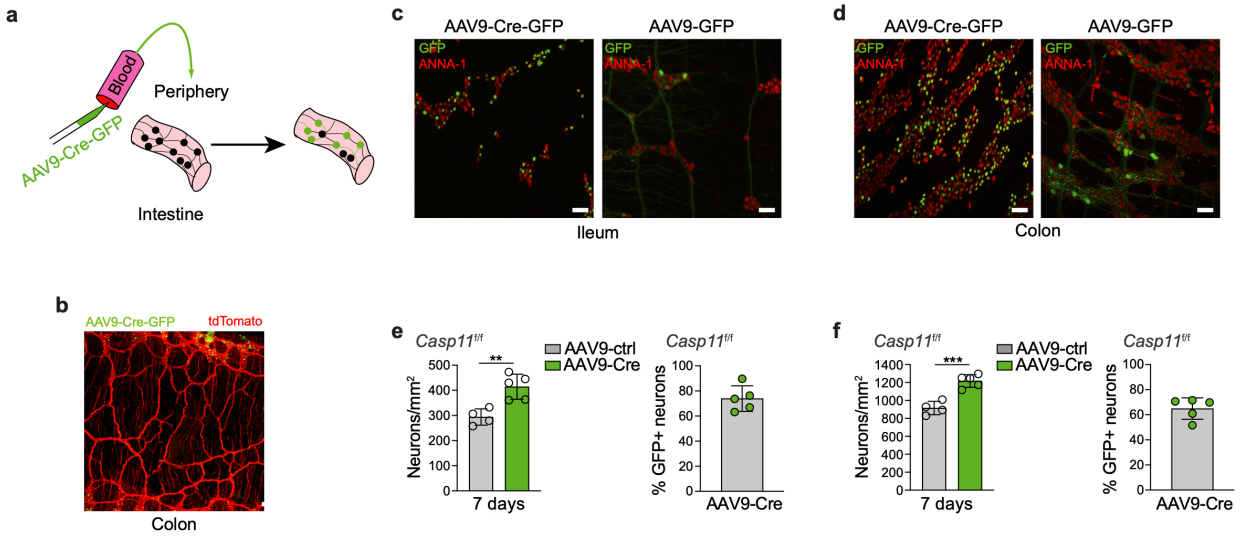

Figure 4.13. Neuronal specific *Casp11* knockout by viral targeting abrogates iEAN loss post-*spiB* infection. (**a**) Scheme of intravenous AAV9–mediated transduction of peripheral neurons, including iEAN. (**b**) Representative confocal immunofluorescence image of the colon muscularis of *Rosa26*$^{lsl\text{-}tdTomato}$ mice given i.v. injection of AAV9-hSyn-Cre-GFP virus. Image representative of at least n=3. Scale bar = 50 μm. (**c**) and colonic (**d**) myenteric plexus of *Casp11*$^{flox/flox}$ mice given i.v. injection of AAV9-hSyn-Cre-GFP or control viruses, stained with anti-ANNA-1 (red) antibodies. (**e**, **f**) (left) Neuronal quantification (ANNA-1 staining) in the myenteric plexus of ileal (**e**) and colonic (**f**) segments from EAN$^{\Delta Casp11}$ or *Casp11*$^{flox/flox}$ mice on day 7 post *spiB* infection. (right) Quantification of the number of Cre-GFP transduced cells in the ileum myenteric plexus of iEAN$^{\Delta Casp11}$ mice. Data are representative of 3-6 mice per condition. At least 2 independent experiments were performed. Data were analyzed by unpaired t-test and represented as mean ± s.d.; n.s. - not significant, *$P \leq 0.05$, ** $P \leq 0.01$, *** $P \leq 0.001$, **** $P \leq 0.0001$.

AAV9 in 60-90% of myenteric iEAN of the ileum and colon (Figure 4.13e,f). Upon infection with *spiB,* we did not observe neuronal loss in mice injected with Cre–expressing AAV9 as compared to mice injected with control virus (Figure 4.13e,f and Appendix), suggesting that neuronal–intrinsic Casp11 expression is required for *Salmonella*-induced iEAN loss.

To address whether neuronal–specific NLRP6 expression was also involved in post–infectious EAN loss, we crossed pan-neuronal *Snap25*$^{\text{RiboTag}}$ mice with a strain carrying a floxed *Nlrp6* locus (*Nlrp6*$^{\text{flox/flox}}$) (Figure 4.14a). We infected *Snap25*$^{\text{RiboTag}\Delta Nlrp6}$, *Snap25*$^{\text{RiboTag}}$x*Nlrp6*$^{\text{flox/+}}$ heterozygous and (Cre-) *Nlrp6*$^{\text{flox/flox}}$ control mice with *spiB* and

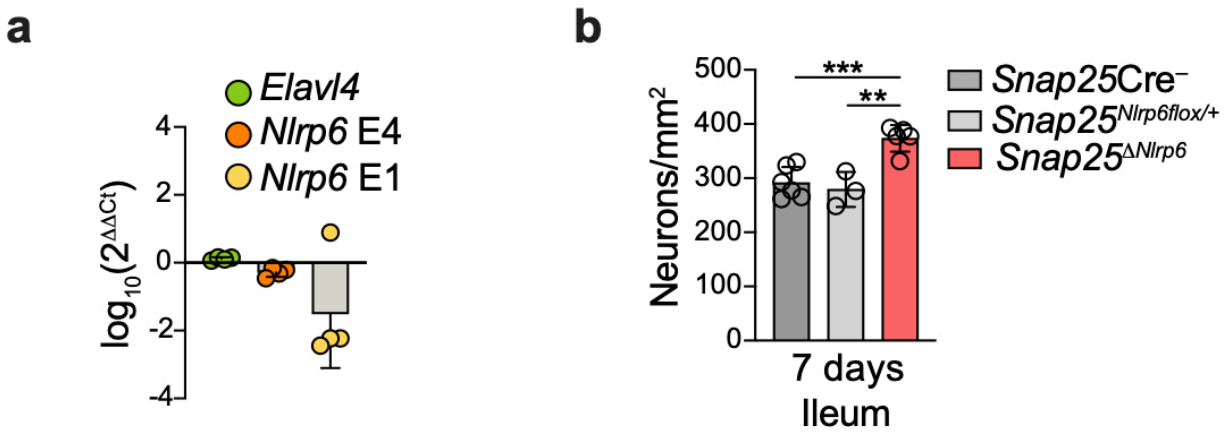

Figure 4.14. Neuronal specific knockout of *Nlrp6* abrogates iEAN loss post-*spiB* infection. (**a**) Log transformed relative expression to *Rpl32* of TRAP-qPCR data of *Elavl4* and *Nlrp6* from *Snap25*$^{\Delta Nlrp6}$:RiboTag as compared to *Snap25*$^{Nlr6flox/+}$:RiboTag. E1=Exon1 of *Nlrp6,* E1=Exon4 of *Nlrp6*. (**b**) Neuronal quantification (ANNA-1 staining) in the myenteric plexus of ileal segments from *Snap25Cre*$^{-}$, *Snap25*$^{Nlrp6flox/+}$ or *Snap25*$^{\square Nlrp6}$ mice on day 7 post *spiB* infection. Data are representative of 3-6 mice per condition. At least 2 independent experiments were performed. Data were analyzed by one way ANOVA with Bonferroni correction and are shown as mean ± s.d.; ** $P \leq 0.01$, *** $P \leq 0.001$.

quantified iEAN numbers post-infection. While both heterozygous and Cre^{-} controls showed reduced iEAN numbers upon *spiB* infection, *Snap25*$^{\Delta Nlrp6}$ did not display EAN loss (Figure 4.14b and Appendix). Together, the above data implicate neuronal-specific NLRP6 and caspase 11 as main effectors involved in iEAN loss following *Salmonella* infection.

4.4 MM respond to luminal infection to limit neuronal damage

Tissue–resident MM, the most abundant immune cell population in the myenteric plexus, are closely juxtaposed to iEAN, and their presence has been linked to normal functioning of these neurons during homeostasis (Gabanyi & Muller et al., 2016; Muller et al., 2014; De Schepper et al., 2018). Our previous observations using both cell-sorting– and TRAP–based approaches, suggested that MM preferentially express tissue-protective and wound healing genes, such as *Retnla* (encoding Fizz1), *Mrc1*, *Cd163* and *Il10* at steady state. This gene signature was reinforced early (2 h) after oral exposure to *spiB*, with an upregulation of additional tissue-protective genes such as *Arg1* and *Chi3l3* (encoding Ym1) (Gabanyi & Muller et al., 2016). To investigate a possible role of MM in infection-induced iEAN damage, we first depleted MM using an antibody blocking colony stimulating factor 1 receptor (CSF1R)-signaling, AFS98 (α-CSF1R). We used a dose that preferentially depletes MM over lamina propria macrophages, due to the fact that MM express higher levels of CSF1R (Muller et al., 2014) (Figure 4.15a-c). Continuous α-CSF1R-mediated MM depletion did not impact iEAN numbers in naïve mice. However, MM depletion resulted in an enhanced iEAN loss in mice infected with *spiB* when compared to mice treated with isotype control antibody, despite similar bacterial load in

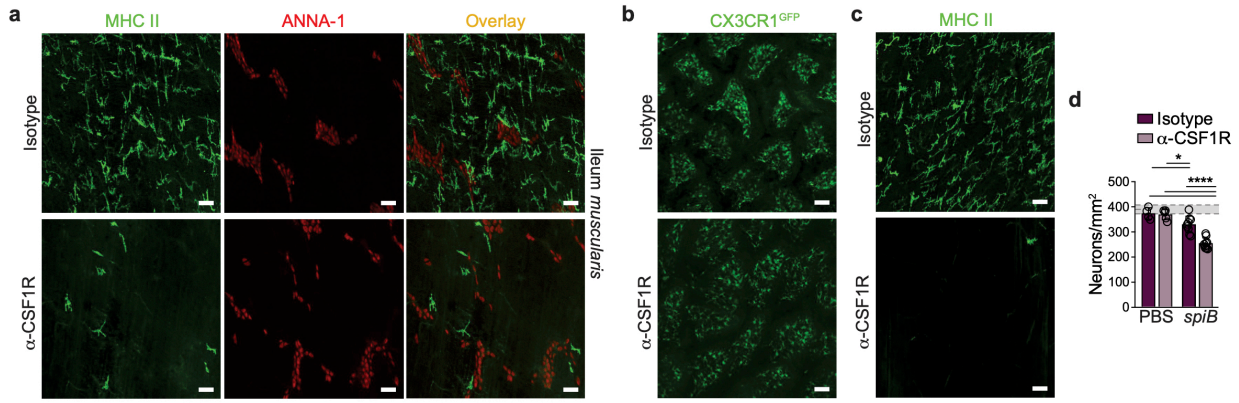

Figure 4.15. Antibody-mediated depletion of MM exacerbates iEAN loss post-*spiB* infection. (**a-d**) C57BL/6J mice were orally gavaged with PBS or 10^9 CFU of *Salmonella spiB* and treated with anti-CSF1R or IgG isotype control antibodies by intraperitoneal injections twice over the course of a 7-day period. (**a**) Representative confocal immunofluorescence staining of MM and iEAN of the ileum myenteric plexus region stained with anti-MHC-II (green) and anti-ANNA-1 (red). Images representative of at least n=5 per condition; (**b**) Representative confocal immunofluorescence image of the ileum submucosal layer of *Cx3cr1*^{GFP} mice treated with anti-CSF1R or IgG isotype control antibody by intraperitoneal injections. Scale bar = 50 μm. Images representative of at least n=3 mice per condition. (**c**) Representative confocal immunofluorescence image of the ileum myenteric plexus of C57BL/6J mice on day 7 post treatment with anti-CSF1R or isotype control antibody. Scale bar = 50 μm. Images representative of at least n=5 mice per condition. (**d**) Neuronal quantification as assessed by immunofluorescence staining (ANNA-1) of ileum myenteric plexus of injection-habituated non-infected and *spiB*-infected mice receiving anti-CSF1R or IgG isotype control antibodies. Data are representative of at least n=3 per condition. At least 2 independent experiments were performed. Data were analyzed by unpaired t-test and represented as mean ± s.d.; * $P < 0.05$, **** $P < 0.0001$.

both conditions (Figure 4.15d and Appendix). These results indicate that, while short–term depletion of MM does not impact iEAN survival in the unperturbed state, MM may play an iEAN–protective role in the context of enteric infection.

Because glia cells, both in the CNS and periphery, have been reported to mediate neuronal protection (Brown et al., 2016; Skatchkov et al., 2015), we also tested whether enteric glia are involved in infection–induced iEAN loss or limiting it thereof. To target enteric glia, we used mice carrying tamoxifen–inducible *Cre* under the glia–specific *Plp1* promotor (*Plp1*^{CreER}) and the *lox*-stop-*lox*-*DTA* transgene in the *Rosa26* locus (Rao et al., 2015, 2017). Depletion of glia in *Plp1*^{iDTA} mice before infection with *spiB* led to a similar loss of iEAN as tamoxifen–treated control animals, indicating that enteric glia do not play either a major neuronal protective, or detrimental role in this model (Figure 4.16a,b and Appendix).

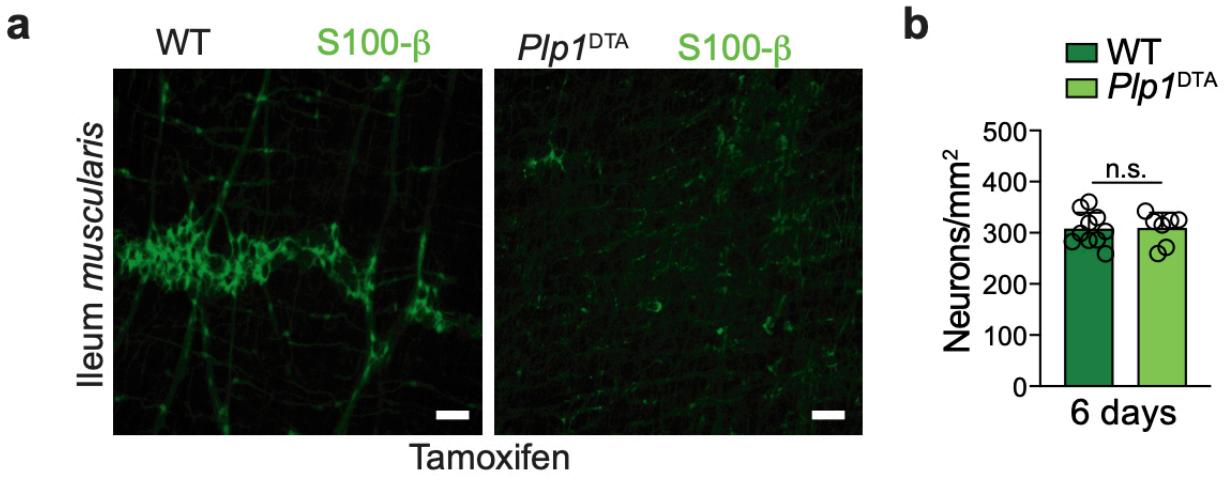

Figure 4.16. Enteric glia are not required for iEAN protection post-*spiB* infection. (**a**) Representative confocal immunofluorescence images from the ileum myenteric plexus of *Plp1*^{iDTA} or control mice using anti-S100b (green). Samples obtained at 6 days post oral gavage of *spiB* (11 days post-tamoxifen). Scale bar = 50 μm. (**b**) Neuronal quantification (ANNA-1 staining) of ileum myenteric plexus from *Plp1*^{DTA} or control mice 6 days post oral gavage of *spiB*. Data are representative of at least n=3 per condition. At least 2 independent experiments were performed. Data were analyzed by unpaired t-test and represented as mean ± s.d.; n.s. - not significant.

Next, we used confocal imaging to investigate MM dynamics early upon infection, which revealed a continuing presence and intercalation into ganglia of the myenteric plexus (Figure 4.17a,b). To assess whether inflammatory monocytes recruited from the

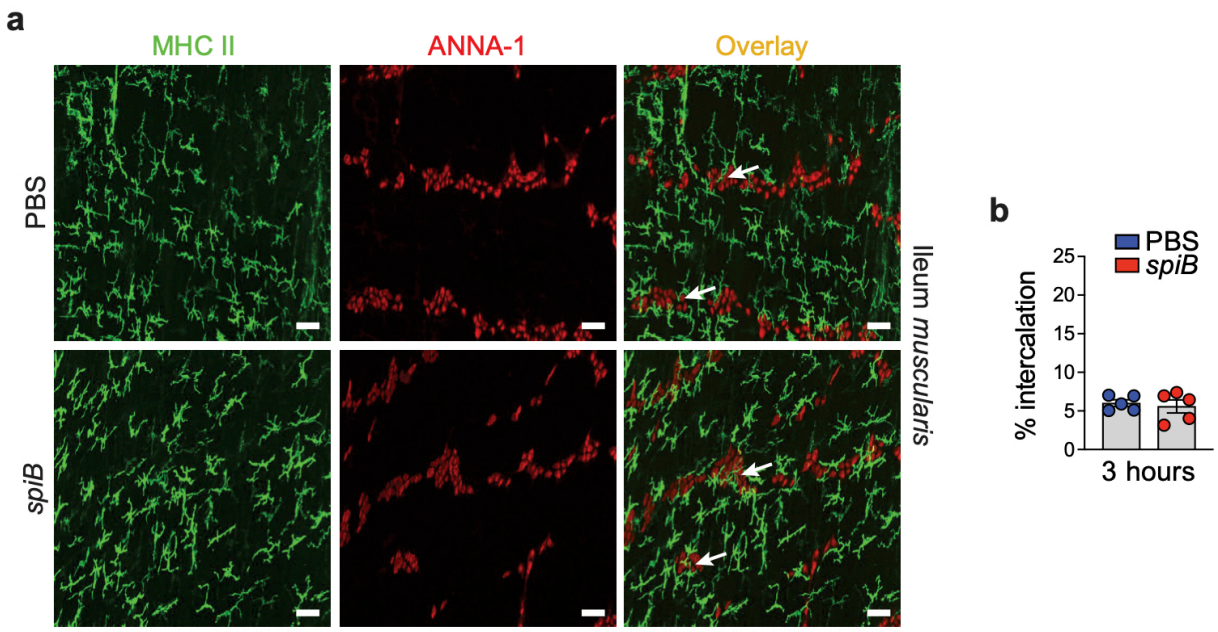

Figure 4.17. MM interactions with iEAN do not change early on in *spiB* infection. (**a**) Representative confocal immunofluorescence images from the ileum myenteric plexus of C57BL/6J mice using anti-MHC II (green) and anti-ANNA-1 (red). Samples obtained at 3 hours post oral gavage of PBS or *spiB*. Scale bar = 50 μm. (**b**) Quantification of MM intercalation into ileum myenteric plexus ganglia as assessed by confocal immunofluorescence imaging and calculations based on Imaris software surface functions. Samples obtained at 3 hours post oral gavage of PBS or *spiB*. Data are representative of at least n=4 per condition. At least 2 independent experiments were performed. Data were analyzed by unpaired t-test and represented as mean ± s.d.

circulation are involved in infection-induced neuronal damage, we used CCR2$^{-/-}$ mice, which exhibit an impairment in mobilizing inflammatory monocytes into tissues (Boring et al., 1997). CCR2$^{-/-}$ mice failed to clear *spiB* infection, likely reflecting a reduced resistance in the mucosal layer (Dunay et al., 2008), and showed mild acceleration, rather than a delay in GITT 17 days post infection (Figure 4.18a,b). Nonetheless, CCR2$^{-/-}$ mice showed similar iEAN loss as WT control mice (˜25%), suggesting that the persistent

luminal pathogen load does not cause an increase in neuronal damage (Figure 4.18a,c). These data also highlight that intestinal macrophages recently differentiated from circulating monocyte precursors may contribute to *spiB* clearance mechanisms but are

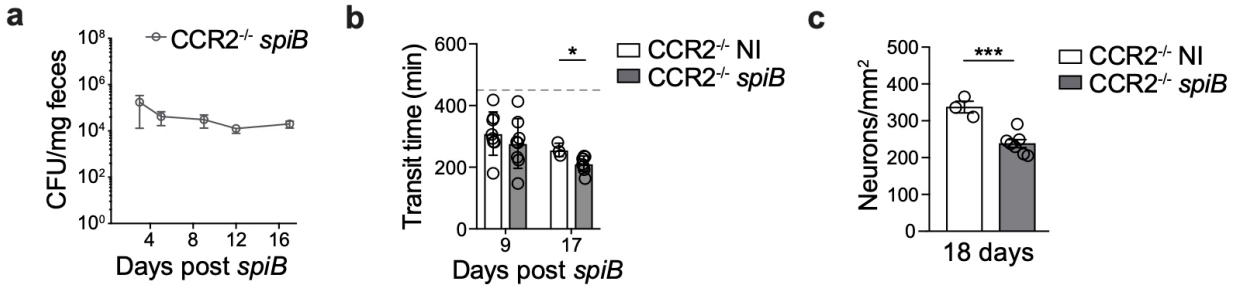

Figure 4.18. Inflammatory monocytes do not contribute to iEAN loss post-*spiB* infection. (**a-c**) CCR2$^{-/-}$ mice were orally infected with 10^9 CFU of *Salmonella spiB* (**a**) Quantification of fecal CFU on the indicated days post infection; (**b**) Gastrointestinal motility activity as assessed by total intestinal transit time on the indicated days post infection; experiments were ended at 450 min (dashed line); (**F**) Quantification of neurons of the ileum myenteric plexus as assessed by immunofluorescence staining (ANNA-1). Data are representative of at least n=4 per condition. At least 2 independent experiments were performed. Data were analyzed by unpaired t-test and represented as mean ± s.d.; * $P < 0.05$, *** $P < 0.0001$.

not required for post–infectious iEAN cell death. The above results suggest a critical response of resident MM to luminal pathogenic stimulation; while MM are likely not essential for resistance mechanisms, they appear to prevent excessive neuronal damage.

4.5 β2-AR signaling in MM constrains infection–induced inflammation and neuronal death

We previously reported that the tissue-protective gene-expression profile of MM was further imprinted following enteric infection via β_2 adrenergic receptors (β_2-ARs) (Gabanyi & Muller et al., 2016). We investigated the capacity of β_2-AR signaling to mediate tissue protection by coupling pharmacological and genetic modulation of this pathway. First, C57BL/6 mice were infected with *spiB* while being treated with a selective

β_2-AR agonist (salbutamol) which was delivered continuously via subcutaneously implanted osmotic pumps for 14 days. We did not observe differences in the pathogen load in mice treated with salbutamol (Appendix). However, administration of salbutamol protected mice from neuronal loss post infection (Figure 4.19a). To directly assess the role of MM in the observed salbutamol–mediated protection from neuronal death post infection, we then depleted MM using α-CSF1R in mice receiving continuous salbutamol treatment. While we observed a rescue of iEAN death in mice treated with IgG isotype control antibody, MM depletion led to a loss of salbutamol-mediated iEAN protection (Figure 4.19b). Taken together, these data suggest that MM are critical for β_2-AR–mediated iEAN protection.

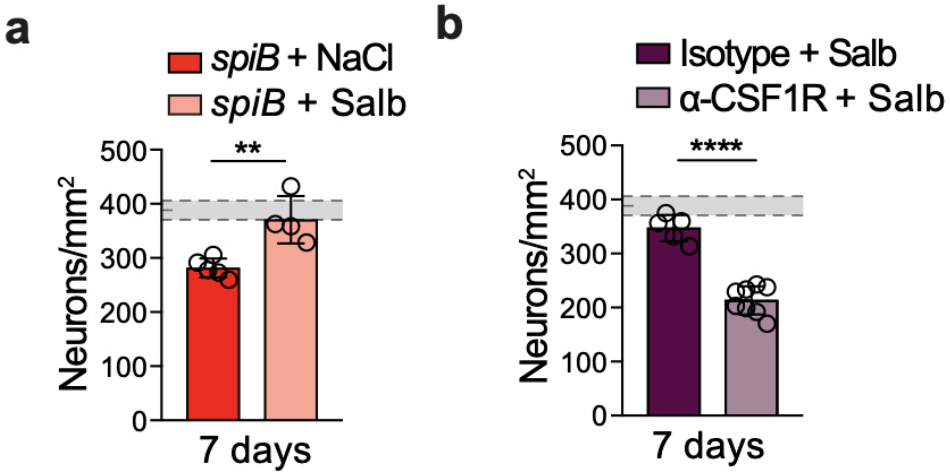

Figure 4.19. MM are critical for β_2-AR–mediated iEAN protection. (**a**) Neuronal quantification (ANNA-1 staining) in the ileum myenteric plexus of C57BL/6J mice continuously receiving either vehicle (NaCl) or salbutamol sulfate delivered by subcutaneous osmotic pumps for 14 days, and orally gavaged with PBS or 10^9 CFU of *Salmonella spiB* on day 7 post-surgical pump implantation. Samples obtained on day 7 post infection. (**b**) Neuronal quantification (ANNA-1 staining) in the ileum myenteric plexus of C57BL/6J mice receiving salbutamol delivered by subcutaneous osmotic pumps for 14 days. Mice were gavaged with PBS or *spiB* on day 7 post-surgical pump implantation and received anti-CSF1R or IgG isotype control antibodies twice over the course 7-day infection. (**a**, **b**) Shaded area bounded by dashed lines indicates mean day 7 iEAN numbers ± SEM of all control C57BL6/J mice analyzed in Figure 4.2a. Data are representative of at least n=3 per condition. At least 2 independent experiments were performed. Data were analyzed by unpaired t-test and represented as mean ± s.d.; ** $P < 0.05$, **** $P < 0.0001$.

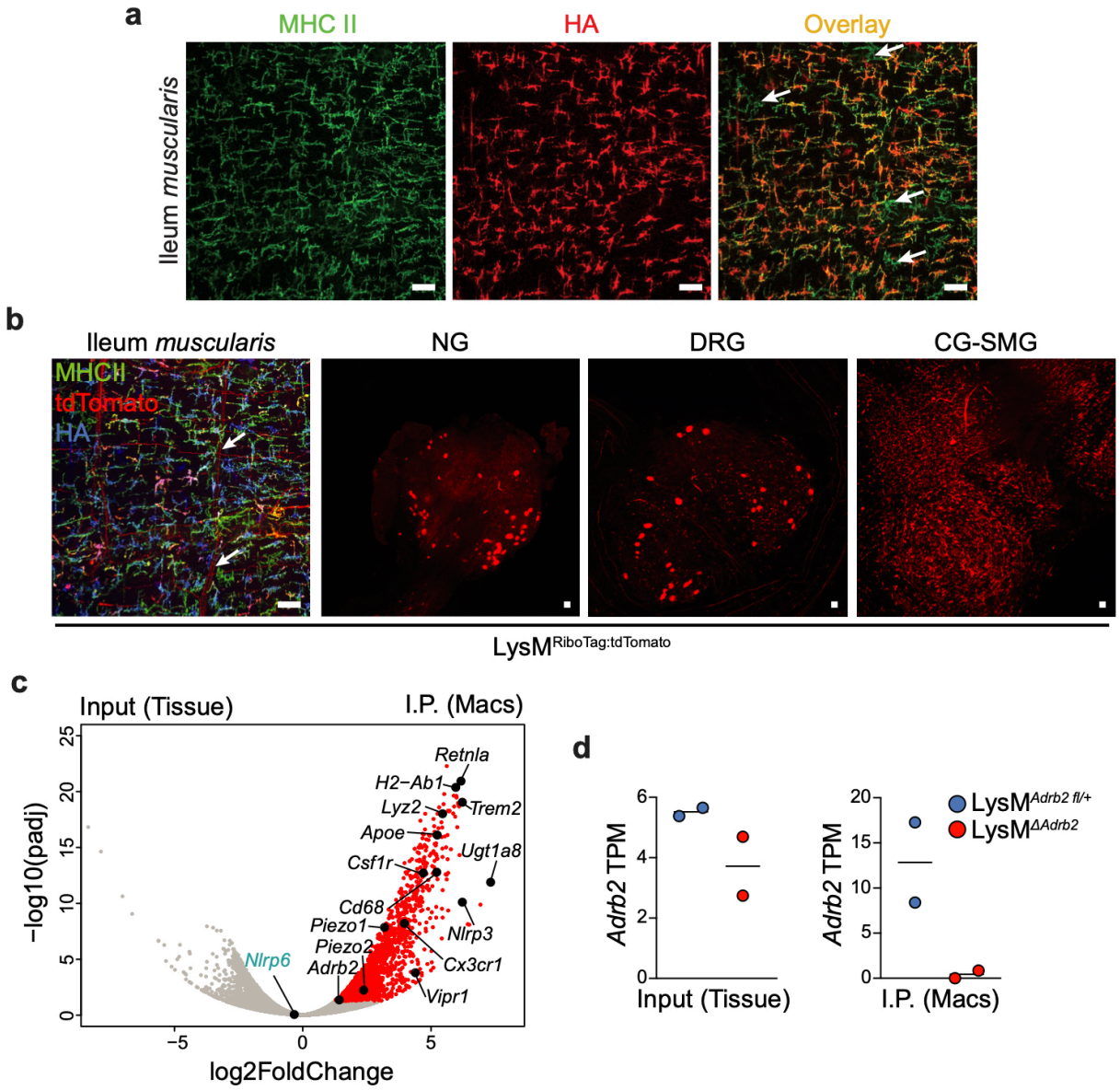

Figure 4.20. Specificity of LysM^{Cre} for targeting of MM. (**a**) Immunofluorescence staining of MM from the ileum of LysM^{RiboTag} mice using anti-MHC II (green) and anti-hemagglutinin (HA, red) antibodies. White arrows indicate MHC II+ HA- macrophages. Scale bars = 50 μm. Images representative of n=2 mice per group. (**b**) Whole mount immunofluorescence images from LysM$^{RiboTag:tdTomato}$ mice in the ileum (stained for MHCII (green) and HA (blue)), nodose ganglion (NG), thoracic dorsal root ganglion (DRG), and celiac-superior mesenteric ganglion. Images representative of n=4. Scale bar = 50 μm. (**c**) Volcano plot of differential expression analysis (DEseq2) of TRAPseq from LysM$^{Adrb2fl/+:RiboTag}$ mice comparing input (ileum tissue) to immunoprecipitated transcripts (red dots) All I.P. samples indicated by red dots are $log_2FC > 0.5$ and $p_{adj} > 0.05$. Relevant macrophage genes highlighted in black text and *Nlrp6* (neuronal specific) highlighted in blue text. (**d**) Transcripts per million (TPM) as calculated by Kallisto alignment of *Adrb2* transcript comparing input (ileum tissue) or immunoprecipitated transcripts from LysM$^{Adrb2\ fl/+}$ and LysM$^{\Delta Adrb2}$ RiboTag mice.

We next addressed whether adrenergic signaling in macrophages plays a role in infection–induced enteric neuronal damage utilizing a genetic approach. We interbred mice carrying Cre recombinase under the myeloid *Lyz2* promoter (LysM^{Cre}) with *Adrb2*$^{flox/flox}$ mice (Hinoi et al., 2008). The specificity of Cre-targeting of macrophages in the intestinal *muscularis* was confirmed by immunohistochemistry using HA as a fate–mapping reporter (Figure 4.20a). Additionally, while we occasionally observed ectopic *Cre* expression in extrinsic ganglia, we were unable to detect iEAN recombination (Figure 4.20b). TRAP-seq of LysM^{RiboTag}:*Adrb2*$^{fl/+}$ demonstrated significant enrichment for classically ascribed macrophage genes such as *Retnla*, *H2-Ab1*, *Lyz2*, *Csf1r*, and *Cx3cr1* (Figure 4.20c). This dataset also revealed the expression of potentially novel receptors involved in immune regulation such as the mechnosensitive *Piezo1* and *Piezo2* (Ranade et al., 2014; Solis et al., 2019), as well as a neuropeptide receptor for vasoactive intestinal peptide, *Vipr1* (Ran et al., 2015; Talbot et al., 2019) (Figure 4.20c). TRAP-seq comparison of LysM^{RiboTag}:*Adrb2*$^{fl/+}$ and LysM^{RiboTag}:*Adrb2*$^{fl/fl}$ mice confirmed the selectivity of this MM targeting strategy, as *Adrb2* was preferentially depleted in LysM^{RiboTag}:*Adrb2*$^{fl/fl}$ immunoprecipitated samples (Figure 4.20c). We did not detect infiltrating neutrophils, also targeted by *Lyz2*, in the intestinal *muscularis* at steady state or early post infection, suggesting that neutrophil-β_2-AR signaling does not play a major role in this model (*data not shown*). Together, these results demonstrate the utility of LysM^{Cre} to target the majority of MM.

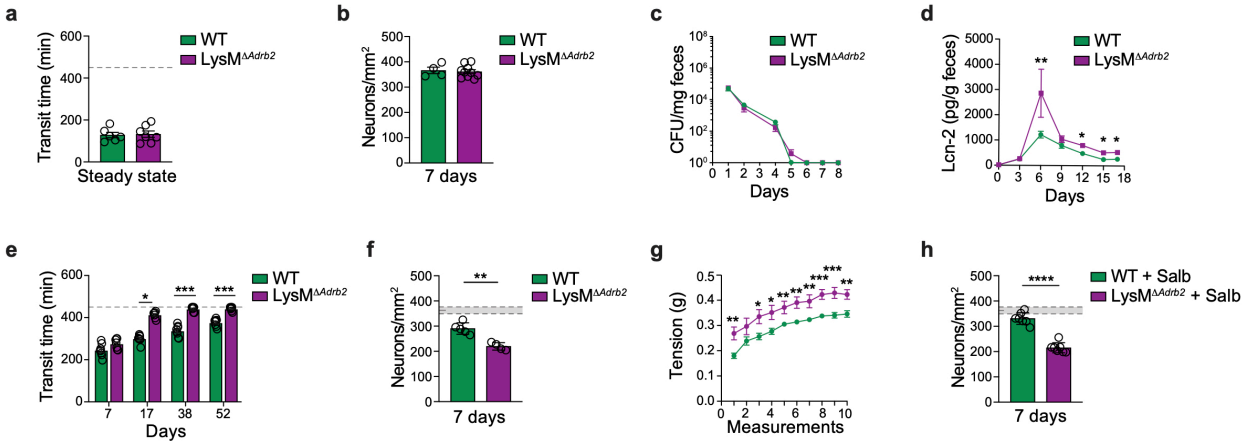

Figure 4.21. Loss of β_2-AR signaling in MM exacerbates neuronal damage during enteric infection. (**a**) Gastrointestinal motility as assessed by total intestinal transit time of naïve LysM$^{\Delta Adrb2}$ and wild-type (WT) littermate control mice; experiments were ended at 450 min (dashed line); (**b**) Neuronal quantification as assessed by immunofluorescence staining (ANNA-1) in the ileum myenteric plexus of naïve LysM$^{\Delta Adrb2}$ and wild-type (WT) littermate control mice. (**c**) Quantification of fecal colony forming units (CFU) on the indicated days post infection. (**d**) Quantification of fecal lipocalin-2 (Lcn-2) on the indicated days post infection. (**e**) Gastrointestinal motility activity as assessed by total gastrointestinal transit time; experiments were ended at 450 min (dashed line); (**f**) Neuronal quantification as assessed by immunofluorescence staining (ANNA-1) in the myenteric plexus of ileal segments on day 7 post infection with *spiB* of LysM$^{\Delta Adrb2}$ and wild-type (WT) littermate control mice; shaded area bounded by dashed lines indicates mean day 7 iEAN numbers +/- SEM of non-infected LysM$^{\Delta Adrb2}$ and WT littermate control mice (**b**); (**g**) Ileal ring myography assessed on day 53 post infection of LysM$^{\Delta Adrb2}$ and wild-type (WT) littermate control mice; (**h**) LysM$^{\Delta Adrb2}$ and wild-type (WT) littermate control mice receiving 400 μg/day salbutamol sulfate delivered by subcutaneous osmotic pumps for 14 days. Mice were infected with *spiB* on day 7 post-surgical pump implantation; shaded area bounded by dashed lines indicates mean day 7 iEAN numbers ± SEM of non-infected LysM$^{\Delta Adrb2}$ and WT littermate control mice (b). Data are representative of at least 3 mice per condition. At least 2 independent experiments were performed. Data were analyzed by unpaired t-test and represented as mean ± s.d.; *$P \leq 0.05$, ** $P \leq 0.01$, *** $P \leq 0.001$, **** $P \leq 0.0001$.

At steady state, we did not observe differences in iEAN numbers or GITT in LysM$^{\Delta Adrb2}$ as compared to Cre^{-} littermate control mice during homeostasis (Figure 4.21a,b). Upon *spiB* infection, LysM$^{\Delta Adrb2}$ also exhibited a similar pathogen clearance (Figure 4.21c). However, we found that LysM$^{\Delta Adrb2}$ mice had further increased fecal Lcn-2 levels following *spiB* infection as compared to Cre^{-} littermates, suggesting a role for myeloid-specific β_2-AR signaling in the regulation of infection–induced inflammation (Figure 4.21d). This enhanced intestinal inflammation was accompanied by further prolonged GITT, which persisted long-term post *spiB* clearance, an increased loss of myenteric neurons and enhanced alterations in ileal ring contractility (Figure 4.21e-g). To complement these results, and to address whether MM themselves require intact β_2-AR signaling to limit neuronal loss, we infected LysM$^{\Delta Adrb2}$ mice and Cre- littermate controls receiving continuous salbutamol treatment. Similar to what we observed in wild-type C57BL/6 mice, salbutamol treatment in Cre- littermate controls carrying an intact β_2-AR signaling in the myeloid compartment resulted in prevention of infection-induced neuronal loss. Conversely, salbutamol-treated LysM$^{\Delta Adrb2}$ mice still displayed significant iEAN loss (Figure 4.21h). These data establish a role for β_2-AR signaling in intestinal macrophages that contributes to a neuroprotective program post enteric infection.

4.6 Local sympathetic activation mediates iEAN protection during enteric infection

It did not escape our attention that mice i.p.-injected multiple times with IgG isotype control antibodies (as in MM depletion experiments) or mice anesthetized with isoflurane

(as in control pump experiments) did not lose usual (˜25%) iEAN numbers post *spiB* infection, suggesting that stress–induced local or systemic catecholamine release could trigger the same protective pathway in MM. Indeed, a short pulse of isoflurane anesthesia, i.p. injections of PBS or IgG isotype antibody, and restraint stress was sufficient to prevent most iEAN cell death following *spiB* infection, suggesting that stress signals that potentiate β_2-AR signaling may help in preventing post–infectious iEAN loss (Figure 4.22a-c). In light of these findings, we sought to determine whether systemic release of

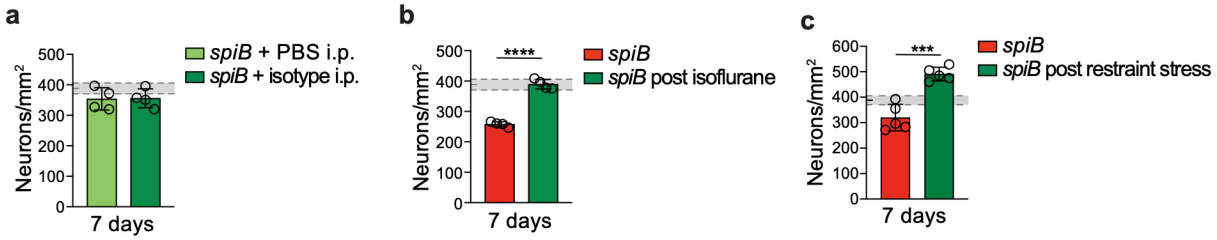

Figure 4.22. Stress can prevent iEAN loss post-*spiB* infection. (**a-c**) Neuronal quantification as assessed by immunofluorescence staining (ANNA-1) in the myenteric plexus of ileal segments on day 7 post infection of C57BL/6 with *spiB* (**a**) receiving mock i.p. injections of PBS or IgG isotype control antibody (**b**) following isoflurane anesthesia for 15 min or (**c**) undergoing 15 min of restraint stress 12 hours prior to infection. Shaded area bounded by dashed lines indicates mean day 7 iEAN numbers ± SEM of all control C57BL6/J mice analyzed in Figure 4.2a; Data are representative of at least 3 mice per condition. At least 2 independent experiments were performed. Data were analyzed by unpaired t-test and represented as mean ± s.d.; *** $P \leq 0.001$, **** $P \leq 0.0001$.

catecholamines from the hypothalamic-pituitary-adrenal axis could be playing a role in neuronal protection during infection (Abe et al., 2017; Prüss et al., 2017). We performed bilateral adrenalectomy on wild-type mice and, after allowing for a 1-week recovery, compared iEAN loss upon *spiB* infection with sham-operated controls. Rather than enhanced iEAN loss post infection, as we observed in LysM$^{\Delta Adrb2}$ mice, adrenalectomized animals showed reduced neuronal loss, excluding the possibility that systemic catecholamines were required for iEAN protection, and also suggesting that additional

stress hormones produced by the adrenal glands, such as corticosteroids, could play a detrimental role in enteric neuronal maintenance during the course of intestinal infections (Aubert et al., 2019) (Figure 4.23a-c and Appendix).

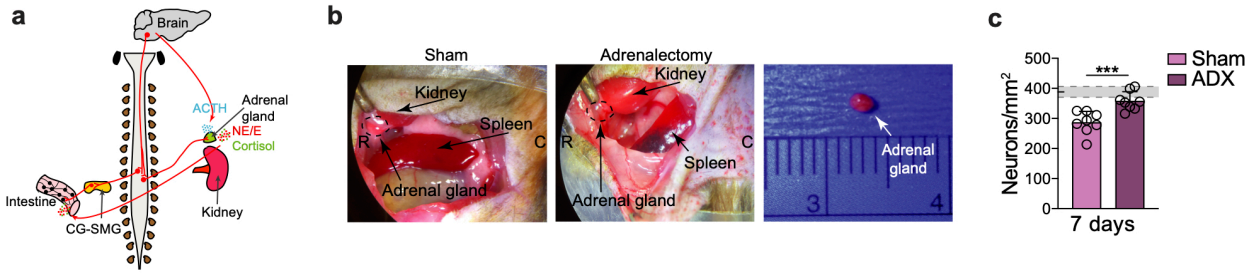

Figure 4.23. The HPA axis is not required for MM-mediated iEAN protection during *spiB* infection. (**a**) Scheme of HPA axis and local sympathetic innervation of the intestine. (b, c) Mice were orally infected with 10^9 CFU of *Salmonella spiB*. (**b**) Images demonstrating a successful removal of adrenal glands from C57BL/6J mice. (**c**) Neuronal quantification as assessed by immunofluorescence staining (ANNA-1) in the myenteric plexus of ileal segments on day 7 post infection with *spiB* of adrenalectomized or sham-operated C57BL/6J mice. Mice were infected on day 9 post-surgery. Data are representative of at least n=7 per condition. At least 2 independent experiments were performed. Data were analyzed by unpaired t-test and represented as mean ± s.d.; *** $P \leq 0.001$.

We previously demonstrated that *spiB* infection led to a significant increase in the number of recently activated, cFos+ sympathetic neurons in the celiac-superior mesenteric ganglion (CG-SMG) (Gabanyi & Muller et al., 2016). We thus assessed whether stimulation of these neurons is sufficient to drive MM-β_2-AR-mediated tissue protection. We utilized two chemogenetic mouse models, in which administration of the synthetic ligand, Compound 21, to mice carrying an inactivating DREADD driven by promoters active in sensory nodose ganglia neurons (SNS^{hM4Di} or $Phox2b^{hM4Di}$) results in a significant increase in cFos expression by gut-projecting sympathetic neurons (Muller et al., 2019b). We found that DREADD-induced activation of gut-projecting neurons prior to *spiB* infection both in SNS^{hM4Di} and $Phox2b^{hM4Di}$ mice significantly rescued iEAN loss

(Figure 4.24a,b and Appendix). These results further support a role for locally–released catecholamines and β2-AR signaling in MM in the limiting of inflammation–induced iEAN loss.

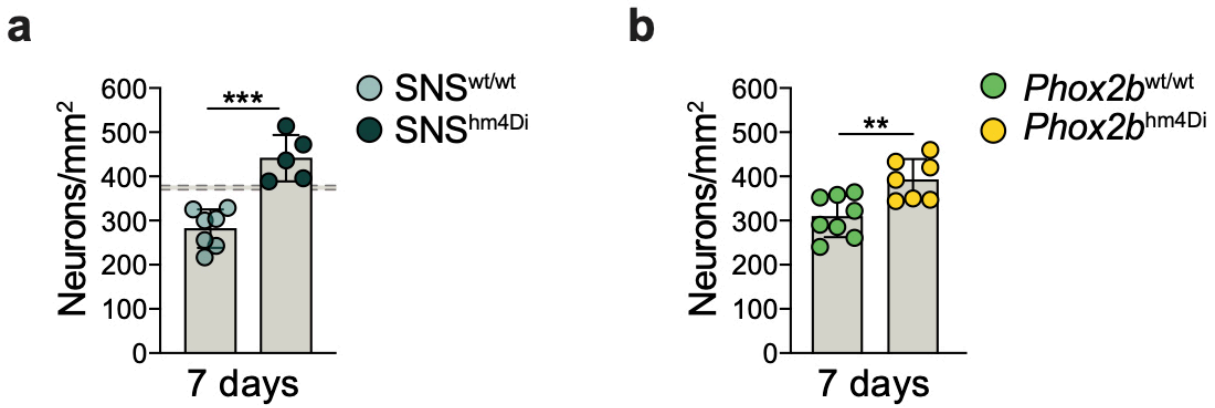

Figure 4.24. Chemogenetic activation of gut-sympathetic neurons rescues iEAN loss post-*spiB* infection. (**a**, **b**) Mice were orally infected with 10^9 CFU of *Salmonella spiB*. Neuronal quantification as assessed by immunofluorescence staining (ANNA-1) in the myenteric plexus of ileal segments on day 7 post infection with *spiB*. (**a**) SNS^{hM4Di} or (**b**) $Phox2b^{hM4D}$ mice were treated with 10mg/kg Compound 21 (C21) 24 hours before oral gavage with *spiB*. Data are representative of at least n=5 per condition. At least 2 independent experiments were performed. Data were analyzed by unpaired t-test and represented as mean ± s.d.; ** $P \leq 0.01$, *** $P \leq 0.001$.

4.7 An adrenergic-arginase-polyamine axis in MM limits infection–induced neuronal loss

To dissect possible mechanisms by which MM β_2-AR signaling is involved in preventing excessive tissue damage post–infection, we analyzed $LysM^{\Delta Adrb2}$ MM gene expression profiles. MM sorted from Cre^- littermate controls responded to *spiB* infection by upregulating tissue protective genes upon infection, but we did not observe this upregulation in MM sorted from infected $LysM^{\Delta Adrb2}$ mice (Figure 4.25a,b). Arginase 1 is known

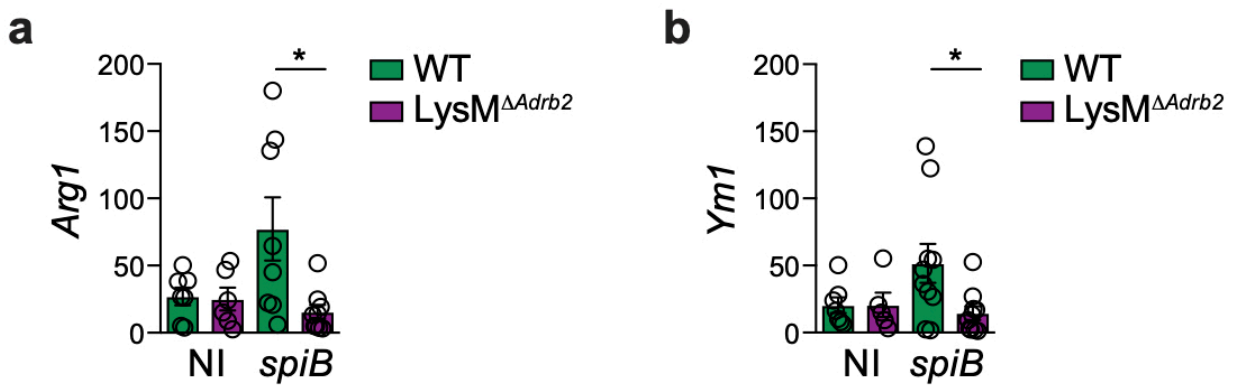

Figure 4.25. Loss of tissue protective gene changes in infected conditional LysM$^{\Delta Adrb2}$ mice. (**a**, **b**) mRNA expression analysis of (**a**) *Arg1* and (**b**) *Ym1* by quantitative real-time PCR in LysM$^{\Delta Adrb2}$ and wild-type (WT) littermate control mice non-infected (NI) or 2 hours post infection with 10^9 CFU of *Salmonella spiB*. Data are representative of at least n=5 per condition. At least 2 independent experiments were performed. Data were analyzed by unpaired t-test and represented as mean ± s.d.; * $P \leq 0.05$.

to mediate the production of neuroprotective polyamines such as spermine (Cai et al., 2002), which in turn were described to suppress NLRP6–caspase1/11 inflammasome activation (Levy et al., 2015). To investigate the participation of polyamines in iEAN cell death, we supplemented the drinking water of mice infected with *spiB* with spermine or with difluoromethylornithine (DFMO), which inhibits polyamine biosynthesis by selective and irreversible inhibition of ornithine decarboxylase 1 (ODC1) (Koomoa et al., 2013). Bacterial load and clearance patterns were similar in either treatment condition; however, mice that received DFMO exhibited enhanced neuronal loss, while those exposed to spermine showed a significant rescue of neuronal loss post *spiB* infection (Figure 4.26a,b and Appendix). Finally, we genetically addressed whether Arginase 1 activity in MM was required for their protective role in infection–induced neuronal damage in the intestine by

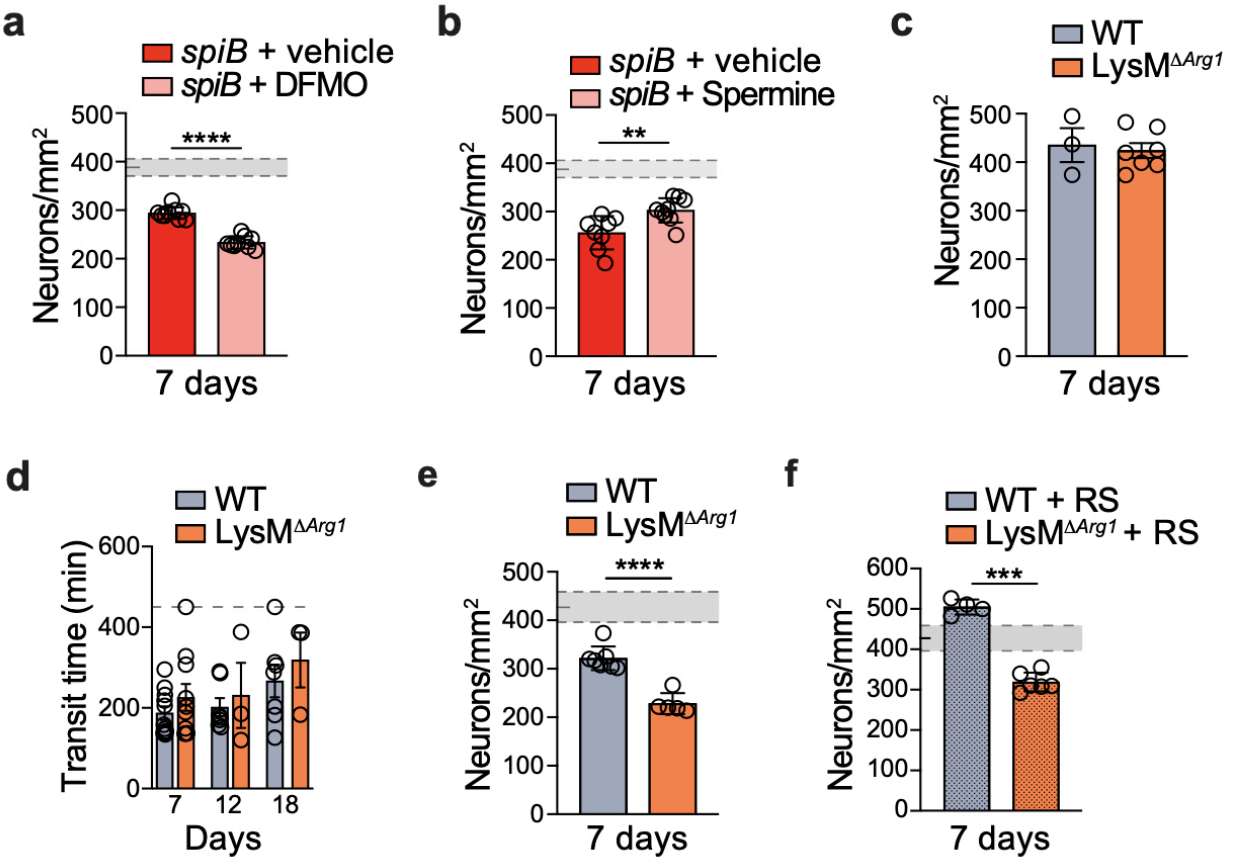

Figure 4.26. MM Arginase 1 and polyamines are important for iEAN protection post-*spiB* infection. (**a**, **b**) Neuronal quantification as assessed by immunofluorescence staining (ANNA-1) in the myenteric plexus of ileal segments on day 7 post infection with *spiB* of (**a**) C57BL/6J mice with access to regular drinking water or water supplemented with difluoromethylornithine (DFMO) over the course of infection starting 5 days prior to infection; shaded area bounded by dashed lines indicates mean day 7 iEAN numbers ± SEM of all control C57BL6/J mice; (**b**) C57BL/6J mice receiving regular drinking water or water supplemented with Spermine over the course of infection starting 3 days prior to infection; shaded area bounded by dashed lines indicates mean day 7 iEAN numbers ± SEM of all control C57BL6/J mice. (**c**) Neuronal quantification as assessed by immunofluorescence staining (ANNA-1) in the ileum myenteric plexus of naïve LysM$^{\Delta Arg1}$ and wild-type (WT) littermate control mice 7 days post–streptomycin treatment (no infection). (**d**) Gastrointestinal motility activity as assessed by total gastrointestinal transit time at the indicated time points of LysM$^{\Delta Arg1}$ and wild-type (WT) littermate control mice orally infected with 10^9 CFU of *spiB*. Experiments were ended at 450 min (dashed line). (**e**, **f**) Neuronal quantification as assessed by immunofluorescence staining (ANNA-1) in the myenteric plexus of ileal segments on day 7 post infection with *spiB* of (**e**) LysM$^{\Delta Arg1}$ mice and wild-type (WT) littermate controls and (**f**) LysM$^{\Delta Arg1}$ mice and wild-type (WT) littermate controls undergoing 15 min of restraint stress 12 hours prior to infection. Shaded area bounded by dashed lines indicates mean day 7 iEAN numbers +/- SEM of non-infected LysM$^{\Delta Arg1}$ and WT littermate control mice (**c**). Data are representative of 3-6 mice per condition. At least 2 independent experiments were performed. Data were analyzed by unpaired t-test and represented as mean ± s.d.; ** $P \leq 0.01$, *** $P \leq 0.001$, *** $P \leq 0.0001$.

interbreeding LysM^{Cre} and *Arg1*$^{flox/flox}$ mice (El Kasmi et al., 2008). Similar to LysM$^{\Delta Adrb2}$, we did not observe differences in iEAN numbers in LysM$^{\Delta Arg1}$ mice as compared to Cre- littermate control mice during homeostasis (Figure 4.26c). Upon *spiB* infection, LysM$^{\Delta Arg1}$ also showed similar pathogen load and clearance patterns, but a trend to increased GITT (Figure 4.26d and Appendix). However, loss of Arginase 1 in the myeloid compartment heightened iEAN loss following *spiB* infection (Figure 4.26e). Finally, restraint stress did not confer iEAN protection in LysM$^{\Delta Arg1}$ mice, while Cre- animals had no iEAN post-*spiB* infection (Figure 4.26f). Together, these results point to a functional role for β2-AR-Arginase 1-polyamines axis in MM-mediated tissue protective programs capable of limiting infection-induced enteric neuronal cell death.

4.8 Conclusions

We investigated how infection-induced inflammation affects intrinsic EAN (iEAN) and the role of intestinal *muscularis* macrophages (MM) in this process. By utilizing imaging, cell sorting–independent transcriptomics, pharmacological and genetic gain– and loss–of-function approaches, surgical lesioning, and chemogenetic manipulations, we report that murine enteric infection results in a rapid and persistent loss of intrinsic enteric-associated neurons (iEAN), which is associated with long–term gastrointestinal changes including intestinal dysmotility. Secondary infections with the same, or heterologous pathogens resulted in no further iEAN loss, while microbial restoration post infection resulted in iEAN recovery. Confocal imaging strategies revealed a subtype–specific neuronal loss, and transcriptomics and genetic approaches uncovered an iEAN

cell death mechanism that is dependent on the NLRP6 inflammasome and its downstream effector caspase 11. Depletion of MM, located in close proximity to enteric neurons, resulted in enhanced infection-induced neuronal loss, suggesting a functional role for a MM tissue protective program induced upon infection. Myeloid–specific targeting of β_2-AR, as well as arginase 1 (Arg1), coupled with pharmacological rescue experiments and chemogenetic modulation of gut–sympathetic neurons implicated MM-adrenergic signaling in post-infectious enteric neuronal protection via the production of polyamines. Our data uncovered a novel mechanism of enteric neuronal cell death or maintenance and identify a functional role for neuron–macrophage interactions in limiting infection-induced neuronal damage.

Chapter 5: Microbiota–modulated enteric neuron translational profiling uncovers a CART+ glucoregulatory subset

5.1 iEAN translational programs are set by regions in the small and large intestine.

To profile iEAN, we opted for a translating ribosomal affinity purification (TRAP) approach; cell type–specific mRNA profiling that gives information on what is being actively translated within the cell and bypasses the need for tissue fixation or single–cell suspension, avoiding possible confounding effects of neuronal dissociation on gene expression. We interbred pan–neuronal *Snap25*^{Cre} (Harris et al., 2014) with *Rpl22*$^{lsl\text{-}HA}$ (RiboTag) (Sanz et al., 2009) mice, which express a hemagglutinin (HA)–tagged ribosomal subunit 22, allowing immunoprecipitation of actively–translated mRNA. Expression of HA–tagged ribosomes was observed in neurons in the myenteric plexus of the duodenum, ileum, and colon of *Snap25*^{RiboTag} mice (Figure 5.1a). We confirmed successful immunoprecipitation (IP) of intact mRNA bound to HA-tagged ribosomes from myenteric neurons in the intestine muscularis. RNA sequencing of bound transcripts revealed significant enrichment of neuronal-specific genes and pathways in *Cre*+ animals when compared to *Cre*- controls (Figure 5.1b-d). The TRAP system allowed the identification of novel enteric neuron markers such as CD9, which was confirmed to be highly expressed in EAN cell bodies and fibers in the myenteric plexus, but not present in other cell types such as enteric glia (Figure 5.1e,f). TRAP RNA-seq (TRAP-seq) analysis of iEAN and extrinsic EAN (nodose, NG; celiac–superior mesenteric, CG-SMG; and

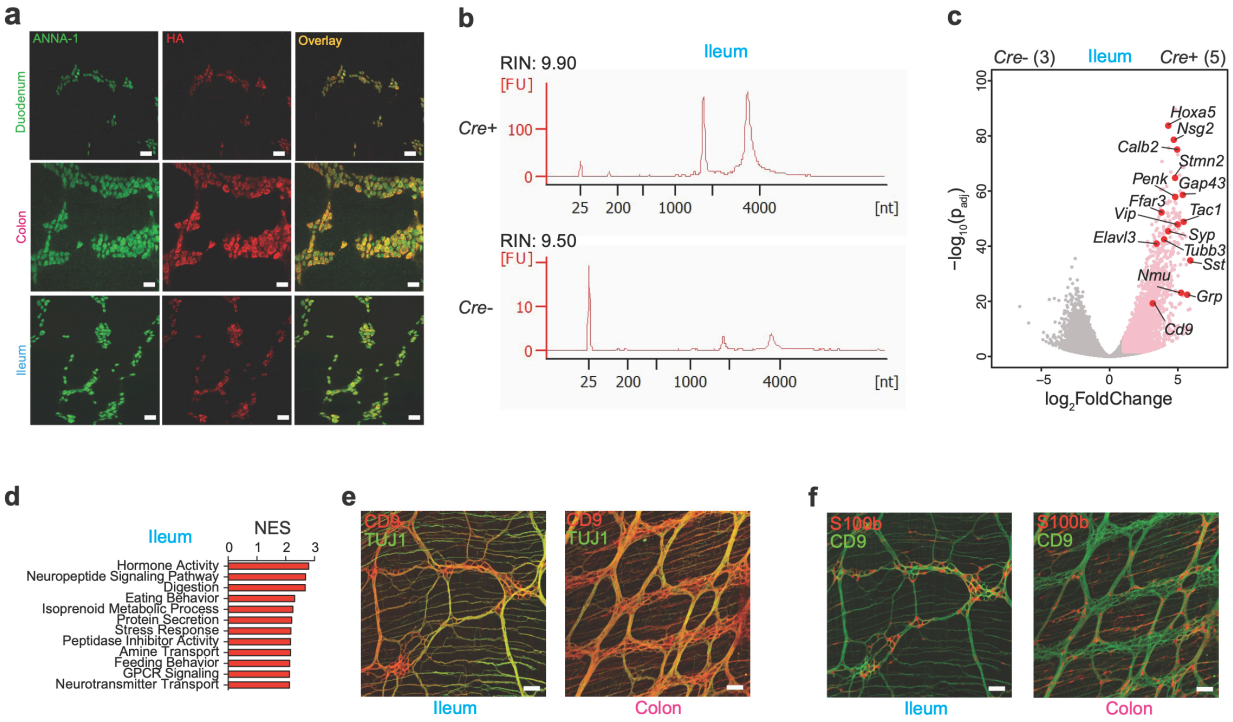

Figure 5.1. Specificity of pan neuronal RiboTag in the gut. (**a**) Representative whole-mount immunofluorescence (IF) image of myenteric plexus neurons from the duodenum, ileum, and colon of *Snap25*^{RiboTag} SPF mice using anti-hemagglutinin (HA) and anti-neuronal nuclear (ANNA-1) antibodies. Scale bars = 50 µm. Images representative of at least n=3. (**b**) Bioanalyzer traces of immunoprecipitated (IP) ribosome-bound mRNA eluted from the ileum muscularis of *Snap25*^{RiboTag} Cre+ and Cre- SPF mice. (**c**) Volcano plot of differentially expressed genes from (**b**). Pink dots highlight those transcripts with a $log_2FC > 1$ and p_{adj}-value <0.05. Red dots and black labels highlight selected IP-enriched genes. Number of samples shown in parentheses. (**d**) Graph of the top 12 gene ontology pathways with a FDR < 25% identified by Gene Set Enrichment Analysis (GSEA) from ileum IP-enriched genes ($log_2FC > 1$, $p_{adj} < 0.05$). NES, normalized enrichment score; FDR, false detection rate. (**e**, **f**) Representative whole-mount immunofluorescence image of the ileum and colon myenteric plexus of C57BL/6J SPF mice stained with anti-CD9 (red) and anti-neuronal-specific TUJ1 (green) (**e**), or anti-CD9 (green) and anti-glia-specific S100b (red) (**f**). Scale bars = 50 µm. Images representative of n = 3.

dorsal root ganglion, DRG) (Muller et al., 2019b) suggested that iEAN possess a distinct translational profile (Figure 5.2a,b). iEAN expressed more neuropeptide transcripts compared to sensory and sympathetic ganglia, which had increased expression of genes involved in nociception and catecholamine production, respectively (Figure 5.2c-f).

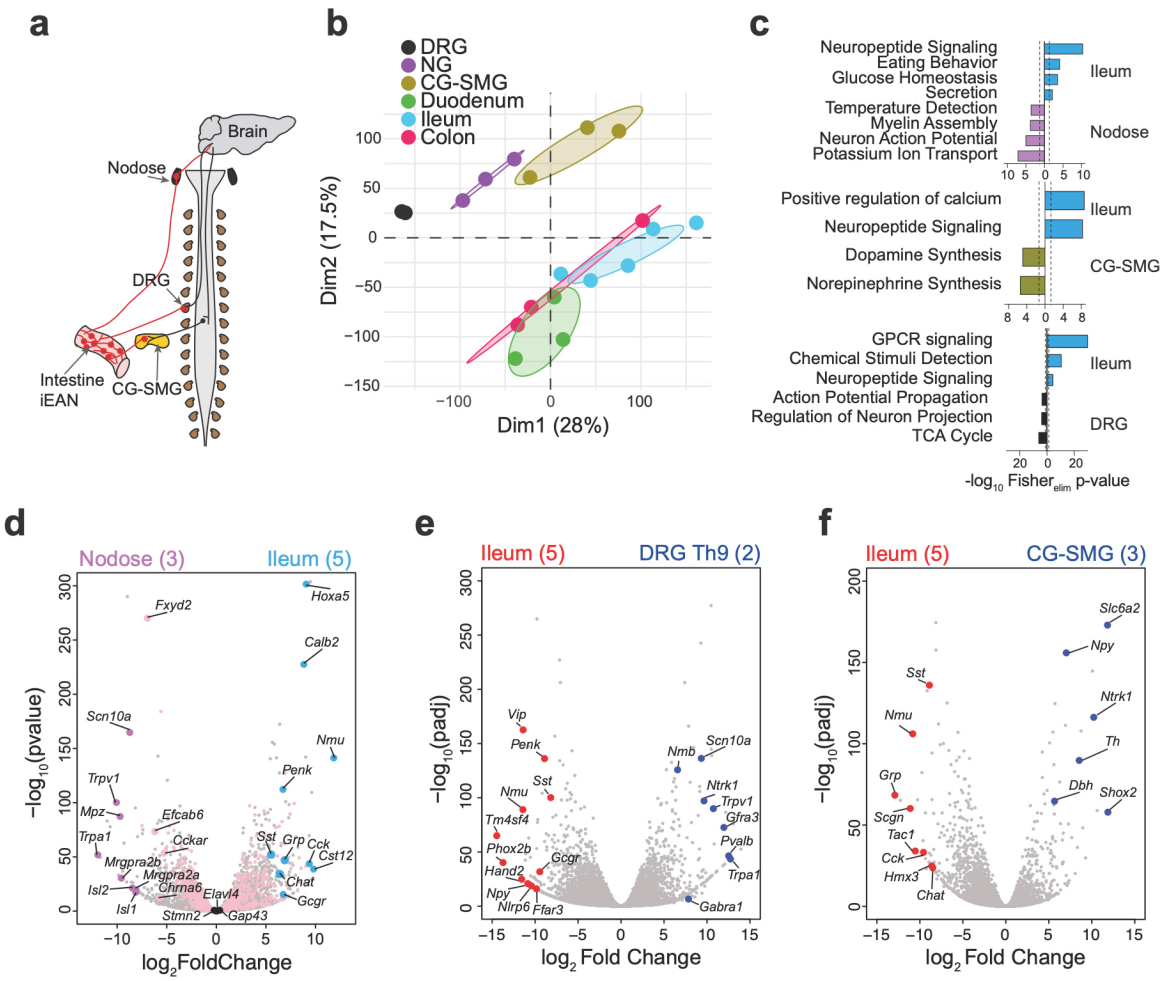

Figure 5.2. iEAN represent a translationally distinct population of peripheral neurons. (**a**) Anatomical diagram of intrinsic and extrinsic EAN. Red lines highlight relevant ganglia and fibers. DRG = dorsal root ganglion, CG-SMG = celiac-superior mesenteric ganglion. (**b**) Principal Component Analysis of translatomes from nodose ganglion, celiac-superior mesenteric ganglion (CG-SMG), dorsal root ganglion (DRG), duodenum, ileum, and colon EAN of C57BL/6J SPF mice. (**c**) Gene ontology pathways from TopGO analysis of differentially expressed genes ($log_2FC > 1$, $p_{adj} < 0.05$), enriched in the ileum (blue) vs nodose ganglion (purple), CG-SMG (gold), and DRG (black). Dashed lines represent threshold of significance (1.3), calculated by Fisher's test with an elimination algorithm. (**d-f**) Volcano plot of differentially expressed genes from the nodose ganglion (**d**), DRG Th9 (**e**), CG-SMG (**f**) and ileum myenteric iEAN of *Snap25*^{RiboTag} SPF mice. Grey dots highlight all genes analyzed by differential expression analysis. In (**d**) pink dots highlight all IP-enriched genes from the ileum. Purple and blue dots highlight differentially expressed genes from nodose ganglion and ileum, respectively. Enlarged pink dots represent ileum IP-enriched transcripts expressed at higher levels than nodose. Black dots highlight neuronal genes that do not significantly differ between samples. In (**e**), enlarged red dots highlight genes enriched in the ileum. Enlarged blue dots highlight genes enriched in DRG. In (**f**), enlarged red dots highlight genes enriched in the ileum. Enlarged blue dots highlight genes enriched in CG-SMG. Sample numbers are indicated in parentheses at top.

Comparison between translational profiles of myenteric neurons isolated from the duodenum, ileum, and colon indicated that iEANs segregate based on their anatomical location (Figure 5.3a). Compartmentalized translational profiles of myenteric neurons are

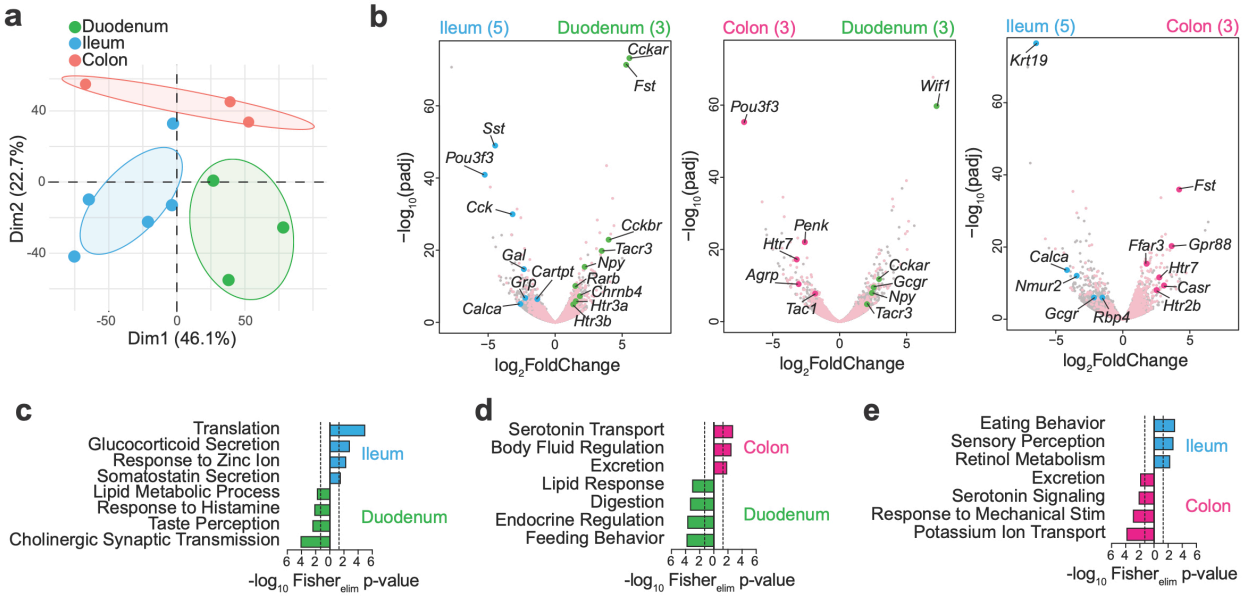

Figure 5.3. The translational profile of iEAN changes along the length of the intestine. (**a**) Principal Component Analysis of translatomes from the duodenum, ileum, and colon EAN of C57BL/6J SPF mice. Immunoprecipitated (IP) transcripts from myenteric iEAN ($log_2FC > 1$, $p_{adj} < 0.05$) were used to generate the list of genes for comparison between all groups. (**b**) Volcano plots of differentially expressed genes between myenteric iEAN populations in the duodenum, ileum and colon. Grey dots highlight all genes analyzed by differential expression analysis. Pink dots highlight all IP-enriched genes from each pair of iEAN. Green, blue, and magenta dots represent differentially expressed genes between duodenum, ileum, and colon, respectively. Sample numbers are indicated in parentheses. (**c**) Gene ontology pathways, identified by TopGO analysis of differentially expressed genes ($log_2FC > 1$, $p_{adj} < 0.05$), enriched in the ileum (blue) vs duodenum (green). Dashed lines represent threshold of significance (1.3) as calculated by Fisher's test with an elimination algorithm. (**d**) Gene ontology pathways, identified by TopGO analysis of differentially expressed genes ($log_2FC > 1$, $p_{adj} < 0.05$), enriched in the colon (magenta) vs duodenum (green). Dashed lines represent threshold of significance (1.3) as calculated by Fisher's test with an elimination algorithm. (**e**) Gene ontology pathways, identified by TopGO analysis of differentially expressed genes ($log_2FC > 1$, $p_{adj} < 0.05$), enriched in the ileum (blue) vs colon (magneta). Dashed lines represent threshold of significance (1.3) as calculated by Fisher's test with an elimination algorithm.

consistent with the anatomically distinct functions of the corresponding segments of the intestine. The proximal small intestine is highly absorptive, enriched with enteroendocrine cell (EEC) subsets associated with lipid and nutrient detection (Gribble and Reimann, 2016). We found that duodenal iEAN, in comparison those of the ileum and colon, express significantly higher levels of transcripts encoding receptors involved in the response to proximal EEC–derived signals such as *Cckar*, *Gcgr*, and *Tacr3*, likely reflecting the duodenum's predominant role in nutrient absorption (Figure 5.3b,d). The terminal ileum and colon iEAN, in contrast, are enriched in neuropeptide transcripts, such as *Sst*, *Cartpt, Penk*, *Grp,* and *Tac1,* which are thought to be involved in the control of secretomotor processes in the gut (Figure 5.3b,e,f). We also found enrichment of the transcription factor *Pou3f3* in the ileum and colon, suggesting a unique gene program in the distal intestine (Figure 5.3b). Immunofluorescence (IF) analysis confirmed a region-specific compartmentalization at the protein level, reflecting regional differences in neuronal number along the intestine (Figure 5.4a,b). For instance, the neuropeptide somatostatin (SST), involved in the regulation of several GI hormones and smooth muscle contraction (Grider, 2003), is highly expressed in the ileum and colon but scarcely expressed by duodenum EAN (Figure 5.5a,b); neuropeptide Y (NPY), typically involved in the regulation of food intake, was enriched in duodenum EAN (Figure 5.6a,b). We also observed increased numbers of cocaine and amphetamine related transcript (CART) neurons, important for metabolic regulation (Hill et al., 2010; Lau and Herzog, 2014), in the distal intestine (Figure 5.7a,b). Finally, we found that the duodenum is particularly enriched in

transcripts such as *Fst1* (encoding follistatin 1) and *Wif1* (encoding WNT inhibitory factor 1) as compared to the ileum and colon, suggesting that these neurons may play a role in the regulation of cell proliferation within this region of the intestine (Dohi et al., 2005; Koyama et al., 2015; Zhang et al., 2009). Immunofluorescence analysis of follistatin confirmed prominent FST1+ neurons and nerve fibers in the duodenum that were absent in the ileum and sparse within the colon (Figure 5.8a,b). These data reveal that the environment of different intestinal regions program a distinct gene profile on iEAN.

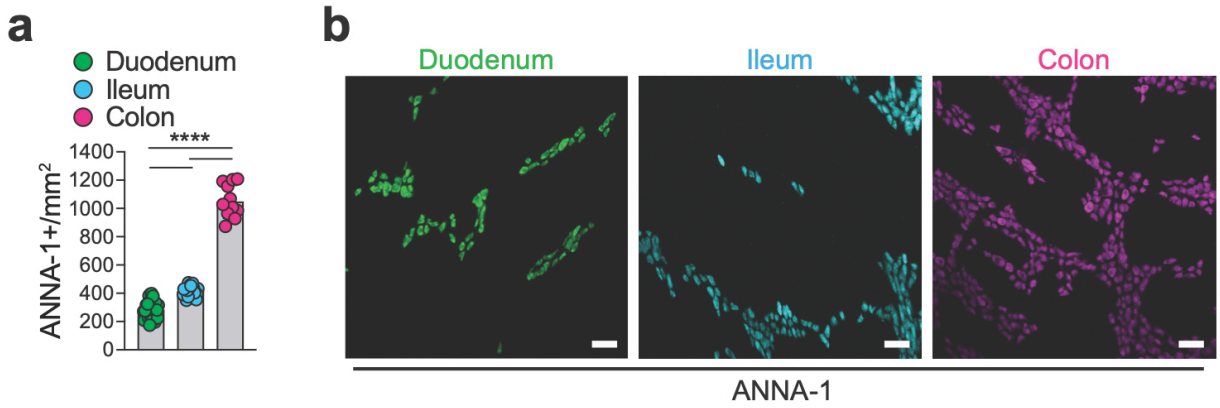

Figure 5.4. iEAN density along the intestine. (**a**) Number of myenteric plexus iEAN per mm^2 in the duodenum, ileum, and colon of C57BL/6J SPF mice. **** $P < 0.0001$ as calculated by unpaired t-test. Data represented as mean ± s.d. (**b**) Representative whole-mount immunofluorescence (IF) images of myenteric iEAN (stained with anti-ANNA-1) in the duodenum, ileum, and colon. Scale bars = 50 μm.

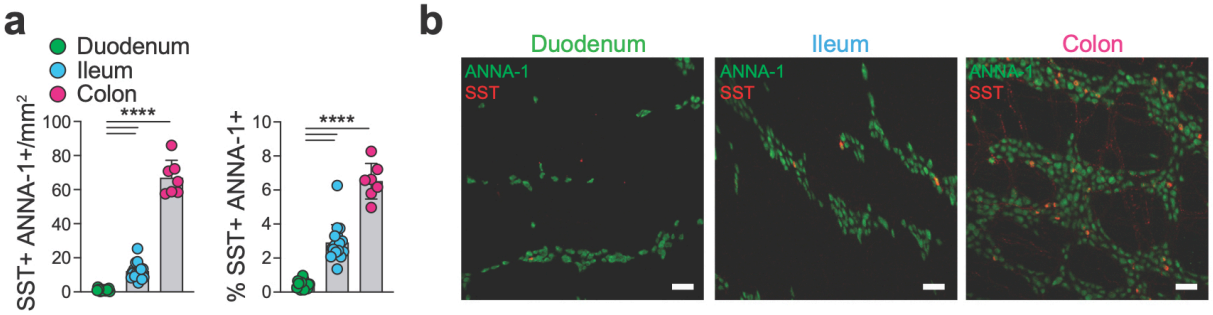

Figure 5.5. Regional differences in SST+ iEAN. (**a**) Number and percentage of somatostatin (SST)+ myenteric plexus iEAN per mm^2 in the duodenum, ileum, and colon of C57BL/6J SPF mice. **** $P < 0.0001$ as calculated by unpaired t-test. Data represented as mean ± s.d. (**b**) Representative whole-mount IF images of SST+ (red) myenteric iEAN in the duodenum, ileum, and colon. Scale bars = 50 μm.

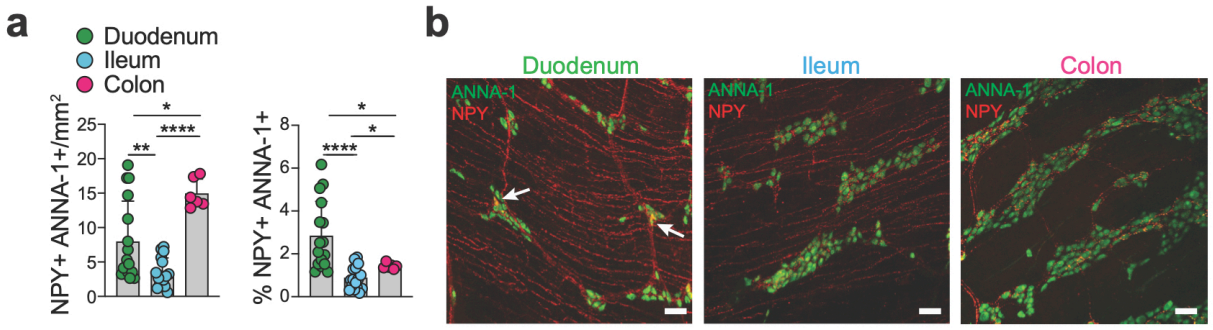

Figure 5.6. Regional differences in NPY+ iEAN. (**a**) Number and percentage of neuropeptide Y (NPY)+ myenteric plexus iEAN per mm^2 in the duodenum, ileum, and colon of C57BL/6J SPF mice. * $P < 0.05$, ** $P < 0.01$, **** $P < 0.0001$ as calculated by unpaired t-test. Data represented as mean ± s.d. (**b**) Representative whole-mount IF images of NPY+ (red) myenteric iEAN in the duodenum, ileum, and colon. Scale bars = 50 μm.

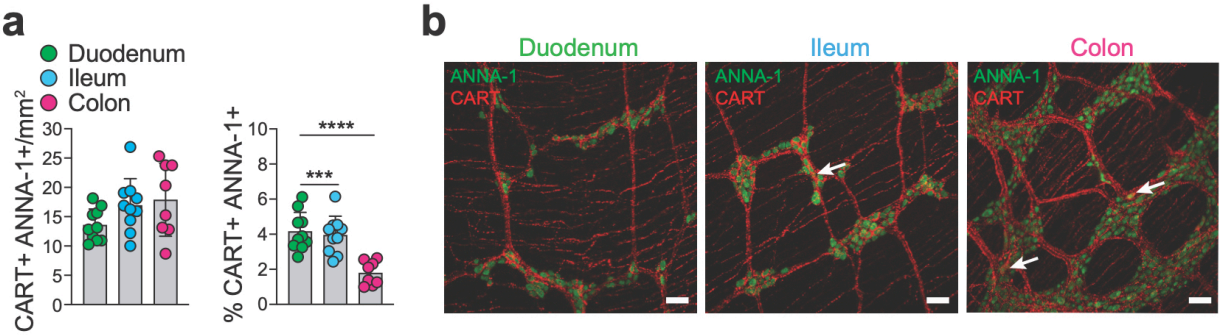

Figure 5.7. Regional differences in CART+ iEAN. (**a**) Number and percentage of CART+ myenteric plexus iEAN per mm^2 in the duodenum, ileum, and colon of C57BL/6J SPF mice. *** $P < 0.001$, **** $P < 0.0001$ as calculated by unpaired t-test. Data represented as mean ± s.d. (**b**) Representative whole-mount IF images of CART+ (red) myenteric iEAN in the duodenum, ileum, and colon. Scale bars = 50 μm.

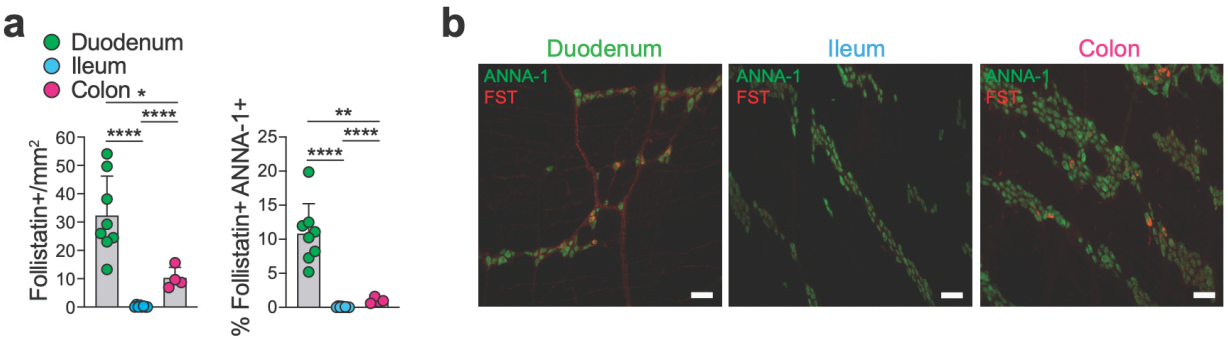

Figure 5.8. Regional differences in FST+ iEAN. (**a**) Number and percentage of follistatin+ myenteric plexus iEAN per mm^2 in the duodenum, ileum, and colon of C57BL/6J SPF mice. * $P < 0.05$, ** $P < 0.01$, **** $P < 0.0001$ as calculated by unpaired t-test. Data represented as mean ± s.d. (**b**) Representative whole-mount IF images of follistatin+ (red) myenteric iEAN in the duodenum, ileum, and colon. Scale bars = 50 μm.

5.2 Distal gut iEAN are impacted by the absence of a microbiota from birth

Because the density and diversity of the gut microbiota increases from the proximal to distal intestine (Martinez-Guryn et al., 2019), we examined whether regionally distinct iEAN translational programs are partially influenced by the microbiota. To address the influence of microbial stimuli on EAN, we first performed AdipoClear (Chi et al., 2018) on whole-mount intestinal tissue followed by light-sheet microscopy to visualize the three-dimensional structure of EAN in the ileum and colon of germ–free (GF) or specific–pathogen free (SPF) mice. The overall organization of iEAN into the two distinct plexuses

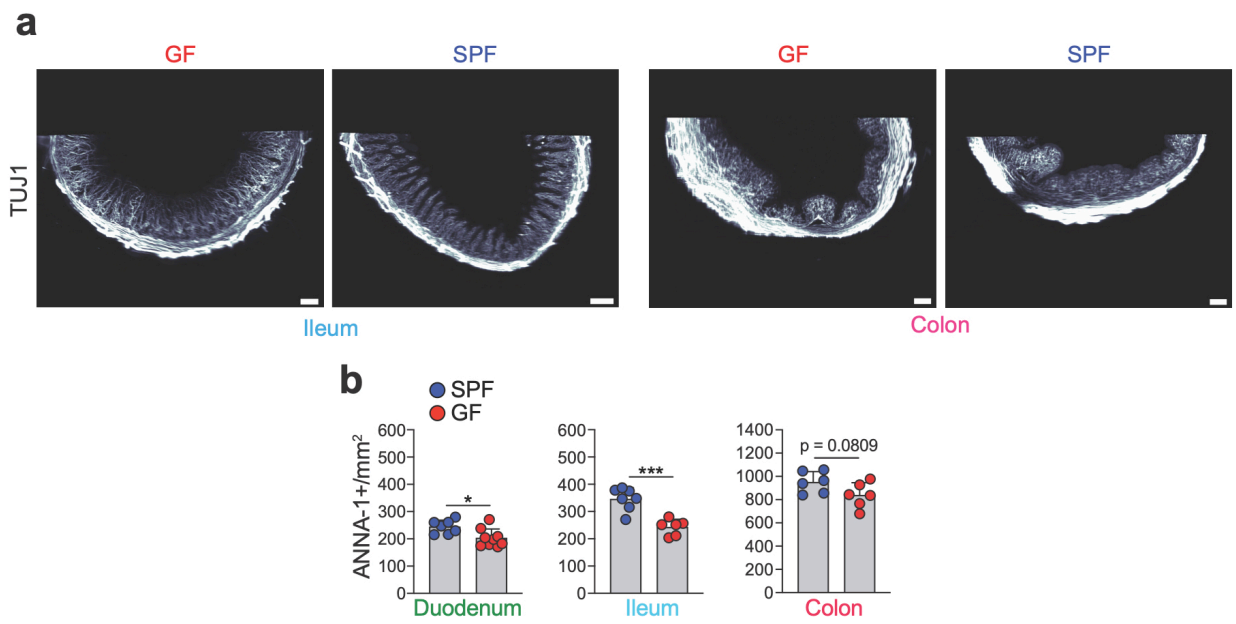

Figure 5.9. Neuronal architecture and iEAN numbers in GF or SPF intestine. (**a**) Light-sheet images of the ileum and colon of AdipoClear-based cleared tissue of C57BL/6J SPF or GF mice stained with anti-β-III-tubulin (TUJ1) antibodies. Images representative of n=5 for all groups. Scale bar GF ileum = 200 μm, SPF ileum = 200 μm, GF colon = 200 μm, SPF colon = 100 μm. (**b**) Number of myenteric iEAN in the duodenum, ileum, and colon of C57BL6/J GF and SPF mice kept on a GF diet. * $P < 0.05$, *** $P < 0.001$ calculated by unpaired t-test. Data represented as mean ± s.d.

appeared unaltered between GF and SPF (Figure 5.9a). We observed vast mucosal innervation in the small and large intestines of both GF and SPF mice reaching into individual villi with fibers adjacent to the epithelium (Figure 5.9a). Analysis of the ileum indicated significant remodeling of nerve fibers reflecting the thin, blunted villi of GF animals (Esterházy et al., 2019; Kennedy et al., 2018; Kernbauer et al., 2014), while colonic innervation did not show gross alterations between mice kept under GF and SPF conditions (Figure 5.9a). However, quantification of iEAN in the myenteric plexus revealed a significant reduction in the duodenum and ileum of GF mice, while in the colon GF and SPF mice displayed similar numbers (Figure 5.9b). To determine whether the microbiota

impacts iEAN gene profile along the intestine, we re-derived *Snap25*^{RiboTag} mice under GF conditions (Figure 5.10a). Analysis of TRAP-seq from duodenum, ileum, and colon muscularis of GF *Snap25*^{RiboTag} mice suggested a significant influence of the microbiota on the compartmentalization of iEAN phenotypes. In SPF mice, principal component analysis segregated proximal and distal intestinal regions. However, ileum, colon and duodenum samples from GF mice all clustered together with the duodenum samples of SPF mice, the region with the lowest microbial density (Figure 5.10b). Analysis of the third principal component showed segregation of colon samples from the small intestine, which may reflect the presence of iEAN derived from sacral progenitors in the large intestine (Obermayr et al., 2013) (Figure 5.10c). Analysis of GF and SPF datasets using predicting associated transcription factors from annotated affinities (PASTAA) (Roider et al., 2009) identified CREB amongst the most enriched transcription factors for the colon and ileum in SPF mice (Figure 5.10d). Because the level of pCREB in neurons is often used as a indirect measure of activation (Cohen et al., 2016), we assessed phosphorylation of CREB (pCREB) at serine 133, key to inducing gene transcription, by IF. We found a significant reduction of pCREB in the ileum myenteric plexus of GF compared to SPF mice (Figure 5.10e,f), demonstrating that iEAN may be hypoexcitable under gnotobiotic conditions, as previously proposed (McVey Neufeld et al., 2013; Yano et al., 2015).

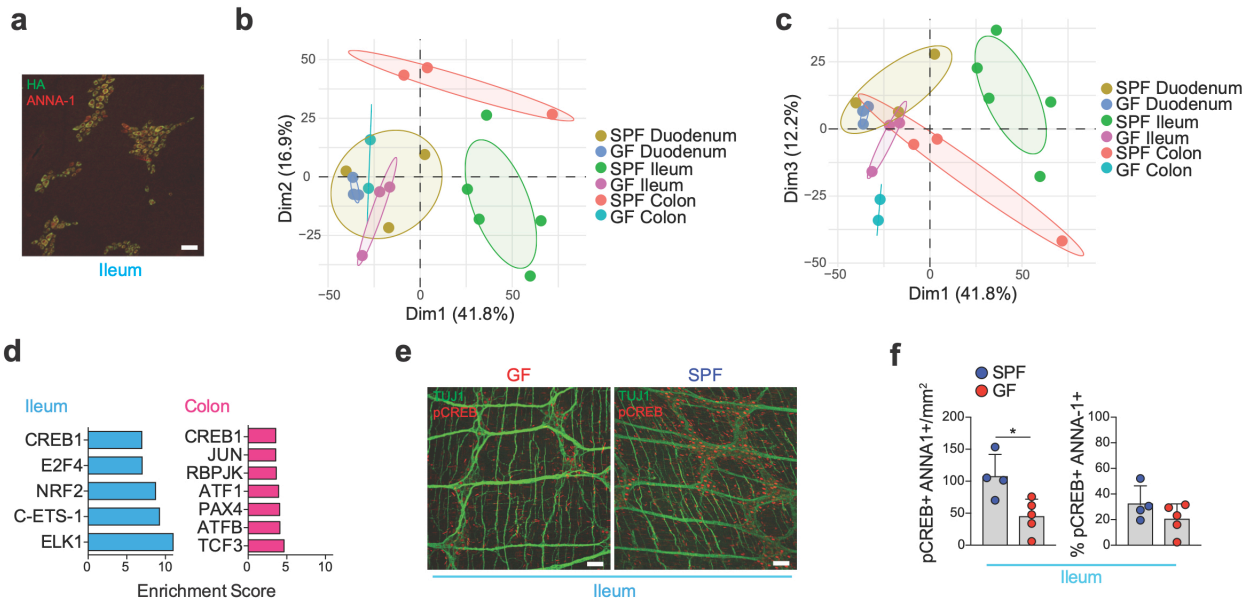

Figure 5.10. The microbiota impacts the regional gut translational profile and plasticity of iEAN. (**a**) Expression of HA in ileum myenteric neurons of *Snap25*^{RiboTag} GF mice. Scale bar = 50 μm. Image representative of duodenum and colon myenteric plexus. (**b**) Principal Component Analysis of iEAN from the duodenum, ileum, and colon of C57BL6/J SPF and GF mice. Total comparative gene list generated from IP-enriched transcripts ($log_2FC > 2.5$, $p_{adj} < 0.05$) from each sample. (**c**) Principal Component Analysis of GF and SPF iEAN from the duodenum, ileum, and colon. Total comparative gene list generated from IP enriched transcripts ($log_2FC > 2.5$, $p_{adj} < 0.05$) from each sample. (**d**) PASTAA analysis showing enrichment of predicted CREB1 transcription factor control of the most significant differentially expressed genes ($log_2FC > 1$, $p_{adj} < 0.05$) of the ileum and colon iEAN between C57BL/6J GF and SPF mice. (**e**) Immunofluorescent (IF) staining of the ileum myenteric plexus from C57BL/6J GF (left) and SPF (right) mice using anti-pCREB (red) and anti-TUJ1 (green) antibodies. Scale bars = 50 μm. (**f**) Number and percentage of pCREB+ myenteric iEAN in the ileum of GF and SPF mice. * $P < 0.05$ as calculated by unpaired t-test. Data represented as mean ± s.d.

Comparison of GF duodenum, ileum, and colon samples also indicated segregation between regions, suggesting that certain features of region-specific iEAN programming are microbiota-independent (Figure 5.11a). However, in the duodenum, only four genes were significantly upregulated in SPF compared to GF including *Nnat* and *Penk*, involved in neuronal development (Ma et al., 2019) and enkephalin production (Lay et al., 2016), respectively. In the ileum and colon, we detected 605 and 117 differentially expressed

genes upregulated, respectively, in SPF as compared to GF groups (Figure 5.11b). Among these were genes encoding neuropeptides associated with a neuro-immune

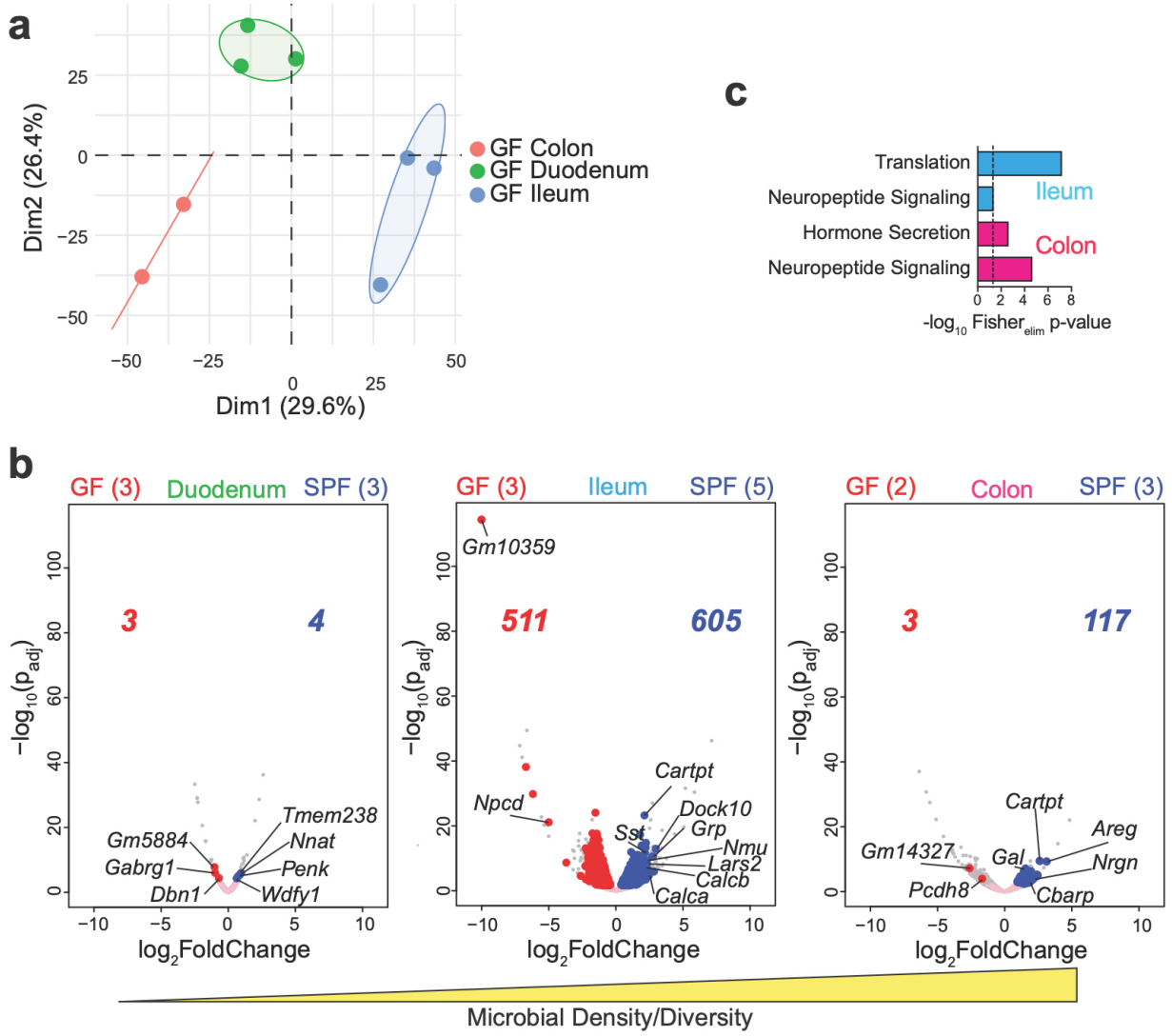

Figure 5.11. Neuropeptide pathways are downregulated in GF mice. (a) Principal Component Analysis of GF iEAN from the duodenum, ileum, and colon. Immunoprecipitated (IP) transcripts ($log_2FC > 1$, $p_{adj} < 0.05$) were used to generate the list of genes for comparison between all groups. (**b**) Volcano plots of differentially expressed genes of iEAN from the duodenum, ileum, and colon of C57BL/6J SPF and GF mice. Grey dots highlight all genes analyzed by differential expression analysis. Pink dots highlight all IP-enriched genes from each pair of compared intestine segments. Red dots and number highlight genes higher in GF samples. Blue dots and number highlight genes significantly higher in SPF samples. Sample numbers are indicated in parentheses. (**c**) Gene ontology pathways, identified by TopGO analysis, of differentially-expressed genes ($log_2FC > 1$, $p_{adj} < 0.05$), enriched in SPF ileum (blue) and colon (magenta) as compared to respective GF samples. Dashed lines represent threshold of significance (1.3) as calculated by Fisher's test with an elimination algorithm.

crosstalk and with EAN physiological function, such as *Nmu* (Cardoso et al., 2017), *Sst* (Gonkowski and Rytel, 2019), *Cartpt* (Lau and Herzog, 2014), and *Agrp* (Lanfray and Richard, 2017) (colon only) (Figure 5.11b,c). SST and CART protein expression changes were confirmed by quantification of immunofluorescence images from SPF and GF mice (Figure 5.12a-i). These results establish regional differences as well as the microbial influence on iEAN gene profiles, particularly on their neurochemical coding. To address

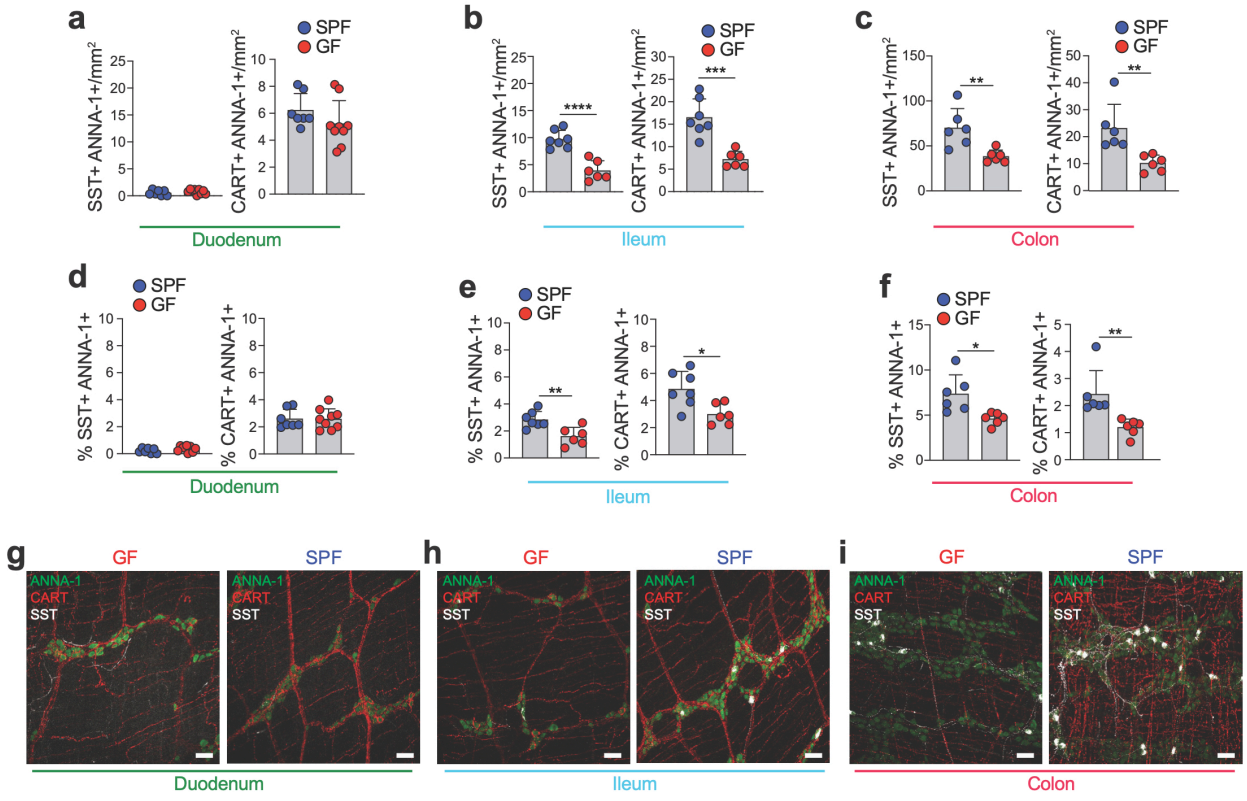

Figure 5.12. Immunofluorescence analysis confirms a reduction of neuropeptides in GF mice. (**a-c**) Number of somatostatin (SST)+ and CART+ myenteric iEAN in the duodenum (**a**), ileum (**b**), and colon (**c**) of C57BL/6J GF and SPF mice. ** $P < 0.01$, *** $P < 0.001$, *** $P < 0.0001$ as calculated by unpaired t-test. Data represented as mean ± s.d. (**d-f**) Percentage of somatostatin (SST)+ (lelft), CART+ (right) myenteric iEAN in the duodenum (**d**), ileum (**e**), and colon (**f**) of C57BL/6J GF and SPF mice. * $P < 0.05$, ** $P < 0.01$ as calculated by unpaired t-test. Data represented as mean ± s.d. (**g-i**) Whole mount IF images of somatostatin (SST)+ and CART+ myenteric iEAN in the duodenum (**g**), ileum (**h**), and colon (**i**) of GF (left) and SPF (right) mice. Scale bar = 50 μm.

whether altered neuropeptide levels in GF mice are the result of a developmental defect, we provided adult C57BL/6 GF with age- and sex- matched feces from SPF mice on a matched GF diet (exGF). Colonization of 8-week old GF animals with SPF feces was sufficient to increase the number of SST+ and CART+ neurons in the colon and ileum to levels similar to SPF animals after 2 weeks, as well as a notable increase in the density of SST+ and CART+ nerve fibers (Figure 5.13a,b,d-i). We also noted that in the ileum there was a trend towards an increase in iEAN numbers, whereas the colon remained unaffected by colonization (Figure 5.13c), an effect that could be attributed to a developmental defect or the lack of a specific bacteria in the recolonization procedures.

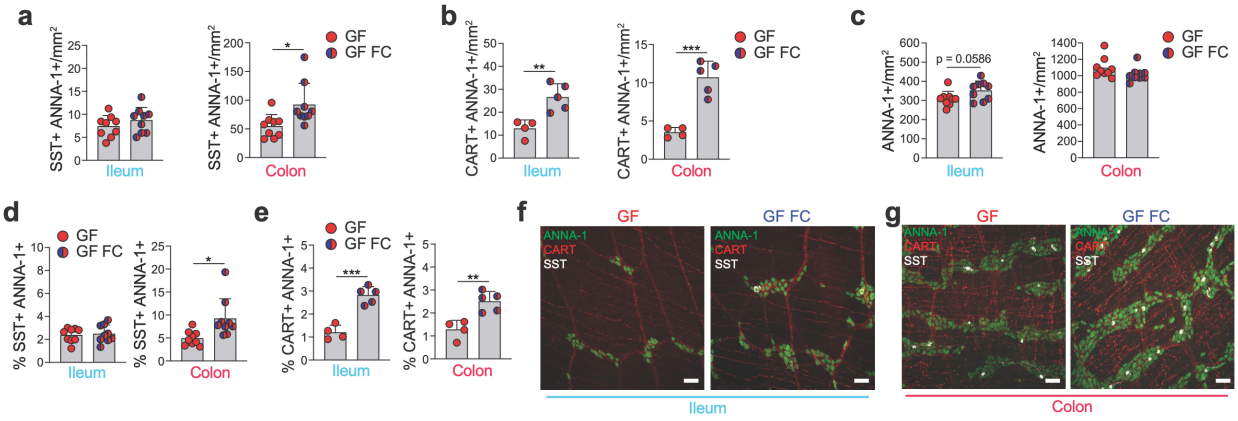

Figure 5.13. Colonization of adult GF mice increases neuropeptide levels. (**a-c**) Number of somatostatin (SST)+ (**a**), CART+ (**b**), and total (**c**) myenteric iEAN in the ileum (left) and colon (right) of GF mice and GF mice 2 weeks post colonization with microbiota of SPF mice (fecal colonization, GF FC). * $P<0.05$, ** $P<0.01$, *** $P<0.001$ as calculated by unpaired t-test. Data represented as mean ± s.d. (**d** and **e**) Percentage of somatostatin (SST)+ (**d**) and CART+ (**e**) myenteric iEAN in the ileum (left), and colon (right) of GF and SPF mice. * $P < 0.05$, ** $P < 0.01$, *** $P < 0.001$ as calculated by unpaired t-test. Data represented as mean ± s.d. (**f** and **g**) Representative whole-mount IF images of SST+ and CART+ myenteric iEAN in the ileum (**f**) and colon (**g**) of GF (left) and GF mice colonized with SPF microbiota (fecal colonization, GF FC, right). Scale bar = 50 μm.

Overall, the lack of significant changes in the microbial–sparse duodenum, along with the accumulation of significant changes in iEAN gene expression and neurochemical coding in areas with increased microbial diversity and density, suggest that iEAN regional differences are largely determined by microbiota stimulation.

5.3 Antibiotic induced microbial depletion leads to an inflammasome-dependent reduction in total and neuropeptide iEAN.

To define whether microbiota-dependent changes were reversible, or imprinted in iEAN upon initial exposure, we administered antibiotics (vancomycin, ampicillin, metronidazole, and neomycin) in the drinking water of SPF mice for 2 weeks. We detected a significant decrease in the number of iEAN in all three intestinal areas analyzed (Figure 5.14a). This neuronal reduction was not permanent, as antibiotic withdrawal for two weeks resulted in the recovery of neuronal numbers to SPF levels, similar to what we observed in GF recolonization experiments (Figure 5.14b). We recently described an inflammasome-dependent post–infection neuronal death pathway (Matheis & Muller et al., 2019). To evaluate whether iEAN loss post microbiota depletion was also dependent on Caspase 11 (Caspase 4 in humans), *Casp1Casp11* (ICE$^{-/-}$) (Kuida et al., 1995) or *Casp11*$^{-/-}$ (Wang et al., 1998) mice were exposed to Splenda or antibiotic on drinking water. Quantification of iEAN in the ileum of antibiotic–treated mice did not reveal iEAN loss in ICE or *Casp11*$^{-/-}$ mice, suggesting an additional role for Caspase 11 in the maintenance of iEAN during dysbiosis (Figure 5.14c,d). Treatment with vancomycin, ampicillin or metronidazole, but not neomycin or single-dose streptomycin, also induced a reduction in total neuronal numbers (Figure 5.14e-g). These results suggest a possible

role for specific bacteria in the physiological maintenance of iEAN. Similar to what we observed in GF mice regarding

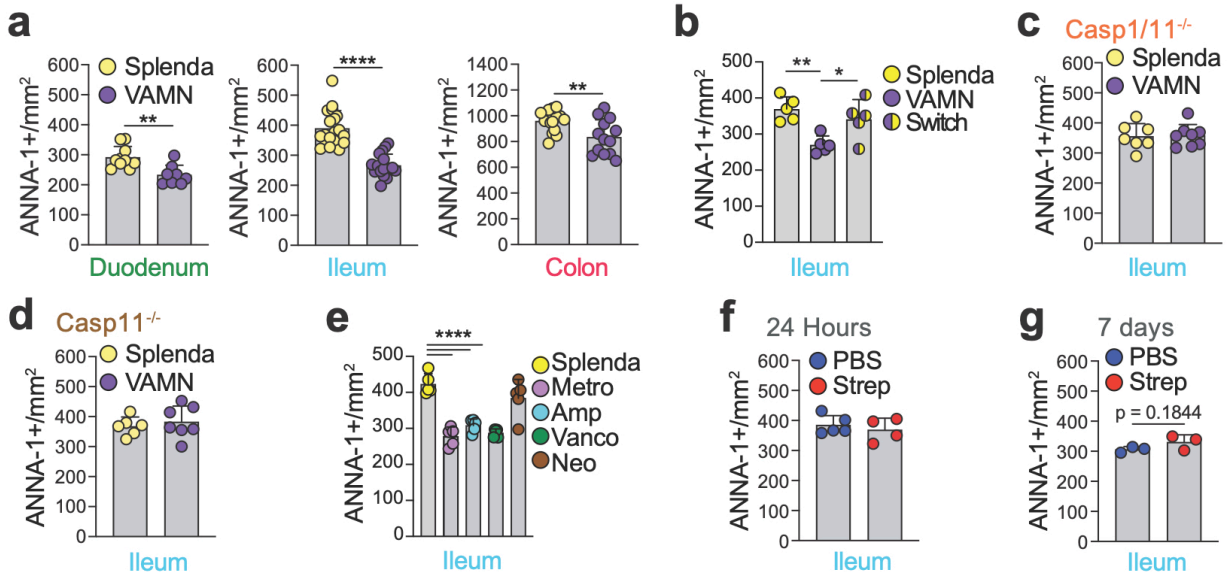

Figure 5.14. Inflammasome-dependent reduction in iEAN number upon chronic microbial depletion. (**a**) Number of myenteric iEAN in the duodenum, ileum, and colon of C57BL6/J mice treated with broad-spectrum antibiotics (vancomycin, ampicillin, metronidazole and neomycin - VAMN) administered in Splenda-supplemented drinking water or Splenda (artificial sweetener, control) in the drinking water for two weeks. ** $P < 0.01$, **** $P < 0.0001$ as calculated by unpaired t-test. (**b**) Number of myenteric iEAN in the ileum of C57BL6/J mice treated with either Splenda or VAMN in the drinking water for 4 weeks or VAMN for 2 weeks followed by Splenda for 2 weeks. * $P < 0.05$, ** $P < 0.01$, as calculated by unpaired t-test. (**c**, **d**) Number of myenteric iEAN in the ileum of *Casp1/11*$^{-/-}$ (**c**) or *Casp11*$^{-/-}$ (**d**) mice treated with either Splenda or VAMN in the drinking water for 2 weeks. (**e**) Number of myenteric iEAN in the ileum of C57BL6/J mice treated with either metronidazole, ampicillin, vancomycin, neomycin, or Splenda in the drinking water for 2 weeks. **** $P < 0.0001$ as calculated by unpaired t-test. (**f**) Number of myenteric iEAN in the ileum of C57BL6/J mice 24 hours post single oral gavage of streptomycin. (**g**) Number of myenteric iEAN in the ileum of C57BL6/J mice 7 days post single oral gavage of streptomycin. p-value calculated by unpaired t-test. (**a**-**g**) Data represented as mean ± s.d.

specific microbiota–modulated neuropeptide pathways, we observed a significant decrease in the number and overall percentage of SST+ and CART+ neurons in the ileum

and colon upon antibiotic treatment, while the duodenum remained unchanged (Figure 5.15a-g). Short-term microbiota depletion with single-dose streptomycin given to wild-

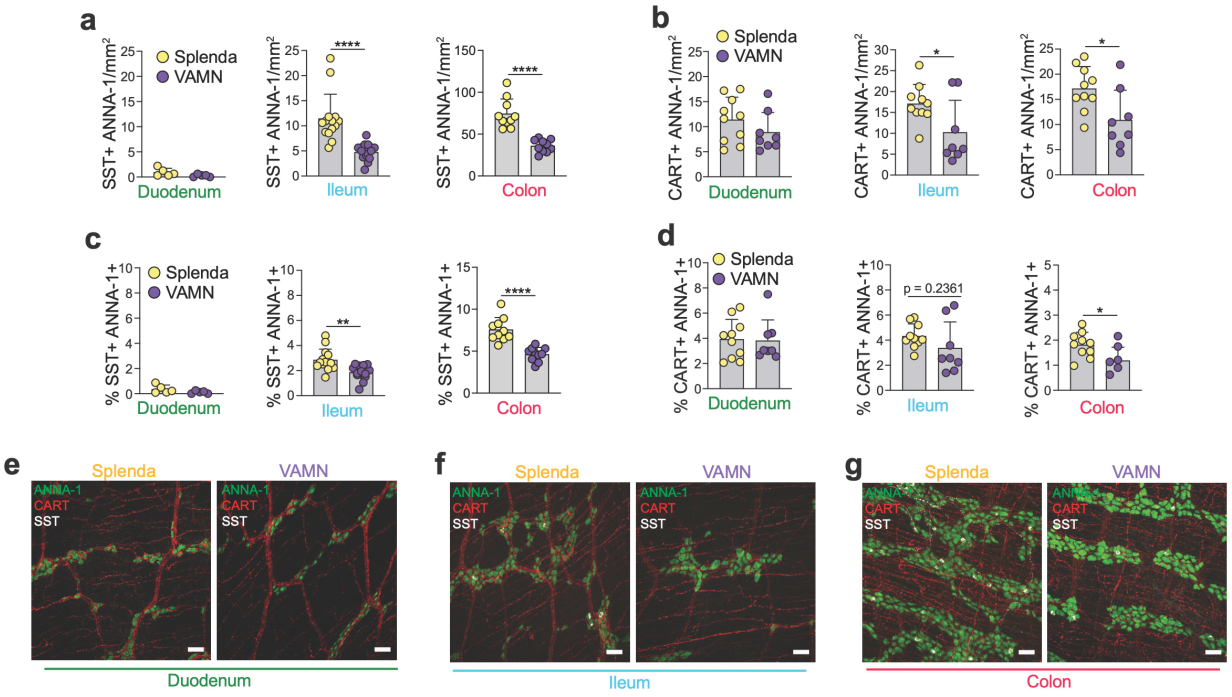

Figure 5.15. Reduction in neuropeptide+ iEAN with antibiotic treatment. (**a**) Number of somatostatin (SST)+ myenteric iEAN in the duodenum, ileum, and colon of C57BL6/J mice treated with broad-spectrum antibiotics (VAMN) or Splenda in the drinking water for two weeks. **** $P < 0.0001$ as calculated by unpaired t-test. (**b**) Numbers of CART+ myenteric iEAN in the duodenum, ileum, and colon of C57BL6/J mice treated with broad-spectrum antibiotics (VAMN) or Splenda in the drinking water for two weeks. * $P < 0.05$ as calculated by unpaired t-test. (**c-e**) Immunofluorescence whole-mount images of myenteric iEAN stained with ANNA-1 (green), CART (red), and somatostatin (SST) (white) of mice treated with Splenda (left) or broad-spectrum antibiotics (VAMN, right) for 2 weeks, in the duodenum (**c**), ileum (**d**), and colon (**e**). Scale bars = 50 μm. Images representative of at least n=5. (**a-d**) Data represented as mean ± s.d.

type mice, or continuous broad-spectrum antibiotic-treatment of *Casp1/11*$^{-/-}$ and *Casp11*$^{-/-}$ mice failed to significantly impact neuropeptide numbers in the distal intestine (Figure 5.16a-g). Together with the results obtained in GF animals, these data establish that

specific subsets of iEAN, including iEAN expressing neuropeptides SST and CART, are dependent on the microbiota for their maintenance.

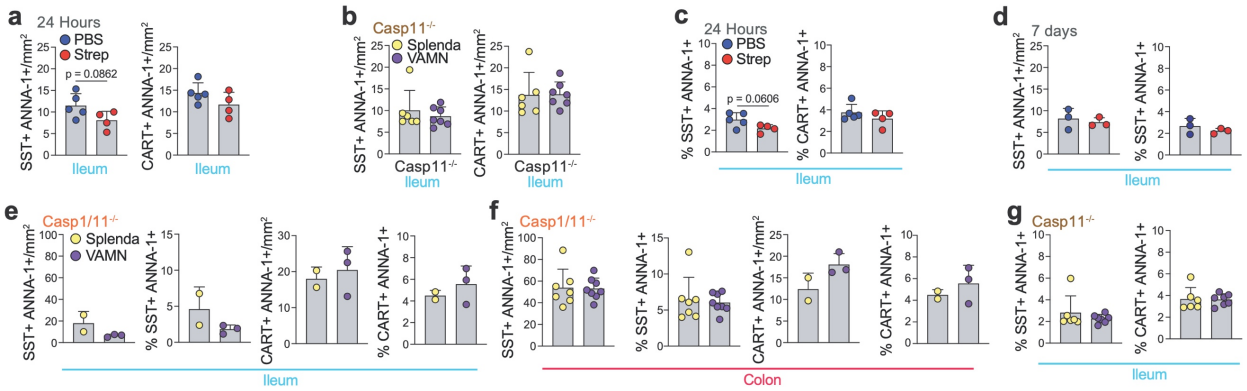

Figure 5.16. No change in neuropeptide levels with acute antibiotics or in mice lacking inflammasome machinery. (**a**) Number of somatostatin (SST)+ and CART+ myenteric iEAN in the ileum of C57BL6/J mice 24 hours post single oral gavage of streptomycin. Non-significant p-value as calculated by unpaired t-test. (**b**) Number of somatostatin (SST)+ and CART+ myenteric iEAN in the ileum of *Casp11*$^{-/-}$ mice treated with either VAMN or Splenda in the drinking water for 2 weeks. (**c** and **d**) Percentage and number of SST+ and CART+ myenteric iEAN in the ileum of C57BL6/J mice treated with one oral gavage of streptomycin and analyzed 24 hours (**c**) or 7 days (**d**) post gavage. (**e** and **f**) Number and percentage of somatostatin (SST)+ (left) and CART+ (right) myenteric iEAN in the ileum (**e**) and colon (**f**) of *Casp1/11*$^{-/-}$mice treated with Splenda or VAMN drinking water for 2 weeks. (**g**) Percentage of SST+ (left) and CART+ (right) myenteric iEAN in the ileum *Casp11*$^{-/-}$ mice treated with Splenda or broad-spectrum antibiotics (VAMN) in the drinking water for 2 weeks. (**a**-**g**) Data represented as mean ± s.d.

5.4 A subset of microbiota-influenced CART+ iEAN are viscerofugal and glucoregulatory.

We sought to functionally characterize iEAN subsets with specific neuropeptide expression that are modulated by the gut microbiota. To define possible functional outcomes of microbiota–modulated iEANs in GI physiology, we focused on CART+ neurons (enriched in the distal intestine, reversible expression upon microbiota depletion,

and unlike SST, not expressed in EECs (Gunawardene et al., 2011), AGRP+ neurons (enriched in the distal intestine and decreased in GF mice), and on NPY+ neurons (enriched in the duodenum and not affected by the microbiota). These are also three neuropeptides expressed by neuronal populations in the hypothalamus that work in concert to regulate energy balance (Waterson and Horvath, 2015), and as such, could potentially play a role in gut-specific circuits influencing feeding behavior. Whole-mount

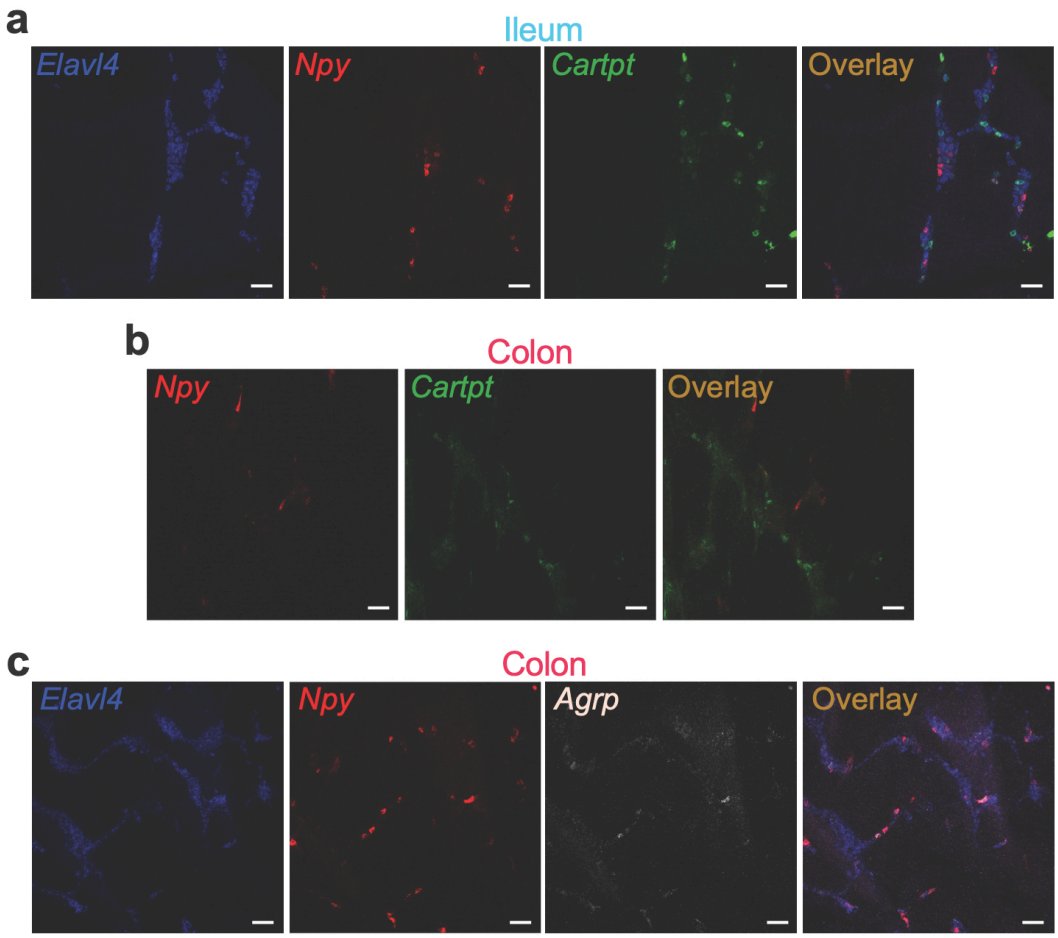

Figure 5.17. In situ hybridization for neuropeptide+ iEAN populations. (**a**-**c**) RNAscope in situ hybridization immunofluorescence whole-mount images of the indicated intestinal segments from C57BL6/J mice using probes for (**a**-**b**) *Elavl4*, *Npy*, and *Cartpt* in the ileum (**a**) and colon (**b**) or *Elavl4*, *Npy*, and *Agrp* in the colon (**c**). Scale bars = 50 μm.

analysis of intestinal muscularis using *in-situ* hybridization confirmed the expression of *Npy* and *Cartpt* in the ileum and colon, and *Agrp* in the mid-colon (Figure 5.17a-c). We

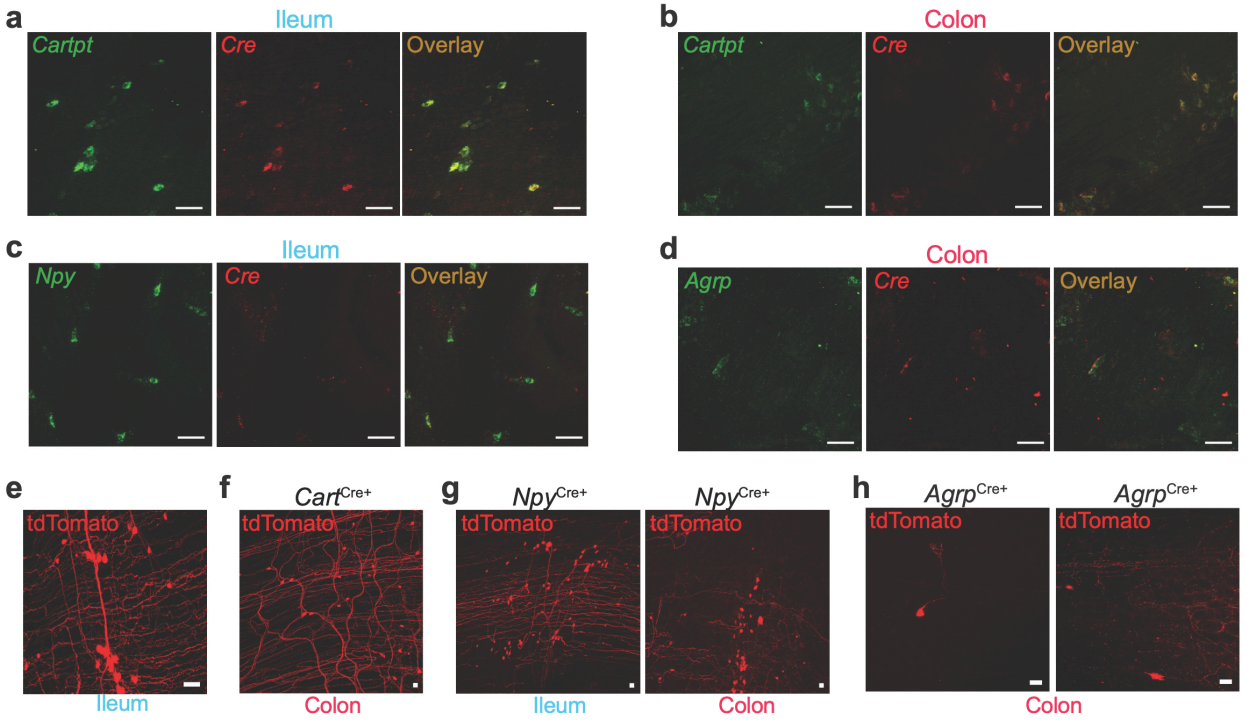

Figure 5.18. Validation of intestine targeting of neuropeptide *Cre* mouse lines. (**a-d**) RNAscope in situ hybridization immunofluorescence whole-mount images of intestinal segments from *Cart*^{Cre} (**a-b**), *Npy*^{Cre} (**c**), and *Agrp*^{Cre} (**d**) of the ileum (**a**, **c**) and colon (**b**, **d**) using probes for *Cre* and (**a-b**) *Cartp*, (**c**) *Npy* and (**d**) *Agrp*. Scale bars = 50 μm. (**e**) Representative whole-mount immunofluorescence (IF) image of the ileum myenteric plexus from *Cart*^{Cre} mice injected with AAVrg-FLEX-tdTomato into the ileum. Scale bars = 50 μm. (**f-g**) Immunofluorescence whole-mount images of the (**f**) the colon from ***Cart***^{Cre} mice, and (**g**) the ileum (left) and colon (right) of *Npy*^{Cre} mice injected with AAVrg-FLEX-tdTomato into the duodenum, ileum, and colon. Scale bar = 50 μm. (**h**) Immunofluorescence whole-mount images of the colon from *Agrp*^{Cre} mice injected with AAVrg-FLEX-tdTomato into the mid-colon. Scale bars = 50 μm.

obtained Cre lines corresponding to the three neuropeptides and validated *Cre* expression, along with *Cartpt, Npy,* or *Agrp*, in the periphery using *in situ* hybridization (Figure 5.18a-d). Because these neuropeptides are known to be expressed both in the periphery (Furlan et al., 2016; Gupta et al., 2017; Shcherbina et al., 2017; Teitelman et

al., 1993; Yuan et al., 2016) and CNS (Waterson and Horvath, 2015), we used a local viral delivery approach to target these neurons and avoid CNS effects. Injection of retrograde adeno-associated virus (AAVrg)-FLEX-tdTomato (Tervo et al., 2016) revealed a prominent population of tdTomato+ neurons in the ileum, and colon myenteric plexus of *Cartpt*^{Cre} (Lovett-Barron et al., 2017) and *Npy*^{Cre} (Milstein et al., 2015) mice (Figure 5.18e-g). *Npy*$^{EAN\text{-}tdTomato}$ and *Cartpt*$^{EAN\text{-}tdTomato}$ neurons displayed considerable innervation of the circular and longitudinal smooth muscle within these segments of the intestine, with *Cartpt*$^{EAN\text{-}tdTomato}$ also exhibiting dense inter-ganglionic patterning. Similar to the above *in situ* observations, we found a sparse population of *tdTomato*+ neurons in the mid-colon of *Agrp*$^{EAN\text{-}tdTomato}$ (Tong et al., 2008) mice, exhibiting muscular and inter-ganglionic innervation (Figure 5.18h). We were unable to find tdTomato expression in NG, DRG, or CG-SMG in *Cartpt*$^{EAN\text{-}tdTomato}$ and *Agrp*$^{EAN\text{-}tdTomato}$ mice, while *Npy*$^{EAN\text{-}tdTomato}$ mice exhibited a population of tdTomato+ synaptically connected neurons in the CG-SMG (Figure 5.19b). Of note, we also observed a significant number of tdTomato+ fibers in the CG-SMG of *Cartpt*^{Cre} mice (Figure 5.18a,c), suggesting targeting of a specific population of viscerofugal neurons, generally defined as mechanosensitive iEAN projecting axons outside of the intestine (Hibberd et al., 2012).

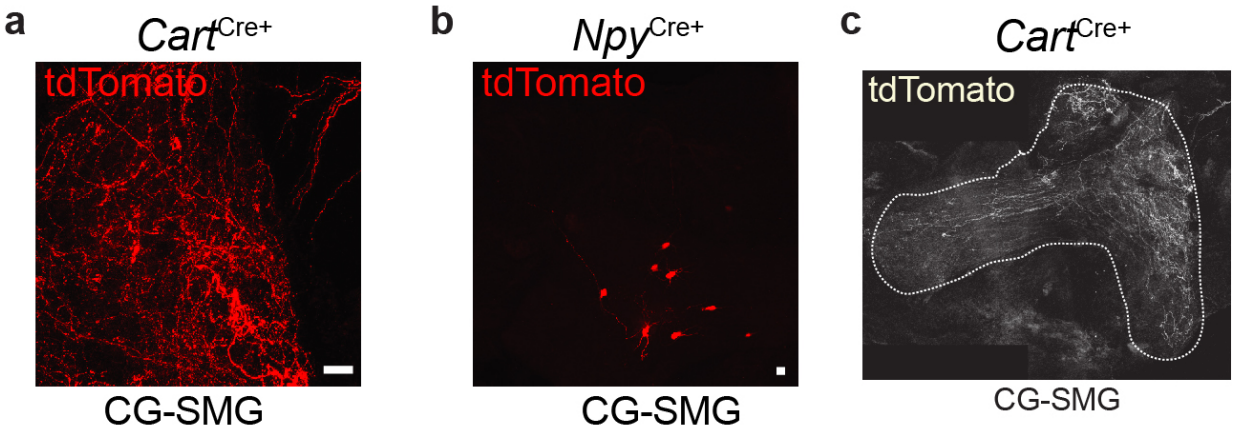

Figure 5.19: Extrinsic neurons innervating the intestine in neuropeptide *Cre* mouse lines. (**a**) Representative whole-mount IF image of the CG-SMG from *Cart*^{Cre} injected with AAVrg-FLEX-tdTomato into the duodenum, ileum, and colon. Scale bars = 50 μm. (**b**-**c**) Immunofluorescence whole-mount image of the CG-SMG from (**b**) *Npy*^{Cre} and (**c**) *Cart*^{Cre} mice injected with AAVrg-FLEX-tdTomato into the duodenum, ileum, and colon. Scale bars = 50 μm.

To directly assess a potential local GI function played by these three neuropeptide populations, we injected excitatory designer receptor exclusively activated by designer drugs (DREADD) virus (AAV9-FLEX-Syn-hM3Dq-mCherry) into the distal ileum and

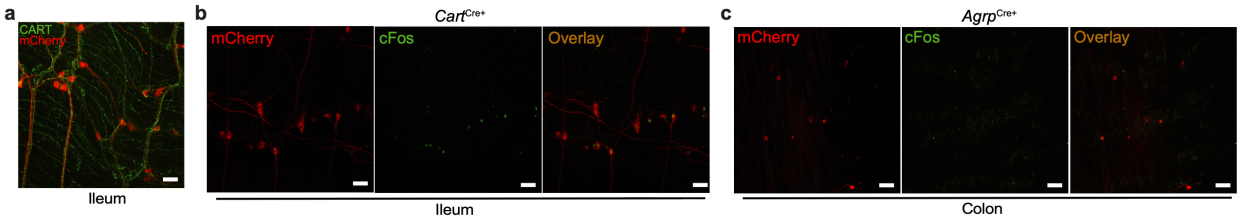

Figure 5.20. Chemogenetic targeting of distal intestine neuropeptide+ iEAN. (**a**) Representative whole-mount IF image of CART+ (green, stained with antibody), and mCherry+ (red, native fluorescence) ileum myenteric iEAN from *Cart*^{Cre} mice injected with AAV9-hSyn-DIO-hM3Dq-mCherry into the ileum. Scale bars = 50 μm. (**b**) Representative whole-mount IF image of cFos+ (green, stained with antibody) and mCherry+ (red, stained with antibody) ileum myenteric iEAN 3 hours post administration of Compound 21 (C21, 1mg/kg) to *Cart*^{Cre} mice injected with AAV9-hSyn-DIO-hM3Dq-mCherry into the ileum. Scale bars = 50 μm. (**c**) Whole-mount immunofluorescence (IF) image 3 hours post administration of Compound 21 (C21, 1mg/kg) of cFos (green, stained with antibody) and mCherry (red, stained with antibody) in the colon myenteric plexus from *Agrp*^{Cre} mice injected with AAV9-hSyn-DIO-hM3Dq-mCherry into the mid-colon. Scale bars = 50 μm

proximal-mid colon of *Cartpt*^{Cre} and *Npy*^{Cre} mice or into the mid-colon of *Agrp*^{Cre} mice (Figure 5.20a-c). We first performed intestinal motility assays following administration of the DREADD ligand, Compound 21 (C21); we did not observe changes in total intestinal transit in any of the three neuropeptide lines tested (Figure 5.21a-c). Analysis of feeding

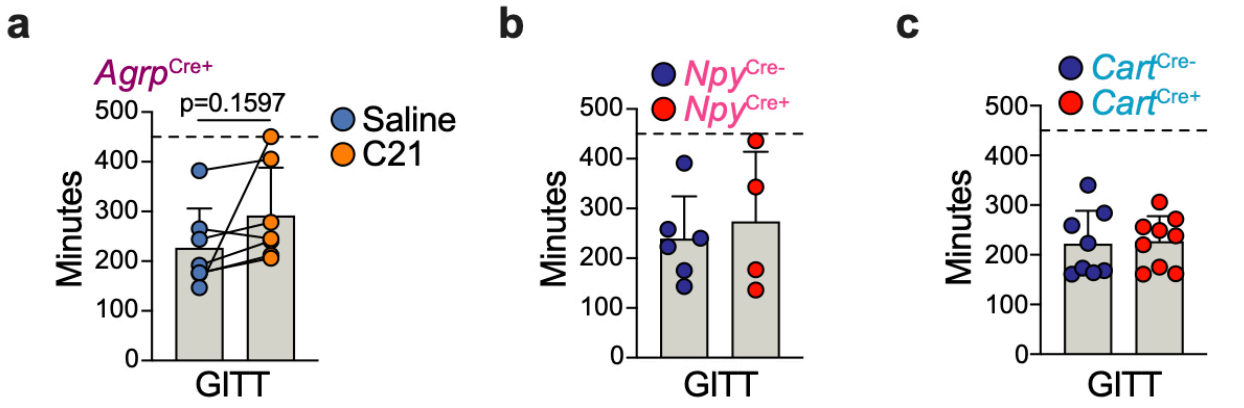

Figure 5.21. Gastrointestinal transit time following chemogenetic activation of neuropeptide+ distal gut neurons. (**a**-**c**) Gastrointestinal transit time (GITT) of *Agrp*^{Cre} (**a**), *Npy*^{Cre} (**b**), and *Cart*^{Cre} (**c**) mice injected with AAV9-hSyn-DIO-hM3Dq-mCherry into the ileum and colon. Non-significant p-value as calculated by paired t-test (**a**).

behavior also failed to detect robust or consistent changes in both *Npy*$^{EAN\text{-}hM3Dq}$ and *Agrp*$^{EAN\text{-}hM3Dq}$ mice; however, we observed a significant decrease in food consumption during day feeding at 1 and 2 hours, as well as during night feeding at 2 and 4 hours post C21 in *Cartpt*$^{EAN\text{-}hM3Dq}$ mice (Figure 5.22a-c). Because CART is expressed by several

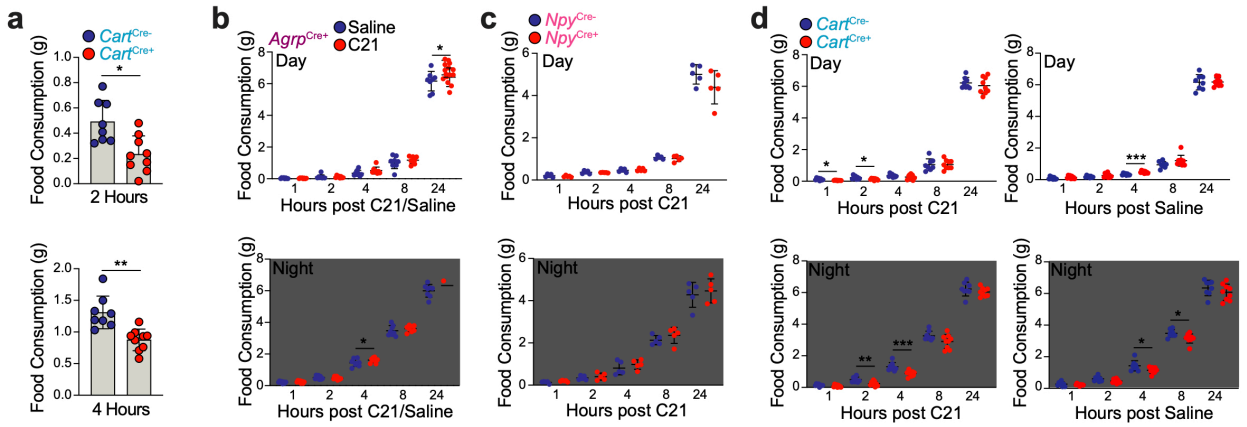

Figure 5.22. Food consumption following chemogenetic activation of neuropeptide+ distal gut neurons. (**a**) Food consumption at night, 2 hours (left) and 4 hours (right), levels post C21 administration (1mg/kg) to *Cart*^{Cre} mice injected with AAV9-hSyn-DIO-hM3Dq-mCherry into the ileum and colon. * $P < 0.05$, ** $P < 0.01$ as calculated by unpaired t-test. (**b**-**d**) Food consumption during the day (top) or at night (bottom) post administration of compound 21 (C21, 1mg/kg) or saline in *Agrp*^{Cre} (**b**), *Npy*^{Cre} (**c**), *Cart*^{Cre} (**d**) mice injected with AAV9-hSyn-DIO-hM3Dq-mCherry into the ileum and colon. * $P < 0.05$, ** $P < 0.01$, *** $P < 0.001$ as calculated by unpaired t-test. (**a**-**d**) Data represented as mean ± s.d.

neuronal populations outside the intestine, including in areas that may influence feeding (Lau and Herzog, 2014; Rogge et al., 2008), and retrograde transport of AAV9 from the gut has been described (Gore et al., 2019), we examined the NG, DRG, CG-SMG, duodenum and the dorsal motor nucleus of the vagus (DMV) for mCherry+ expression by neuronal populations. We found no clear evidence for hM3Dq expression outside of the distal ileum and proximal colon, indicating that an iEAN-restricted neuronal stimulation can influence feeding (*data not shown*). We evaluated whether the reduction in feeding was related to acute changes in blood glucose or glucoregulatory hormone levels, which can regulate the activity of CNS nuclei controlling feeding behavior (Dunn-Meynell et al., 2009; Gielkens et al., 1998; Havrankova et al., 1978; Woods et al., 1979). We detected

significantly higher blood glucose levels in *Cartpt*$^{EAN\text{-}hM3Dq}$ mice injected with C21 as compared to control mice (Figure 5.23a-c). To define whether these changes in basal

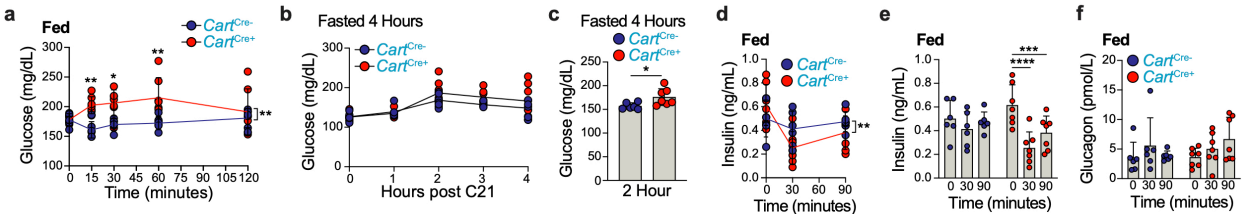

Figure 5.23. Changes in blood glucose and glucoregulatory hormones post-chemogenetic activation of distal CART+ iEAN. (**a**) Blood glucose post C21 administration (1mg/kg) to *Cart*^{Cre} mice injected with AAV9-hSyn-DIO-hM3Dq-mCherry into the ileum and colon. * $P < 0.05$, ** $P < 0.01$ as calculated by unpaired t-test by two-way ANOVA with Tukey's multiple comparisons post hoc test. (**b**) Blood glucose levels of *Cart*^{Cre} mice fasted for 4 hours followed by administration of C21 (1mg/kg), injected with AAV9-hSyn-DIO-hM3Dq-mCherry into the ileum and colon 2 weeks prior to analysis. (**c**) Blood glucose levels of *Cart*^{Cre} mice fasted for 4 hours, followed by administration of C21 (1mg/kg), and analyzed 2 hours later. Mice were injected with AAV9-hSyn-DIO-hM3Dq-mCherry into the ileum and colon 2 weeks prior to analysis. * $P < 0.05$ as calculated by unpaired t-test. (**d-e**) Plasma insulin (**d**,**e**) and plasma glucagon (**f**) levels post C21 administration (1mg/kg) to *Cart*^{Cre} mice injected with AAV9-hSyn-DIO-hM3Dq-mCherry into the ileum and colon. ** $P < 0.01$, *** $P < 0.001$, *** $P < 0.0001$ as calculated by unpaired t-test (**e-f**), or by two-way ANOVA (**d**). (**a-f**) Data represented as mean ± s.d.

blood glucose were directly related to typical glucoregulatory mechanisms, we measured insulin and glucagon levels following C21 administration. We found a significant decrease in insulin levels at 30 and 90 minutes post-C21 administration to *Cartpt*$^{EAN\text{-}hM3Dq}$ mice, while glucagon levels were only marginally (non-significantly) increased at 90 minutes (Figure 5.23d-f). These data indicate that stimulation of distal intestine CART+ neurons result in decrease insulin levels with a subsequent decrease in feeding in mice.

We next asked how CART+ neurons can exert their glucoregulatory function. Imaging analyses confirmed that at least some CART+ neurons in the distal intestine, in particular the ileum, are viscerofugal. These CART+ neurons send axonal projections to the CG-SMG (Figure 5.24a,b), which in turn provides sympathetic innervation to a number

of visceral organs, including the pancreas and liver (Love et al., 2007; Mizuno and Ueno, 2017). Sympathetic innervation of the pancreatic islets can stimulate the release of glucagon and inhibit insulin through adrenergic receptor engagement on alpha and beta cells, respectively (Love et al., 2007; Thorens, 2014), while sympathetic stimulation of the liver can drive gluconeogenesis (Mizuno and Ueno, 2017). To characterize a possible gut-sympathetic ganglia-pancreas/liver circuit, we performed polysynaptic retrograde tracing using pseudo-rabies virus (PRV). We injected GFP-expressing PRV into the pancreas and RFP-expressing PRV into the parenchyma of the liver and assessed their synaptic connections to the CG-SMG and the intestine (Figure 5.24c). We detected viral spread from both organs to the CG-SMG upon dissection of intestine muscularis at day four; we observed GFP+ neurons in the myenteric plexuses of the duodenum, ileum, and colon after four days with the highest concentration of neurons in the colon and ileum, while RFP+ neurons were only observed in the ileum (Figure 5.24c,d). To investigate whether CART+ viscerofugal neuron activation could directly modulate sympathetic neuronal activity, we dissected the CG-SMG post-C21 administration and measured cFos expression as an indicator of sympathetic activation (Mei et al., 2001; Muller et al., 2019b). As expected, we observed a significant increase in cFos expression in C21-injected $Cart^{EAN\text{-}hM3Dq}$ mice as compared to control animals (Figure 5.24e).

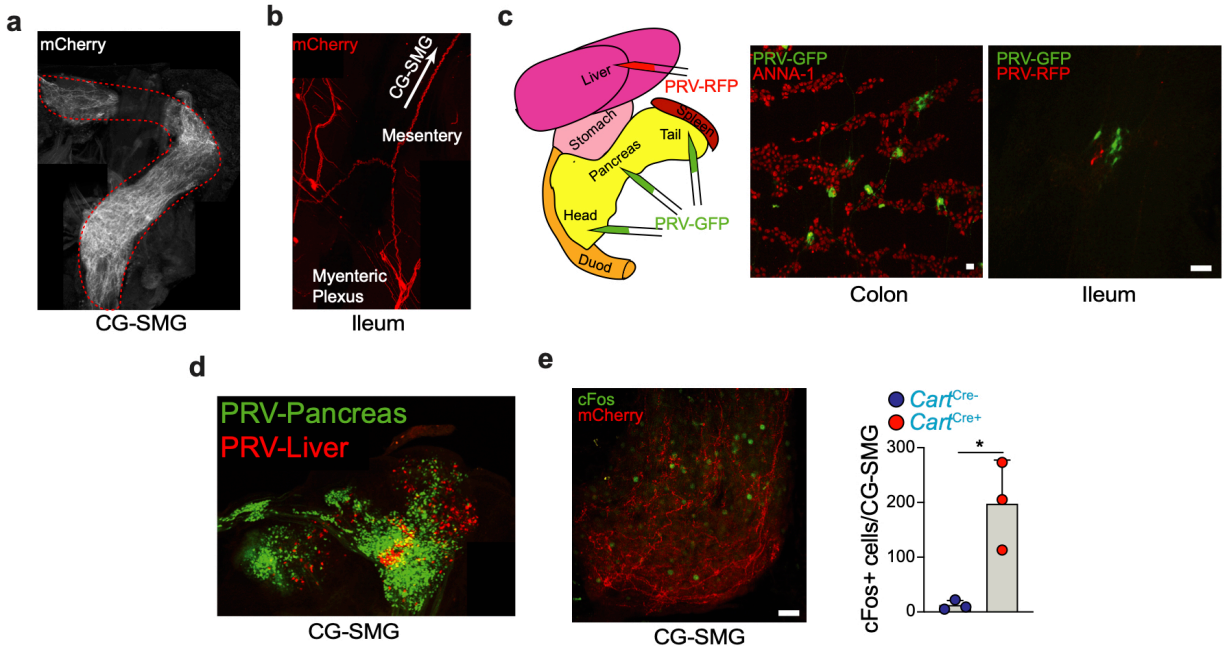

Figure 5.24. iEAN are polysynpatically connected to the pancreas and liver. (**a**) Whole-mount immunofluorescence image of the CG-SMG from *Cart*^{Cre} mice injected with AAV9-hSyn-DIO-hM3Dq-mCherry into the ileum and colon. (**b**) Representative whole-mount IF image of the ileum myenteric plexus from *Cart*^{Cre} mice injected with AAV9-hSyn-DIO-hM3Dq-mCherry into the ileum. (**c**) (Left) Scheme of fluorescent PRV injection into the liver and pancreas; (Right) Whole-mount IF image of the colon (left) and ileum (right) myenteric plexus from C57BL6/J mice injected with PRV-GFP into the pancreas and PRV-RFP into the liver. Scale bars = 50 μm. (**d**) Whole-mount IF image of the CG-SMG 4 days post injection of PRV-GFP into the pancreas and PRV-RFP into the liver. (**e**) (left) cFos (green, stained with antibody) and mCherry (red, native fluorescence) expression in *Cart*^{Cre} mice expressing AAV9-hSyn-DIO-hM3Dq-mCherry in the distal intestine only, 3 hours post-injection of C21 (1mg/kg). (right) Number of cFos+ neurons in the CG-SMG of *Cart*^{Cre} mice injected with AAV9-hSyn-DIO-hM3Dq-mCherry into the ileum and colon 3 hours post injection of C21 (1mg/kg). * $P < 0.05$ as measured by unpaired t-test. Scale bars = 50 μm. Data represented as mean ± s.d.

To evaluate whether the above observations correlate to the microbiota-dependent changes in iEAN numbers, we quantified viscerofugal neurons in the all areas of the intestine upon microbial depletion. Indeed, retrograde fluorescent cholera toxin beta subunit (CTB) tracing from the CG-SMG revealed a preferential loss of CTB+ neurons in

the ileum of antibiotic-treated mice, with no change in the colon or the sparsely retrograde–labeled duodenum (Figure 5.25a-d). We measured glucose regulation in

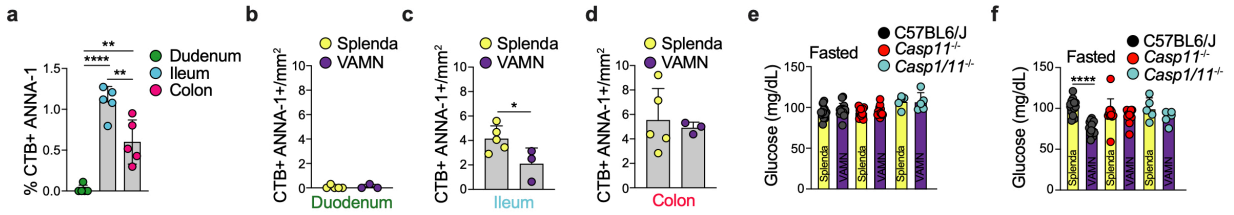

Figure 5.25. Loss of viscerofugal iEAN with antibiotics correlates with a reduction in blood glucose. (**a**-**d**) Percentage (**a**) or number (**b**-**d**) of CTB-AF647+ neurons in the duodenum (**b**), ileum (**c**), and colon (**d**) after injection of CTB into the CG-SMG of C57BL6J mice treated with broad-spectrum antibiotics (vancomycin, ampicillin, metronidazole and neomycin - VAMN) administered in Splenda-supplemented drinking water or Splenda (artificial sweetener, control) in the drinking water for two weeks. ** $P <$ 0.01, **** $P < 0.0001$ as calculated by unpaired t-test. (**e**) Blood glucose levels of C57BL6/J, Casp1/11$^{-/-}$, and Casp11$^{-/-}$ before antibiotic treatment. All mice on Splenda (artificial sweetener) only in the drinking water. * $P < 0.05$ as calculated by unpaired t-test. (**f**) Blood glucose levels of C57BL6J, Casp1/11–/–, and Casp11–/– mice treated with broad-spectrum antibiotics (vancomycin, ampicillin, metronidazole and neomycin - VAMN) administered in Splenda-supplemented drinking water or Splenda (artificial sweetener) only in the drinking water for two weeks. **** $P < 0.0001$ as calculated by unpaired t-test. (**a**-**f**) Data represented as mean ± s.d.

antibiotic–treated mice and found a significant reduction in blood glucose levels (Figure 5.25e,f), results that corroborate previously reported microbiome–based modulations in glucose tolerance (Martin et al., 2019a; Zarrinpar et al., 2018). To determine whether microbiota–mediated changes in glucose levels are associated to loss of iEAN, we measured blood glucose in ICE$^{-/-}$ and *Casp11*$^{-/-}$ mice, which did not display iEAN (or CART+) loss post antibiotics treatment. In contrast to wild–type control mice, neither ICE$^{-/-}$ nor *Casp11*$^{-/-}$ mice showed significant changes in blood glucose levels following antibiotic treatment (Figure 5.25e,f). Finally, to directly implicate CART neurons in glucose

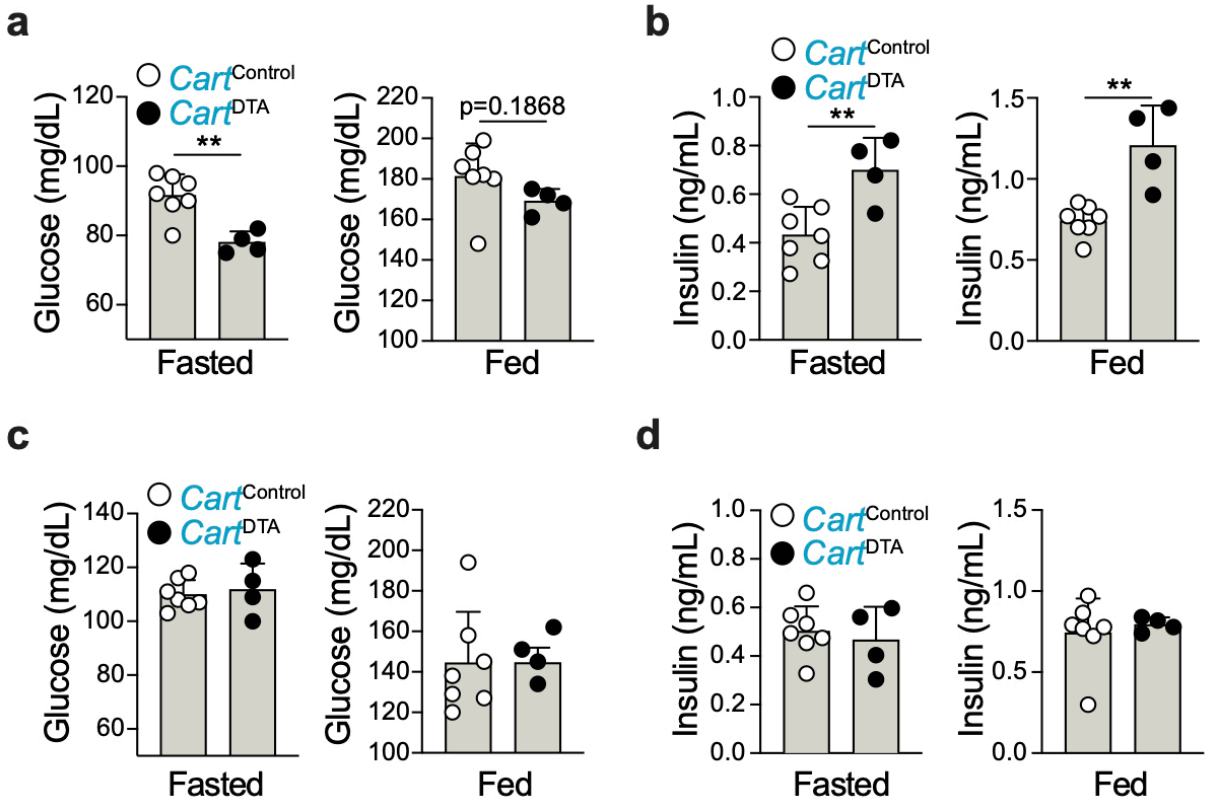

Figure 5.26. Ablation of distal CART+ leads to hypoglycemia and hyperinsulinemia. (**a**) Blood glucose levels of fasted (left) or fed (right) *Cart*^{Cre} mice injected AAV5-mCherry-FLEX-DTA or control virus into the ileum and colon. P-value, ** $P < 0.01$ as calculated by unpaired t-test. (**b**) Plasma insulin levels of fasted (left) or fed (right) *Cart*^{Cre} mice injected AAV5-mCherry-FLEX-DTA or control virus into the ileum and colon ** $P < 0.01$ as calculated by unpaired t-test. (**c**) Blood glucose levels of fasted (left) or fed (right) *Cart*^{Cre} mice before injection with AAV5-mCherry-FLEX-DTA or control virus. (**d**) Plasma insulin levels of fasted (left) or fed (right) *Cart*^{Cre} mice before injection with AAV5-mCherry-FLEX-DTA or control virus. (**a**-**d**) Data represented as mean ± s.d.

regulation, we injected AAV5-mCherry-FLEX-DTA into the ileum and colon of *Cartpt*^{Cre} mice, to selectively delete CART+ neurons. CART+ neuron ablation resulted in a significant reduction in blood glucose and a significant increase in insulin levels as compared to *Cartpt*^{Cre} mice injected with a control AAV5 virus (Figure 5.26a-d). These experiments demonstrate that the loss of CART+ viscerofugal iEAN can significantly

impact blood glucose levels, presumably due to the lack of pancreas-specific sympathetic regulation. Together, these experiments establish a distal gut-pancreas/liver circuit that originates in microbiota-modulated CART+ viscerofugal neurons to regulate blood glucose levels.

5.5 Conclusions

We aimed to understand how iEAN are adapted to different segments of the intestine, with a particular focus on the influence of the microbiota, through a combination of molecular, anatomic and functional approaches. We found that iEAN are translationally adapted to the intestinal segment they occupy, with a stronger microbiota influence on distal intestine neurons. In particular neuropeptide populations in the distal intestine were significantly decreased in the distal intestine in the absence of microbes. Microbial control of these neuropeptide populations, as well as iEAN numbers in general, was found to be mediated by the inflammasome. Chemogenetic characterization of microbiota-influenced iEAN identified a subset of viscerofugal CART+ neurons, enriched in the distal intestine, able to modulate feeding through insulin-glucose levels. Retro- and anterograde tracing revealed that CART+ viscerofugal neurons send axons to the gut sympathetic ganglion and are synaptically connected to the liver and pancreas. Our results demonstrate an anatomical and microbiota-dependent adaptation of enteric neurons, signals which can impact particular iEAN subsets, including one capable of regulating host physiology independently from the central nervous system.

Chapter 6: Discussion

Through the prior four chapters we investigated the impact of both broad and targeted changes to the gut microbiota on the EANS and related functions. Unexpectedly, we found that the sympathetic nervous system is a key integrator of changes in the gut luminal microbial composition. The SNS is activated by changes in the commensal microbiome and during pathogenic infections, and its activation can drive several important physiological or immunological responses. In the steady state we found that a diverse commensal gut microbiota, capable of producing SCFA, tonically suppresses gut-sympathetic activation and maintains the survival of a select set of neuropeptide positive iEAN, inclusive of a glucoregulatory CART+ population. Depletion of the microbiota leads to altered sympathetic activation, resulting in impaired intestinal motility and glucose regulation. Finally, we observed that detection of an enteric pathogen led to activation of gut-projecting sympathetic neurons, which in turn rapidly shaped MM transcriptional programming to confer iEAN neuronal protection. We will highlight how these findings relate to our current understanding of the EANS and its role in physiology and immunity, along with unanswered questions and future directions.

6.1 Muscularis macrophages are critical mediators of tissue homeostasis

6.1.1 MM adapt to the tissue environment to perform their function

Both resident (long-lived) and monocyte-derived (replenished) macrophages adapt to their surrounding microenvironment in different tissues (Davies et al., 2013). Within the intestine a broad anatomical distinction had been previously drawn between

MM and LpM (Phillips and Powley, 2012), including a functional inflammatory distinction for MM when the *muscularis* is directly manipulated in murine models of POI (Kalff et al., 1998). By utilizing several imaging approaches and transcriptional profiling of sorted populations of macrophages from the gut, we have established that this anatomical separation is linked to a segregation in overall gene expression profile of MM when compared to LpM. Furthermore, these differences in gene expression are reflected in the ability of MM to influence neuronal activity in the steady state and survival during the course of an enteric infection (Gabanyi et al., 2016; Matheis et al., 2019; Muller et al., 2014). While corroborating our findings of control over steady state intestinal motility, another group has recently reported that MM are necessary for the maintenance of iEAN (De Schepper et al., 2018). By targeting tissue-resident MM by DTR ablation, they found rapid degeneration of iEAN. Use of diptheria toxin versus antibody-mediated depletion in our case could be one explanation for this discrepancy. Concomitantly, counting methods utilized in this study may have led to under sampling of iEAN numbers in the myenteric plexus.

The concept of the intestine as primarily comprised of recruited monocyte-derived macrophages (Bain et al., 2014) was recently revised with the discovery of self-maintaining macrophage populations in the gut (De Schepper et al., 2018; Shaw et al., 2018), many of which are thought to be MM. In line with these studies we have found that in CCR2$^{-/-}$ mice, which lack inflammatory monocytes, there is no change in neuronal survival post-infection despite the fact that the pathogen is never cleared. Coupled with the fact that we do not observe upregulation of tissue-protective genes in LpM at early

timepoints post-infection, an anatomically segregated model in which continuously replenished lamina propria macrophages help mediate pathogen resistance and distally located long-lived MM boost tissue protection is conceivable.

While we have focused on neuronal-specific tissue adaptations, MM also interact with smooth muscle cells, enteric glia, lymphatics, and blood vasculature. Recent work has shown that MM in the small and large intestines were found to express transient receptor potential cation channel 4 (TRPV4) (Luo et al., 2018). Specific loss of *Trpv4* in CX3CR1+ macrophages led to deficits in colonic motility, an effect that was attributed to TRPV4-stimulation of prostaglandin E production by MM, which in turn directly modulates smooth muscle contractility. The mechanosensitive properties of TRPV4 (Liedtke et al., 2000), suggest that MM may be tuned to detect changes in peristalsis. We have found further evidence for mechanosensation in our MM TRAP-seq data showing *Piezo1* and *Piezo2* expression by MM. While roles for the mechanosensitive channels PIEZO1 and PIEZO2 have been explored primarily in sensory neurons, lymphatic vasculature, and stromal cells (Chang et al., 2019; Nencini and Ivanusic, 2017; Nonomura et al., 2017; Zeng et al., 2018), recent evidence suggests that PIEZO1 in myeloid cells can promote their pro-inflammatory responses which leads to exacerbated infection in the lung (Solis et al., 2019). In the mechanically dynamic intestine, especially within the muscle layers, mechanosensation in innate immune populations like MM could be a key signal by which both steady-state and inflammatory responses are mediated. For example, although the role for MM in POI is clear (Cremon et al., 2014; Farro et al., 2017; Pohl et al., 2017), how they are activated by intestinal manipulation is an active area of investigation. It will be

interesting to see whether MM-specific deletion of these mechanosensitive channels has an impact on tissue physiology or POI.

Beyond the distinction of LpM and MM, there are likely further subdivisions of macrophages within these compartments. Recent targeting of self-maintaining intestinal macrophages has revealed a potential role for maintenance of vasculature integrity (De Schepper et al., 2018), a role also shown to be played by macrophages in adipose tissue (Silva et al., 2019). Single-cell sequencing of the large and small intestine *muscularis* and mucosa may aid in defining further novel roles for macrophages within the gut.

6.1.2 Possible role of MM in mediating long-term neuroprotection

The concept of innate immune memory, or training, is based on the long-noted observation that exposure of innate immune cells to an inflammatory signal can impact a subsequent response from the same cell type (Boraschi and Italiani, 2018). This differs from adaptive immune memory, as innate immune memory is generally considered short-lived, non-specific, and involves epigenetic changes rather than genomic rearrangement. The prevention of further neuronal loss we observed during subsequent heterologous infections is highly suggestive of a form of tissue immune memory, which recently has been described outside of immune cells. Work from Fuchs and colleagues in the skin, has elegantly demonstrated that stem cells in the hair follicle can better respond to a secondary inflammatory insult by “recalling” a prior immunological program (Naik et al., 2017). This long-term recall is possible through enhanced chromatin accessibility to key inflammasome components, likely mediated by epigenetic mechanisms. Evidence of

long-lived innate immune memory is also not without precedent, as microglia in the brain of mice have been shown to be imprinted upon exposure to inflammatory stimuli such as peripherally delivered LPS or cytokines (Wendeln et al., 2018). Conditional deletion of the epigenetic enzymes *Hdac1* and *Hdac2*, eliminated microglial imprinting thus implicating epigenetic modifications as key to innate immunological memory. It may be that similar mechanisms in MM in the myenteric plexus are employed in response to an enteric infection. Depletion of MM after an initial enteric infection, followed by a heterologous infection would be necessary to first determine whether extended protection is afforded by this macrophage population. Bulk or single-cell ATAC-seq coupled with relevant chromatin immunoprecipitation sequencing would then be required to probe whether MM are epigenetically modified following an initial inflammatory insult.

The aforementioned examples of inflammatory memory were described in cell populations that are present in their relevant tissues throughout the lifetime of the animal. As referenced earlier, recent work has shown that long-lived tissue-resident macrophages do exist in the intestine, contrary to prior models, particularly in the *muscularis* (De Schepper et al., 2018; Shaw et al., 2018). Thus, there is a mix of long-lived and newly arrived macrophage populations that can potentially mediate iEAN protection. Are long-lived MM populations necessary for iEAN protection, or can newly recruited macrophages also retain immunological memory? MM depletion in naïve mice, followed by repopulation, subsequent infection, and heterologous infection could be one possible route to determine whether long-lived MM are required.

It is also possible to consider that MM may exert their neuroprotective effect through *in trans* modulation of additional cell types. Thus, it will be crucial to target additional cell types in the myenteric plexus in close proximity to MM and neurons, such as enteric glia (Belkind-Gerson et al., 2017; Gulbransen et al., 2012; Joseph et al., 2011), to probe whether they play any role in tissue memory. Finally, neurons or neuronal precursors (Kulkarni et al., 2017) in the gut may also be capable of retaining immune memory to restrain further neuronal loss following subsequent enteric infections. A better understanding of the identity of neuronal populations that are lost or maintained post-enteric infection will provide an opportunity to probe this question.

6.1.3 Adrenergic modulation of MM programming

Sympathetic signaling through adrenergic receptors, particularly β2AR, has been well-documented as a potent immunoregulatory mechanism (Kenney and Ganta, 2014; Scanzano and Cosentino, 2015). These findings include reduction in lymphocyte egress from lymph nodes (Nakai et al., 2014), suppression of cytokine production in sepsis (Bassi et al., 2017), and mobilization of hematopoietic stem cells from the bone marrow (Katayama et al., 2006) to name just a few examples. Despite the extensive innervation of the GI tract and its large immune cell repertoire, neuro-immune interactions in the gut have only recently begun to be explored, including sympathetic effects. In light of the discovery of the cholinergic anti-inflammatory pathway by Tracey and colleagues (Borovikova et al., 2000), much of the initial work regarding gut neuro-immune interactions revolved around vagal modulation of macrophages in inflammatory models

such as colitis or POI (Cailotto et al., 2012; Costes et al., 2014; de Jonge et al., 2005). While the vagus, afferent and efferent, likely play a role in modulation of MM, we have found that that the sympathetic nervous system may be the principle autonomic arm involved in mediating intestinal responses to infection. Indeed, recent work from Artis and colleagues has shown that β2AR signaling in gut ILC2s is necessary to shut down a type 2 immune response (Moriyama et al., 2018). It is also important to point out that we failed to detect enrichment of acetylcholine receptors in MM, and expression of the proposed anti-inflammatory nicotinic acetylcholine receptor 7 was not detected (Bosmans et al., 2019; Costes et al., 2014; de Jonge et al., 2005). It may be necessary to revisit previous findings of the anti-inflammatory effects of vagal stimulation on MM in light of these results. It is likely that we have only begun to uncover potential sympathetic-immune cell interactions within the intestine, given the ubiquitous expression of β2AR on immune cells (Heng et al., 2008).

Beyond a role for adrenergic or cholinergic signaling, other groups have identified neuro-immune pathways in the gut that are relevant for inflammation. These pathways have been primarily focused on innate lymphoid cells (ILCs), the innate counterparts of T-cells, which lack adaptive antigen receptors (Vivier et al., 2018). Intestine ILC immune responses can be augmented by NMU (ILC2) and VIP (ILC3), or suppressed by NE (ILC2) (Cardoso et al., 2017; Klose et al., 2017; Moriyama et al., 2018; Talbot et al., 2019). Thus, it is likely that MM are readily impacted by the vast array of neurotransmitters and neuropeptides in the myenteric plexus (Furness, 2000). We find that MM also express *Vipr1*, one of the two receptors for VIP. Literature suggests that VIP may act on

macrophages to suppress a pro-inflammatory program (Carrión et al., 2016b; Ran et al., 2015), although these effects are likely dependent on the tissue in which the macrophage resides. Thus, VIP may act in conjunction with NE on MM to aid in tissue protection. Our work has thus far uncovered an anti-inflammatory neuro-immune pathway, but it is likely that pro-inflammatory crosstalk is possible as demonstrated by the potent actions of NMU on ILCs (Cardoso et al., 2017; Klose et al., 2017; Wallrapp et al., 2017). While our bulk sorted RNA-sequencing and ileum-specific TRAP-seq have not yielded many additional neuropeptide or neurotransmitter receptor targets, such as the receptors for NMU (NMUR1/2), better coverage of macrophage populations in different regions of the intestine may reveal new targets. Screening of potential neuropeptide or neurotransmitters for their effects on MM transcriptional profiles or maintenance could lead to the discovery of new avenues of neuro-immune crosstalk.

Mammalian stress can have profound effects on physiology, primarily through the activation of the sympathetic nervous system (Kvetnansky et al., 2009) and the hypothalamic pituitary axis (HPA) (Smith and Vale, 2006). The effects of stress are typically thought to be immunosuppressive although in the context of cellular damage and death, glucocorticoids can promote pro-inflammatory immune responses particularly in the CNS (Bellavance and Rivest, 2014; Di Giovangiulio et al., 2015; Scanzano and Cosentino, 2015). We found that acute stress in mice could provide significant protection to iEAN during enteric infection, and that MM loss of Arginase induction downstream of β2AR signaling could attenuate this protective effect. A stress response or stress induced by an infection can result in the release of catecholamines from gut-sympathetic neurons

or from the adrenal-medulla. However, we found that removal of the adrenals led to improved iEAN survival, indicating that neither adrenal-catecholamines nor glucocortcoids are required for MM-mediated iEAN protection. As suggested by the literature (Bellavance and Rivest, 2014), it may be that in the case of pyroptotic cell death, HPA-derived glucocorticoids actually promote inflammation. It would be intriguing to determine how and when the HPA axis is triggered, and what role glucocorticoids are playing during the course of enteric infection. While we examined acute stress, it remains to be seen whether there is a difference between acute and chronic stress. The prolonged production of glucocorticoids might prove detrimental to the survival of iEAN populations. There may also be a role for habituation to stress, for example in the case where the animal has become adjusted to a stressor they may be less likely to trigger this sympathetic pathway.

6.1.4 MM-Polyamine neuroprotection

The aliphatic polycations, polyamines, are ubiquitous in mammalian, plant, and bacterial cells (Handa et al., 2018). Polyamine production in mammals begins with the production of putrescine through the required enzyme ornithine decarboxylase 1, and subsequent enzymatic processing leads to the generation of spermine and spermidine (Pegg, 2016). Their function varies widely including stabilization of proteins, a required component for cell proliferation, modulation of ion channels in neurons, and regulation of the circadian clock (Handa et al., 2018; Pegg, 2016; Zwighaft et al., 2015). Additionally polyamines have been shown to be neuroprotective in cases of ischemic insults, and they

are a hallmark of anti-inflammatory macrophages (Clarkson et al., 2004; Gilad and Gilad, 1999; Hesterberg et al., 2018; Latour et al., 2019). We observed a rapid induction of Arg1 upon *spiB* infection, and MM-specific deletion led to a significant increase in iEAN loss. These results were not correlated with a change in nitric oxide production in macrophages, as is typically presumed, but rather it appears that MM-produced polyamines may have a directly inhibitory role on the activation of the inflammasome (Levy et al., 2015). In addition to this effect on the inflammasome, there is evidence to suggest that polyamines can impact epigenetic modifications such as DNA methylation (Soda, 2018). It is tempting to speculate that a potential for epigenetic modification could be a method by which MM retain immune memory, or confer immune memory to additional cells within the *muscularis*.

6.2 The gut microbiota regulates the sympathetic nervous system

6.2.1 Microbial control of motility through the SNS

Differences in gut motility are a pronounced deficit in GF and antibiotic treated mice as compared to SPF mice (Kashyap et al., 2013; Muller et al., 2014; Yang et al., 2017; Yano et al., 2015). Our finding that gut sympathetic neurons are significantly activated in the absence of a microbiota may be a logical explanation for these differences in motility. The sympathetic nervous system is a potent inhibitor of gut motility (Browning and Travagli, 2014; Gonella et al., 1987; Straub et al., 2006), an effect we have confirmed in vivo through modulation of sympathetic premotor neurons. Sympathetic effects on gut motility are thought to be mediated by direct inhibition of iEAN networks, although there

is sparse innervation of the longitudinal and smooth muscle (Burnstock and Costa, 1973; Furness and Costa, 1974; Tack and Wood, 1992; Womack et al., 1988). Inhibition of iEAN is reflected in the decrease in pCREB we observe in GF mice, and the reported reductions in immediate early gene and electrophysiological deficits in GF iEAN (McVey Neufeld et al., 2013; Yano et al., 2015). We have also noted that ileal iEAN have less phosphorylated S6 kinase (pS6) as compared to SPF animals, which emphasizes the decreased metabolic capacity of iEAN (Knight et al., 2012). Still further we performed calcium imaging of antibiotic treated *Snap25*^{GCaMP6s} mice and observed increased activity in ICCs. This increase in pacemaker cell activity mirrors the effects seen when tetrodotoxin, a potent neurotoxin, is added to an in-vitro intestinal ring or muscle preparation to silence iEAN activity (Bortoff and Muller, 1975; Wood, 1972). Thus, silencing of iEAN with tetrodotoxin has parallels to effects that may be mediated by gut-SNS inhibition of iEAN.

What are other potential explanations for microbiota control of gut motility? Levels of gut-derived GLP-1 have been reported to increase significantly in GF and antibiotic-treated mice (Wichmann et al., 2013; Zarrinpar et al., 2018), an effect that may be dependent upon SCFA. Abrogation of GLP-1 signaling was sufficient to normalize motility in microbial-depleted animals. We have also found that a GLP-1 agonist can slow intestinal transit and activate CG-SMG neurons, however in cases of microbial depletion this signaling pathway is not required to activate sympathetic neurons. Therefore, GLP-1 could likely be acting on local iEAN circuits (Varin et al., 2019) to mediate changes in intestine motility in concert with sympathetic activation.

A recent preprint publication claims that reduced expression of aryl hydrocarbon receptor (*Ahr*), a xenobiotic-induced transcription factor (Korecka et al., 2016), in colonic iEAN in mice lacking a microbiota is a primary driver of microbial-mediated motility effects (Obata et al., 2019). However, i.v. delivery of AAV9 is not restricted to iEAN, as we have found from our work that NG, CG-SMG, and CNS neurons can all be transduced (Schuster et al., 2014). Coupled with the fact that *Ahr* is expressed in a large number of PNS and CNS neurons (Zeisel et al., 2018), it is not possible to attribute motility changes exclusively to iEAN-specific ablation of *Ahr* with this approach.

Another recent preprint has utilized single cell sequencing to define iEAN populations along the length of the colon (Drokhlyansky et al., 2019). Their results mirror recent functional findings in the mouse colon, namely that iEAN networks are constructed differently when moving in the proximal to distal direction (Li et al., 2019b). Analysis of iEAN single cell populations led to the proposal that *Piezo1* detection of mechanical stretch may be augmented by mucosal release of serotonin. Certainly this wiring seems plausible, particularly in light of another recent publication showing activation of myenteric iEAN by mucosal-delivered serotonin (Hao et al., 2019). Microbial effects on motility have been proposed to be the result of a decrease in mucosal serotonin production (Yano et al., 2015). However, we and others have found that a lack of mucosal serotonin does not impact intestine motility (Li et al., 2011). Mechanical distension of the intestinal tissue in microbial-depleted mice (Loesche, 1969; Savage and McAllister, 1971) would be expected to continuously driving PIEZO1 activation and likely neuronal activation. Thus, it seems unlikely that mucosal serotonin and iEAN mechanosensation are responsible for

changes in gut motility associated with a lack of microbes. Nonetheless, mechanosensation by sensory afferents (Williams et al., 2016) is another potential route for driving motility changes and is an avenue of investigation worth pursuing.

We propose that a major driver of gut dysmotility upon microbial depletion is inhibition of iEAN networks by gut sympathetic neurons. Confirmation of this hypothesis would require conditional removal of iEAN adrenergic receptors, silencing of sympathetic premotor neurons, or silencing of gut-sympathetic neurons under conditions of microbial depletion.

6.2.2 Microbial control of immunity by the SNS

Through our *spiB* or wild-type *Salmonella* infection experiments we found that enteric infections lead to activation of gut-projecting sympathetic neurons. Rapid activation of vagal sensory afferents has been previously reported with intestinal *Campylobacter* infection (Goehler et al., 2005). Conversely, suppression of sympathetic activity has been noted in infection with *Trichinella spiralis* (Swain et al., 1991). While we have comprehensively confirmed that noradrenergic innervation is crucial for MM-mediated iEAN protection, what remains unclear is the signal that leads to gut-sympathetic activation. There are several possibilities for pathogen detection in the context of *Salmonella* infections that we can speculate on. Establishment of a *S. typhimurium* infection is the result of a large number of changes to the luminal environment including, but not limited to, a reduction in SCFA (particularly butyrate) (Bronner et al., 2018; Rivera-Chávez et al., 2016a), a boost in bile acid concentration

(Crawford et al., 2012), and an increase in epithelial oxygenation (Rivera-Chávez et al., 2016a). These changes could be directly detected by sensory neurons expressing receptors for SCFA (Nøhr et al., 2013), bile acids (Lieu et al., 2014), or low oxygen (Bleymehl et al., 2016) respectively. Evidence also exists that EEC-derived signals, such as GLP-1, can increase significantly upon tissue damage (Lebrun et al., 2017). It is conceivable that *Salmonella* induced epithelial damage could lead to an increase in distal intestine GLP-1 release, which we know from our work can increase cFos in the CG-SMG.

Activation of the gut-sympathetic nervous system following microbial depletion may also explain the anti-inflammatory effects of specific types of antibiotics (Kanoh and Rubin, 2010). These findings are relevant for patients being pre-emptively treated with antibiotics before surgery. While the initial effects are beneficial, improper restoration of the microbiota could prolong sympathetic activation and change the course of wound healing. Additional CG-SMG targets such as the spleen may also be regulated by the microbiota with conceivable impacts systemic immunity. Furthermore, sympathetic signaling can impact gene transcription in a variety of immune cell targets, including gut–resident macrophages and innate lymphoid cells (Gabanyi & Muller et al., 2016; Moriyama et al., 2018). Determining additional targets of CG-SMG neurons that are activated upon microbial depletion could provide further mechanistic understanding of the immunosuppressive effects of antibiotic treatment.

6.2.3 SCFA can suppress sympathetic activation

The absence of a microbiota has a significant impact on the levels of key microbial metabolites such as SCFA and secondary bile acids (Levy et al., 2016). These metabolites can play a role in mediating not only gut function, but they have been implicated in the proper function of extraintestinal tissues such as the brain, where microglial morphology and reactivity are linked to SCFA levels (Erny et al., 2015; Sampson et al., 2016). Given the broad metabolic, neurologic, and immunologic impact of SCFA (Goswami et al., 2018; Schulthess et al., 2019; Szentirmai et al., 2019; De Vadder et al., 2014) it is perhaps not surprising that a detection system is in place to monitor levels in the intestine. Shifts in SCFA levels could reflect dietary changes (Llewellyn et al., 2017) or an active enteric infection (Rivera-Chávez et al., 2016a). Activation of the gut SNS to slow motility could allow for changes in nutrient absorption or modulate the ongoing immune response respectively. Given the preponderance of antibiotic usage in the developed world, our findings are particularly relevant (Chokshi et al., 2019). Without proper attention paid to make sure that patients maintain a normalized microbiota following antibiotic treatment, it is plausible that some patients may experience chronic activation of their gut SNS. This could in principle impact not only the gut immune system, but could contribute to visceral pain (Gil et al., 2016). Finally, co-evolution of bacteria within the intestine or in line with the host may dictate this adaptive response to dysbiosis (O'Brien et al., 2019). For example, work in zebrafish has demonstrated how specific microbes control motility in order to maintain a specific niche within the GI tract (Logan et al., 2018). Loss of SCFA would mean the absence of essential metabolites for

some bacteria (Biggs et al., 2017), and a shift in motility could allow for remaining bacteria to relocate or adapt to this altered environment.

While we found that SCFA are sufficient to suppress sympathetic activation, we were not able to determine whether this signal is required. Given the multitude of signals that we found could impact sympathetic activity, it is likely that while important, SCFA are not the sole microbial signal that can impact these neurons. In addition, how SCFA are sensed is also an open question. Through the work performed in this thesis we were able to eliminate direct sympathetic sensing and viscerofugal iEAN input as possible drivers of sympathetic activity. There could be at least four possible remaining routes, which we can now detail: EEC, gut vagal, hepatic vagal, or CNS.

We also investigated possible EEC-derived signals related to sympathetic modulation, downstream or not of SCFA. Given that EEC express SCFA receptors such as GPR41, GPR43, GPR109a, and OLFR78 (Martin et al., 2019b), and the fact that SCFA can induce production of neuropeptides such as PYY (Latorre et al., 2015), it is plausible that steady state EEC signaling can tonically suppress SNS activity. We found that PYY is sufficient to suppress sympathetic activity similar to SCFA. It is interesting to note that PYY production and release from EEC has been linked to the presence of SCFA (Christiansen et al., 2018; Priyadarshini et al., 2018). Despite this link, it is not clear how the absence of the microbiota changes PYY production as there are conflicting reports in the literature (Bindels et al., 2017; Duca et al., 2012; Mikkelsen et al., 2015). Despite its effects, we did not investigate where PYY might exert its SNS suppressive role as systemic administration could allow for vagal, iEAN, or CNS modulation. To determine a

definitive role of EECs or neuropod cells in the control of the gut-SNS, the use of EEC-specific knockout mice or possible chemogenetic modulation of these cells would prove fruitful.

NG neurons also have the capacity to respond to SCFA, including butyrate. For instance, we detected expression of *Ffar3* and *Ffar2* in the nodose ganglion using TRAPseq, results corroborated by scSeq database (Kupari et al., 2019). Additionally, sodium butyrate was able to modulate vagal neuron activity in culture, as evidenced by a reliable suppression of GCaMP signal. Despite these findings, we did not look at gut-projecting vagal neurons specifically and, as we note below, detection of SCFA can occur elsewhere in the periphery such as in the portal vein. It would be necessary to generate mice that lack SCFA receptors such as *Ffar3* in nodose neurons specifically, such as with *Phox2b*^{Cre}, to make a definite claim about vagal afferent detection of SCFA. Alternatively, an intersectional viral approach could be used selectively ablate gut-projecting vagal afferents with DTA virus for example.

SCFA taken up by enterocytes and colonocytes in the intestine are then released into the circulation where they will enter the liver via the portal vein (Den Besten et al., 2013). Previous studies have indicated that butyrate can be detected in the portal vein to mediate gluconeogenesis (De Vadder et al., 2014). If vagal detection of SCFA is happening in the portal vein, either hepatic-selective vagotomy or targeted intersectional viral depletion could be used to test its requirement.

Although we typically think of the brain as being cut-off from circulating factors, the circumventricular organs (CVOs) such as the area postrema can receive signals from the

bloodstream (Price et al., 2008; Young, 2012). Therefore, it is possible that changes in AP cFos we observed in GF, antibiotic-treated, and tributyrin-supplemented mice could be related to direct detection of SCFA in these neurons. Beyond CVOs, SCFA are also reported to be permeable to the blood brain barrier, and can even influence BBB permeability (Braniste et al., 2014), where they can affect central regulation of appetite or impact microglial morphology and function (Conn et al., 1983; Erny et al., 2015; Frost et al., 2014; Sampson et al., 2016). Effects of SCFA on additional brain nuclei connected to sympathetic pre-motor neurons could also explain the effects we see with SCFA administration. Direct infusion of SCFA into the brain via i.c.v. route would be one way to address peripheral versus central effects.

6.2.4 The role of Nav1.5+ vagal afferents

Our data suggests that a particular population of gut–projecting vagal sensory neurons, enriched in transcript for the voltage gated sodium channel *Nav1.5*, may play a role in mediating CNS–driven sympathetic suppression. Prior single cell profiling has confirmed the expression of this mechanosensitive channel (Beyder et al., 2010; Peeters et al., 2006) in vagal neurons (Kupari et al., 2019). It is intriguing to note that mutations in *Nav1.5* have been described as a hallmark of a subset of irritable bowel syndrome (IBS) patients with constipation (Beyder et al., 2014; Strege et al., 2018). Whether this mutation has an effect on vagal neuronal activity is unknown. However, based on our chemogenetic manipulation of vagal neurons, if this population were silenced it could lead to increased sympathetic activity and downstream effects on motility. Alternatively, it is

plausible that expression of mutated *Nav1.5* in the intestine smooth muscle or iEAN (Osorio et al., 2014) could lead to dysbiosis and changes in the local availability of SCFAs or additional microbial metabolites, resulting in increased sympathetic activity. Neuromodulation of this population of nodose neurons or neuronal-specific deletion of *Nav1.5* could be used to determine its role in microbial control of sympathetic activation.

Much of the GI vagal literature, both recent and past, refer to the proximal intestine as highly innervated by vagal afferents whereas the distal intestine is sparse and lacking mucosal or epithelial contact (Berthoud et al., 1997; Serlin and Fox, 2019; Williams et al., 2016). However, we have found that labeling of only the right nodose ganglion with a fiber filling membrane-bound fluorescent ChR2 fusion protein was sufficient to visualize extensive innervation to the distal intestine inclusive of the ileum, cecum, and proximal colon. This labeling was not restricted to the muscle layers of the intestine, rather we found that the majority of these fibers project to the epithelium in these areas of the gut. There is evidence from prior work that epithelial contact from vagal neurons is present in the distal intestine both in mice where they can contact neuropod cells (Kaelberer et al., 2018), but also in rats (Wang and Powley, 2007, 2000). In light of our findings, we believe that the dogma of proximal intestine heavy vagal sensing should be reformulated. While there is a necessity to detect nutrients and mechanical distension in the upper intestine (Han et al., 2018; Williams et al., 2016), one can argue that it is equally important to monitor these same parameters in the distal intestine (Kaelberer et al., 2018), with the inclusion of a multitude of microbial metabolites that have significant impact on host physiology. Tracing techniques used, even viral expression of tdTomato, may not have

been sufficient to properly fill the distal-gut projecting nodose afferents. Based on this work we believe that further mapping of nodose innervation to the distal intestine will yield a wealth of new information that can be leveraged to better understand how microbes impact mammalian physiology through the nervous system.

6.3 iEAN Inflammasome Function

Within the gut, the inflammasome has been primarily linked with mucosal macrophage responses and intestinal epithelial production of antimicrobial peptides and IL18 (Nowarski et al., 2015; Seo et al., 2015; Wang et al., 1998). The role of the inflammasome in iEAN death has been suggested previously, as knockout mice for different inflammasome components exhibited attenuated iEAN loss in a chemical mode of colitis (Gulbransen et al., 2012). We ultimately found that inflammasome activation in iEAN represents a novel immunological pathway by which these neurons can respond to the presence of enteric pathogens and the microbiota in general. Through TRAP-seq and *in situ* hybridization we found that iEAN express the inflammasome innate immune receptor *Nlrp6*. Our results may explain a recent observation that in patients with Hirschsprung Disease, characterized by an absence of iEAN in portions of the gut, there is a significant reduction in NLRP6 within aganglionic tissue (Tomuschat et al., 2018). While NLRP6 was thought to drive mucus production in the intestinal epithelium as well as shape the microbiota (Levy et al., 2015; Nowarski et al., 2015; Wlodarska et al., 2014), these concepts have recently been challenged (Lemire et al., 2017; Mamantopoulos et al., 2017; Volk et al., 2019). We propose a novel role for NLRP6 in the maintenance of a

specific subset of iEAN in the murine gut. Based on the reversible nature of iEAN loss in cases of dybiosis and enteric infection, one could argue that this immune sensor can allow for a rapid and restricted neuronal response to microbes within deeper layers of the gut.

Therefore, what role does inflammasome play in iEAN beyond neuronal integrity? We also have evidence that iEAN are enriched for additional inflammasome genes including *Casp1*, *Casp11*, and *Pycard*. While we did not interrogate canonical inflammasome pathways here, mediated by *Casp1*, work by Flavell and colleagues (personal communication) indicates that iEAN may be a key source of the cytokine IL-18, which in turn can promote the production of anti-microbial peptides by the intestinal epithelium (Nowarski et al., 2015). Our findings suggest that *Casp11* is key to the loss of a specific set of iEAN, although the loss may be context-dependent. For example, we did not specifically investigate whether similar iEAN subsets are between between *spiB* infection and microbial depletion, although we noted that SST iEAN were reduced upon microbial depletion and marginally affected by *Salmonella* infection. Activation of CASP11 may lead to pyroptosis of iEAN, which could coincide with the release of pro-inflammatory cytokines such as IL-1β or IL-18 (Lee et al., 2018). Thus, pyroptosis of iEAN could aid in the recruitment of other immune cells, such as neutrophils, to defend against enteric infection (Lee et al., 2018). Conditional deletion of gasdermin D or pro-inflammatory cytokines from neurons would be necessary to determine whether iEAN are required for a proper immune response to enteric infection. At the same time, altered resistance of *Snap25*$^{\Delta Nlrp6}$ mice to *Salmonella* infection would be indicative of a crucial role for iEAN

non-canonical inflammasome activation. In mining a recent single cell iEAN database (Zeisel et al., 2018), we have found that the expression of *Casp1* and *Casp11* do not always overlap in neuronal populations, although each of these subtypes do express *Nlrp6*. Thus, it could be that different populations of iEAN could be recruited during the same infection to mediate a broad response, or perhaps these separate *Casp1* or *Casp11* populations are activated individually based on the type of inflammation.

What are the signals that trigger inflammasome activation in iEAN? Functionally, neuronal specific loss of *Casp11* and *Nlrp6* is sufficient to prevent *spiB* inflammation-induced iEAN loss. Due to the fact that we observed neuronal recovery upon re-conventionalization of *spiB* infected mice and in the case of long-term *S. typhimurium* infection, it is not clear what the potential inflammasome trigger may be. *Salmonella* alone has been shown to induce *Nlrp6*-dependent inflammasome activation (Hara et al., 2018), but it may also be possible that dysbiosis will cause shifts in *Nlrp6* activating ligands derived from the microbiota or even the host, such as histamine (Levy et al., 2015).

Both antibiotic-treatment and *spiB* infection are linked to severe dysbiosis and we found that these perturbations lead to reductions in iEAN number, suggesting that specific bacteria could be involved in the maintenance of enteric neurons. Another possibility is that an alteration in host-derived factors, such as the production of the cytokine IL1β by macrophages (Seo et al., 2015), is driving inflammasome activation and caspase 11-mediated iEAN loss. Bile acids and derivatives, such as taurine, have been shown to be potent activators of the inflammasome (Alimov et al., 2019; Levy et al., 2015) and germ free mice or antibiotic treated mice have increased levels of primary bile acids in the

intestine, serum, and liver (Khan et al., 2019; Selwyn et al., 2015). There is also evidence to suggest that *Salmonella* infection can increase luminal bile acid concentrations (Crawford et al., 2012). Thus, microbial depletion and/or *Salmonella* infection increases in luminal bile acid concentrations could lead to activation of iEAN inflammasomes and subsequent cell death. Gall bladder removal before infection or neutralization of bile acids with cholestyramine (Crawford et al., 2012; Lewis et al., 1995) during infection could answer whether this pathway is relevant for inflammasome-dependent iEAN loss.

Our finding of iEAN inflammasome adds to prior descriptions of iEAN-intrinsic detection of microbes. While previous literature has pointed to a role of neuronal-intrinsic TLR signaling in detection of microbes (Anitha et al., 2012; Brun et al., 2013; Burgueño et al., 2016) or MYD88 dependent alarmin signaling in the case of nematodes (Cardoso et al., 2017), we did not find significant enrichment for these genes in our TRAP-seq. It should be noted that the previous use of *Wnt1*^{Cre} to knockout *Myd88* (Anitha et al., 2012) is not neuronal-specific. Use of this Cre line will remove *Myd88* from enteric glial cells, where *Myd88* plays a key role in mediating intestinal inflammation (Ibiza et al., 2016). Nevertheless, scRNAseq data suggests the expression of *Tlr* and *Myd88* by murine iEAN (Zeisel et al., 2018). However, this pool of mRNA is not necessarily indicative of functional expression. Confirmation of expression by *in situ* hybridization coupled with neuronal-specific conditional knockouts for PRR genes would bolster these previous observations. Certainly it may be possible for microbial metabolites to directly modulate iEAN, as has been seen in other peripheral neuron populations such as the DRG (Chiu et al., 2013; Sessenwein et al., 2017b). Finally, iEAN detection of the microbiota could be achieved

through responses to signals derived from cells that can intrinsically respond to bacteria such as EEC (Nøhr et al., 2013; Worthington et al., 2017), immune cells (Diehl et al., 2013; Seo et al., 2015), and enteric glia (Ibiza et al., 2016; Kabouridis et al., 2015).

Given the proximity of iEAN to the gut lumen and the commensal microbiota, as well as deep integration into the surrounding tissue, it is likely that these neurons are equipped to monitor the luminal microbiota in other capacities. Leveraging of current single-cell databases (Drokhlyansky et al., 2019; Zeisel et al., 2018) in combination with gnotobiotic manipulations could give insight into how specific types of bacteria are detected or influence iEAN function, development, and maintenance.

6.3.2 iEAN-intrinsic control of blood glucose

The control of blood glucose involves a complex network of cross-organ communication including the gut, liver, adipose tissue, brain, kidneys, skeletal muscle and pancreas (Kowalski and Bruce, 2014; Previs et al., 2009; Roh et al., 2016). The primary role of the intestine in glucose regulation is through absorption of glucose, release of satiety hormones, and secretion of incretins (Holst et al., 2016). Recent work has implicated the distal intestine in the production of glucose, termed intestinal gluconeogenesis, that is thought to be able to supplement liver gluconeogenesis (Croset et al., 2001; Koh et al., 2016). There is also anatomical evidence that the gut may be able to control the pancreas directly, these neurons have been termed entero-pancreatic (Kirchgessner and Gershon, 1990; Kirchgessner et al., 1996). Despite their description, these entero-pancreatic neurons have never been formally interrogated to determine

whether they can indeed influence pancreatic function or possibly integrate pancreatic information. In our studies we did not detect labeling of duodenal iEAN at one-day post PRV injection when we might expect to see these first-order connections as we see in the CG-SMG. We also did not detect duodenum-labeled neurons after AAV9 injection in the distal intestine, despite our observation that duodenum-ileum connections do exist (unpublished observations). Therefore, the finding that distal gut neurons can potently control blood-glucose presents a novel concept in the field of glucose regulation. It will be important to investigate this glucoregulatory iEAN population in the context of human metabolic diseases, as the ability to target the gut presents an attractive target amenable to pharmacologic or even viral treatments. This work begs the question as to whether the gut, and specifically iEAN, are directly integrated into other homeostatic functions such as the control of systemic immunity or blood pressure.

Viscerofugal neurons are thought to be involved in mediating an intestino-intestinal inhibitory reflex (Hibberd et al., 2012; Palmer et al., 2016) thus we were surprised to find that activation of this subset did not lead to any appreciable change in gastro-intestinal transit time. While the effects of viscerofugal neurons have been primarily been implicated in the control of gastro-intestinal motility (Hibberd et al., 2012; Luckensmeyer and Keast, 1998; Semba, 1954; Szurszewski et al., 2002), this hypothesis has never been formally tested through selective activation of iEAN. It may very well be that an effect on GI-motility would be too restricted to pick up with this measure. However, given how little is known about this population of iEAN it is intriguing to think of these neurons as a diverse set of sympathetic specialists. Through a combination of chemogenetics and diptheria

toxin ablation we have established that distal gut CART+ viscerofugal neurons are a necessary component of murine glucose regulation. While this CART+ population appears gluco-regulatory through connections to the pancreas and liver, there likely exist additional subpopulations that could potentially control sympathetic innervation to other visceral organs including the spleen, kidneys, gall bladder, adrenals, and any associated visceral white adipose tissue (Burnstock, 1969a, 1969b; Chi et al., 2018; Prüss et al., 2017; Ueno et al., 2016). To better understand whether diverse populations of viscerofugal neurons exist, retrograde tracing coupled with single-cell transcriptional profiling or TRAP of additional viscerofugal populations along the length of the small and large intestine could yield useful insights. Our anatomical tracing suggests that the majority of CART+ viscerofugal neurons originate from the ileum. However, it will be necessary to explicitly test whether ileum viscerofugal neurons alone are required by performing chemogenetic activation and DTA-mediated ablation in the distal ileum or proximal colon only. We also demonstrated that CART+ chemogenetic activation could increase cFos in the CG-SMG. Whether CART itself plays a role in changing sympathetic activity remains to be seen. Prior attempts to elucidate peripheral functions of CART failed to detect changes in GI motility or feeding behavior when CART was given systemically, whereas central administration of CART induced robust phenotypes (Ekblad, 2006; Lau and Herzog, 2014).

What are the signals that normally regulate the activity of this population of neurons? We can formulate four possible routes by which CART+ neurons are modulated: direct detection of luminal contents, mechanical distention based on

classically ascribed mechanosensitive viscerofugal function (Hibberd et al., 2014), IPAN direct detection of luminal ligands, or the release of epithelial-derived neurotransmitters and neuropeptides. When we examined the tissue distribution of CART+ neurons in the ileum and colon using cleared-tissue and confocal imaging, we did not observe nerve fibers that extended to the mucosa. Thus, we find it unlikely that these CART+ neurons are directly sensing changes in the lumen of the gut. If this population viscerofugal neurons is inherently mechanosensitive, then they may be tuned to respond to the arrival of chyme that has made its way from the stomach. Alternatively, initiation of the gastroileal or gastrocolic reflex, designed to propel fecal matter through the lower intestine when the stomach is activated by food, could be a trigger for the activation of these neurons (Tansy and Kendall, 1973). Glucose-responsive iEAN have been previously identified in the ileum of guinea pigs (Liu et al., 1999). Integration of luminal glucose through IPANs could then be performed by CART+ viscerofugal iEAN. A final possibility is that IPANs are responding to the release of EEC-derived signals, which are acting as the primary luminal sensors. Based on the work of Borhquez and colleagues, it is likely that EECs and neuropods are synaptically integrated into local iEAN networks in a similar fashion to what is described for vagal afferents (Bohórquez et al., 2015; Kaelberer et al., 2018). Additionally the distal gut is the major site for release of the incretin, GLP-1 (Song et al., 2019; Varin et al., 2019). GLP-1 producing EECs, L-cells, can be activated by a variety of signals including glucose and SCFA (Christiansen et al., 2018; Reimann et al., 2008; Wichmann et al., 2013). We and others have found expression of *Glp1r* in iEAN (Drokhlyansky et al., 2019; Zeisel et al., 2018), thus specific luminal signals that drive

EEC release of GLP-1 can potentially modulate iEAN activity. Calcium imaging of virally transduced or transgenically driven GCaMP in iEAN or CART+ iEAN specifically would be an important next step to determine the range of viscerofugal modulatory stimuli. It would be possible to take advantage of our intestinal intravital 2-photon imaging preparation to deliver luminal stimuli while recording GCaMP fluorescence in the myenteric plexus.

It would also be interesting to investigate whether there are changes in CART+ viscerofugal neurons in mouse models of diabetes. For example, it has been reported that high fat diet can lead to dysbiosis and subsequent enteric neuronal loss (Anitha et al., 2016; Nyavor et al., 2019). Based on our findings that CART+ viscerofugal loss leads to hyperinsulinemia, this could be a possible contributing factor to insulin resistance that precedes type 2 diabetes (DeFronzo et al., 2015). On a related note, the glucoregulatory properties of distal ileum neurons might be an additional factor in the effectiveness of gastric bypass surgery to induce type 2 diabetes remission (Dixon et al., 2008; Harris et al., 2019). While much of the benefit of gastric bypass is thought to be the result of caloric restriction and enhanced EEC glucoregulatory peptide production due to shunting of nutrients to the distal small intestine (Batterham and Cummings, 2016), it is possible that effects of altered distal gut nutrient detection on CART+ glucoregulatory iEAN could modulate insulin secretion in a beneficial manner.

Beyond interrogation of viscerofugal populations, the majority of iEAN in the myenteric and submucosal plexuses in general have yet to be functionally characterized. Some work has begun to probe network dynamics through calcium imaging in different

areas of the intestine (Lasrado et al., 2017; Li et al., 2019b), which is crucial for understanding how iEAN are connected and in what manner excitation or inhibition is propagated. Nevertheless, targeted *in vivo* chemogenetics and, if feasible, optogenetics will be required to not only confirm classically ascribed iEAN functions, but to uncover further novel roles.

6.5 Conclusion

The gut microbiota is a key component of mammalian physiology, with a significant impact on development, metabolism, immune function, and the nervous system. The bulk of research into microbiota effects on the nervous system have been centered around the CNS, while the periphery, particularly the locally integrated EANS in the gut, has been largely overlooked. Our goal in this thesis work was to uncover how the EANS, is impacted by changes in the microbiota. Based upon the work presented here, we find that the sympathetic nervous system is emerging as the main hub in mediating the physiological and immunological effects of changes in the gut microbial environment. This sympathetic view presents an alternative to the large body of work that has focused on the vagus and its parasympathetic effects. It will be exciting to see how mammalian sympathy for the microbiota fits into additional components of mammalian physiology and disease in the future.

Materials and Methods

Animals

Arg^{YFP}(*Arg1*$^{tm1Lky/J}$), *Adrb1*^{tm1Bkk}*Adrb2*^{tm1Bkk}, C57BL/6J, *Cx3cr1*^{GFP}(*Cx3cr1*$^{tm1Litt/LittJ}$), *Rosa26*$^{LSL\text{-}GCaMP3}$, *Rosa26*$^{LSL\text{-}tomato}$, *Itgax*(CD11c)^{eYFP}, *Lyz2*$^{Cre/Cre}$ (*Lyz2*$^{tm1(cre)Ifo/J}$), *fos*^{GFP}(B6.Cg-Tg$^{(Fos/EGFP)1\text{-}3Brth/J}$), *Snap25*^{Cre}, *Rpl22*$^{tm1.1Psam/J}$, *Wnt1*^{Cre} and zDC^{DTR} mice were purchased from the Jackson Laboratories and maintained in our facilities. *Hand2*^{Cre} and *Th*^{Cre}, mice were generously provided by D. Clouthier (UC Denver) and J. Friedman (RU), respectively. Wild-type mice used: C57BL/6 (C57BL/6J, Jackson #000664 or C57BL/6NTac, Taconic #B6-M/F), CBA/J (Jackson #000656), BALB/cJ (Jackson #000651). Transgenic mice used: *Fos*^{GFP} (B6.Cg-Tg(Fos/EGFP)1-3Brth, Jackson #014135), RiboTag (B6N.129-*Rpl22*$^{tm1.1Psam}$, Jackson #011029), *Snap25*^{cre} (B6;129S-*Snap25*$^{tm2.1(cre)Hze}$, Jackson #023525), *Rosa26*$^{lsl\text{-}hM4Di}$ (B6N.129-*Gt(ROSA)26Sor*$^{tm1(CAG\text{-}CHRM4*,\text{-}mCitrine)Ute}$, Jackson #026219), *Rosa26*$^{lsl\text{-}tdTomato}$ (B6.Cg-*Gt(ROSA)26Sor*$^{tm14(CAG\text{-}tdTomato)Hze}$, Jackson #007914), *Vgat*^{cre} (*Slc32a1*$^{tm2(cre)Lowl}$, Jackson #016962), *Chat*^{cre} (B6;129S6-*Chat*$^{tm2(cre)Lowl}$, Jackson #006410). SNS^{cre} (Tg(*Scn10a*^{cre})1Rkun, gift of R. Kuhner), *Nav1.8*^{cre} (*Scn10a*$^{tm2(cre)Jnw}$, gift of J. Wood), *Vgat*^{cre} (*Slc32a1*$^{tm2(cre)Lowl}$, Jackson #016962), *Advillin*^{CreERT2} (B6.Cg-Tg(*Avil*-icre/ERT2)AJwo/J Jackon # 026516), *Vglut2*^{cre} (*Slc17a6*$^{tm2(cre)Lowl}$/J, Jackson #016963), *Glp1r*^{cre} (*Glp1r*$^{tm1.1(cre)Lbrl}$/J, Jackson #029283), *Phox2b*^{cre} (B6(Cg)-Tg(Phox2b-cre)3Jke/J, Jackson #016223), *Villin*^{creERT2} (Tg(*Vil*-cre/ERT2)23Syr), *Fos*^{TRAP2} (*Fos*$^{tm2.1(icre/ERT2)Luo}$/J, Jackson #030323) *Tph1*^{flox} (*Tph1*^{tm1Kry}, gift of G. Karsenty), *Htr3a*^{Cre} (Gift of N. Heintz), Glp1r^{tm1Ddr} or *Glp1r*$^{-/-}$ (gift of D. Drucker and generously provided by J. Ayala), *Gpr43*$^{-/-}$ (Gift of N. Arpaia), *Gpr43*$^{-/-}$/*Gpr109a*$^{-/-}$

(gift of S. Mehandru), *Gpr41*$^{-/-}$ (gift of J. Gordon and M. Yanagisawa, generously provided by J. Pluznick), *Cart*^{Cre} (B6;129S-Cartpttm1.1(cre)Hze/J, Jackson #028533), *Npy*^{Cre} (B6.Cg-Npytm1(cre)Zman/J, Jackson #027851), *Agrp*^{Cre} (Agrptm1(cre)Lowl/J, Jackson #012899), *Casp1*$^{-/-}$ *Casp11*$^{-/-}$(B6N.129S2-Casp1tm1Flv/J, Jackson #016621), *Casp11*$^{-/-}$ (Casp4tm1Yuan/J, Jackson #024698) *Nlrp6*$^{flox/flox}$ by P. Rosenstiel (targeting of Exon 1 of *Nlrp6*, frozen sperm generously provided by T. Kanneganti), and *Casp11*$^{flox/flox}$ by KOMP and A. Wullaert, *Arg1*$^{flox/flox}$ (C57BL/6-*Arg1*^{tm1Pmu}/J), Rosa26^{tdTomato} (B6.Cg-Gt(ROSA)26Sor$^{tm14(CAG-tdTomato)Hze}$/J), VGLUT2^{Cre} (*Slc17a6*$^{tm2(cre)Lowl}$/J), *Rpl22*^{HA} (B6N.129-Rpl22$^{tm1.1Psam}$/J), 129S1(129S1/SvImJ) , CBA/J, *Cx3cr1*^{GFP}(*Cx3cr1*$^{tm1Litt/LittJ}$), *Phox2b*^{cre} (B6(Cg)-Tg(Phox2b-cre)3Jke/J), *Snap25*^{Cre}(*Snap25*$^{tm2.1(cre)Hze}$), NSG (NOD.Cg-*Prkdc*^{scid}*Il2rgtm1*^{Wjl}/SzJ), *Casp11*$^{-/-}$ (Casp4tm1Yuan/J) , and R26-CAG-ASC-citrine (B6.Cg-Gt(ROSA)26Sortm1.1(CAG-Pycard/mCitrine*,-CD2*)Dtg/J), *Plp1*^{creERT} (B6.Cg-Tg(Plp1-cre/ERT)3Pop/J), *Rosa26*$^{lsl-hM4Di}$ (B6N.129-*Gt(ROSA)26Sor*$^{tm1(CAG-CHRM4*,-mCitrine)Ute}$), and ROSA-DTA (B6.129P2-*Gt(ROSA)26Sortm1(DTA)*Lky/J) were purchased from The Jackson Laboratories and maintained in our facilities. SNS^{cre} (Tg(*Scn10a*^{cre})1Rkun were a gift of R. Kuhner, *Nestin*^{GFP} (Tg(Nes-EGFP)33Enik were generously provided by P. Frenette and G. Enikolopov, *Adrb2*$^{flox/flox}$ (Adrb2^{tm1Kry}) by G. Karsenty, Sox10^{CreERT2} (Tg(Sox10-icre/ERT2)26Vpa) were generously provided by B. Gulbransen and V. Pachnis, *Nlrp6*$^{flox/flox}$ by P. Rosenstiel (targeting of Exon 1 of *Nlrp6*, frozen sperm generously provided by T. Kanneganti), and *Casp11*$^{flox/flox}$ by KOMP and A. Wullaert. Gnotobiotic mice used: Germ-Free (GF) C57BL/6, *Snap25*^{RiboTag}, SFB-mono-colonized, ASF-colonized (Rockefeller University), GF C57BL/6J (gift of J. Faith), GF

C57BL/6J 6J and *Clostridium spp.* colonized mice (gift of D. Artis and G. Sonnenberg). Mice were bred within our facility to obtain strains described and were 7-12 weeks of age for all experiments unless otherwise indicated. For comparisons to GF mice, mice were maintained on sterilized Autoclavable Mouse Breeder Diet (5021, LabDiet, USA), the same used in the gnotobiotic facility. Female mice were used for all sequencing experiments. Male and female mice were used for all other experiments. Animal care and experimentation were consistent with NIH guidelines and approved by the Institutional Animal Care and Use Committee (IACUC) at The Rockefeller University.

Microorganisms. *Salmonella enterica* serovar Typhimurium (SL1344) and its mutant *spiB* were used for infection experiments and cultured prior to infection as described below. *Yersinia pseudotuberculosis* (IP32777) was cultured prior to infection as described below. *S. venezuelensis* was maintained in our facility by periodically infecting NSG mice and culturing larvae as described below. *Toxoplasma gondii* was maintained in our lab by periodically infecting C57BL/6 mice with 5 cysts administrated intraperitoneally (i.p.). Cysts were isolated from brain tissue 30 days after infection. *Trypanosoma cruzi*. The *T. cruzi* Y strain was maintained by serial passage from mouse to mouse.

Method Details

Infections. *Salmonella enterica* Typhimurium. For infections with *Salmonella spiB*, mice were pre-treated with a single dose of Streptomycin (20 mg/mouse dissolved in 100 μl of DPBS) administered by oral gavage 18-24 hours prior to infection Mice were then orally

inoculated with 10^9 CFU of *spiB*. For *Salmonella* re-infection experiments, mice were subjected to *spiB* infection as described above. 1 week post-clearance of *spiB* from the feces, mice were fasted for 4 hours and infected with 10^6 CFU of wild-type *Salmonella enterica* Typhimurium (SL1344). For all *Salmonella* infections, a single aliquot of either strain of *Salmonella* was grown in 3 ml of LB overnight at 37 ºC with agitation. Bacteria were then sub-cultured (1:300) into 3 ml of LB for 3.5 hours at 37 ºC with agitation, and diluted to final concentration in 1 ml of DPBS. Bacteria were inoculated by gavage into recipient mice in a total volume of 100 µl. For experiments using heat-killed *spiB*, samples subjected to heat treatment (95 °C for 10 min in water bath), prior to gavage and successful inactivation was confirmed by plating a serial dilution made from the suspension and then 5 µL onto Salmonella-Shigella plates.

Yersinia pseudotuberculosis. *Y. pseudotuberculosis* (strain IP32777) was grown as previously described with some adjustments (Fonseca et al., 2015). Briefly a single aliquot of the strain was grown in 3 ml of 2xYT media overnight at 28°C with vigorous agitation. Mice were fasted for 12 hours prior to infection with 10^8 CFU by oral gavage.

For heterologous re-infection experiments, mice infected with *spiB* or *Y. pseudotuberculosis* as described above were subjected to either 10^8 of *Y. pseudotuberculosis* or 10^9 CFU of *Salmonella spiB* on day 21 days post-infection with *spiB* or *Y. pseudotuberculosis* infection, and sacrificed 10 days post-secondary infection.

Strongyloides. venezuelensis. S. venezuelensis was maintained in our facility in NSG mice by subcutaneous infection with 700 larvae, resulting in chronic infection of this strain. For each experiment, feces of infected NSG mice were collected and spread on Whatman

paper, which was placed into a beaker with water and incubated at 28 °C. The hatching larvae were collected over 2-3 days. Mice were infected subcutaneously with 700 larvae/100 µl water per mouse. *S. venezuelensis* was passaged by periodically infecting naïve adult NSG mice.

Toxoplasma gondii. *T. gondii* was maintained in the lab by periodically infecting mice administered by intraperitoneal injection of 5 cysts/mouse in a total volume of 100 µl of DPBS.

Trypanosoma cruzi (*T. cruzi, Y strain)*. For each experiment, blood from an infected mouse was collected, parasites were quantified and naïve recipient mice infected by intraperitoneal injection of 10^4 parasites. Infected mice were sacrificed for tissue analysis at day 22 post-infection, when the parasite load reaches a plateau (Arantes et al., 2004).

Antibodies and flow cytometry. *Antibodies used for whole-mount immunofluorescence imaging.* The following primary antibodies were used, and unless otherwise indicated concentrations apply to all staining techniques: Somatostatin (1:200, Millipore Sigma, MAB354) , ANNA-1 (1:200,000, Gift of Dr. Vanda A. Lennon), HA (1:400, Cell Signaling Technologies, 3724S), nNOS (1:200, ABCAM, ab76067), MHC II (1:400, Millipore Sigma, MABF33), S100 beta (1:200, Abcam, ab52642), ASC (1:200, Adipogen, AL177), GFP (1:400, Nacalai, GF090R). Fluorophore-conjugated secondary antibodies were either H&L or Fab (Thermo Fisher Scientific) at a consistent concentration of 1:400 in the following species and colors: Goat anti-rabbit (AF488/568/647), goat anti-rat (AF488/647), goat anti-chicken (AF488/568/647), goat anti-human (AF568/647).

Antibodies used for cell sorting of intestinal macrophages: Fluorescent-dye-conjugated antibodies were purchased from BD-Pharmingen (USA) (anti-CD45.2, 104; anti-CD45R, RA3-6B2); eBioscience (USA) (anti-CD103, 2E7; anti-MHC II, M5; anti-F4/80, BM8; anti-CD11b, M1/70; anti-CD11c, N418; anti-Siglec F, E50-2440; anti-CD3e,145-2C11; anti-Ly6G, RB6-8C5) or BioLegend (USA) (anti-CD64 X54-5/7.1). Live/Dead staining was performed using Aqua fixable dead cell stain (Invitrogen). Macrophages were sorted as Aqua–CD45+Lin–(CD3–B220–Siglec F–LY6G–) MHCII+F4/80+CD11B+CD11C+CD103–) using a FACS Aria cell sorter flow cytometer (Becton Dickinson).

Ileal smooth muscle contractility. Ileal ring tension was assessed by organ bath (Radnoti) myography as previously described (Muller et al., 2014). Briefly, distal ileal rings were mounted and equilibrated for one hour and were distended to 0.5 g followed by 10 minutes of relaxation. The data was acquired using the PowerLab acquisition system and analyzed using LabChart Software (AD Instruments).

Lipocalin-2 ELISA. Lipocalin-2 levels in fecal samples were quantified using a Mouse Lipocalin-2 ELISA kit (R&D Systems) according to manufacturer's instructions.

Drug Administration. *Salbutamol.* Salbutamol sulfate (Selleck Chemicals) was dissolved in sterile NaCl to a concentration of 56 mg/ml, loaded into osmotic pumps and

administered by subcutaneous osmotic pumps implanted as described below at a final dose of 400 μg/day for 14 days.

Pan caspase inhibition. zVAD-FMK (Selleck Chemicals) was dissolved in DMSO and administered at a dose of 50 μg/mouse by daily intraperitoneal injections over the course of a 7-day infection starting 1 day prior to infection.

Polyamine administration. Spermine (Sigma-Aldrich) was administered at a concentration of 2% in drinking water. Spermine-substituted drinking water was changed daily and fluid intake was monitored. Treatment was started 3 days prior to infection with *Salmonella spiB* and continued over the course of experiments.

ODC1 inhibition. Difluoromethylornithine (DFMO, gift from P. Woster, MSSM) was dissolved in tap water, filter-sterilized, and administered at a concentration of 4% in drinking water. DFMO-substituted water was changed daily, and fluid intake was monitored. Treatment was started 4 days prior to infection with *Salmonella spiB* and continued over the course of experiments.

Isoflurane induction. A plexiglass induction chamber was placed on a heating pad set to 37°C. Isoflurane was set at 1% with an oxygen flow of 1 liter/minute. Mice were placed in the induction chamber and monitored for loss of movement, after which a period of 15 minutes was elapsed. Respiration was monitored continuously during this period. Following isoflurane treatment, mice were returned to their home cage for a period of 1 hour prior to receiving Streptomycin pre-treatment, followed by *spiB* infection as described above.

Sham intraperitoneal injections. Sham intraperitoneal injections of DPBS or IgG (isotype control from MM depletion experiments, see below) were performed by mimicking the anti-CSF1R MM depletion protocol, by intraperitoneal injection of 200 μl of DPBS or IgG/ mouse (100 μl/flank). Injections were performed 12 hours prior to *spiB* infection, and an additional injection was performed at day 3.5 post-infection. Mice were sacrificed and tissue was analyzed at 7 days post-infection.

Subcutaneous pump implantation. Mice were anesthetized using isoflurane and, under sterile conditions, a small incision was made on the dorsal side of the neck. An Alzet pump (Model 1002) filled with Salbutamol sulfate prepared as described above was placed under the skin and moved back towards the right flank. The incision was then closed with surgical wound clips (Kent Scientific). Mice were then left to rest for 7 days before infection with *spiB*.

Adrenalectomy. Mice were anesthetized using isoflurane and, under sterile conditions, bilateral incisions were made dorsally just below the rib cage. The adrenal glands were then grasped by forceps from the suprarenal blood vessels and extracted from the surrounding tissue. Care was taken to minimize any bleeding before the muscle incision was closed with absorbable sutures. Surgical wound clips were then used to close the skin. Mice were then kept on 0.9% saline drinking water for 9 days prior to infection with *spiB*.

Generation of *Nlrp6*$^{flox/flox}$ mice. The *Nlrp6*$^{flox/flox}$ strain was generated by Flp-Neo-mediated insertion of loxP sites flanking exon 1 of the *Nlrp6* locus. ES cells were used to generate the conditional knockout allele. The strain was generated in collaboration with genoWay (Lyon, France).

Antibiotic-mediated microbiota depletion and recolonization. 7 days post-oral gavage with *spiB* mice were given drinking water supplemented with 10g/L Splenda (artificial sweetener, control), or broad-spectrum antibiotics (1g/L ampicillin, 0.5g/L vancomycin, 1g/L neomycin, 0.5g/L metronidazole) in the drinking water supplemented with 10g/L Splenda for 2 weeks. Mice on antibiotics were then put onto Splenda-containing water and all mice were given feces from an uninfected cage of age-matched C57BL/6J mice. All tissues were then harvested 2 weeks after recolonization.

Anti-CSF1R (ASF98) antibody production. Anti-CSF1R was produced by suspension culture of the ASF98 hybridoma cell line (gift from Miriam Merad). Cells were thawed and passaged twice (1:10) in PFHM-II (Thermo Fisher) media supplemented with P/S (Thermo Fisher). Cells were then seeded at $5x10^6$ in 15 mL of PFHM-II in the cellular compartment of a 1000 mL bioreactor (Wheaton) and allowed to grow for 7-10 days. The cell compartment was then harvested, spun down and the supernatant collected. Supernatant was filtered and antibody was purified from the supernatant by affinity purification using protein G sepharose (GE Healthcare) in a gravity column (Bio-Rad).

Briefly, the protein G was equilibrated with 100 mL binding buffer (Thermo Fisher Scientific) and supernatant was loaded onto and run through the column. The column was then washed with 200 mL of binding buffer and eluted with 10 mL elution buffer (Thermo Fisher Scientific). Antibody was eluted in fractions directly into 100 μl 1 M Tris-HCL pH 8 (Invitrogen) and the concentrations were measured on a Nanodrop 2000 spectrophotometer (Thermo Fisher Scientific). Fractions were combined and dialyzed in 2 L DPBS for 2 days at 4°C using 14,000 MWCO dialysis tubing (Spectrum Labs) changing once. The antibody was then concentrated using centrifugal filters (30,000 MW, Amicon) and stored at 4°C until use.

MM depletion using anti-CSF1R. Anti-CSF1R was diluted in sterile DPBS to a final concentration of 6.25 mg/ml and 50 mg/kg of anti-CSF1R or isotype control (IgG from rat serum, Sigma-Aldrich) were administered by i.p. injections. Mice were previously habituated to i.p. injections for at least 5 days prior to the start of depletion and *spiB* infection. For all experiments, depletion was performed twice over the course of 7 days (day 0 and day 3.5). For infection experiments, depletion was performed 12 hours prior to infection. Animals were then subjected to the *Salmonella spiB* infection protocol as described above, and received and additional dose of either anti-CSF1R or isotype control 3.5 days after the initial dose. Animals were sacrificed at 7 dpi and intestinal tissue dissected for analysis.

Immunocytochemistry. Cuprolinic blue staining for visualization of enteric neurons was performed as previously described (Holst and Powley, 1995). The method was utilized for quantification of enteric neurons in *T. gondii* and *T. cruzi* infection experiments.

Mining of published iEAN scRNA-seq. The published single-cell analysis of the mouse nervous system at mousebrain.org/genesearch.html (PMID: 30096314) was searched for *Nrlp6* and filtered for clusters that express the gene at a trinarization score >= 0.95. Relative expression was then plotted as a heatmap in Prism 8. *Vglut2*+ subsets were defined based on the same single-cell analysis.

Cryosectioning of fresh-frozen tissue. Mice were given a lethal dose of isoflurane and then perfused with 30 ml ice cold DPBS. The ileum and colon were removed and flushed of luminal contents. The tissue was then transferred to OCT, positioned, flash frozen, moved to -20 for 2 hours, and finally moved to -80 for long term storage. Prior to cryosectioning, OCT blocks were equilibrated in the cryostat for 20 minutes. Sections were cut at 15 μm, put onto SuperfrostPlus slides, and left to dry for 10-15 minutes. Slides were then transferred to dry ice and finally to -80°C before RNAscope® processing.

RNA fluorescence *in situ* hybridization (FISH) using RNAscope® technology. RNAscope® *in situ* hybridization was performed using probes against *Nlrp6* and *Elavl4* on 15 μm sections of fresh frozen ileum or colon tissue isolated from C57BL/6J mice according to the manufacturer's instruction with the following modification, tissue was

pretreated with Protease IV for 20 min at RT. Samples were then mounted in Fluoromount-G with DAPI and 1 ½ coverslips were applied.

Neuronal quantification. A minimum of 10 images were randomly acquired across a piece of whole-mount *muscularis*. These images were then opened in ImageJ, and the cell counter was used to count the number of ANNA-1+ cells in a given field. This number was then multiplied by a factor of 2.95 (20x objective) or 3.125 (25x objective), to calculate the number of counted neurons per square millimeter (mm^2). The average of 10 (or more) images was then calculated and plotted. Thus, every point on a given graph corresponds to a single animal. For determining iEAN subtype changes, the number of nNOS+, SST+, and tdTomato+ neurons were also counted. These numbers were then reported as both number per mm^2 and percent of ANNA-1+ neurons.

Macrophage intercalation calculation. Raw data as imported from the microscope was used for all cell identification and subsequent analyses. Some post –analysis pseudo-color adjustment was performed for individual images to account for differences in auto-fluorescence and labeling. *Imaris* (Bitplane AG) software was used for cell identification, using the "*Surfaces*" algorithm as described by the manufacturer. A surface was created based on anti-ANNA-1 (neuron) staining to define neuronal ganglia. A masked channel was then created to capture fluorescence in other channels within the neuronal ganglia volume. A second surface was created based on anti-MHCII (macrophage) staining only within the masked channel. Volume statistics on both neuron (total) and macrophage

(neuronal ganglia masked) surfaces were then exported. Percent macrophage intercalation per image was calculated as:

$$Macrophage\ Intercalation = \frac{(\Sigma(Macrophage\ surface\ volumes) + \Sigma(Neuronal\ ganglia\ surface\ volumes)}{\Sigma(Neuronal\ ganglia\ surface\ volumes)} \times 100$$

The average of at least 10 random macrophage intercalation percentages was used to determine the percentage for each individual animal.

3D image reconstruction for MM ganglionic intercalation calculations. Images were adjusted post hoc using Imaris x64 software (version 9.1 Bitplane) and 3D reconstructions were recorded as mp4 video files. Optical slices were taken using the orthoslicer or oblique slicer tools.

Colony forming unit counting. Fecal pellets from *Salmonella spiB*-infected mice were weighed and then disrupted in 400 μL of DPBS. Serial dilutions were made from the original suspension and then 5 μL of each dilution was plated onto Salmonella-Shigella plates. The plates were then incubated overnight and the number of black colonies were counted for the serial dilution with the clearest delineation of single units. This number was then multiplied by the dilution factor and by 80 to give the number of colony forming units (CFU) in the original suspension. CFU numbers were then divided by the original fecal pellet weight to give the number of CFU per mg of feces.

Determination of caspase 11 mutation status by PCR and Sanger Sequencing. DNA was extracted from ear pieces of mice using QuickExtract™ DNA Extraction Solution (Lucigen). Target sequences were amplified using the following primers: Forward 5'-AGGCATATCTATAATCCCTTCACTG-3'; Reverse 5'-GAATATATCAAAGAGATGACAAGAGC- 3'. The following PCR conditions were used: 4 min 94°C, 1 min 94 °C, 0.5 min 58°C, 1 min 72 °C, 7 min 72 °C, and end at 12 °C. Samples were loaded on 3% agarose gels, and bands from all strains were compared to samples from C57BL/6J and 129S mice. The 5 bp deletion in *Casp11* described in the 129S1 strain fragment runs slightly higher than the wild-type fragment at a height of approximately 220 bp (Vanden Berghe et al., 2015). *Casp11* mutation status was further confirmed in C57BL/6J, CBA/J and 129S1 mice by Sanger sequencing of a gel-purified PCR product using primers 5′-CAGTATTATTATTGGTGATGCAAATG-3′ and 5′-GGAATATATCAAAGAGATGACAAGAGC-3′. *Casp11* mutation status was also confirmed in further relevant mouse strains utilized in this study.

Single Cell Suspension of Intestinal Macrophages. Mice were euthanized, and the small intestine was carefully removed, cleaned, cut open longitudinally and washed 2X in HBSS $Mg^{2+}Ca^{2}$Gibco) and 1X in HBSS $Mg^{2+}Ca^{2}$ with 1 mM DTT (Sigma- Aldrich). The tissue was cut in two and the *muscularis* region was carefully dissected from the underlying mucosa. *Muscularis* tissue was then finely cut and digested in HBSS $Mg^{2+}Ca^{2+}$+ 5% FBS + 1x NaPyr + 25mM HEPES + 50 µg/ml DNase I (Roche) + 400 U/ml Collagenase D (Roche) + 2.5U/ml Dispase (Corning) at 37°C. The *muscularis* was digested for 40 min. The tissue was then homogenized with an 18-gauge needle, filtered

through a 70 µm cell strainer and washed with HBSS $Mg^{2+}Ca^{2}$. Cells were incubated with Fc block and antibodies against the indicated cell surface markers in FACS buffer (PBS, 1% BSA, 10 mM EDTA, 0.02% NaN_3).

Quantitative PCR. Total RNA was isolated using TRIzol™ (Invitrogen), from which cDNA libraries were reverse transcribed using Superscript II (Invitrogen) and random primers following the instructions provided by the manufacturer. Quantitative PCR (qPCR) was performed using SYBR green (Bio-Rad Laboratories). Data were collected and analyzed on a QuantStudio 3 (Thermo Scientific). The *Rpl32* housekeeping gene was used to normalize samples. For TRAP-qPCR, RiboTag purified mRNA was reverse transcribed using iScript cDNA Synthesis Kit (BioRad) and qPCR was performed using SYBR green (Bio-Rad Laboratories). The following primers were used: *Rpl32* forward 5'-ACAATGTCAAGGAGCTGGAG-3', *Rpl32* reverse 5'- TTGGGATTGGTGACTCTGATG-3', *Arg1* forward 5'-CTCCAAGCCAAAGTCCTTAGAG- 3', *Arg1* reverse 5'-AGGAGCTGTCATTAGGGACATC-3', *Ym1* forward 5'-AGACTTGCGTGACTATGAAGCATT-3', *Ym1* reverse 5'-GCAGGTCCAAACTTCCATCCTC- 3', *Nlrp6* exon 4 forward 5'-CAGACGCTGTGGACCTTGT-3', *Nlrp6* exon 4 reverse 5'-ACGTGCTCGCGGTACTTCTT- 3', *Nlrp6* exon 1 forward 5'-TTGACTGTCAGCAAGAGTCC-3', *Nlrp6* exon 1 reverse 5'-GGTGATCCTTTCTGGGCTAAA-3', *Elavl4* forward 5'-GATCAGGGATGCTAACCTGTATG-3', *Elavl4* reverse 5'-GGTGATGATGCGACCGTATT-3', *Nos2*-forward 5'-

GTTCTCAGCCCAACAATACAAGA-3', *Nos2*-reverse 5'-GTGGACGGGTCGATGTCAC-3'; *Il12b*-forward 5'-TGGTTTGCCATCGTTTTGCTG-3', *Il12b*-reverse 5'-ACAGGTGAGGTTCACTGTTTCT-3'; *Adrb2*-forward 5'-TAGCGATCCACTGCAATCAC-3', *Adrb2*-reverse 5'-ATTTTGGCAACTTCT-3'; *Il10*-forward 5'-CCCATTCCTCGTCACGATCTC-3', *Il10*-reverse 5'-TCAGACTGGTTTGGGATAGGTTT-3'; *Il1b*-forward 5'-TCGTGCTGTCGGACCCATAT-3', *Il1b*-reverse 5'-GTCGTTGCTTGGTTCTCCTTGT-3'; *Il6*-forward 5'-ACCAGAGGAAATTTTCAATAGGC-3', *Il6*-reverse 5'-TGATGCACTTGCAGAAAA-3'; *Th*-forward 5'-CAGGAACTATGCCTCTCGTATC-3', *Th-reverse* 5'GAGGACTGTCCAGTACATCAAT-3'*; Dbh*-forward 5'-GATCTCATCATGCTCTGGACTG-3'*, Dbh*-reverse 5'-CTG GTA GTC TTG CTG GGA ATC-3'. To calculate a fold change, the final qPCR cycle of 45 was chosen in cases in which there was no amplification. This was comparable to water, which was used as a control and did not amplify.

Neuron Calcium Signaling Quantification

IVM movies from *Hand2*^{GCaMP3}xCD11c^{eYFP} were analyzed using ImageJ. Circular regions of interest (ROI) were drawn over neuronal cell bodies. A separate ROI of identical size was placed over an area of the image corresponding to background. Gray scale values were determined for both neuronal ROIs and background ROIs at the initial frame as well as each subsequent frame. The following calculation was done to determine the fluorescence at each time point: $(F_n)10$, $n=1 = (EN_{ROI} - Background_{ROI})_n$

Enteric-associated neurons - Neurosphere Culture and Differentiation

Pregnant females approximately 18 days post-*coitum* were euthanized, their uteri were removed, placed on cold HBSS and the embryos subsequently dissected. The intestines were removed by manual dissection and placed in a 1.5 ml tube containing 1 ml of HBSS + 2% FBS. After chopping into small pieces, the tissue was centrifuged for 4 min at 400g and the supernatant was discarded. This process was repeated at least 3 times. The tissue was placed in a 48 well plate with 1ml HBSS + 0,05% trypsin-EDTA (Gibco) + 50□g/ml DNaseI (Roche) and digested for 15 min at 37°C. The cells were then mechanically dissociated, washed and resuspended in DMEM/F12 + 1X N2 (Gibco) + EGF-eFGF (20ng/ml) + 1x Antibiotic/Antimycotic (Gibco) and plated on a non-adherent plate. New media was added on the next day and every 4-5 days. EGF-eFGF (20ng/ml) was added every other day. After neurosphere expansion, cells were dissociated and plated on a 24-well adherent plate previously coated with fibronectin in NEUROBASAL media (Gibco) + 1X B27 (Gibco) for differentiation. After 15 days, cells were ready to be used for the co-culture experiments.

Cell culture and co-culture conditions

RAW 264 macrophages were cultured in Dulbecco's modified Eagle medium (DMEM) (Gibco) supplemented with 10% heat-inactivated FCS, 100 U/ml penicillin, 100 µg/ml streptomycin (all Sigma). Peritoneal macrophages were cultured on RPMI (Gibco) supplemented in the same way as DMEM. For the co-culture experiments, either peritoneal or RAW 264 macrophages were seeded into the plate that contained the

differentiated enteric neurons. The co-culture was maintained for 24 h in NEUROBASAL media (Gibco), and after this period, macrophages were sorted using a FACS Aria cell sorter flow cytometer (Becton Dickinson), and the conditioned media was collected and applied to previously cultured macrophages for 24 h, followed by RNA extraction using TRIZol (Invitrogen).

Drug Administrations

Butaxamine was used *in vivo* at a dose of 5mg/kg i.p., 5-10 min before gavage with the bacteria. For *in vitro* studies 100µM was added 30min prior to the co-culture experiments. Plated peritoneal macrophages were exposed to 100µM of Norepinephrine (Sigma) or 10µM of Salbumatol (Sigma) for 1 hour prior to analysis.

AAV9 Transduction of iEAN. *Casp11*$^{flox/flox}$ mice were retro-orbitally injected with ~5 x 10^{11} GC of AAV9-hSyn-HI-eGFP-Cre-WPRE-SV40 (105540-AAV9) or AAV9-hSyn-eGFP-WPRE-bGH (Addgene #105539-AAV9) diluted in 100 µl of sterile DPBS. Mice were then infected at least 2 weeks post-viral injection.

Induction of glia depletion. *Plp1*^{CreERT};Rosa26^{DTA} (*Plp1*^{iDTA}, Cre+) and Rosa26^{DTA} mice (Cre-) received a single oral gavage of 8 mg tamoxifen (Sigma) solubilized in 250 µl sterile corn oil (Sigma) at 6-7 weeks of age. Mice were infected with Salmonella *spiB* 5 days post-tamoxifen administration and sacrificed at day 6 post-infection (day 11 post-tamoxifen).

Total RNA Sequencing Analysis

RNA libraries from biological replicates were prepared using the SMARTer Ultra Low Input RNA for Illumina Sequencing kit (Clontech Laboratories) and sequenced using 50 base pair paired end reading on a HiSeq 2500 instrument (Illumina). The reads were aligned using the STAR version 2.3.0 software that permits unique alignments to Mouse Ensembl genes. Differential expression was determined by use of the Cufflinks software with default settings. Gene Ontology analysis was performed using DAVID (Database for Annotation, Visualization and Integrated Discovery).

cFos Quantification

Fos^{GFP} mice were given *Spib* or PBS by intragastric gavage and SMG-CG along with 6 cm of terminal ileum were dissected after 2 hours. The samples were then stained with anti-GFP-AF488 or anti-ELAVL4/TH followed by streptavidin-AF568 or goat-anti rabbit AF568 secondary antibodies, respectively. We attempted to capture all sympathetic neurons associated with the SMG-CG in separate images and took 10 random images from across each ileal sample. Fluorescent images of the SMG-CG and ileum were analyzed in Image-J. Each image was separated into two channels; GFP-AF488 and ELAVL4/TH-AF568. Using the Cell Counter plugin, the number of neurons and GFP+ nuclei were counted. The number of GFP+ nuclei were divided by the total number of neurons to give a percentage of activated neurons. Data from SMG-CG were represented

with each GFP+ neuronal nucleus quantified as an independent data point to properly capture all sympathetic neurons within this anatomical location.

Norepinephrine ELISA

Spib or DPBS was given by intragastric gavage and the cecum was removed after 2 hours. One third of the cecum was dissected including the ileum-cecal and colon-cecal junctions. Contents were removed and placed into 600 μL of norepinephrine stabilization buffer (10 mM HCl, 1 mM EDTA, 4 mM $Na_2S_2O_5$) and then homogenized. Homogenized cecal samples were spun at 4°C for 5 minutes 2,300 RCF. The supernatant was then collected and 100 μL was used to run a NE ELISA according to the manufacturer protocol (Labor Diagnostika Nord: BA E-5200 Noradrenaline Research ELISA).

Intravital Two-Photon Imaging

Mice were anesthetized with a ketamine/xylazine/acepromazine cocktail at 10 μl/g of body weight. 10 min following induction of anesthesia, mice were placed on a custom platform heated to 37°C. Isofluorane was given through a nose cone at a dose of 1.5% with 1% oxygen. Upon loss of recoil to paw compression, a small incision was made in the abdomen. The *ileum* entrance to the *caecum* was located and a loop of *ileum* was exposed and placed onto a raised block of thermal paste covered with a wetted wipe. A coverslip was placed on top of the loop to immobilize the intestine. The platform was then

transferred to the FV1000MPE Twin upright multiphoton system (Olympus) heated stage. A 25x heated objective was used and images were taken at 4-8us/pixel.

Diphtheria Toxin (DT) Administration.

The first dose of DT (Sigma, D0564) was delivered intraperitoneally (i.p.) as 500 ng in 200 µl PBS/ 20 g body weight followed by two doses of 100 ng in 200 µl PBS/ 20 g body weight, 48h and 12h before analysis. Depletion efficiency was monitored in each animal by the serum Flt3 ligand surge upon cDC depletion (zDC^{DTR}) and the loss of blood monocytes 24h post DT administration in *lyz2*$^{csfr1\text{-}DTR}$ mice.

Tamoxifen treatment. For Villin^{Tph1} mice 1mg of tamoxifen (Sigma) was injected i.p. on two consecutive days. Mice were then analysed 2 weeks following the last dose of tamoxifen. For *Advillin*^{CreERT2} strains, mice were given 1mg of tamoxifen by i.p. injection on five consecutive days. Mice were then analyzed at least 1 week following the final dose of tamoxifen.

Tph1-flox recombination PCR. DNA was extracted from the epithelial fraction of cells made by Percoll gradient of homogenized colon from Villin□*Tph1* mice two weeks following tamoxifen administration using Quick Extract (Lucigen) DNA extraction buffer. Target sequences were amplified using the following primers: Tph1-forward 5'-GGATCCTAACCGAGTGTTCC-3' Thp1-reverse-flox: 5'-GCACACCACCAACTCTTTCC-3' Tph1-reverse-recombined: 5'-

CTTGGAAGGTTTTGTATCACC-3' PCR products were run on a 2% agarose gel and bands were analyzed for the presence of the recombined band (Yadav et al., 2008).

Controlling for stress. Due to the sensitivity of the sympathetic nervous system to stress, the following steps were taken eliminate this potential confounding factor. Experiments were not performed on days when cage changing took place. Mice were transported to the lab and sacrificed immediately, and all experiments with injections were done after a minimum of 5 days of i.p./handling habituation.

SFB colonization. Mice mono-colonized with segmented filamentous bacteria (SFB) were kept in GF isolators and originally colonized by gavage with fecal extract from SFB mono-colonized mice kept at NYU (Littman lab). SFB colonization was verified by real time PCR using SFB-specific 16S primers; GF feces served as a negative control, Taconic Farms C57BL/6 feces as a positive control (Ivanov et al., 2009).

***Clostridium* spp. colonization.** Mice were colonized with *Clostridium spp.* (Atarashi et al., 2013) in the Cornell Weill gnotobiotic facility.

Altered Schaedler Flora colonization. C57BL/6 mice were maintained in germ-free conditions in ISOcage biocontainment isolator cages (Tecniplast, PA, USA) in the gnotobiotic facility at Rockefeller University. ASF colonization was achieved by inoculating germ-free mice with cecal contents of ASF donor mice stably colonized by

vertical transmission (kindly provided by Amanda Ramer-Tait, University of Nebraska-Lincoln). Ceca were prepared by homogenization through a 100 μm filter in sterile phosphate-buffered saline (PBS) at a ratio of one cecum per 1 ml of PBS. Mice received 200 μl of ASF inoculum via oral-gavage twice, one week apart. The presence of members of the ASF microbial community was confirmed by a real-time PCR-based assay previously described (Gomes-Neto et al., 2017). All mice were analyzed at least four weeks post colonization, with colonization further confirmed by 16s RNA sequencing of both faeces and ceca of analysed mice. We could detect RNA of at least 6 species by qPCR and 16s RNA sequencing after colonization.

Antibiotic treatments. Broad spectrum antibiotics (0.25 g Vancomycin, 0.25 g metronidazole, 0.5 g ampicillin, and 0.5 g neomycin) (Rakoff-Nahoum et al., 2004) were dissolved in 500 mL of filtered water and supplemented with 5 g Splenda. Individual antibiotics (0.25 g vancomycin, 0.25 g metronidazole, 0.5 g ampicillin and 0.5 g neomycin) were dissolved in 500 mL of filtered water and supplemented with 5 g Splenda. To control for the sweet taste of the antibiotic solution, 5 g of Splenda was dissolved in filtered water. Water controls were given filtered water as their drinking water. All solutions were passed through a SteriCup 0.22 μm filter. Streptomycin was prepared in sterile DPBS at a concentration of 200 mg/mL and then filtered with a 0.22 μm (EMD Millipore PES Express) syringe filter. A dose of 20 mg was given as an oral gavage of 100 μL of this stock solution (Barthel et al., 2003).

Tributyrin treatment. Tributyrin (Sigma W222305) was filter sterilized through a 0.22 μm (EMD Millipore PES Express) syringe filter prior to oral gavage or i.p. injection. 200 μL of tributyrin was given by oral gavage (Rivera-Chávez et al., 2016b). Two oral gavages were given over a period of 24 h, with the second dose given 8 h before sacrifice.

Exendin treatment. Exendin-4 (Sigma E7144) was dissolved in sterile 0.9% saline and aliquots were kept at -20°C. 20 μg/kg Exendin-4 or saline was given by i.p. injection. Tissue was isolated 4 hours post-injection or motility was measured 2 minutes following injection.

PYY treatment. PYY (Sigma P1306) was dissolved in sterile 0.9% saline and aliquots were kept at -20°C. 50 μg/kg PYY or saline was given by i.p. injection. Tissue was isolated 4 hours post-injection.

DREADD agonist. Water soluble Compound 21 (HelloBio HB6124) was dissolved in sterile 0.9% saline and aliquots were stored at -80°C. Mice were given intraperitoneal injection at a dose of 10 mg/kg or 1mg/kg.

Tracing injections. Mice were anesthetized with 2% isoflurane with 1% oxygen followed by 1% isoflurane with 1% oxygen to maintain anaesthesia. After shaving and sterilization of the abdomen, mice were placed on a sterile surgical pad on top of a heating pad and covered with a sterile surgical drape. Ophthalmic ointment was placed over the eyes to

prevent dehydration and the incision site was sterilized. Upon loss of recoil paw compression, a midline incision was made through the abdominal wall exposing the peritoneal cavity. For injections into the CG-SMG or duodenum an additional incision was made laterally to allow for better access. The duodenum, ileum, colon, or CG-SMG were located and exposed for injection. All injections were made with a pulled glass pipette using a Nanoject III. Following injection, the abdominal wall was closed using absorbable sutures and the skin was closed using surgical staples. Antibiotic ointment was applied to the closed surgical site and mice were given 0.05 mg/kg buprenorphine every 12 h for 2 days.

Stereotactic Surgery. Mice were anesthetized using isoflurane, with induction at 4% and maintenance at 1.5-2%. Coordinates were identified using the Paxinos mouse brain atlas. For tracing studies of the nucleus tractus solitarius (NTS), mice were bilaterally injected with 150 nL of rgAAV-FLEX-CAG-tdTomato (Addgene #28306-AAVrg) into the NTS at AP -7.2, DV -4.3, ML 0.35 relative to bregma. For tracing studies of the LPGi/RVLM, mice were bilaterally injected with PRV-GFP at -6.35 AP, ML 0.9, DV -6.0. For chemogenetic activation studies, VGAT^{Cre} mice were injected with 50nL of AAV5-hSyn-DIO-hM3D(Gq)-mCherry virus into the gigantocellular reticular nucleus (Gi) at AP-6.35, DV -5.8, ML 0.5 relative to bregma. VGLUT2^{Cre} mice were injected with AAV5-hSyn-DIO-hM3D(Gq)-mCherry into the rostral ventrolateral medulla (LPGi/RVLM) at -6.35 AP, ML 0.9, DV -6.0 relative to bregma. Skin was closed using sutures.

Subdiaphragmatic vagotomy (sdVx). Mice were anesthetized using isoflurane (induction: 2% isoflurane with 1% oxygen, maintenance: 1% isoflurane with 1% oxygen). After shaving and sterilization of the abdomen, mice were placed on a sterile surgical pad on top of a heating pad and covered with a sterile surgical drape. Ophthalmic ointment was placed over the eyes to prevent dehydration and the incision site was sterilized. Adequate depth of anaesthesia was confirmed by loss of recoil paw compression. A midline abdominal incision was then made along the *linea alba*, exposing the peritoneal cavity. The liver was retracted using sterile, saline-dampened cotton Q-tips. The right and left vagus nerve were visualized along the esophagus below the diaphragm by a surgical microscope and cut using microscissors. This included the hepatic, gastric, ventral and dorsal vagal trunks. 0.5 μL of CTB555/594 was then injected into the stomach or ileum to confirm successful vagotomy by a lack of labelling in the nodose ganglion. Following the procedure, the abdominal wall was closed using absorbable sutures and the skin was closed using surgical staples. Antibiotic ointment was applied to the closed surgical site and mice were given 0.05 mg/kg buprenorphine every 12 h for 2 days. For sham-operated animals the vagus nerve was similarly exposed but not cut.

PRV tracing with sdVx. Mice were given sdVx as described above, followed by injection of a 1 μL mixture of (0.5 μL PRV-152 and 0.5 μL CTB594) into the proximal colon. The inclusion of CTB was necessary to confirm successful vagotomy and to ensure that nodose neurons observed came from retrograde transport of PRV originating in the CG-SMG and traveling through the CNS. Antibiotic ointment was applied to the closed

surgical site and mice were given 0.05 mg/kg buprenorphine every 12 h for 2 days. For sham-operated animals the vagus nerve was similarly exposed but not cut.

Whole mount intestine immunofluorescence. Briefly, mice were sacrificed by cervical dislocation and the small intestine was removed and placed in HBSS $Mg^{2+}Ca^{2+}$(Gibco) + 5% FCS. The intestine was cut open longitudinally and the luminal contents washed away in DPBS. The muscularis was then carefully dissected away from the underlying mucosa in one intact sheet. The tissue was pinned down in a plate coated with Sylgard and then fixed O/N with 4% PFA with gentle agitation. After washing in DPBS whole mount samples were then permeabilized first in 0.5% Triton X-100/0.05% Tween-20/4 μg heparin (PTxwH) for 2 hours at room temperature (RT) with gentle shaking. Samples were then blocked for 2 h in blocking buffer (PTxwH with 5% bovine serum albumin/5% donkey/goat serum) for 2 hr at RT with gentle agitation. Antibodies were added to the blocking buffer at appropriate concentrations and incubated for 2 days at 4°C. After primary incubation the tissue was washed 4 times in PTxwH and then incubated in blocking buffer with secondary antibody at concentrations within the primary antibody range for 2 hours at RT. Samples were again washed 4 times in PTxwH and then mounted with FluoroMount G on slides with 1 ½ coverslips. Slides were kept in the dark at 4°C until they were imaged.

Restraint stress. For restraint stress experiments, each mouse was placed in a properly ventilated 50 mL conical plastic tube for 15 min. The mice could rotate but could not turn head to tail.

Cholera toxin tracing. Mice were anesthetized and operated on as described above. 1.5 uL of 1% CTB 488, 555, or 647 in PBS with 0.1% FastGreen was injected with a pulled glass pipette using a Nanoject III into the ileum, duodenum, colon and celiac-superior mesenteric ganglion. For triple labelling, 0.5uL of 1% CTB488, 555, or 647 was injected into the duodenum, ileum, and proximal colon of the same mice. The tissue was carefully washed several times with PBS to prevent possible spill over of tracer to other tissues. Relevant tissues were then dissected after a minimum of 2- 4 days post-injection.

Ileal denervation to confirm cholera toxin tracing specificity. Mice were anesthetized as described above and the ileal vein and artery to the distal ileum was identified. A cauterizer was used to sever the main ileal artery/vein and surrounding nerves. Once the mesentery was resected, 0.5uL of CTB594 with 0.1% FastGreen was injected with a pulled glass pipette using a Nanoject III was injected into the distal ileum between the two most distal lymph nodes. The tissue was carefully washed several times with PBS to prevent possible spill over of tracer to other tissues. LNG, RNG, and CG-SMG tissues were then dissected after 2 days post-injection followed by overnight fixation in 4% PFA. Sham was identical to the previous procedure, but the mesentery was left intact.

Nodose ganglion injection. Mice were anesthetized as described above and the ventral neck surface was cut open. Associated muscle was removed by blunt dissection to expose the trachea. The NG was located by following the vagus nerve along the carotid

artery to the base of the skull. Fine forceps were used to separate the vagus from the carotid artery, and the NG body was exposed by careful dissection. 1uL of AAV9-Syn-ChrimsonR-tdTomato (Addgene #59171-AAV9) with 0.1% FastGreen was injected with a pulled glass pipette using a Nanoject III. The skin was then closed with absorbable sutures and antibiotic cream was applied. Relevant tissues were dissected at a minimum of 2 weeks post-injection.

FosTRAP2-PRV analysis. *Fos*^{TRAP2} mice were crossed with *Rosa26*$^{lsl\text{-}tdTomato}$:RiboTag mice to generate a TRAP2$^{Tom:RiboTag}$ reporter strain. Mice were habituated and singly housed for at least 5 days. A single oral gavage of streptomycin (20mg/mouse) was given and after 24 hours mice were injected i.p. with an aqueous solution 4 hydroxytamoxifen (Ye et al., 2016) to induce Cre recombinase activity in *Fos* expressing cells, resulting in tdTomato and RPL22-HA expression by recently activated neurons. After 7 days, we injected 1uL of PRV-152 (GFP) into the proximal colon. Four days later, were perfused and relevant brain areas were analysed for the presence of Tomato+ and GFP+ neurons.

CTB NG and CG-SMG counting. CTB488 was injected into the duodenum, ileum, and proximal colon. Mice were sacrificed by cervical dislocation and the CG-SMG and NG were harvested and fixed overnight in 4% PFA. Tissue was then washed four times in DPBS at RT and permeabilized in PTxwH for 4 h at RT. Primary antibody anti-AlexaFluor488 (1:400, Thermo Fisher Scientific, A-11094) was added to the samples in PTxwH and incubated at 4°C for 48 h. Samples were washed four times in PTxwH at RT

and then stained with goat-anti rabbit AF555/568/647 at 4°C for 24 h. Samples were washed four times in PTxwH at RT, covered in Fluormount G, and coverslipped for confocal imaging. Each ganglion was captured in full by multiple z-stacks and the total number of CTB+ neurons were counted.

Celiac ganglion tracing. Mice were anesthetized and operated on as described above. 1.5 uL of AAVrg-hSyn1-Cre with 0.1% FastGreen was injected into the CG-SMG of *Rosa26*$^{lsl\text{-}tdTomato}$ mice. 1.5 uL of AAV2-CAG-FLEX-tdTomato with 0.1% FastGreen was injected into the CG-SMG of *Snap25*^{cre} mice. Intestine samples were dissected after 2.5 weeks for AdipoClear, RIMS, or Focus Clear analysis.

Viscerofugal tracing. Mice were anesthetized and operated on as described above. 1.5 uL of AAV6-CAG-FLEX-tdTomato with 0.1% FastGreen was injected into the ileum wall of *Snap25*^{cre} mice. CG-SMG samples were then dissected after 2.5 weeks for whole mount immunofluorescence analysis.

Virus. All viruses used in these studies were: AAV5-hSyn-DIO-mCherry (Addgene), AAVrg-CAG-tdTomato (Addgene), AAVrg-CAG-FLEX-tdTomato (Addgene), AAV6-CAG-FLEX-tdTomato (Addgene), AAVrg-hSyn1-Cre (Janelia), AAV2-hSyn-hM3Dq-mCherry (Addgene), AAV2-hSyn-hM4Di-mCherry (Addgene) , AAV9-Syn-ChrimsonR-tdTomato (Addgene #59171-AAV9), PRV-152 (Gift of L. Enquist), PRV-614 (Gift of L. Enquist). Fast Green (Sigma) was added (0.1%) to virus injected into peripheral tissues.

Fluorogold Labelling. A stock solution of 4 mg/mL Fluorogold (Fluorochrome) was made in sterile 0.9% saline and then filter sterilized through a 0.22 μm syringe filter. An i.p. injection of 300 μL of Fluorogold solution was given 3 days before tissue harvesting.

Retrograde PRV Tracing. Mice were anesthetized and operated as described above. PRV Bartha 152 (GFP) or 614 (RFP) were a gift of L. Enquist. 3uL with 0.1% FastGreen was injected with a pulled glass pipette using a Nanoject III into the wall of the ileum, duodenum, and colon. Brains and spinal columns were harvested three and four days after injection.

Chemogenetics of CG-SMG neurons. 1 μL of AAV2-hSyn-hM3Dq-mCherry or AAV2-hSyn-hM4Di-mCherry (Addgene) was injected into the CG-SMG of C57BL/6J mice. Mice were then sutured, and staples were applied. Antibiotic ointment was applied to the closed surgical site and mice were given 0.05 mg/kg buprenorphine every 12 h for 2 days. After 2 weeks mice were habituated to i.p. injections for 5 days before administration of 1 mg/kg or 10mg/kg Compound 21.

Antibodies. The following primary antibodies were used, and unless otherwise indicated concentrations apply to all staining techniques: NeuroTrace AF569/AF647 (1:200, Thermo Fisher Scientific, N21482/ N21483), GFP Tag AF488/555/594/647 (1:400, Thermo Fisher Scientific A21311/A31851/A21312/A31852), TH (1:200, Aves Labs, TYH;

1:400, Millipore Sigma, AB152; 1:200 Millipore Sigma, AB1542), BIII-Tubulin (1:400, Millipore Sigma, T2200; 1:200, Aves Labs, TUJ), NPY (1:200, Immunostar, 22940), RFP (1:200, Sicgen, AB8181; 1:200 and 1:1000 AdipoClear brain, Rockland, 600-401-379), ANNA-1 (1:200,000, Gift of Dr. Vanda A. Lennon), cFos (1:500, Cell Signaling Technologies, 2250S), HA (1:400, Cell Signaling Technologies, 3724S), 5-HT (1:200, Millipore Sigma, MAB352), anti-AlexaFluor488 (1:400, Thermo Fisher Scientific, A-11094), and VGLUT2 (1:200, Millipore Sigma, AB2251-I). Fluorophore-conjugated secondary antibodies were either H&L or Fab (Thermo Fisher Scientific) at a consistent concentration of 1:400 in the following species and colors: goat anti-rabbit (AF488/568/647), goat anti-rat (AF488/647), goat anti-chicken (AF488/568/647), goat anti-human (AF568/647), donkey anti-guinea pig (AF488/647), donkey anti-rabbit (AF568/647), donkey anti-goat (AF568/647), donkey anti-sheep (AF568/790).

Intestine dissections. Mice were sacrificed and duodenum (1 cm moving proximal from the gastroduodenal junction), ileum (1 cm moving proximal from the ileocecal junction), or colon (4 cm moving proximal from the rectum) was removed. For AdipoClear fecal contents were flushed from the lumen and tissue was left intact. Tissue used for RIMS or FocusClear were cut open longitudinally and fecal contents were washed out. For dissection of the muscularis, following the above procedures, the intestinal tissue was placed on a chilled aluminium block with the serosa facing up (Gabanyi & Muller et al., 2016). Curved forceps were then used to carefully remove the muscularis.

Nodose ganglion (NG) dissections. Mice were sacrificed and the ventral neck surface was cut open. Associated muscle was removed by blunt dissection to expose the trachea. The NG was then located by following the vagus nerve along the carotid artery to the base of the skull. Fine scissors were used to cut the vagus nerve below the NG and superior to the jugular ganglion.

Celiac-superior mesenteric ganglion dissections. Mice were sacrificed and a midline incision was made, and the viscera were reflected out of the peritoneal cavity. The intersection of the descending aorta and left renal artery was identified, from which the superior mesenteric artery was located. The CG-SMG is wrapped around the superior mesenteric artery and associated lymphatic vessels. Fine forceps and scissors were used to remove the CG-SMG.

Dorsal root ganglion dissections. The spinal column was isolated, cleaned of muscle, and bisected sagittally (Sleigh et al., 2016). The spinal cord was removed leaving the dorsal root ganglion (DRG) held in place by the meninges. The thoracic 13 DRG was identified by its position just caudal to thoracic vertebra. The meninges were cleared and individual DRGs were removed with fine forceps and scissors.

Spinal cord dissections. For 3DISCO analysis the spinal cord was isolated by hydraulic extrusion as previously described (Richner et al., 2017). For whole spinal column calAdipoClear imaging, the entire spinal column was removed with associated tissue.

Costae and muscle were carefully trimmed to reduce the size of the sample to fit into a 5 mL Eppendorf tube while avoiding disrupt ventral tissue attached to the spinal cord.

RiboTag. Heterozygous or homozygous *Snap25*^{RPL22HA} were used for TRAP-seq analysis as no differences were found between either genotype. For NG, DRG, and CG-SMG IP, tissues were isolated as described above. The RiboTag IP protocol was then followed (http://depts.washington.edu/mcklab/RiboTagIPprotocol2014.pdf) with the following modifications. All samples were homogenized by hand with a dounce homogenizer in 2.5 mL supplemented homogenization buffer (changes per 2.5 mL: 50 μL Protease Inhibitor, 75 μL heparin (100 mg/mL stock), 25 uL SUPERase• In RNase Inhibitor). Samples were then centrifuged for 10 minutes at 10,000 G, after which 800 μL of supernatant was removed and 5 μL of anti-HA antibody (Abcam, ab9110) was added. Samples were kept rotating at 4°C with antibody for 1 hour. 200 μL of Thermo Protein magnetic A/G beads were washed with homogenization buffer, added to the sample, and kept rotating for 30 minutes at 4°C. The beads were washed four times with high-salt buffer and samples were eluted with 100 μL of PicoPure lysis buffer. RNA was extracted using the Arcturus PicoPure RNA isolation kit (Applied Biosystems) according to the manufacturer's instructions.

RiboTag RNA-sequencing. RNA libraries were prepared using SMARTer Ultra Low Input RNA (ClonTech Labs) and sequenced using 75 base-pair single end reads on a NextSeq 500 instrument (Illumina). Reads were aligned using Kallisto to the Mouse

transcriptome (Ensembl, release v91). Transcript abundance files were then used in the DESeq2 R package (Love et al., 2014), which was used for all downstream differential expression analysis and generation of volcano plots. For intestine samples cre+ samples were compared with cre- samples to generate a list of immunoprecipitated (IP) enriched genes (log2FC > 1 and padj < 0.05). This IP enriched list was then used to perform downstream analysis. Differentially expressed genes between samples were defined as those contained within the total IP enriched list from tissues being compared and with a cutoff of log2FC > 1. PCA plots were generated from log transformed DEseq2 data, as indicated in figure legends, with the FactoMineR R package. GSEA pre-ranked analysis was performed with desktop software and the C5 gene ontology database using 1000 permutations. Gene ontology enrichment analysis was performed with differentially expressed genes (log2FC > 1, padj < 0.05) using the TopGO R package and a Fisher test with an elimination algorithm was used to calculate significance.

16S sample processing. 16s samples were processed utilizing a Promega Maxwell® RSC 48 Instrument. Following DNA extraction from all samples, DNA samples were quantified using a ThermoFisher Quant-It dsDNA High-Sensitivity Kit on a microplate reader.

16S sequencing. 16s sequencing was performed on either the Illumina HiSeq 2500 or the Illumina MiSeq depending on project-specific needs. Raw paired-end fastq files containing sequence reads were merged at the overlapping region to produce a single

16s contig. All merged sequences having more than 1 expected error per read were filtered. Operational taxonomic units (OTUs) were generated by clustering sequences with a 99% correspondence and chimera sequences were removed using usearch (Edgar, 2010) (v11). Reads were mapped against the OTU reference to generate a matrix of counts. Subsequently, OTU taxonomy and classification were performed with mothur (Schloss et al., 2009) (v1.40.5) using the greengenes database. Next, statistical analysis were implemented using the phyloseq package (McMurdie and Holmes, 2013) for R (v1.40.5) using the greengenes database. Next, statistical analysis were implemented using the phyloseq package for R.

Brain immunofluorescence. Mice were sacrificed and transcardially perfused with cold PBS with heparin followed by cold 4% PFA (Electron Microscopy Sciences). The intact brain was separated carefully from the skull and placed in 4% PFA, and then rotated for 48 h at 4°C. Whole brains were washed with PBS/0.03%Azide and sectioned at 50 μm on a Leica vibratome for immunofluorescence. Samples were then permeabilized in 0.5% Triton/0.05 Tween-20 in PBS (PTx) followed by blocking in 5% goat serum in PTx each for 2 h at room temperature. Primary antibody was added to the blocking buffer and samples were incubated with constant rotation at 4°C overnight. Four 15-minute washes were done in PTx at RT after which samples were moved to blocking buffer with secondary antibody. Slices were incubated in secondary antibody for 2 hours at room temperature followed by four 15-minute washes in PTx at room temperature. Samples were then placed on microscope slides, covered in Fluormount G, and coverslipped.

Confocal imaging. Whole mount intestine, NG, DRG, and CG-SMG samples were imaged on an inverted LSM 880 NLO laser scanning confocal and multiphoton microscope (Zeiss) and on an inverted TCS SP8 laser scanning confocal microscope (Leica).

PRV counting. Images of brainstem vibratome slices were taken at 10x magnification. The raphe pallidus, gigantocellular nucleus, and lateral paragigantocellular nucleus/rostral ventrolateral medulla were identified based on the Allen Brain Atlas. All $VGAT^{GFP}$ and $VGLUT2^{GFP}$ cells were counted within this region, as well as all PRV-RFP+ cells. These numbers were then averaged across each brainstem region for all slices from a single animal. Thus, each point on the graph is representative of one animal.

RIMS clearing. Briefly, following secondary staining CG-SMG, nodose and DRG were submerged in Refractive Index Matching Solution (RIMS) for 30-120 min then mounted in RIMS solution on a glass slide and sealed with a coverslip for confocal imaging (Yang et al., 2014).

FocusClear. Whole intestine and celiac ganglion samples were first fixed in 4% PFA overnight at 4°C. Samples were then washed three times in DPBS at RT. Samples were placed into 250 μL of FocusClear solution for 15-20 minutes. They are then transferred to MountClear solution on a glass slide and a 1 ½ coverslip was used to seal the sample

in place.

3DISCO. 3DISCO clearing of whole spinal cord was done as previously described (Ertürk et al., 2012).

AdipoClear. Adipoclear whole tissue clearing was adapted from Adipoclear protocol (Chi et al., 2018). Mice were sacrificed and intestinal sections were removed followed by overnight fixation in 4% PFA. Tissues were washed in PBS then dehydrated in 20/40/60/80/100% Methanol in B1N followed by dichloromethane. Tissues were then rehydrated in 100/80/60/40/20% methanol in B1N. Subsequently, samples were washed in PTxwH and then incubated in primary antibody dilutions in PTxwH for 7 Days. Samples were washed in PTxwH then incubated in secondary antibody at 1:400 in PTxwH for 7 days. Samples were again washed in PTxwH followed by PBS then dehydrated in 20/40/60/80/100% methanol followed by dichloromethane and finally cleared in dibenzyl ether.

calAdipoClear. CalAdipoclear whole tissue clearing was adapted from Adipoclear protocol. Briefly, mice were sacrificed and perfused with PBS followed by 4% PFA. Whole spinal columns were removed and put into 4% PFA overnight. Tissues were washed in PBS then dehydrated in 20/40/60/80/100% methanol in B1N followed by dichloromethane. Tissues were then rehydrated in 100/80/60/40/20% methanol in B1N. Subsequently, samples were decalcified in Morse Solution (1-part 45% formic acid/1-part

0.68 mM sodium citrate dihydrate) overnight followed by PTxwH washes. Samples were then incubated in primary antibody dilutions in PTxwH for 7 Days. Samples were washed in PTxwH then incubated in secondary antibody at 1:400 in PTxwH for 7 days. Samples were again washed in PTxwH followed by PBS then dehydrated in 20/40/60/80/100% methanol followed by dichloromethane and finally cleared in dibenzyl ether.

Light sheet microscopy and 3D reconstructions. Whole-tissue cleared samples were imaged submerged in DBE on a LaVision Biotech Ultramicroscope II with 488 nm, 561nm, 640 nm, or 785 light sheet illumination using a 1.3x or 4x objective with 2.5um Z-slices. Images were adjusted post hoc using Imaris x64 software (version 9.1 Bitplane) and 3D reconstructions were recorded as mp4 video files. Optical slices were taken using the orthoslicer or oblique slicer tools.

ClearMap analysis. All analyses for whole-brain studies were performed adapting ClearMap pipeline (latest version available from www.idisco.info, see also).

Quantification of iEAN. A minimum of 10 images were randomly acquired across a piece of whole mount muscularis. These images were then opened in ImageJ, and the cell counter was used to count the number of ANNA-1+ cells in a given field. This number was then multiplied by a factor of 2.95 (20x objective) or 3.125 (25x objective), to calculate the number of counted neurons per square millimeter (mm^2). The average of 10 (or more) images were then calculated and plotted. Thus, every point on a given graph corresponds

to a single animal.

Quantification of CG-SMG cFos. Mice were sacrificed by cervical dislocation and CG-SMG were harvested and fixed overnight in 4% PFA. CG-SMG were then washed four times in DPBS at RT and permeabilized in PTxwH overnight RT. Primary antibody cFos (1:500, Cell Signaling Technologies, 2250S) was added to the samples in PTxwH and incubated at RT for 48 h. Samples were washed four times in PTxwH at RT and then stained with goat-anti rabbit AF555/568/647 at RT for 48 h. Samples were washed four times in PTxwH at RT, covered in Fluormount G, and coverslipped for confocal imaging. We first established criteria for identifying neuronal cFos+ nuclei by staining CG-SMG from restraint-stressed mice, a condition known to activate the sympathetic nervous system (Abe et al., 2017; Mei et al., 2001). FluoroGold was used to identify sympathetic neurons and cFos+ nuclei were defined as morphologically circular with a diameter of 8-14um. These criteria were sufficient to distinguish between small intensely fluorescent cells and possibly macrophages that also have cFos expression. We captured all sympathetic neurons within the CG-SMG, as defined by tyrosine hydroxylase staining, FluoroGold fluorescence, tdTomato fluorescence, or autofluorescence (experiment dependent), with multiple z-stack images. All images were analyzed in Image-J. Total cFos+ nuclei were counted using the Cell Counter plugin for Image-J, and data were not normalized to area or volume. Each data point represents the number of cFos+ cells per CG-SMG.

Brainstem cFos counting experiments. All mice (GF, exGF, SPF, SNS^{hM4Di}, and $VGLUT2^{RiboTag:tdTomato}$) were fasted for 18-24 hours before perfusion (exGF, SPF, and $VGLUT2^{RiboTag:tdTomato}$) or injection of Compound 21 (SNS^{hM4Di}). Mice were then perfused 3 hours post Compound 21 injection or 24 hours post streptomycin gavage. Brains were sectioned as described above and sections were permeabilized in 0.5% Triton/0.05 Tween-20 in PBS (PTxwH) followed by blocking in 5% goat serum in PTxwH each for 2 h at room temperature. cFos primary antibody was added to the blocking buffer and samples were incubated with constant rotation for 48 hours at 4°C. Four 15-minute washes were done in PTxwH at RT after which samples were moved to blocking buffer with secondary antibody. Slices were incubated in secondary antibody for 2 hours at room temperature followed by four 15-minute washes in PTxwH at room temperature. Samples were placed on microscope slides, covered in Fluormount G, and coverslipped. All sections containing NTS/AP were imaged and included in counting of cFos+ cells. Therefore, each data point represents the total number of cFos+ cells per relevant brain area captured.

RNAScope. Nodose ganglia (NG) from C57Bl/6 mice were dissected as described above. Once removed ganglia were dipped in Fast Green (1%, Sigma-Aldrich) to assist with visualization when slicing and flash frozen in OCT. 15 um sections of NG were sliced on a cryostat for RNAScope. Samples were processed and stained with Scn5a, positive control or negative control probes according to the manufacturer's instructions. Samples were mounted in Prolong gold antifade with DAPI (Thermo-Fisher) for imaging and

imaged within 24 hours on an inverted LSM 880 NLO laser scanning confocal and multiphoton microscope (Zeiss) and images were processed using Image J.

RNAScope/IHC. C57Bl/6 mice were injected bilaterally with CTB 488 into the colon as described above. NG were dissected 1 week post injection as described above, dipped in Fast Green (1%, Sigma-Aldrich) to assist with visualization and flash frozen in OCT. 15 um sections of NG were sliced on a cryostat for RNAScope/IHC. Samples were processed and stained with Scn5a, positive or negative control probes according to the manufacturer's instructions. After in situ hybridization sections were washed three times in wash buffer (1X, ACDBio) and then fixed in 1% PFA in TBS for 10 minutes at 4 C to stabilize the ISH labeling. Samples were next washed three times in TBS-T and incubated in 10% Goat Serum in TBS with 1% BSA for 30 minutes. Samples were stained with anti Alexafluor-488 antibody (1:500, Thermo-Fisher) for 1 hour in TBS-1% BSA. After primary antibody staining, sections were washed three times for 5 minutes each in TBST and stained with Goat anti rabbit AF488 (1:500, Thermo-Fisher) in TBS-1% BSA for 30 minutes. Samples were again washed three times for 5 minutes each in TBST and finally mounted in Prolong gold antifade with DAPI (Thermo-Fisher) for imaging. Slides were imaged within 24 hours of mounting on an inverted LSM 880 NLO laser scanning confocal and multiphoton microscope (Zeiss) and images were processed using Image J.

Intestine motility measurements. For measurement of total intestinal transit time, mice were given an oral gavage of 6% carmine red dissolved in 0.5% methylcellulose (made

with sterile 0.9% saline). Total intestinal transit time was measured as the time from oral gavage it took for mice to pass a fecal pellet that contained carmine. To measure colonic motility a glass bead (3 mm diameter) was pushed into the colon to a distance of 2 cm from the anal verge. The time required for expulsion of the glass bead was measured and taken as an estimate of colonic motility. Mice in both assays were injected 2 minutes before starting with i.p. Compound 21 (1mg/kg or 10mg/kg as indicated).

Open Field Test. For locomotion activity assessment an open field test (OFT) was performed using a small cubic box, measuring 27.3 cm^3. The top of the cube of the OFT box is uncovered. Mice were placed in the bottom surface, and movements were recorded over the course of 2 sessions of 5 minutes. The first session was measured without manipulating the animal (basal). The second session was measured immediately after an I.P. injection of Compound 21 (10mg/kg). Computer-tracking program EthoVision XT (Noldus) was used to analyse the movements of the animal over time. Total distance travelled and velocity was assessed.

***Salmonella* infections.** CBA/J mice were given an oral gavage of 10^9 WT *Salmonella* typhimurium (IR715). For all *Salmonella* infections, a single aliquot of either strain of *Salmonella* was grown in 3 ml of luria broth (LB) overnight at 37ºC with agitation. Bacteria were then sub-cultured (1:300) into 3 ml of LB for 3.5 hours at 37ºC with agitation, and diluted to final concentration in 1 ml of LB. Bacteria were inoculated by gavage into recipient mice in a total volume of 100 μl and mock infected mice were given an oral gavage of 100 μl LB.

Colony forming unit counting. Faecal pellets from *Salmonella*-infected mice were weighed and then disrupted in 400 □L of DPBS. Serial dilutions were made from the original suspension and then 5□L of each dilution was plated onto Salmonella-Shigella plates. The plates were then incubated overnight, and the number of black colonies were counted for the serial dilution with the clearest delineation of single units. This number was then multiplied by the dilution factor and by 80 to give the number of colony forming units (CFUs) in the original suspension. CFU numbers were then divided by the original fecal pellet weight to give the number of CFUs per mg of faeces.

Cecal butyrate measurements. Concentrations of acetate, propionate, and butyrate were measured as previously described (Haak et al., 2018). Briefly murine cecal content samples were collected directly into Bead-Ruptor tubes with 2.8-mm ceramic beads (OMNI International) and immediately frozen on dry ice. After thawing, samples were extracted with 80% methanol containing internal standards of deuterated SCFA (d-3 acetate, d-5 propionate, and d-7 butyrate; Cambridge Isotope Laboratories). Pellets were resuspended at a ratio of 100 mg/ml and homogenized. Homogenized samples were centrifuged at 20,000 *g* for 15 min at 4°C. The supernatant was derivatized for 60 min at 65°C with one volume of 50 mM, pH 11.0 borate buffer, and four volumes of 100 mM pentafluorobenzyl bromide (Thermo Scientific) in acetone (Fisher Scientific). The SCFA were extracted in n-hexane and then further diluted 1:10 in n-hexane. Extracted SCFA

were quantified by GCMS (Agilent 7890A GC System; Agilent 5975C MS detector) operating in negative chemical ionization mode with methane as the reagent gas. MassHunter software was used for data analysis (B07.0; Agilent Technologies).

Feeding assay. Mice were singly housed for at least 2 days prior to beginning the experiment. Before testing mice with Compound 21, feeding behavior was first assessed with saline injection during the light cycle (starting at 7:00AM) and dark cycle (starting at 19:00PM). The food intake assays were performed in the home cage. Mice were given ad libitum access to food prior to, during, and after the assay. Measurement of food intake (weighing of remaining food at each timepoint) was made at 1, 2, 4, 8, and 24 hr post i.p. injection of C21.

Blood glucose measurement. Mice were not fasted, or fasted for either 4 or 16 hours (indicated in the figure legends) prior to analysis. Mouse tails were cut at the very tip and the first drop of blood was discarded. A single drop of blood was applied to a Breeze2 (Bayer) blood glucose test strip loaded into a Breeze2 blood glucose monitoring system (Bayer). All samples were obtained at the same time of day during the light cycle (10:00-10:30AM).

Blood and plasma collection. Mice were not fasted, or fasted for either 4 or 16 hours (indicated in the figure legends) prior to analysis. Mouse tails were cut at the very tip and the first drop of blood was discarded. At least 100uL of blood was then collected in a

Microvette (CB300) coated with Potassium/EDTA. Tubes were then centrifuged at 3600 RPM for 20 min at 4°C. Plasma was then collected and frozen at -80°C until analysis. All samples were obtained at the same time of day during the light cycle (10:00-10:30AM).

Insulin ELISA. Insulin levels in serum samples were measured using an Ultrasensitive Mouse Insulin ELISA kit (Crystal Chem) according to the manufacturer's instructions.

Glucagon ELISA. Serum glucagon concentrations were determined using a Mouse Glucagon ELISA kit (Mercodia) according to the manufacturer's protocol.

Retrograde PRV Tracing. Mice were anesthetized and operated as described above. PRV Bartha 152 (GFP) or 614 (RFP) were a gift of L. Enquist. 3uL with 0.1% FastGreen was injected with a pulled glass pipette using a Nanoject III into the parenchyma of the right liver lobe or into the head, neck, body, and tail of the pancreas. The intestine *muscularis* and CG-SMG were harvested one to four days after injection.

PASTAA analysis. Differentially expressed Ensembl gene ID lists (log2FC > 1, padj < 0.05) from ileum and colon samples (GF vs SPF) were used in the Predicting Associated Transcription factors from Annotated Affinities (PASTAA) web tool (http://trap.molgen.mpg.de/PASTAA.htm). Significant (p-value < 0.05) association scores for transcription factors were plotted.

RNAscope whole-mount intestine immunofluorescence. C57Bl/6, *Cartp*^{cre}, *Agrp*^{cre} or *Npy*^{cre} mice were sacrificed and the duodenum, Ileum and colon removed and dissected as described above. Pieces of *muscularis externa* were pinned on sylgard coated plates and fixed in 4% PFA at room temperature for 3 hours. Samples were removed from the sylgard plates and washed in PBS twice for 10 minutes. Samples were further washed twice more in PBS or PBST for 10 minutes depending on the origin of the tissue (see table). After washing, pieces of muscularis were pinned again to sylgard plates and dehydrated along a gradient of 25/50/75/100/100 % ethanol in PBS or PBST for 10 minutes at each step (see table). 5mm x 5mm sections were cut from the tissue and mounted on slides and left to dry (~2 minutes). Samples were digested with 50 μL of protease III digestion solution (ACDbio) at room temperature for between 30 and 45 minutes. After digestion, tissue was removed from slides using forceps and washed three times in PBS for 5 minutes each. Tissue was then hybridized using overnight at 40°C in a humidified oven (ACDbio) using relevant probe targets. Tissue was next amplified and stained according to the RNAScope protocol for whole tissue staining with the following modifications: each amplification step was extended by 5 minutes and following the final amplification samples were washed three times for 10 minutes each. Tissue samples were mounted in Prolong gold antifade with DAPI (Thermo-Fisher). Samples were imaged within 24 hours on an inverted LSM 880 NLO laser scanning confocal and multiphoton microscope (Zeiss) and images processed using Image J.

Statistical analysis. Significance levels indicated are as follows: *P < 0.05, **P < 0.01, ***P < 0.001. All data are presented as mean ± s.d.. All statistical tests used were two-tailed. The experiments were not randomized, and no statistical methods were used to predetermine sample size. Multivariate data was analysed by one-way ANOVA and Tukey's multiple comparisons post hoc test. Comparisons between two conditions were analyzed by unpaired Student's t-test. We used GraphPad PRISM version 8.0d and R 3.4.3 for generation of graphs and statistics.

Appendix

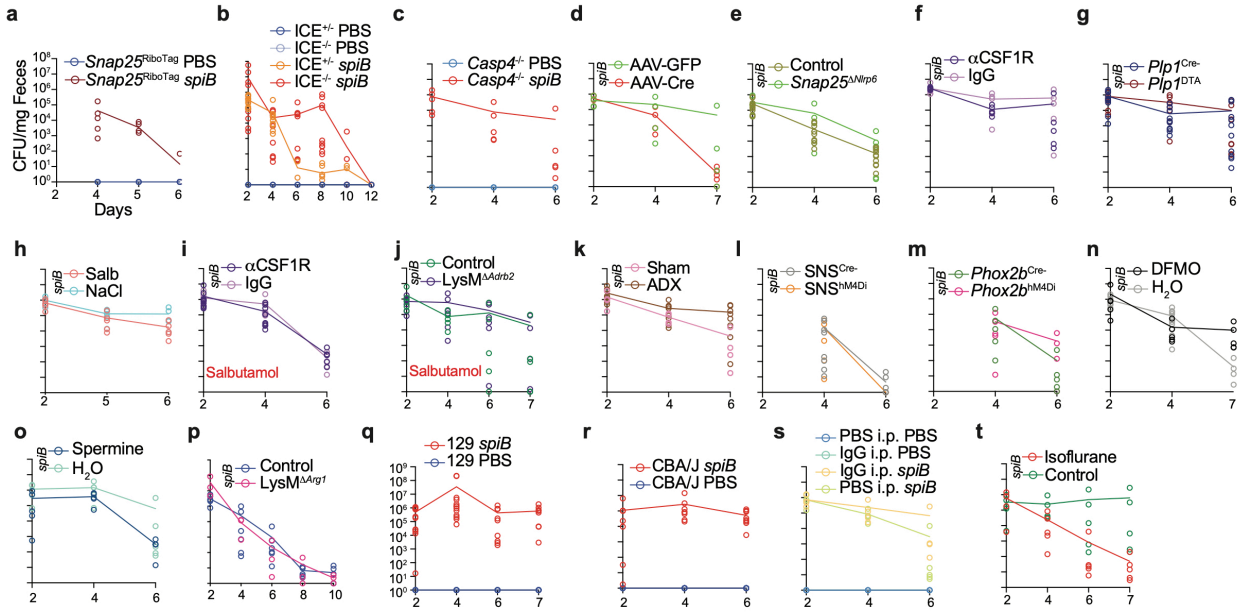

***spiB* CFU Plots (related to Chapter 4).** (**a**-**l**) Quantification of fecal *Salmonella spiB* CFU on the indicated days post infection of the experiment displayed in (**a**) Figure 4.7a; (**b**) Figure 4.12c; (**c**) Figure 4.12d; (**d**) Figure 4.13e-f; (**e**) Figure 4.14b; (**f**) Figure 4.15d; (**g**) Figure 4.16b; (**h**) Figure 4.19a; (**i**) Figure 4.19b; (**j**) Figure 4.21h; (**k**) Figure 4.23c; (**l**) Figure 4.24a; (**m**) Figure 4.24b; (**n**) Figure 4.26a; (**o**) Figure 4.26b; (**p**) Figure 4.26e; (**q**) Figure 4.12i; (**r**) Figure 4.12j; (**s**) Figure 4.22a; (**t**) Figure 4.22b. Data are represented as mean (line), and individual values, with each point on a graph representing CFU obtained from an individual animal.

References

Abe, C., Inoue, T., Inglis, M.A., Viar, K.E., Huang, L., Ye, H., Rosin, D.L., Stornetta, R.L., Okusa, M.D., and Guyenet, P.G. (2017). C1 neurons mediate a stress-induced anti-inflammatory reflex in mice. Nat. Neurosci. *20*, 700–707.

Adameyko, I. (2016). Neural circuitry gets rewired. Science (80-.). *354*, 833–834.

Agarwal, N., Offermanns, S., and Kuner, R. (2004). Conditional gene deletion in primary nociceptive neurons of trigeminal ganglia and dorsal root ganglia. Genesis *38*, 122–129.

Alimov, I., Menon, S., Cochran, N., Maher, R., Wang, Q., Alford, J., Concannon, J.B., Yang, Z., Harrington, E., Llamas, L., et al. (2019). Bile acid analogues are activators of pyrin inflammasome. J. Biol. Chem. *294*, 3359–3366.

Allen, W.E., DeNardo, L.A., Chen, M.Z., Liu, C.D., Loh, K.M., Fenno, L.E., Ramakrishnan, C., Deisseroth, K., and Luo, L. (2017). Thirst-associated preoptic neurons encode an aversive motivational drive. Science *357*, 1149–1155.

Andermann, M.L., and Lowell, B.B. (2017). Toward a Wiring Diagram Understanding of Appetite Control. Neuron *95*, 757–778.

Anitha, M., Vijay-Kumar, M., Sitaraman, S. V., Gewirtz, A.T., and Srinivasan, S. (2012). Gut microbial products regulate murine gastrointestinal motility via toll-like receptor 4 signaling. Gastroenterology *143*, 1006-1016.e4.

Anitha, M., Reichardt, F., Tabatabavakili, S., Nezami, B.G., Chassaing, B., Mwangi, S., Vijay-Kumar, M., Gewirtz, A., and Srinivasan, S. (2016). Intestinal Dysbiosis Contributes to the Delayed Gastrointestinal Transit in High-Fat Diet Fed Mice. Cmgh *2*, 328–339.

Anthoney, N., Foldi, I., and Hidalgo, A. (2018). Toll and toll-like receptor signalling in development. Dev. *145*, 1–6.

Atarashi, K., Tanoue, T., Oshima, K., Suda, W., Nagano, Y., Nishikawa, H., Fukuda, S., Saito, T., Narushima, S., Hase, K., et al. (2013). Treg induction by a rationally selected mixture of Clostridia strains from the human microbiota. Nature *500*, 232–236.

Aubert, P., Oleynikova, E., Rizvi, H., Ndjim, M., Le Berre-Scoul, C., Grohard, P.A., Chevalier, J., Segain, J.-P., Le Drean, G., Neunlist, M., et al. (2019). Maternal protein restriction induces gastrointestinal dysfunction and enteric nervous system remodeling in rat offspring. FASEB J. *33*, 770–781.

Auerbach, L. (1864). Fernere vorlaufige Mittheilung uiber den Nerven apparat des Darmes. Virchows Arch. *30*.

Avetisyan, M., Rood, J.E., Huerta, S., Sengupta, R., and Wright-jin, E. (2018). Muscularis macrophage development in the absence of an enteric nervous system. *115*, 1–6.

Ayush, E.-A., Iwasaki, Y., Iwamoto, S., Nakabayashi, H., Kakei, M., and Yada, T. (2015). Glucagon directly interacts with vagal afferent nodose ganglion neurons to induce Ca(2+) signaling via glucagon receptors. Biochem. Biophys. Res. Commun. *456*, 727–732.

Bain, C.C., and Schridde, A. (2018). Origin, Differentiation, and Function of Intestinal Macrophages. Front. Immunol. *9*, 1–15.

Bain, C.C., Bravo-Blas, A., Scott, C.L., Perdiguero, E.G., Geissmann, F., Henri, S., Malissen, B., Osborne, L.C., Artis, D., and Mowat, A.M. (2014). Constant replenishment from circulating monocytes maintains the macrophage pool in the intestine of adult mice. Nat. Immunol. *15*.

Banfield, B.W., Kaufman, J.D., Randall, J.A., and Pickard, G.E. (2003). Development of Pseudorabies Virus Strains Expressing Red Fluorescent Proteins: New Tools for Multisynaptic Labeling Applications. J. Virol. *77*, 10106–10112.

Barbara, G., Stanghellini, V., Brandi, G., Cremon, C., Di Nardo, G., De Giorgio, R., and Corinaldesi, R. (2005). Interactions between commensal bacteria and gut sensorimotor function in health and disease. Am. J. Gastroenterol. *100*, 2560–2568.

Barron, F., Woods, C., Kuhn, K., Bishop, J., Howard, M.J., and Clouthier, D.E. (2011). Downregulation of Dlx5 and Dlx6 expression by Hand2 is essential for initiation of tongue morphogenesis. Development *138*, 2249–2259.

Barth, A.L., Gerkin, R.C., and Dean, K.L. (2004). Alteration of neuronal firing properties after in vivo experience in a FosGFP transgenic mouse. J. Neurosci. *24*, 6466–6475.

Barthel, M., Hapfelmeier, S., Kremer, M., Rohde, M., Hogardt, M., Pfeffer, K., Rüssmann, H., Hardt, W., Barthel, M., Hapfelmeier, S., et al. (2003). Pretreatment of Mice with Streptomycin Provides a Salmonella enterica Serovar Typhimurium Colitis Model That Allows Analysis of Both Pathogen and Host Pretreatment of Mice with Streptomycin Provides a Salmonella enterica Serovar Typhimurium Colitis Model . *71*, 2839–2858.

Bassi, G.S., Dias, D.P.M., Franchin, M., Talbot, J., Reis, D.G., Menezes, G.B., Castania, J.A., Garcia-Cairasco, N., Resstel, L.B.M., Salgado, H.C., et al. (2017). Modulation of experimental arthritis by vagal sensory and central brain stimulation. Brain. Behav. Immun. *64*, 330–343.

Batterham, R.L., and Cummings, D.E. (2016). Mechanisms of diabetes improvement following bariatric/metabolic surgery. Diabetes Care *39*, 893–901.

Baver, S.B., Hope, K., Guyot, S., Bjørbaek, C., Kaczorowski, C., and O'Connell, K.M.S. (2014). Leptin modulates the intrinsic excitability of AgRP/NPY neurons in the arcuate nucleus of the hypothalamus. J. Neurosci. *34*, 5486–5496.

Bayliss, W.M., and Starling, E.H. (1899). The movements and innervation of the small intestine. J. Physiol. *24*, 99–143.

Beatty, J.K., Bhargava, A., and Buret, A.G. (2014). Post-infectious irritable bowel syndrome: mechanistic insights into chronic disturbances following enteric infection. World J. Gastroenterol. *20*, 3976–3985.

Becker, L., Nguyen, L., Gill, J., Kulkarni, S., Pasricha, P.J., and Habtezion, A. (2017). Age-dependent shift in macrophage polarisation causes inflammation-mediated degeneration of enteric nervous system. Gut gutjnl-2016-312940.

Belkaid, Y., and Hand, T.W. (2014). Role of the microbiota in immunity and inflammation. Cell *157*, 121–141.

Belkind-Gerson, J., Graham, H.K., Reynolds, J., Hotta, R., Nagy, N., Cheng, L., Kamionek, M., Shi, H.N., Aherne, C.M., and Goldstein, A.M. (2017). Colitis promotes neuronal differentiation of Sox2+ and PLP1+ enteric cells. Sci. Rep. *7*.

Bellavance, M.A., and Rivest, S. (2014). The HPA - immune axis and the immunomodulatory actions of glucocorticoids in the brain. Front. Immunol. *5*, 1–13.

Bellono, N.W., Bayrer, J.R., Leitch, D.B., Brierley, S.M., Ingraham, H.A., Julius, D., Bellono, N.W., Bayrer, J.R., Leitch, D.B., Castro, J., et al. (2017). Enterochromaffin Cells Are Gut Chemosensors that Couple to Sensory Neural Pathways Article Enterochromaffin Cells Are Gut Chemosensors that Couple to Sensory Neural Pathways. Cell 1–14.

Benskey, M.J., Kuhn, N.C., Galligan, J.J., Garcia, J., Boye, S.E., Hauswirth, W.W., Mueller, C., Boye, S.L., and Manfredsson, F.P. (2015). Targeted Gene Delivery to the Enteric Nervous System Using AAV : A Comparison Across Serotypes and Capsid Mutants. Mol. Ther. *23*, 488–500.

Vanden Berghe, T., Hulpiau, P., Martens, L., Vandenbroucke, R.E., Van Wonterghem, E., Perry, S.W., Bruggeman, I., Divert, T., Choi, S.M., Vuylsteke, M., et al. (2015). PasSenger Mutations Confound Interpretation Of All Genetically Modified Congenic Mice. Immunity *43*, 200–209.

Bernardo, D., Marin, A.C., Fernández-Tomé, S., Montalban-Arques, A., Carrasco, A., Tristán, E., Ortega-Moreno, L., Mora-Gutiérrez, I., Díaz-Guerra, A., Caminero-

Fernández, R., et al. (2018). Human intestinal pro-inflammatory CD11chighCCR2+CX3CR1+ macrophages, but not their tolerogenic CD11c−CCR2−CX3CR1− counterparts, are expanded in inflammatory bowel disease. Mucosal Immunol. *11*, 1114–1126.

Berthoud, H. (1990). Simultaneous labeling of vagal innervation of the gut and afferent projections from the visceral forebrain with dil injected into the dorsal vagal complex in the rat. J. Comp. … *301*, 65–79.

Berthoud, H.R., and Powley, T.L. (1993). Characterization of vagal innervation to the rat celiac, suprarenal and mesenteric ganglia. J. Auton. Nerv. Syst. *42*, 153–169.

Berthoud, H.R., and Powley, T.L. (1996). Interaction between parasympathetic and sympathetic nerves in prevertebral ganglia: morphological evidence for vagal efferent innervation of ganglion cells in the rat. Microsc. Res. Tech. *35*, 80–86.

Berthoud, H.R., Patterson, L.M., Neumann, F., and Neuhuber, W.L. (1997). Distribution and structure of vagal afferent intraganglionic laminar endings (IGLEs) in the rat gastrointestinal tract. Anat. Embryol. (Berl). *195*, 183–191.

Den Besten, G., Van Eunen, K., Groen, A.K., Venema, K., Reijngoud, D.J., and Bakker, B.M. (2013). The role of short-chain fatty acids in the interplay between diet, gut microbiota, and host energy metabolism. J. Lipid Res. *54*, 2325–2340.

Beyder, A., Rae, J.L., Bernard, C., Strege, P.R., Sachs, F., and Farrugia, G. (2010). Mechanosensitivity of Nav1.5, a voltage-sensitive sodium channel. J. Physiol. *588*, 4969–4985.

Beyder, A., Mazzone, A., Strege, P.R., Tester, D.J., Saito, Y.A., Bernard, C.E., Enders, F.T., Ek, W.E., Schmidt, P.T., Dlugosz, A., et al. (2014). Loss-of-function of the voltage-gated sodium channel Na V 1.5 (Channelopathies) in patients with irritable bowel syndrome. Gastroenterology *146*, 1659–1668.

Biggs, M.B., Medlock, G.L., Moutinho, T.J., Lees, H.J., Swann, J.R., Kolling, G.L., and Papin, J.A. (2017). Systems-level metabolism of the altered Schaedler flora, a complete gut microbiota. ISME J. *11*, 426–438.

Bindels, L.B., Segura Munoz, R.R., Gomes-Neto, J.C., Mutemberezi, V., Martínez, I., Salazar, N., Cody, E.A., Quintero-Villegas, M.I., Kittana, H., de los Reyes-Gavilán, C.G., et al. (2017). Resistant starch can improve insulin sensitivity independently of the gut

microbiota. Microbiome *5*, 1–16.

Blander, J.M., Longman, R.S., Iliev, I.D., Sonnenberg, G.F., and Artis, D. (2017). Regulation of inflammation by microbiota interactions with the host. Nat. Immunol. *18*, 851–860.

Bleymehl, K., Pérez-Gómez, A., Omura, M., Moreno-Pérez, A., Macías, D., Bai, Z., Johnson, R.S., Leinders-Zufall, T., Zufall, F., and Mombaerts, P. (2016). A Sensor for Low Environmental Oxygen in the Mouse Main Olfactory Epithelium. Neuron *92*, 1196–1203.

Bogunovic, M., Ginhoux, F., Helft, J., Shang, L., Hashimoto, D., Greter, M., Liu, K., Jakubzick, C., Ingersoll, M.A., Leboeuf, M., et al. (2009). Origin of the Lamina Propria Dendritic Cell Network. Immunity *31*, 513–525.

Bohórquez, D. V, Shahid, R.A., Erdmann, A., Kreger, A.M., Wang, Y., Calakos, N., Wang, F., and Liddle, R.A. (2015). Neuroepithelial circuit formed by innervation of sensory enteroendocrine cells. J. Clin. Invest. *125*, 782–786.

Bonaz, B., Bazin, T., and Pellissier, S. (2018). The vagus nerve at the interface of the microbiota-gut-brain axis. Front. Neurosci. *12*, 1–9.

Boraschi, D., and Italiani, P. (2018). Innate immune memory: Time for adopting a correct terminology. Front. Immunol. *9*, 1–4.

Boring, L., Gosling, J., Chensue, S.W., Kunkel, S.L., Farese, R. V., Broxmeyer, H.E., and Charo, I.F. (1997). Impaired monocyte migration and reduced type 1 (Th1) cytokine responses in C-C chemokine receptor 2 knockout mice. J. Clin. Invest. *100*, 2552–2561.

Borovikova, L. V, Ivanova, S., Zhang, M., Yang, H., Botchkina, G.I., Watkins, L.R., Wang, H., Abumrad, N., Eaton, J.W., and Tracey, K.J. (2000). Vagus nerve stimulation attenuates the systemic inflammatory response to endotoxin. Nature *405*, 458–462.

Bortoff, A., and Muller, R. (1975). Stimulation of intestinal smooth muscle by atropine, procaine, and tetrodotoxin. Am. J. Physiol. *229*, 1609–1613.

Bosmans, G., Appeltans, I., Stakenborg, N., Gomez-Pinilla, P.J., Florens, M. V., Aguilera-Lizarraga, J., Matteoli, G., and Boeckxstaens, G.E. (2019). Vagus nerve stimulation dampens intestinal inflammation in a murine model of experimental food allergy. Allergy Eur. J. Allergy Clin. Immunol. 1–12.

Braniste, V., Al-Asmakh, M., Kowal, C., Anuar, F., Abbaspour, A., Tóth, M., Korecka, A., Bakocevic, N., Guan, N.L., Kundu, P., et al. (2014). The gut microbiota influences blood-brain barrier permeability in mice. Sci. Transl. Med. *6*, 1–12.

Bronner, D.N., Faber, F., Olsan, E.E., Byndloss, M.X., Sayed, N.A., Xu, G., Yoo, W., Kim, D., Ryu, S., Lebrilla, C.B., et al. (2018). Genetic Ablation of Butyrate Utilization Attenuates Gastrointestinal Salmonella Disease. Cell Host Microbe *23*, 266-273.e4.

Brookes, S.J.H., Spencer, N.J., Costa, M., and Zagorodnyuk, V.P. (2013). Extrinsic primary afferent signalling in the gut. Nat. Rev. Gastroenterol. Hepatol. *10*, 286–296.

Brown, D.E., Libby, S.J., Moreland, S.M., McCoy, M.W., Brabb, T., Stepanek, A., Fang, F.C., and Detweiler, C.S. (2013). Salmonella enterica Causes More Severe Inflammatory Disease in C57/BL6 Nramp1G169Mice Than Sv129S6 Mice. Vet. Pathol. *50*, 867–876.

Brown, I.A.M., McClain, J.L., Watson, R.E., Patel, B.A., and Gulbransen, B.D. (2016). Enteric Glia Mediate Neuron Death in Colitis Through Purinergic Pathways That Require Connexin-43 and Nitric Oxide. C. Cell. Mol. Gastroenterol. Hepatol. *2*, 77–91.

Browning, K.N., and Lees, G.M. (2000). Inhibitory effects of NPY on ganglionic transmission in myenteric neurones of the guinea-pig descending colon. Neurogastroenterol. Motil. *12*, 33–41.

Browning, K.N., and Travagli, R.A. (2014). Central nervous system control of gastrointestinal motility and secretion and modulation of gastrointestinal functions. Compr. Physiol. *4*, 1339–1368.

Browning, K.N., and Travagli, R.A. (2019). Central control of gastrointestinal motility.

Browning, K.N., Verheijden, S., and Boeckxstaens, G.E. (2017). The Vagus Nerve in Appetite Regulation, Mood, and Intestinal Inflammation. Gastroenterology *152*, 730–744.

Broz, P., and Dixit, V.M. (2016). Inflammasomes: Mechanism of assembly, regulation and signalling. Nat. Rev. Immunol. *16*, 407–420.

Brun, P., Giron, M.C., Qesari, M., Porzionato, A., Caputi, V., Zoppellaro, C., Banzato, S., Grillo, A.R., Spagnol, L., De Caro, R., et al. (2013). Toll-like receptor 2 regulates intestinal inflammation by controlling integrity of the enteric nervous system. Gastroenterology *145*, 1323–1333.

Buckinx, R., Alpaerts, K., Pintelon, I., Cools, N., Van Nassauw, L., Adriaensen, D., and Timmermans, J.P. (2017). In situ proximity of CX3CR1-positive mononuclear phagocytes and VIP-ergic nerve fibers suggests VIP-ergic immunomodulation in the mouse ileum. Cell Tissue Res. *368*, 459–467.

Bujko, A., Atlasy, N., Landsverk, O.J.B., Richter, L., Yaqub, S., Horneland, R., Øyen, O., Aandahl, E.M., Aabakken, L., Stunnenberg, H.G., et al. (2018). Transcriptional and functional profiling defines human small intestinal macrophage subsets. J. Exp. Med. *215*, 441–458.

Burgueño, J.F., Barba, A., Eyre, E., Romero, C., Neunlist, M., and Fernández, E. (2016). TLR2 and TLR9 modulate enteric nervous system inflammatory responses to lipopolysaccharide. J. Neuroinflammation 1–15.

Burnstock, G. (1969a). Evolution of the autonomic innervation of visceral and cardiovascular systems in vertebrates. Pharmacol. Rev. *21*, 247–324.

Burnstock, G. (1969b). Evolution of the autonomic innervation of visceral and cardiovascular systems in vertebrates. Pharmacol. Rev. *21*, 247–324.

Burnstock, G., and Costa, M. (1973). Inhibitory Innervation of the Gut. Gastroenterology *64*, 141–144.

Cai, D., Deng, K., Mellado, W., Lee, J., Ratan, R.R., and Filbin, M.T. (2002). Arginase I and polyamines act downstream from cyclic AMP in overcoming inhibition of axonal growth MAG and myelin in vitro. Neuron *35*, 711–719.

Cailotto, C., Costes, L.M.M., van der Vliet, J., van Bree, S.H.W., van Heerikhuize, J.J., Buijs, R.M., and Boeckxstaens, G.E. (2012). Neuroanatomical evidence demonstrating the existence of the vagal anti-inflammatory reflex in the intestine. Neurogastroenterol. Motil. *24*, 191–201.

Campos, C.A., Shiina, H., Silvas, M., Page, S., and Ritter, R.C. (2013). Vagal afferent NMDA receptors modulate CCKInduced reduction of food intake through synapsin i phosphorylation in adult male rats. Endocrinology *154*, 2613–2625.

Cani, P.D. (2018). Human gut microbiome: Hopes, threats and promises. Gut *67*, 1716–1725.

Capelli, P., Pivetta, C., Soledad Esposito, M., and Arber, S. (2017). Locomotor speed control circuits in the caudal brainstem. Nature.

Carabotti, M., Scirocco, A., Maselli, M.A., and Severi, C. (2009). The gut-brain axis: interactions between enteric microbiota, central and enteric nervous systems. Ann. Gastroenterol. *28*, 203–209.

Carbone, S.E., Jovanovska, V., Nurgali, K., and Brookes, S.J.H. (2014). Human enteric neurons: morphological, electrophysiological, and neurochemical identification. Neurogastroenterol. Motil. 1–5.

Cardoso, V., Chesné, J., Ribeiro, H., García-Cassani, B., Carvalho, T., Bouchery, T., Shah, K., Barbosa-Morais, nuno L., Harris, N., and Veiga-Fernandes, H. (2017). Neuronal regulation of type 2 innate lymphoid cells via neuromedin U. Nature *549*, 277–281.

Carrión, M., Pérez-García, S., Martínez, C., Juarranz, Y., Estrada-Capetillo, L., Puig-Kröger, A., Gomariz, R.P., and Gutiérrez-Cañas, I. (2016a). VIP impairs acquisition of the macrophage proinflammatory polarization profile. J. Leukoc. Biol. *100*, 1385–1393.

Carrión, M., Pérez-García, S., Martínez, C., Juarranz, Y., Estrada-Capetillo, L., Puig-Kröger, A., Gomariz, R.P., and Gutiérrez-Cañas, I. (2016b). VIP impairs acquisition of the macrophage proinflammatory polarization profile. J. Leukoc. Biol. *100*, 1385–1393.

Chalazonitis, A., and Rao, M. (2018). Enteric nervous system manifestations of neurodegenerative disease. Brain Res. *1693*, 207–213.

Chan, K.Y., Jang, M.J., Yoo, B.B., Greenbaum, A., Ravi, N., Wu, W., Sánchez-guardado, L., Lois, C., Mazmanian, S.K., Deverman, B.E., et al. (2017). Engineered adeno-associated viruses for efficient and noninvasive gene delivery throughout the central and peripheral nervous systems. Nat. Publ. Gr. 1–30.

Chang, J.E., Buechler, M.B., Gressier, E., Turley, S.J., and Carroll, M.C. (2019). Mechanosensing by Peyer's patch stroma regulates lymphocyte migration and mucosal antibody responses. Nat. Immunol. *39*, 758–769.

Chang, R.B., Strochlic, D.E., Williams, E.K., Umans, B.D., and Liberles, S.D. (2015). Vagal sensory neuron subtypes that differentially control breathing. Cell *161*, 622–633.

Chen, H., Nwe, P.-K., Yang, Y., Rosen, C.E., Bielecka, A.A., Kuchroo, M., Cline, G.W., Kruse, A.C., Ring, A.M., Crawford, J.M., et al. (2019a). A Forward Chemical Genetic Screen Reveals Gut Microbiota Metabolites That Modulate Host Physiology. Cell *177*, 1217-1231.e18.

Chen, Y., Lin, Y.-C., Kuo, T.-W., and Knight, Z.A. (2015). Sensory Detection of Food Rapidly Modulates Arcuate Feeding Circuits. Cell *160*, 829–841.

Chen, Y., Essner, R.A., Kosar, S., Miller, O.H., Lin, Y.C., Mesgarzadeh, S., and Knight, Z.A. (2019b). Sustained NPY signaling enables AgRP neurons to drive feeding. Elife *8*, 1–15.

Chi, J., Wu, Z., Choi, C.H.J., Nguyen, L., Tegegne, S., Ackerman, S.E., Crane, A., Marchildon, F., Tessier-Lavigne, M., and Cohen, P. (2018). Three-Dimensional Adipose Tissue Imaging Reveals Regional Variation in Beige Fat Biogenesis and PRDM16-

Dependent Sympathetic Neurite Density. Cell Metab. *27*, 226-236.e3.

Chieppa, M., Rescigno, M., Huang, A.Y.C., and Germain, R.N. (2006). Dynamic imaging of dendritic cell extension into the small bowel lumen in response to epithelial cell TLR engagement. J. Exp. Med. *203*, 2841–2852.

Chiu, I.M., Heesters, B.A., Ghasemlou, N., Von Hehn, C.A., Zhao, F., Tran, J., Wainger, B., Strominger, A., Muralidharan, S., Horswill, A.R., et al. (2013). Bacteria activate sensory neurons that modulate pain and inflammation. Nature *501*, 52–57.

Chiu, I.M., Barrett, L.B., Williams, E.K., Strochlic, D.E., Lee, S., Weyer, A.D., Lou, S., Bryman, G.S., Roberson, D.P., Ghasemlou, N., et al. (2014). Transcriptional profiling at whole population and single cell levels reveals somatosensory neuron molecular diversity. Elife *3*, e04660.

Chokshi, A., Sifri, Z., Cennimo, D., and Horng, H. (2019). Global Contributors to Antibiotic Resistance. J. Glob. Infect. Dis. *11*, 36–42.

Christiansen, C.B., Gabe, M.B.N., Svendsen, B., Dragsted, L.O., Rosenkilde, M.M., and Holst, J.J. (2018). The impact of short-chain fatty acids on glp-1 and pyy secretion from the isolated perfused rat colon. Am. J. Physiol. - Gastrointest. Liver Physiol. *315*, G53–G65.

Cipriani, G., Gibbons, S.J., Miller, K.E., Yang, D.S., Terhaar, M.L., Eisenman, S.T., Ördög, T., Linden, D.R., Gajdos, G.B., Szurszewski, J.H., et al. (2018). Change in Populations of Macrophages Promotes Development of Delayed Gastric Emptying in Mice. Gastroenterology *154*, 2122-2136.e12.

Cipriani, G., Terhaar, M.L., Eisenman, S.T., Ji, S., Linden, D.R., Wright, A.M., Sha, L., Ordog, T., Szurszewski, J.H., Gibbons, S.J., et al. (2019). Muscularis Propria Macrophages Alter the Proportion of Nitrergic but Not Cholinergic Gastric Myenteric Neurons. Cmgh *7*, 689-691.e4.

Clarkson, A.N., Liu, H., Pearson, L., Kapoor, M., Harrison, J.C., Sammut, I.A., Jackson, D.M., and Appleton, I. (2004). Neuroprotective effects of spermine following hypoxicischemic-induced brain damage: A mechanistic study. FASEB J. *18*, 1114–1116.

Cohen, L.J., Esterhazy, D., Kim, S.H., Lemetre, C., Aguilar, R.R., Gordon, E.A., Pickard, A.J., Cross, J.R., Emiliano, A.B., Han, S.M., et al. (2017). Commensal bacteria make GPCR ligands that mimic human signalling molecules. Nature *549*, 48–53.

Cohen, S.M., Ma, H., Kuchibhotla, K. V., Watson, B.O., Buzsáki, G., Froemke, R.C., and Tsien, R.W. (2016). Excitation-Transcription Coupling in Parvalbumin-Positive

Interneurons Employs a Novel CaM Kinase-Dependent Pathway Distinct from Excitatory Neurons. Neuron *90*, 292–307.

Collins, J., Borojevic, R., Verdu, E.F., Huizinga, J.D., and Ratcliffe, E.M. (2014). Intestinal microbiota influence the early postnatal development of the enteric nervous system. Neurogastroenterol. Motil. *26*, 98–107.

Conn, A.R., Fell, D.I., and Steele, R.D. (1983). Characterization of α-keto acid transport across blood-brain barrier in rats. Am. J. Physiol. - Endocrinol. Metab. *8*.

Costa, M., Brookes, S.H.J., and Zagorodnyuk, V. (2004). How many kinds of visceral afferents ? 1–5.

Costes, M., Vliet, J. Van Der, Giovangiulio, M. Di, Cailotto, C., Gomez-pinilla, P.J., Matteoli, G., and Boeckxstaens, G.E. (2014). Neuro-Anatomical Evidence Indicating Indirect Modulation of Macrophages by Vagal Efferents in the Intestine but Not in the Spleen. *9*.

Crawford, R.W., Keestra, A.M., Winter, S.E., Xavier, M.N., Tsolis, R.M., Tolstikov, V., and Bäumler, A.J. (2012). Very Long O-antigen Chains Enhance Fitness during Salmonella-induced Colitis by Increasing Bile Resistance. PLoS Pathog. *8*.

Cremon, C., Stanghellini, V., Pallotti, F., Fogacci, E., Bellacosa, L., Morselli-Labate, A.M., Paccapelo, A., Di Nardo, G., Cogliandro, R.F., De Giorgio, R., et al. (2014). Salmonella gastroenteritis during childhood is a risk factor for irritable bowel syndrome in adulthood. Gastroenterology *147*, 69–77.

Croset, M., Rajas, F., Zitoun, C., Hurot, J.M., Montano, S., and Mithieux, G. (2001). Rat small intestine is an insulin-sensitive gluconeogenic organ. Diabetes *50*, 740–746.

Cryan, J.F., O'Riordan, K.J., Cowan, C.S.M., Sandhu, K. V., Bastiaanssen, T.F.S., Boehme, M., Codagnone, M.G., Cussotto, S., Fulling, C., Golubeva, A. V., et al. (2019). The Microbiota-Gut-Brain Axis. Physiol. Rev. *99*, 1877–2013.

Cuche, G., Blat, S., and Malbert, C.H. (2001). Desensitization of ileal vagal receptors by short-chain fatty acids in pigs. Am. J. Physiol. - Gastrointest. Liver Physiol. *280*, 1013–1021.

Dabke, K., Hendrick, G., and Devkota, S. (2019). The gut microbiome and metabolic syndrome. J. Clin. Invest. *129*, 4050–4057.

Dampney, R.A.L. (1994). Functional organization of central pathways regulating the cardiovascular system. Physiol. Rev. *74*, 323–364.

Danne, C., Ryzhakov, G., Martínez-López, M., Ilott, N.E., Franchini, F., Cuskin, F., Lowe, E.C., Bullers, S.J., Arthur, J.S.C., and Powrie, F. (2017). A Large Polysaccharide Produced by Helicobacter hepaticus Induces an Anti-inflammatory Gene Signature in Macrophages. Cell Host Microbe *22*, 733-745.e5.

Davies, L.C., Jenkins, S.J., Allen, J.E., and Taylor, P.R. (2013). Tissue-resident macrophages. Nat. Immunol. *14*, 986–995.

DeFronzo, R.A., Ferrannini, E., Groop, L., Henry, R.R., Herman, W.H., Holst, J.J., Hu, F.B., Kahn, C.R., Raz, I., Shulman, G.I., et al. (2015). Type 2 diabetes mellitus. Nat. Rev. Dis. Prim. *1*, 15019.

Deuchars, S.A., and Lall, V.K. (2015). Sympathetic preganglionic neurons: properties and inputs. Compr. Physiol. *5*, 829–869.

Dewhirst, F.E., Chien, C.C., Paster, B.J., Ericson, R.L., Orcutt, R.P., Schauer, D.B., and Fox, J.G. (1999). Phylogeny of the defined murine microbiota: Altered Schaedler flora. Appl. Environ. Microbiol. *65*, 3287–3292.

Diehl, G.E., Longman, R.S., Zhang, J.X., Breart, B., Galan, C., Cuesta, A., Schwab, S.R., and Littman, D.R. (2013). Microbiota restricts trafficking of bacteria to mesenteric lymph nodes by CX 3 CR1 hi cells. Nature *494*, 116–120.

Dietrich, M.O., Zimmer, M.R., Bober, J., and Horvath, T.L. (2015). Hypothalamic Agrp neurons drive stereotypic behaviors beyond feeding. Cell *160*, 1222–1232.

Dixon, J.B., O'Brien, P.E., Playfair, J., Chapman, L., Schachter, L.M., Skinner, S., Proietto, J., Bailey, M., and Anderson, M. (2008). Adjustable gastric banding and conventional therapy for type 2 diabetes: A randomized controlled trial. JAMA - J. Am. Med. Assoc. *299*, 316–323.

Dohi, T., Ejima, C., Kato, R., Kawamura, Y.I., Kawashima, R., Mizutani, N., Tabuchi, Y., and Kojima, I. (2005). Therapeutic potential of follistatin for colonic inflammation in mice. Gastroenterology *128*, 411–423.

Douglass, J., McKinzie, A.A., and Couceyro, P. (1995). PCR differential display identifies a rat brain mRNA that is transcriptionally regulated by cocaine and amphetamine. J. Neurosci. *15*, 2471–2481.

Drokhlyansky, E., Smillie, C.S., Van Wittenberghe, N., Ericsson, M., Griffin, G.K., Dionne, D., Cuoco, M.S., Goder-Reiser, M.N., Sharova, T., Aguirre, A.J., et al. (2019). The enteric nervous system of the human and mouse colon at a single-cell resolution. BioRxiv.

Duale, H., Hou, S., Derbenev, A. V, Smith, B.N., and Rabchevsky, A.G. (2017). Spinal Cord Injury Reduces the Efficacy of Pseudorabies Virus Labeling of Sympathetic Preganglionic Neurons. *68*.

Duca, F.A., Swartz, T.D., Sakar, Y., and Covasa, M. (2012). Increased oral detection, but decreased intestinal signaling for fats in mice lacking gut microbiota. PLoS One *7*, e39748.

Dunay, I.R., Damatta, R.A., Fux, B., Presti, R., Greco, S., Colonna, M., and Sibley, L.D. (2008). Gr1(+) inflammatory monocytes are required for mucosal resistance to the pathogen Toxoplasma gondii. Immunity *29*, 306–317.

Dunn-Meynell, A.A., Sanders, N.M., Compton, D., Becker, T.C., Eiki, J., Zhang, B.B., and Levin, B.E. (2009). Relationship among brain and blood glucose levels and spontaneous and glucoprivic feeding. J. Neurosci. *29*, 7015–7022.

Dupont, J. -R, Jervis, H.R., and Sprinz, H. (1965). Auerbach's plexus of the rat cecum in relation to the germfree state. J. Comp. Neurol. *125*, 11–18.

Dutra, W.O., Menezes, C.A.S., Villani, F.N.A., da Costa, G.C., da Silveira, A.B.M., Reis, D. d'Avila, and Gollob, K.J. (2009). Cellular and genetic mechanisms involved in the generation of protective and pathogenic immune responses in human Chagas disease. Mem. Inst. Oswaldo Cruz *104 Suppl*, 208–218.

Van Dyken, S.J., and Locksley, R.M. (2013). Interleukin-4- and Interleukin-13-Mediated Alternatively Activated Macrophages: Roles in Homeostasis and Disease. Annu. Rev. Immunol. *31*, 317–343.

Edgar, R.C. (2010). Search and clustering orders of magnitude faster than BLAST. Bioinformatics *26*, 2460–2461.

Ekblad, E. (2006). CART in the enteric nervous system. *27*, 2024–2030.
Ellis, L.M., and Mawe, G.M. (2003). Distribution and chemical coding of cocaine- and amphetamine-regulated transcript peptide (CART)-immunoreactive neurons in the guinea pig bowel. Cell Tissue Res. *312*, 265–274.

Ernsberger, U., and Rohrer, H. (2018). Sympathetic tales: Subdivisons of the autonomic nervous system and the impact of developmental studies. Neural Dev. *13*, 1–21.

Erny, D., Hrabě de Angelis, A.L., Jaitin, D., Wieghofer, P., Staszewski, O., David, E., Keren-Shaul, H., Mahlakoiv, T., Jakobshagen, K., Buch, T., et al. (2015). Host microbiota constantly control maturation and function of microglia in the CNS. Nat. Neurosci. *18*.

Ertürk, A., Becker, K., Jahrling, N., Mauch, C.P., Hojer, C.D., Egen, J.G., Hellal, F., Bradke, F., Sheng, M., and Dodt, H.U. (2012). Three-dimensional imaging of solvent-cleared organs using 3DISCO. Nat Protoc *7*, 1983–1995.

Espinosa-Medina, I., Saha, O., Boismoreau, F., Chettouh, Z., Rossi, F., Richardson, W.D., and Brunet, J.-F. (2016). The sacral autonomic outflow is sympathetic. Science *354*, 893–897.

Esterházy, D., Canesso, M.C.C., Mesin, L., Muller, P.A., de Castro, T.B.R., Lockhart, A., ElJalby, M., Faria, A.M.C., and Mucida, D. (2019). Compartmentalized gut lymph node drainage dictates adaptive immune responses. Nature *569*, 126–130.

Farache, J., Koren, I., Milo, I., Gurevich, I., Kim, K.W., Zigmond, E., Furtado, G.C., Lira, S.A., and Shakhar, G. (2013). Luminal Bacteria Recruit CD103+ Dendritic Cells into the Intestinal Epithelium to Sample Bacterial Antigens for Presentation. Immunity *38*, 581–595.

Faria, A.M.C., Reis, B.S., and Mucida, D. (2017). Tissue adaptation: Implications for gut immunity and tolerance. J. Exp. Med. *214*, 1211–1226.

Farro, G., Stakenborg, M., Gomez-Pinilla, P.J., Labeeuw, E., Goverse, G., Giovangiulio, M. Di, Stakenborg, N., Meroni, E., D'Errico, F., Elkrim, Y., et al. (2017). CCR2-dependent monocyte-derived macrophages resolve inflammation and restore gut motility in postoperative ileus. Gut gutjnl-2016-313144.

Fetissov, S.O. (2017). Role of the gut microbiota in host appetite control: Bacterial growth to animal feeding behaviour. Nat. Rev. Endocrinol. *13*, 11–25.

Fischer, K., Ruiz, H.H., Jhun, K., Finan, B., Oberlin, D.J., van der Heide, V., Kalinovich, A. V, Petrovic, N., Wolf, Y., Clemmensen, C., et al. (2017). Alternatively activated macrophages do not synthesize catecholamines or contribute to adipose tissue adaptive thermogenesis. Nat. Med.

Fonseca, D.M. da, Hand, T.W., Han, S.-J., Gerner, M.Y., Glatman Zaretsky, A., Byrd, A.L., Harrison, O.J., Ortiz, A.M., Quinones, M., Trinchieri, G., et al. (2015). Microbiota-Dependent Sequelae of Acute Infection Compromise Tissue-Specific Immunity. Cell *163*, 354–366.

Franklin, C.L., and Ericsson, A.C. (2017). Microbiota and reproducibility of rodent models. Lab Anim. (NY). *46*, 114–122.

Frost, G., Sleeth, M.L., Sahuri-Arisoylu, M., Lizarbe, B., Cerdan, S., Brody, L., Anastasovska, J., Ghourab, S., Hankir, M., Zhang, S., et al. (2014). The short-chain fatty acid acetate reduces appetite via a central homeostatic mechanism. Nat. Commun.

5, 1–11.

Fung, C., Koussoulas, K., Unterweger, P., Allen, A.M., Bornstein, J.C., and Foong, J.P.P. (2018). Cholinergic Submucosal Neurons Display Increased Excitability Following in Vivo Cholera Toxin Exposure in Mouse Ileum. Front. Physiol. *9*, 260.

Fung, T.C., Olson, C.A., and Hsiao, E.Y. (2017). Interactions between the microbiota, immune and nervous systems in health and disease. Nat. Neurosci. *20*, 145–155.

Furlan, A., La Manno, G., Lübke, M., Häring, M., Abdo, H., Hochgerner, H., Kupari, J., Usoskin, D., Airaksinen, M.S., Oliver, G., et al. (2016). Visceral motor neuron diversity delineates a cellular basis for nipple- and pilo-erection muscle control. Nat. Neurosci. *19*, 1331–1340.

Furness, J.. (2000). Types of neurons in the enteric nervous system. J. Auton. Nerv. Syst. *81*, 87–96.

Furness, J.B. (2012). The enteric nervous system and neurogastroenterology. Nat. Rev. Gastroenterol. Hepatol. *9*, 286–294.

Furness, J.B., and Costa, M. (1974). The adrenergic innervation of the gastrointestinal tract. Ergeb. Physiol. *69*, 2–51.

Furness, J.B., Rivera, L.R., Cho, H.-J., Bravo, D.M., and Callaghan, B. (2013). The gut as a sensory organ. Nat. Rev. Gastroenterol. Hepatol. *10*, 729–740.

Gabanyi, I., Muller, P.A., Feighery, L., Oliveira, T.Y., Costa-Pinto, F.A., and Mucida, D. (2016). Neuro-immune Interactions Drive Tissue Programming in Intestinal Macrophages. Cell *164*, 378–391.

Gautier, E.L., Shay, T., Miller, J., Greter, M., Jakubzick, C., Ivanov, S., Helft, J., Chow, A., Elpek, K.G., Gordonov, S., et al. (2012). Gene-expression profiles and transcriptional regulatory pathways that underlie the identity and diversity of mouse tissue macrophages. Nat. Immunol. *13*, 1118–1128.

Ghisletti, S., Barozzi, I., Mietton, F., Polletti, S., De Santa, F., Venturini, E., Gregory, L., Lonie, L., Chew, A., Wei, C.L., et al. (2010). Identification and Characterization of Enhancers Controlling the Inflammatory Gene Expression Program in Macrophages. Immunity *32*, 317–328.

Gielkens, H.A.J., Verkijk, M., Lam, W.F., Lamers, C.B.H.W., and Masclee, A.A.M. (1998). Effects of hyperglycemia and hyperinsulinemia on satiety in humans. Metabolism. *47*, 321–324.

Gil, D.W., Wang, J., Gu, C., Donello, J.E., Cabrera, S., and Al-Chaer, E.D. (2016). Role of sympathetic nervous system in rat model of chronic visceral pain. Neurogastroenterol. Motil. *28*, 423–431.

Gilad, G.M., and Gilad, V.H. (1999). Novel polyamine derivatives as neuroprotective agents. J. Pharmacol. Exp. Ther. *291*, 39–43.

Di Giovangiulio, M., Verheijden, S., Bosmans, G., Stakenborg, N., Boeckxstaens, G.E., and Matteoli, G. (2015). The neuromodulation of the intestinal immune system and its relevance in inflammatory bowel disease. Front. Immunol. *6*.

Goehler, L.E., Gaykema, R.P.A., Opitz, N., Reddaway, R., Badr, N., and Lyte, M. (2005). Activation in vagal afferents and central autonomic pathways: Early responses to intestinal infection with Campylobacter jejuni. Brain. Behav. Immun. *19*, 334–344.

Gombash, S.E., Cowley, C.J., Fitzgerald, J.A., Hall, J.C.E., Mueller, C., Christofi, F.L., and Foust, K.D. (2014). Intravenous AAV9 efficiently transduces myenteric neurons in neonate and juvenile mice. *7*, 1–11.

Gomes-Neto, J.C., Mantz, S., Held, K., Sinha, R., Segura Munoz, R.R., Schmaltz, R., Benson, A.K., Walter, J., and Ramer-Tait, A.E. (2017). A real-time PCR assay for accurate quantification of the individual members of the Altered Schaedler Flora microbiota in gnotobiotic mice. J. Microbiol. Methods *135*, 52–62.

Gonçalves, J.P.L., Palmer, D., and Meldal, M. (2018). MC4R Agonists: Structural Overview on Antiobesity Therapeutics. Trends Pharmacol. Sci. *39*, 402–423.

Gonella, J., Bouvier, M., and Blanquet, F. (1987). Extrinsic nervous control of motility of small and large intestines and related sphincters. Physiol. Rev. *67*, 902–961.

Gonkowski, S., and Rytel, L. (2019). Somatostatin as an Active Substance in the Mammalian Enteric Nervous System. Int. J. Mol. Sci. *20*, 4461.

Gordon, H.A., and Pesti, L. (1971). The gnotobiotic animal as a tool in the study of host microbial relationships. Bacteriol. Rev. *35*, 390–429.

Gore, R., Riedl, M.S., Kitto, K.F., Fairbanks, C.A., and Vulchanova, L. (2019). AAV-Mediated Gene Delivery to the Enteric Nervous System by Intracolonic Injection. Methods Mol. Biol. *1950*, 407–415.

Goswami, C., Iwasaki, Y., and Yada, T. (2018). Short-chain fatty acids suppress food intake by activating vagal afferent neurons. J. Nutr. Biochem. *57*, 130–135.

Gribble, F.M., and Reimann, F. (2016). Enteroendocrine Cells: Chemosensors in the

Intestinal Epithelium. Annu. Rev. Physiol. *78*, 277–299.

Grider, J.R. (2003). Neurotransmitters mediating the intestinal peristaltic reflex in the mouse. J. Pharmacol. Exp. Ther. *307*, 460–467.

Gulbransen, B.D., Bashashati, M., Hirota, S. a, Gui, X., Roberts, J. a, MacDonald, J. a, Muruve, D. a, McKay, D.M., Beck, P.L., Mawe, G.M., et al. (2012). Activation of neuronal P2X7 receptor–pannexin-1 mediates death of enteric neurons during colitis. Nat. Med. *18*, 600–604.

Gunawardene, A.R., Corfe, B.M., and Staton, C.A. (2011). Classification and functions of enteroendocrine cells of the lower gastrointestinal tract. Int. J. Exp. Pathol. *92*, 219–231.

Gupta, R., Ma, Y., Wang, M., and Whim, M.D. (2017). AgRP-Expressing Adrenal Chromaffin Cells Are Involved in the Sympathetic Response to Fasting. Endocrinology *158*, 2572–2584.

Haak, B.W., Littmann, E.R., Chaubard, J.L., Pickard, A.J., Fontana, E., Adhi, F., Gyaltshen, Y., Ling, L., Morjaria, S.M., Peled, J.U., et al. (2018). Impact of gut colonization with butyrate-producing microbiota on respiratory viral infection following allo-HCT. Blood *131*, 2978–2986.

Han, W., Tellez, L.A., Perkins, M.H., Perez, I.O., Qu, T., Ferreira, J., Ferreira, T.L., Quinn, D., Liu, Z.W., Gao, X.B., et al. (2018). A Neural Circuit for Gut-Induced Reward. Cell *175*, 665-678.e23.

Handa, A.K., Fatima, T., and Mattoo, A.K. (2018). Polyamines: Bio-Molecules with Diverse Functions in Plant and Human Health and Disease. Front. Chem. *6*, 1–18.

Hao, M.M., Fung, C., Boesmans, W., Lowette, K., Tack, J., and Vanden Berghe, P. (2019). Development of the intrinsic innervation of the small bowel mucosa and villi. Am. J. Physiol. Gastrointest. Liver Physiol.

Hara, H., Seregin, S.S., Yang, D., Fukase, K., Chamaillard, M., Alnemri, E.S., Inohara, N., Chen, G.Y., and Núñez, G. (2018). The NLRP6 Inflammasome Recognizes Lipoteichoic Acid and Regulates Gram-Positive Pathogen Infection. Cell 1651–1664.

Harris, J.A., Hirokawa, K.E., Sorensen, S.A., Gu, H., Mills, M., Ng, L.L., Bohn, P., Mortrud, M., Ouellette, B., Kidney, J., et al. (2014). Anatomical characterization of Cre driver mice for neural circuit mapping and manipulation. Front. Neural Circuits *8*, 76.

Harris, L., Kayser, B.D., Cefalo, C., Marini, L., Watrous, J.D., Ding, J., Jain, M., McDonald, J.G., Thompson, B.M., Fabbrini, E., et al. (2019). Biliopancreatic Diversion

Induces Greater Metabolic Improvement Than Roux-en-Y Gastric Bypass. Cell Metab. 1–10.

Havrankova, J., Roth, J., and Brownstein, M. (1978). Insulin receptors are widely distributed in the central nervous system of the rat. Nature *272*, 827–829.

Hayashi, A., Sato, T., Kamada, N., Mikami, Y., Matsuoka, K., Hisamatsu, T., Hibi, T., Roers, A., Yagita, H., Ohteki, T., et al. (2013). A Single Strain of Clostridium butyricum Induces Intestinal IL-10-Producing Macrophages to Suppress Acute Experimental Colitis in Mice. Cell Host Microbe *13*, 711–722.

Heiman, M., Kulicke, R., Fenster, R.J., Greengard, P., and Heintz, N. (2014). Cell type-specific mRNA purification by translating ribosome affinity purification (TRAP). Nat. Protoc. *9*, 1282–1291.

Helmink, B.A., Khan, M.A.W., Hermann, A., Gopalakrishnan, V., and Wargo, J.A. (2019). The microbiome, cancer, and cancer therapy. Nat. Med. *25*, 377–388.

Hendershot, T.J., Liu, H., Sarkar, A.A., Giovannucci, D.R., Clouthier, D.E., Abe, M., and Howard, M.J. (2007). Expression of Hand2 is sufficient for neurogenesis and cell type-specific gene expression in the enteric nervous system. Dev. Dyn. *236*, 93–105.

Heng, T.S.P., Painter, M.W., Elpek, K., Lukacs-Kornek, V., Mauermann, N., Turley, S.J., Koller, D., Kim, F.S., Wagers, A.J., Asinovski, N., et al. (2008). The immunological genome project: Networks of gene expression in immune cells. Nat. Immunol. *9*, 1091–1094.

Hesterberg, R., Cleveland, J., and Epling-Burnette, P. (2018). Role of Polyamines in Immune Cell Functions. Med. Sci. *6*, 22.

Heuckeroth, R.O. (2018). Hirschsprung disease — integrating basic science and clinical medicine to improve outcomes. Nat. Rev. Gastroenterol. Hepatol. *15*, 152–167.

Hibberd, T.J., Zagorodnyuk, V.P., Spencer, N.J., and Brookes, S.J.H. (2012). Identification and mechanosensitivity of viscerofugal neurons. Neuroscience *225*, 118–129.

Hibberd, T.J., Spencer, N.J., Zagorodnyuk, V.P., Chen, B.N., and Brookes, S.J.H. (2014). Targeted electrophysiological analysis of viscerofugal neurons in the myenteric plexus of guinea-pig colon. Neuroscience *275*, 272–284.

Hill, J.W., Elias, C.F., Fukuda, M., Williams, K.W., Berglund, E.D., Holland, W.L., Cho, Y.-R., Chuang, J.-C., Xu, Y., Choi, M., et al. (2010). Direct insulin and leptin action on pro-opiomelanocortin neurons is required for normal glucose homeostasis and fertility.

Cell Metab. *11*, 286–297.

Hine, A.M., and Loke, P. (2019). Intestinal Macrophages in Resolving Inflammation. J. Immunol. *203*, 593–599.

Hinoi, E., Gao, N., Jung, D.Y., Yadav, V., Yoshizawa, T., Myers, M.G., Chua, S.C., Kim, J.K., Kaestner, K.H., and Karsenty, G. (2008). The sympathetic tone mediates leptin's inhibition of insulin secretion by modulating osteocalcin bioactivity. J. Cell Biol. *183*, 1235–1242.

Hockley, J.R.F., Taylor, T.S., Callejo, G., Wilbrey, A.L., Gutteridge, A., Bach, K., Winchester, W.J., Bulmer, D.C., McMurray, G., and Smith, E.S.J. (2019). Single-cell RNAseq reveals seven classes of colonic sensory neuron. Gut *68*, 633–644.

Holst, J.J., Gribble, F., Horowitz, M., and Rayner, C.K. (2016). Roles of the gut in glucose homeostasis. Diabetes Care *39*, 884–892.

Holzer, P., Reichmann, F., and Farzi, A. (2012). Neuropeptide Y, peptide YY and pancreatic polypeptide in the gut-brain axis. Neuropeptides *46*, 261–274.

Hooper, L. V., and Gordon, J.I. (2001). Commensal host-bacterial relationships in the gut. Science (80-.). *292*, 1115–1118.

Huang, Y., and Thathiah, A. (2015). Regulation of neuronal communication by G protein-coupled receptors. FEBS Lett. *589*, 1607–1619.

Hung, L.Y., Boonma, P., Unterweger, P., Parathan, P., Haag, A., Luna, R.A., Bornstein, J.C., Savidge, T.C., and Foong, J.P.P. (2019). Neonatal Antibiotics Disrupt Motility and Enteric Neural Circuits in Mouse Colon. Cell. Mol. Gastroenterol. Hepatol. *8*, 298-300.e6.

Ibiza, S., García-cassani, B., Ribeiro, H., Carvalho, T., Almeida, L., Marques, R., Misic, A.M., Bartow-mckenney, C., Larson, D.M., Pavan, W.J., et al. (2016). Glial-cell-derived neuroregulators control type 3 innate lymphoid cells and gut defence. Nature *535*, 440–443.

Ilnytska, O., and Argyropoulos, G. (2008). The role of the Agouti-Related Protein in energy balance regulation. Cell. Mol. Life Sci. *65*, 2721–2731.

Ishifune, C., Maruyama, S., Sasaki, Y., Yagita, H., Hozumi, K., Tomita, T., Kishihara, K., and Yasutomo, K. (2014). Differentiation of CD11c+CX3CR1+ cells in the small intestine requires Notch signaling. Proc. Natl. Acad. Sci. *111*, 5986–5991.

Ivanov, I.I., Atarashi, K., Manel, N., Brodie, E.L., Shima, T., Karaoz, U., Wei, D.,

Goldfarb, K.C., Santee, C.A., Lynch, S. V., et al. (2009). Induction of Intestinal Th17 Cells by Segmented Filamentous Bacteria. Cell *139*, 485–498.

de Jonge, W.J., van der Zanden, E.P., The, F.O., Bijlsma, M.F., van Westerloo, D.J., Bennink, R.J., Berthoud, H.R., Uematsu, S., Akira, S., van den Wijngaard, R.M., et al. (2005). Stimulation of the vagus nerve attenuates macrophage activation by activating the Jak2-STAT3 signaling pathway. Nat. Immunol. *6*, 844–851.

Joseph, N.M., He, S., Quintana, E., Kim, Y., Núñez, G., and Morrison, S.J. (2011). Enteric glia are multipotent in culture but primarily form glia in the adult rodent gut. J. Clin. Invest. *121*, 3398–3411.

Kabouridis, P.S., Lasrado, R., McCallum, S., Chng, S.H., Snippert, H.J., Clevers, H., Pettersson, S., and Pachnis, V. (2015). Microbiota Controls the Homeostasis of Glial Cells in the Gut Lamina Propria. Neuron *85*, 289–295.

Kaelberer, M.M., Buchanan, K.L., Klein, M.E., Barth, B.B., Montoya, M.M., Shen, X., and Bohórquez, D. V (2018). A gut-brain neural circuit for nutrient sensory transduction. *5236*.

Kaestner, C.L., Smith, E.H., Peirce, S.G., and Hoover, D.B. (2019). Immunohistochemical analysis of the mouse celiac ganglion: An integrative relay station of the peripheral nervous system. J. Comp. Neurol. 2742–2760.

Kalff, J.C., Schraut, W.H., Simmons, R.L., and Bauer, A.J. (1998). Surgical Manipulation of the Gut Elicits an Intestinal Muscularis Inflammatory Response Resulting in Postsurgical leus. *228*, 652–663.

Kalff, J.C., Lee, K.W., Bauer, J., Mark, K., Kalff, C., Billiar, R., Lee, K.W., and Lipopolysaccha-, J.B. (2019). Lipopolysaccharide activates the muscularis macrophage network and suppresses circular smooth muscle activity. 727–734.

Kang, B., Alvarado, L.J., Kim, T., Lehmann, M.L., Cho, H., He, J., Li, P., Kim, B.H., Larochelle, A., and Kelsall, B.L. (2020). Commensal microbiota drive the functional diversification of colon macrophages. Mucosal Immunol. *13*, 216–229.

Kanoh, S., and Rubin, B.K. (2010). Mechanisms of action and clinical application of macrolides as immunomodulatory medications. Clin. Microbiol. Rev. *23*, 590–615.

Kashyap, P.C., Marcobal, A., Ursell, L.K., Larauche, M., Duboc, H., Earle, K.A., Sonnenburg, E.D., Ferreyra, J.A., Higginbottom, S.K., Million, M., et al. (2013). Complex interactions among diet, gastrointestinal transit, and gut microbiota in humanized mice. Gastroenterology *144*, 967–977.

El Kasmi, K.C., Qualls, J.E., Pesce, J.T., Smith, A.M., Thompson, R.W., Henao-Tamayo, M., Basaraba, R.J., König, T., Schleicher, U., Koo, M.-S., et al. (2008). Toll-like receptor-induced arginase 1 in macrophages thwarts effective immunity against intracellular pathogens. Nat. Immunol. *9*, 1399–1406.

Katayama, Y., Battista, M., Kao, W.M., Hidalgo, A., Peired, A.J., Thomas, S.A., and Frenette, P.S. (2006). Signals from the sympathetic nervous system regulate hematopoietic stem cell egress from bone marrow. Cell *124*, 407–421.

Kennedy, E.A., King, K.Y., and Baldridge, M.T. (2018). Mouse Microbiota Models: Comparing Germ-Free Mice and Antibiotics Treatment as Tools for Modifying Gut Bacteria. Front. Physiol. *9*, 1534.

Kenneth, N.S., Younger, J.M., Hughes, E.D., Marcotte, D., Barker, P.A., Saunders, T.L., and Duckett, C.S. (2012). An inactivating caspase 11 passenger mutation originating from the 129 murine strain in mice targeted for c-IAP1. Biochem. J. *443*, 355–359.

Kenney, M.J., and Ganta, C.K. (2014). Autonomic nervous system and immune system interactions. Compr. Physiol. *4*, 1177–1200.

Kernbauer, E., Ding, Y., and Cadwell, K. (2014). An enteric virus can replace the beneficial function of commensal bacteria. Nature *516*, 94–98.

Khan, T.J., Hasan, M.N., Azhar, E.I., and Yasir, M. (2019). Association of gut dysbiosis with intestinal metabolites in response to antibiotic treatment. Hum. Microbiome J. *11*, 100054.

Kim, M., Galan, C., Hill, A.A., Wu, W.J., Fehlner-Peach, H., Song, H.W., Schady, D., Bettini, M.L., Simpson, K.W., Longman, R.S., et al. (2018). Critical Role for the Microbiota in CX 3 CR1 + Intestinal Mononuclear Phagocyte Regulation of Intestinal T Cell Responses. Immunity *49*, 151-163.e5.

Kimura, H., Imura, Y. ki, Tomiyasu, H., Mihara, T., Kaji, N., Ohno, K., Unno, T., Tanahashi, Y., Jan, T.R., Tsubone, H., et al. (2019). Neural anti-inflammatory action mediated by two types of acetylcholine receptors in the small intestine. Sci. Rep. *9*, 1–11.

Kimura, I., Inoue, D., Maeda, T., Hara, T., Ichimura, A., Miyauchi, S., Kobayashi, M., Hirasawa, A., and Tsujimoto, G. (2011). Short-chain fatty acids and ketones directly regulate sympathetic nervous system via G protein-coupled receptor 41 (GPR41). Proc Natl Acad Sci U S A *108*, 8030–8035.

Kinoshita, K., Horiguchi, K., Fujisawa, M., Kobirumaki, F., Yamato, S., Hori, M., and Ozaki, H. (2007). Possible involvement of muscularis resident macrophages in

impairment of interstitial cells of Cajal and myenteric nerve systems in rat models of TNBS-induced colitis. Histochem. Cell Biol. *127*, 41–53.

Kirchgessner, A.L., and Gershon, M.D. (1990). Innervation of the pancreas by neurons in the gut. J. Neurosci. *10*, 1626–1642.

Kirchgessner, A.L., Liu, M.T., and Gershon, M.D. (1996). In situ identification and visualization of neurons that mediate enteric and enteropancreatic reflexes. J. Comp. Neurol. *371*, 270–286.

Klose, C.S.N., Mahlakõiv, T., Moeller, J.B., Rankin, L.C., Flamar, A.-L., Kabata, H., Monticelli, L.A., Moriyama, S., Putzel, G.G., Rakhilin, N., et al. (2017). The neuropeptide neuromedin U stimulates innate lymphoid cells and type 2 inflammation.

Knight, Z. a, Tan, K., Birsoy, K., Schmidt, S., Garrison, J.L., Wysocki, R.W., Emiliano, A., Ekstrand, M.I., and Friedman, J.M. (2012). Molecular profiling of activated neurons by phosphorylated ribosome capture. Cell *151*, 1126–1137.

Koh, A., De Vadder, F., Kovatcheva-Datchary, P., and Bäckhed, F. (2016). From dietary fiber to host physiology: Short-chain fatty acids as key bacterial metabolites. Cell *165*, 1332–1345.

Koomoa, D.-L.T., Geerts, D., Lange, I., Koster, J., Pegg, A.E., Feith, D.J., and Bachmann, A.S. (2013). DFMO/eflornithine inhibits migration and invasion downstream of MYCN and involves p27Kip1 activity in neuroblastoma. Int. J. Oncol. *42*, 1219–1228.

Korecka, A., Dona, A., Lahiri, S., Tett, A.J., Al-Asmakh, M., Braniste, V., D'Arienzo, R., Abbaspour, A., Reichardt, N., Fujii-Kuriyama, Y., et al. (2016). Bidirectional communication between the Aryl hydrocarbon Receptor (AhR) and the microbiome tunes host metabolism. Npj Biofilms Microbiomes *2*.

Kowalski, G.M., and Bruce, C.R. (2014). The regulation of glucose metabolism: Implications and considerations for the assessment of glucose homeostasis in rodents. Am. J. Physiol. - Endocrinol. Metab. *307*, E859–E871.

Koyama, N., Hakura, A., Toritsuka, N., Sonoda, J., Seki, Y., Tohyama, O., Asakura, S., Nakano-Ito, K., and Hosokawa, S. (2015). Wif1 and Ifitm3 gene expression preferentially altered in the colon mucosa of benzo[a]pyrene pre-treated mice following exposure to dextran sulfate sodium. Chem. Biol. Interact. *240*, 164–170.

Kristensen, P., Judge, M.E., Thim, L., Ribel, U., Christjansen, K.N., Wulff, B.S., Clausen, J.T., Jensen, P.B., Madsen, O.D., Vrang, N., et al. (1998). Hypothalamic CART is a new anorectic peptide regulated by leptin. Nature *393*, 72–76.

Kügler, S., Kilic, E., and Bähr, M. (2003). Human synapsin 1 gene promoter confers highly neuron-specific long-term transgene expression from an adenoviral vector in the adult rat brain depending on the transduced area. Gene Ther. *10*, 337–347.

Kuida, K., Lippke, J.A., Ku, G., Harding, M.W., Livingston, D.J., Su, M.S.S., and Flavell, R.A. (1995). Altered cytokine export and apoptosis in mice deficient in interleukin-1 beta converting enzyme. Science *267*, 2000–2003.

Kulkarni, S., Micci, M.-A., Leser, J., Shin, C., Tang, S.-C., Fu, Y.-Y., Liu, L., Li, Q., Saha, M., Li, C., et al. (2017). Adult enteric nervous system in health is maintained by a dynamic balance between neuronal apoptosis and neurogenesis. Proc. Natl. Acad. Sci. U. S. A. *114*, E3709–E3718.

Kupari, J., Häring, M., Agirre, E., Castelo-Branco, G., and Ernfors, P. (2019). An Atlas of Vagal Sensory Neurons and Their Molecular Specialization. Cell Rep. 2508–2523.

Kvetnansky, R., Sabban, E.L., and Palkovits, M. (2009). Catecholaminergic Systems in Stress : Structural and Molecular Genetic Approaches. 535–606.

Lai, N.Y., Musser, M.A., Pinho-Ribeiro, F.A., Baral, P., Ma, P., Potts, D.E., Chen, Z., Paik, D., Soualhi, S., Shi, H., et al. (2019). Gut-innervating nociceptor neurons protect against enteric infection by modulating the microbiota and Peyer's patch microfold cells. BioRxiv 580555.

Lal, S., Kirkup, A.J., Brunsden, A.M., Thompson, D.G., and Grundy, D. (2001). Vagal afferent responses to fatty acids of different chain length in the rat. Am. J. Physiol. Gastrointest. Liver Physiol. *281*, G907-15.

Lanfray, D., and Richard, D. (2017). Emerging signaling pathway in arcuate feeding-related neurons: Role of the Acbd7. Front. Neurosci. *11*, 1–8.

Langley, J.N. (1921). The autonomic nervous system (Pt. I).

Laranjeira, C., and Pachnis, V. (2009). Enteric nervous system development: Recent progress and future challenges. Auton. Neurosci. *151*, 61–69.

Laranjeira, C., Sandgren, K., Kessaris, N., Richardson, W., Potocnik, A., Vanden Berghe, P., and Pachnis, V. (2011). Glial cells in the mouse enteric nervous system can undergo neurogenesis in response to injury. J. Clin. Invest. *121*, 3412–3424.

Lasrado, R., Boesmans, W., Kleinjung, J., Pin, C., Bell, D., Bhaw, L., McCallum, S., Zong, H., Luo, L., Clevers, H., et al. (2017). Lineage-dependent spatial and functional organization of the mammalian enteric nervous system. Science *356*, 722–726.

Latorre, R., Sternini, C., De Giorgio, R., and Greenwood-Van Meerveld, B. (2015). Enteroendocrine cells: a review of their role in brain-gut communication. Neurogastroenterol. Motil. 1–11.

Latour, Y.L., Gobert, A.P., and Wilson, K.T. (2019). The role of polyamines in the regulation of macrophage polarization and function. Amino Acids.

Lau, J., and Herzog, H. (2014). CART in the regulation of appetite and energy homeostasis. Front. Neurosci. *8*.

Lau, J., Minett, M., Zhao, J., Dennehy, U., Wang, F., Wood, J., and Bogdanov, Y. (2011). Temporal control of gene deletion in sensory ganglia using a tamoxifen-inducible Advillin-Cre-ERT2 recombinase mouse. Mol. Pain *7*, 100.

Lavin, Y., Mortha, A., Rahman, A., and Merad, M. (2015). Regulation of macrophage development and function in peripheral tissues. Nat. Rev. Immunol. *15*, 731–744.

Lay, J., Carbone, S.E., DiCello, J.J., Bunnett, N.W., Canals, M., and Poole, D.P. (2016). Distribution and trafficking of the μ-opioid receptor in enteric neurons of the guinea pig. Am. J. Physiol. Gastrointest. Liver Physiol. *311*, G252-66.

Lebrun, L.J., Lenaerts, K., Kiers, D., Pais de Barros, J.P., Le Guern, N., Plesnik, J., Thomas, C., Bourgeois, T., Dejong, C.H.C., Kox, M., et al. (2017). Enteroendocrine L Cells Sense LPS after Gut Barrier Injury to Enhance GLP-1 Secretion. Cell Rep. *21*, 1160–1168.

Lee, B.L., Stowe, I.B., Gupta, A., Kornfeld, O.S., Roose-Girma, M., Anderson, K., Warming, S., Zhang, J., Lee, W.P., and Kayagaki, N. (2018). Caspase-11 auto-proteolysis is crucial for noncanonical inflammasome activation. J. Exp. Med. *215*, 2279–2288.

Lemire, P., Robertson, S.J., Maughan, H., Tattoli, I., Streutker, C.J., Platnich, J.M., Muruve, D.A., Philpott, D.J., and Girardin, S.E. (2017). The NLR Protein NLRP6 Does Not Impact Gut Microbiota Composition. Cell Rep. *21*, 3653–3661.

Levy, M., Thaiss, C.A., Zeevi, D., Dohnalová, L., Zilberman-Schapira, G., Mahdi, J.A., David, E., Savidor, A., Korem, T., Herzig, Y., et al. (2015). Microbiota-Modulated Metabolites Shape the Intestinal Microenvironment by Regulating NLRP6 Inflammasome Signaling. Cell *163*, 1428–1443.

Levy, M., Thaiss, C.A., and Elinav, E. (2016). Metabolites: Messengers between the microbiota and the immune system. Genes Dev. *30*, 1589–1597.

Levy, M., Shapiro, H., Thaiss, C.A., and Elinav, E. (2017). NLRP6: A Multifaceted Innate

Immune Sensor. Trends Immunol. *38*, 248–260.

Lewis, M.C., Brieaddy, L.E., and Root, C. (1995). Effects of 2164U90 on ileal bile acid absorption and serum cholesterol in rats and mice. J. Lipid Res. *36*, 1098–1105.

Li, C., Wu, X., Liu, S., Zhao, Y., Zhu, J., and Liu, K. (2019a). Roles of Neuropeptide Y in Neurodegenerative and Neuroimmune Diseases. Front. Neurosci. *13*, 1–11.

Li, Z., Caron, M.G., Blakely, R.D., Margolis, K.G., and Gershon, M.D. (2010). Dependence of serotonergic and other nonadrenergic enteric neurons on norepinephrine transporter expression. J. Neurosci. *30*, 16730–16740.

Li, Z., Chalazonitis, a., Huang, Y. -y., Mann, J.J., Margolis, K.G., Yang, Q.M., Kim, D.O., Cote, F., Mallet, J., and Gershon, M.D. (2011). Essential Roles of Enteric Neuronal Serotonin in Gastrointestinal Motility and the Development/Survival of Enteric Dopaminergic Neurons. J. Neurosci. *31*, 8998–9009.

Li, Z., Wang, Q., He, Z., Hong, Q., and Xiang, H. (2018). Neuroanatomical autonomic substrates of brainstem-gut circuitry identified using transsynaptic tract-tracing with pseudorabies virus recombinants. *7*, 20–22.

Li, Z., Hao, M.M., Van den Haute, C., Baekelandt, V., Boesmans, W., and Vanden Berghe, P. (2019b). Regional complexity in enteric neuron wiring reflects diversity of motility patterns in the mouse large intestine. Elife *8*.

Liedtke, W., Choe, Y., Martí-Renom, M.A., Bell, A.M., Denis, C.S., AndrejŠali, Hudspeth, A.J., Friedman, J.M., and Heller, S. (2000). Vanilloid receptor-related osmotically activated channel (VR-OAC), a candidate vertebrate osmoreceptor. Cell *103*, 525–535.

Lieu, T., Jayaweera, G., Zhao, P., Poole, D.P., Jensen, D., Grace, M., McIntyre, P., Bron, R., Wilson, Y.M., Krappitz, M., et al. (2014). The bile acid receptor TGR5 activates the TRPA1 channel to induce itch in mice. Gastroenterology *147*, 1417–1428.

Linden, D.R. (2012). Colitis is associated with a loss of intestinofugal neurons. Am. J. Physiol. Liver Physiol. *303*, G1096–G1104.

Linden, D.R., Couvrette, J.M., Ciolino, A., McQuoid, C., Blaszyk, H., Sharkey, K.A., and Mawe, G.M. (2005). Indiscriminate loss of myenteric neurones in the TNBS-inflamed guinea-pig distal colon. Neurogastroenterol. Motil. *17*, 751–760.

Liu, M.T., Seino, S., and Kirchgessner, A.L. (1999). Identification and characterization of glucoresponsive neurons in the enteric nervous system. J. Neurosci. *19*, 10305–10317.

Liu, M.T., Kuan, Y.H., Wang, J., Hen, R., and Gershon, M.D. (2009). 5-HT4 receptor-mediated neuroprotection and neurogenesis in the enteric nervous system of adult mice. J. Neurosci. *29*, 9683–9699.

Llewellyn, S.R., Britton, G.J., Contijoch, E.J., Mortha, A., Colombel, F., Grinspan, A., Clemente, J.C., Merad, M., and Jeremiah, J. (2017). Deciphering the combinatorial influence of diet and the microbiota on experimental colitis.

Loesche, W.J. (1969). Effect of bacterial contamination on cecal size and cecal contents of gnotobiotic rodents. J. Bacteriol. *99*, 520–526.

Logan, S.L., Thomas, J., Yan, J., Baker, R.P., Shields, D.S., Xavier, J.B., Hammer, B.K., and Parthasarathy, R. (2018). The *Vibrio cholerae* type VI secretion system can modulate host intestinal mechanics to displace gut bacterial symbionts. Proc. Natl. Acad. Sci. *115*, 201720133.

Lomax, A.E., Pradhananga, S., Sessenwein, J.L., and O'Malley, D. (2019). Bacterial modulation of visceral sensation: mediators and mechanisms. Am. J. Physiol. Liver Physiol. *317*, G363–G372.

Love, J.A., Yi, E., and Smith, T.G. (2007). Autonomic pathways regulating pancreatic exocrine secretion. Auton. Neurosci. *133*, 19–34.

Love, M.I., Huber, W., and Anders, S. (2014). Moderated estimation of fold change and dispersion for RNA-seq data with DESeq2. Genome Biol. *15*, 550.

Lovett-Barron, M., Andalman, A.S., Allen, W.E., Vesuna, S., Kauvar, I., Burns, V.M., and Deisseroth, K. (2017). Ancestral Circuits for the Coordinated Modulation of Brain State. Cell *171*, 1411-1423.e17.

Lucey, M.R. (1986). Endogenous somatostatin and the gut. Gut *27*, 457–467.
Luckensmeyer, G.B., and Keast, J.R. (1995). Distribution and morphological characterization of viscerofugal projections from the large intestine to the inferior mesenteric and pelvic ganglia of the male rat. Neuroscience *66*, 663–671.

Luckensmeyer, G.B., and Keast, J.R. (1998). Projections of pelvic autonomic neurons within the lower bowel of the male rat: An anterograde labelling study. Neuroscience *84*, 263–280.

Luo, J., Qian, A., Oetjen, L.K., Stenson, W.F., Kim, B.S., Luo, J., Qian, A., Oetjen, L.K., Yu, W., Yang, P., et al. (2018). TRPV4 Channel Signaling in Macrophages Promotes Gastrointestinal Motility via Direct Effects on Smooth Muscle Cells Article TRPV4 Channel Signaling in Macrophages Promotes Gastrointestinal Motility via Direct Effects on Smooth Muscle Cells. Immunity 1–13.

Ma, N.-X., Yin, J.-C., and Chen, G. (2019). Transcriptome Analysis of Small Molecule-Mediated Astrocyte-to-Neuron Reprogramming. Front. Cell Dev. Biol. *7*, 82.

Maizels, R.M., Smits, H.H., and McSorley, H.J. (2018). Modulation of Host Immunity by Helminths: The Expanding Repertoire of Parasite Effector Molecules. Immunity *49*, 801–818.

Mamantopoulos, M., Ronchi, F., Van Hauwermeiren, F., Vieira-Silva, S., Yilmaz, B., Martens, L., Saeys, Y., Drexler, S.K., Yazdi, A.S., Raes, J., et al. (2017). Nlrp6- and ASC-Dependent Inflammasomes Do Not Shape the Commensal Gut Microbiota Composition. Immunity *47*, 339-348.e4.

El Marjou, F., Janssen, K.P., Chang, B.H.J., Li, M., Hindie, V., Chan, L., Louvard, D., Chambon, P., Metzger, D., and Robine, S. (2004). Tissue-specific and inducible Cre-mediated recombination in the gut epithelium. Genesis *39*, 186–193.

Martin, A.M., Yabut, J.M., Choo, J.M., Page, A.J., Sun, E.W., Jessup, C.F., Wesselingh, S.L., Khan, W.I., Rogers, G.B., Steinberg, G.R., et al. (2019a). The gut microbiome regulates host glucose homeostasis via peripheral serotonin. Proc. Natl. Acad. Sci. U. S. A. *116*, 19802–19804.

Martin, A.M., Sun, E.W., Rogers, G.B., and Keating, D.J. (2019b). The Influence of the Gut Microbiome on Host Metabolism Through the Regulation of Gut Hormone Release. Front. Physiol. *10*, 428.

Martinez-Guryn, K., Leone, V., and Chang, E.B. (2019). Regional Diversity of the Gastrointestinal Microbiome. Cell Host Microbe *26*, 314–324.

Martinon, F., Burns, K., and Tschopp, J. (2002). The Inflammasome: A molecular platform triggering activation of inflammatory caspases and processing of proIL-β. Mol. Cell *10*, 417–426.

Matheis, F., Muller, P.A., Graves, C.L., Gabanyi, I., Kerner, Z.J., Costa-Borges, D., and Mucida, D. (2019). Adrenergic signaling in muscularis macrophages limits neuronal death following enteric infection. BioRxiv 556340.

Mathias, M. (2018). Autointoxication and historical precursors of the microbiome–gut–brain axis. Microb. Ecol. Health Dis. *29*, 1548249.

Mawe, G.M. (2015). Colitis-induced neuroplasticity disrupts motility in the inflamed and post-inflamed colon. J. Clin. Invest. *125*, 949–955.

Mayer, E.A. (2011). Gut feelings: the emerging biology of gut-brain communication. Nat.

Rev. Neurosci. *12*, 453–466.

Mayer, E. a, Tillisch, K., and Gupta, A. (2015). Gut / brain axis and the microbiota. *125*, 49–53.

McMurdie, P.J., and Holmes, S. (2013). Phyloseq: An R Package for Reproducible Interactive Analysis and Graphics of Microbiome Census Data. PLoS One *8*.

McVey Neufeld, K. a., Mao, Y.K., Bienenstock, J., Foster, J. a., and Kunze, W. a. (2013). The microbiome is essential for normal gut intrinsic primary afferent neuron excitability in the mouse. Neurogastroenterol. Motil. *25*, 183–e88.

McVey Neufeld, K. a., Perez-Burgos, a., Mao, Y.K., Bienenstock, J., and Kunze, W. a. (2015). The gut microbiome restores intrinsic and extrinsic nerve function in germ-free mice accompanied by changes in calbindin. Neurogastroenterol. Motil. *27*, 627–636.

Mei, Q., Mundinger, T.O., Kung, D., Baskin, D.G., and Taborsky, G.J. (2001). Fos expression in rat celiac ganglion : an index of the activation of postganglionic sympathetic nerves. Am. J. Physiol. Endocrinol. Metab. *281*, 655–664.

Meissner, G. (1857). Über die nerven der darmwand. Z Ration Med NF *8*, 364–366.
Messenger, J.P., and Furness, J.B. (1992). Distribution of enteric nerve cells that project to the coeliac ganglion of the guinea-pig. Cell Tissue Res. *269*, 119–132.

Mikkelsen, H.B., Thuneberg, L., Rumessen, J.J., and Thorball, N. (1985). Macrophage-like cells in the muscularis externa of mouse small intestine. Anat. Rec. *213*, 77–86.

Mikkelsen, H.B., Garbarsch, C., Tranum-Jensen, J., and Thuneberg, L. (2004). Macrophages in the small intestinal muscularis externa of embryos, newborn and adult germ-free mice. J. Mol. Histol. *35*, 377–387.

Mikkelsen, K.H., Frost, M., Bahl, M.I., Licht, T.R., Jensen, U.S., Rosenberg, J., Pedersen, O., Hansen, T., Rehfeld, J.F., Holst, J.J., et al. (2015). Effect of antibiotics on gut microbiota, gut hormones and glucose metabolism. PLoS One *10*, 1–14.

Miller, I. (2018). The gut–brain axis: historical reflections. Microb. Ecol. Health Dis. *29*, 1542921.

Milstein, A.D., Bloss, E.B., Apostolides, P.F., Vaidya, S.P., Dilly, G.A., Zemelman, B. V., and Magee, J.C. (2015). Inhibitory Gating of Input Comparison in the CA1 Microcircuit. Neuron *87*, 1274–1289.

Mizuno, K., and Ueno, Y. (2017). Autonomic Nervous System and the Liver. Hepatol. Res. *47*, 160–165.

Montgomery, R.K., Mulberg, A.E., and Grand, R.J. (1999). Development of the human gastrointestinal tract: Twenty years of progress. Gastroenterology *116*, 702–731.

Moriyama, S., Brestoff, J.R., Flamar, A.-L., Moeller, J.B., Klose, C.S.N., Rankin, L.C., Yudanin, N.A., Monticelli, L.A., Putzel, G.G., Rodewald, H.-R., et al. (2018). β2-adrenergic receptor-mediated negative regulation of group 2 innate lymphoid cell responses. Science *359*, 1056–1061.

Morrison, S.F., and Nakamura, K. (2011). Central neural pathways for thermoregulation. Front. Biosci. (Landmark Ed. *16*, 74–104.

Muller, P.A., Koscsó, B., Rajani, G.M., Stevanovic, K., Berres, M.L., Hashimoto, D., Mortha, A., Leboeuf, M., Li, X.M., Mucida, D., et al. (2014). Crosstalk between muscularis macrophages and enteric neurons regulates gastrointestinal motility. Cell *158*, 300–313.

Muller, P.A., Kerner, Z., Schneeberger, M., and Mucida, D. (2019a). Microbiota imprint gut-intrinsic neuronal programming and sympathetic activity 1 2. BioRxiv 545806.

Muller, P.A., Kerner, Z., Schneeberger Pane, M., and Mucida, D. (2019b). Microbiota imprint gut-intrinsic neuronal programming and sympathetic activity. BioRxiv 545806.

Naik, S., Larsen, S.B., Gomez, N.C., Alaverdyan, K., Sendoel, A., Yuan, S., Polak, L., Kulukian, A., Chai, S., and Fuchs, E. (2017). Inflammatory memory sensitizes skin epithelial stem cells to tissue damage. Nature *550*, 475–480.

Nakai, A., Hayano, Y., Furuta, F., Noda, M., and Suzuki, K. (2014). Control of lymphocyte egress from lymph nodes through β2-adrenergic receptors. J. Exp. Med. *211*, 2583–2598.

Nassar, M.A., Stirling, L.C., Forlani, G., Baker, M.D., Matthewst, E.A., Dickenson, A.H., and Wood, J.N. (2004). Nociceptor-specific gene deletion reveals a major role for Nav 1.7 (PN1) in acute and inflammatory pain. Proc. Natl. Acad. Sci. U. S. A. *101*, 12706–12711.

Nencini, S., and Ivanusic, J. (2017). Mechanically sensitive Aδ nociceptors that innervate bone marrow respond to changes in intra-osseous pressure. J. Physiol. *595*, 4399–4415.

Newman, K.D., Mhalhal, T.R., Washington, M.C., Heath, J.C., and Sayegh, A.I. (2017). Peptide Tyrosine Tyrosine 3-36 Reduces Meal Size and Activates the Enteric Neurons in Male Sprague–Dawley Rats. Dig. Dis. Sci. *62*, 3350–3358.

Nguyen, K.D., Qiu, Y., Cui, X., Goh, Y.P.S., Mwangi, J., David, T., Mukundan, L., Brombacher, F., Locksley, R.M., and Chawla, A. (2011). Alternatively activated macrophages produce catecholamines to sustain adaptive thermogenesis. Nature *480*, 104–108.

Nicholson, J.K., Holmes, E., Kinross, J., Burcelin, R., Gibson, G., Jia, W., and Pettersson, S. (2012). Host-gut microbiota metabolic interactions. Science *336*, 1262–1267.

Niess, J.H., Brand, S., Gu, X., Landsman, L., Jung, S., McCormick, B.A., Vyas, J.M., Boes, M., Ploegh, H.L., Fox, J.G., et al. (2005). CX3CR1-mediated dendritic cell access to the intestinal lumen and bacterial clearance. Science *307*, 254–258.

Nijhuis, L.E.J., Olivier, B.J., and de Jonge, W.J. (2010). Neurogenic regulation of dendritic cells in the intestine. Biochem. Pharmacol. *80*, 2002–2008.

Nøhr, M.K., Pedersen, M.H., Gille, A., Egerod, K.L., Engelstoft, M.S., Husted, A.S., Sichlau, R.M., Grunddal, K. V., Poulsen, S.S., Han, S., et al. (2013). GPR41/FFAR3 and GPR43/FFAR2 as cosensors for short-chain fatty acids in enteroendocrine cells vs FFAR3 in enteric neurons and FFAR2 in enteric leukocytes. Endocrinology *154*, 3552–3564.

Nøhr, M.K., Egerod, K.L., Christiansen, S.H., Gille, A., Offermanns, S., Schwartz, T.W., and Møller, M. (2015). Expression of the short chain fatty acid receptor GPR41/FFAR3 in autonomic and somatic sensory ganglia. Neuroscience *290*, 126–137.

Nonomura, K., Woo, S., Chang, R.B., Gillich, A., Qiu, Z., Francisco, A.G., Ranade, S.S., Liberles, S.D., and Patapoutian, A. (2017). Piezo2 senses airway stretch and mediates lung inflation-induced apnoea. Nature *541*, 176–181.

Nowarski, R., Jackson, R., Gagliani, N., De Zoete, M.R., Palm, N.W., Bailis, W., Low, J.S., Harman, C.C.D., Graham, M., Elinav, E., et al. (2015). Epithelial IL-18 Equilibrium Controls Barrier Function in Colitis. Cell *163*, 1444–1456.

Nuttall, G.H.F., and Thierfelder., H. (1896). Thierisches Leben ohne Bakterien im Verdauungskanal. Hoppe-Seyler´s Zeitschrift Für Physiol. Chemie *21*, 109–121.

Nyavor, Y., Estill, R., Edwards, H., Ogden, H., Heideman, K., Starks, K., Miller, C., May, G., Flesch, L., McMillan, J., et al. (2019). Intestinal nerve cell injury occurs prior to insulin resistance in female mice ingesting a high-fat diet. Cell Tissue Res. 325–340.

O'Brien, P.A., Webster, N.S., Miller, D.J., and Bourne, D.G. (2019). Host-Microbe Coevolution: Applying Evidence from Model Systems to Complex Marine Invertebrate Holobionts. MBio *10*, 1–14.

Obata, Y., and Pachnis, V. (2016). The Effect of Microbiota and the Immune System on the Development and Organization of the Enteric Nervous System. Gastroenterology *151*, 836–844.

Obata, Y., Boeing, S., Castaño, Á., Bon-Frauches, A.C., Agüero, M.G. de, Boesmans, W., Yilmaz, B., Lopes, R., Huseynova, A., Maradana, M.R., et al. (2019). Neuronal programming by microbiota enables environmental regulation of intestinal motility. BioRxiv 579250.

Obermayr, F., Hotta, R., Enomoto, H., and Young, H.M. (2013). Development and developmental disorders of the enteric nervous system. Nat. Rev. Gastroenterol. Hepatol. *10*, 43–57.

Ødegaard, S., Nesje, L.B., Lærum, O.D., and Kimmey, M.B. (2012). High-frequency ultrasonographic imaging of the gastrointestinal wall. Expert Rev. Med. Devices *9*, 263–273.

Ohman, L., and Simrén, M. (2010). Pathogenesis of IBS: role of inflammation, immunity and neuroimmune interactions. Nat. Rev. Gastroenterol. Hepatol. *7*, 163–173.

Osorio, N., Korogod, S., and Delmas, P. (2014). Specialized functions of Nav1.5 and Nav1.9 channels in electrogenesis of myenteric neurons in intact mouse ganglia. J. Neurosci. *34*, 5233–5244.

Palay, S.L. (1959). An Electron Microscopic Study of the Intestinal Villus: I. The Fasting Animal. J. Cell Biol. *5*, 363–371.

Palmer, G., Hibberd, T.J., Roose, T., Brookes, S.J.H., and Taylor, M. (2016). Measurement of strains experienced by viscerofugal nerve cell bodies during mechanosensitive firing using digital image correlation. Am. J. Physiol. - Gastrointest. Liver Physiol. *311*, G869–G879.

Pasteur, L. (1885). Observations relatives à la Note précédente de M. Duclaux. Acad. Des Sci. *100*, 68.

Pawel R, K., and Fayez K, G. (2016). Physiology of intestinal absorption. Best Pr. Res Clin Gastroenterol 1–20.

Payne, S.C., Furness, J.B., Burns, O., Sedo, A., Hyakumura, T., Shepherd, R.K., and Fallon, J.B. (2019). Anti-inflammatory Effects of Abdominal Vagus Nerve Stimulation on Experimental Intestinal Inflammation. Front. Neurosci. *13*, 1–15.

Peeters, P.J., Aerssens, J., de Hoogt, R., Stanisz, A., Göhlmann, H.W., Hillsley, K.,

Meulemans, A., Grundy, D., Stead, R.H., and Coulie, B. (2006). Molecular profiling of murine sensory neurons in the nodose and dorsal root ganglia labeled from the peritoneal cavity. Physiol. Genomics *24*, 252–263.

Pegg, A.E. (2016). Functions of polyamines in mammals. J. Biol. Chem. *291*, 14904–14912.

Perez-Burgos, A., Mao, Y., Bienenstock, J., and Kunze, W.A. (2014). The gut-brain axis rewired: adding a functional vagal nicotinic “sensory synapse.” FASEB J. *28*, 3064–3074.

Perez-Lopez, A., Behnsen, J., Nuccio, S.-P., and Raffatellu, M. (2016). Mucosal immunity to pathogenic intestinal bacteria. Nat Rev Immunol *advance on*, 135–148.

Phillips, R.J., and Powley, T.L. (2012). Macrophages Associated with the Intrinsic and Extrinsic Autonomic Innervation of the Rat Gastrointestinal Tract. Auton. Neurosci. *169*, 12–27.

Pohl, J.-M., Gutweiler, S., Thiebes, S., Volke, J.K., Klein-Hitpass, L., Zwanziger, D., Gunzer, M., Jung, S., Agace, W.W., Kurts, C., et al. (2017). Gut immunity Irf4-dependent CD103 + CD11b + dendritic cells and the intestinal microbiome regulate monocyte and macrophage activation and intestinal peristalsis in postoperative ileus. Gut *0*, 1–11.

Powley, T.L. (2000). Vagal input to the enteric nervous system. Gut *47*, 30–32.
Prescott, S.L. (2017). History of medicine: Origin of the term microbiome and why it matters. Hum. Microbiome J. *4*, 24–25.

Previs, S.F., Brunengraber, D.Z., and Brunengraber, H. (2009). Is There Glucose Production Outside of the Liver and Kidney? Annu. Rev. Nutr. *29*, 43–57.

Price, C.J., Hoyda, T.D., and Ferguson, A. V. (2008). The area postrema: A brain monitor and integrator of systemic autonomic state. Neuroscientist *14*, 182–194.

Priyadarshini, M., Kotlo, K.U., Dudeja, P.K., and Layden, B.T. (2018). Role of short chain fatty acid receptors in intestinal physiology and pathophysiology. Compr. Physiol. *8*, 1065–1090.

Prüss, H., Tedeschi, A., Thiriot, A., Lynch, L., Loughhead, S.M., Stutte, S., Mazo, I.B., Kopp, M.A., Brommer, B., Blex, C., et al. (2017). Spinal cord injury-induced immunodeficiency is mediated by a sympathetic-neuroendocrine adrenal reflex. Nat. Neurosci. *20*, 1549–1559.

Qu, Z., Thacker, M., Castelucci, P., Bagyánszki, M., Epstein, M.L., and Furness, J.B.

(2008). Immunohistochemical analysis of neuron types in the mouse small intestine. Cell Tissue Res. *334*, 147–161.

Rakoff-Nahoum, S., Paglino, J., Eslami-Varzaneh, F., Edberg, S., and Medzhitov, R. (2004). Recognition of commensal microflora by toll-like receptors is required for intestinal homeostasis. Cell *118*, 229–241.

Ran, W., Dong, L., Tang, C., Zhou, Y., Sun, G., Liu, T., Liu, Y.-P., and Guan, C.-X. (2015). Vasoactive intestinal peptide suppresses macrophage-mediated inflammation by downregulating interleukin-17A expression via PKA- and PKC-dependent pathways. Int. J. Exp. Pathol. *96*, 269–275.

Ranade, S.S., Woo, S.-H., Dubin, A.E., Moshourab, R.A., Wetzel, C., Petrus, M., Mathur, J., Bégay, V., Coste, B., Mainquist, J., et al. (2014). Piezo2 is the major transducer of mechanical forces for touch sensation in mice. Nature *516*, 121–125.

Rao, M., Nelms, B.D., Dong, L., Salinas-Rios, V., Rutlin, M., Gershon, M.D., and Corfas, G. (2015). Enteric glia express proteolipid protein 1 and are a transcriptionally unique population of glia in the mammalian nervous system. Glia *63*, 2040–2057.

Rao, M., Rastelli, D., Dong, L., Chiu, S., Setlik, W., Gershon, M.D., and Corfas, G. (2017). Enteric Glia Regulate Gastrointestinal Motility but Are Not Required for Maintenance of the Epithelium in Mice. Gastroenterology *153*, 1068-1081.e7.

Reese, T.A., Liang, H.E., Tager, A.M., Luster, A.D., Van Rooijen, N., Voehringer, D., and Locksley, R.M. (2007). Chitin induces accumulation in tissue of innate immune cells associated with allergy. Nature *447*, 92–96.

Reichlin, S. (1983). Somatostatin. N. Engl. J. Med. *309*, 1495–1501.
Reimann, F., Habib, A.M., Tolhurst, G., Parker, H.E., Rogers, G.J., and Gribble, F.M. (2008). Glucose Sensing in L Cells: A Primary Cell Study. Cell Metab. *8*, 532–539.

Renier, N., Wu, Z., Simon, D.J., Yang, J., Ariel, P., and Tessier-Lavigne, M. (2014). IDISCO: A simple, rapid method to immunolabel large tissue samples for volume imaging. Cell *159*, 896–910.

Renier, N., Adams, E.L., Kirst, C., Wu, Z., Azevedo, R., Kohl, J., Autry, A.E., Kadiri, L., Umadevi Venkataraju, K., Zhou, Y., et al. (2016). Mapping of Brain Activity by Automated Volume Analysis of Immediate Early Genes. Cell *165*, 1789–1802.

Reyniers, J.A., Trexler, P.C., and Ervin, R.F. (1946). Rearing germ-free albino rats. Lobund Reports 1–84.

Rhee, S.H., Pothoulakis, C., and Mayer, E.A. (2009). Principles and clinical implications

of the brain-gut-enteric microbiota axis. Nat. Rev. Gastroenterol. Hepatol. *6*, 306–314.

Richner, M., Jager, S.B., Siupka, P., and Vaegter, C.B. (2017). Hydraulic Extrusion of the Spinal Cord and Isolation of Dorsal Root Ganglia in Rodents. J. Vis. Exp. e55226–e55226.

Rinaman, L., Roesch, M.R., and Card, J.P. (1999). Retrograde transynaptic pseudorabies virus infection of central autonomic circuits in neonatal rats. Brain Res. Dev. Brain Res. *114*, 207–216.

Rivera-Chávez, F., Zhang, L.F., Faber, F., Lopez, C.A., Byndloss, M.X., Olsan, E.E., Xu, G., Velazquez, E.M., Lebrilla, C.B., Winter, S.E., et al. (2016a). Depletion of Butyrate-Producing Clostridia from the Gut Microbiota Drives an Aerobic Luminal Expansion of Salmonella. Cell Host Microbe *19*, 443–454.

Rivera-Chávez, F., Zhang, L.F., Faber, F., Lopez, C.A., Byndloss, M.X., Olsan, E.E., Xu, G., Velazquez, E.M., Lebrilla, C.B., Winter, S.E., et al. (2016b). Depletion of Butyrate-Producing Clostridia from the Gut Microbiota Drives an Aerobic Luminal Expansion of Salmonella. Cell Host Microbe *19*, 443–454.

Rogge, G., Jones, D., Hubert, G.W., Lin, Y., and Kuhar, M.J. (2008). CART peptides: Regulators of body weight, reward and other functions. Nat. Rev. Neurosci. *9*, 747–758.

Roh, E., Song, D.K., and Kim, M.S. (2016). Emerging role of the brain in the homeostatic regulation of energy and glucose metabolism. Exp. Mol. Med. *48*.

Roider, H.G., Manke, T., O'Keeffe, S., Vingron, M., and Haas, S.A. (2009). PASTAA: identifying transcription factors associated with sets of co-regulated genes. Bioinformatics *25*, 435–442.

Rooks, M.G., and Garrett, W.S. (2016). Gut microbiota, metabolites and host immunity. Nat. Rev. Immunol. *16*, 341–352.

Rorsman, P., and Huising, M.O. (2018). The somatostatin-secreting pancreatic δ-cell in health and disease. Nat. Rev. Endocrinol. *14*, 404–414.

Rosas-Ballina, M., Ochani, M., Parrish, W.R., Ochani, K., Harris, Y.T., Huston, J.M., Chavan, S., and Tracey, K.J. (2008). Splenic nerve is required for cholinergic antiinflammatory pathway control of TNF in endotoxemia. Proc. Natl. Acad. Sci. U. S. A. *105*, 11008–11013.

Roth, B.L. (2016). DREADDs for Neuroscientists. Neuron *89*, 683–694.
Rowland, I., Gibson, G., Heinken, A., Scott, K., Swann, J., Thiele, I., and Tuohy, K. (2018). Gut microbiota functions: metabolism of nutrients and other food components.

Eur. J. Nutr. *57*, 1–24.

Rumessen, J.J., Thuneberg, L., and Mikkelsen, H.B. (1982). Plexus muscularis profundus and associated interstitial cells. II. Ultrastructural studies of mouse small intestine. Anat. Rec. *203*, 129–146.

Sampson, T.R., Debelius, J.W., Thron, T., Janssen, S., Shastri, G.G., Ilhan, Z.E., Challis, C., Schretter, C.E., Rocha, S., Gradinaru, V., et al. (2016). Gut Microbiota Regulate Motor Deficits and Neuroinflammation in a Model of Parkinson's Disease. Cell *167*, 1469-1480.e12.

Samuel, B.S., Shaito, A., Motoike, T., Rey, F.E., Backhed, F., Manchester, J.K., Hammer, R.E., Williams, S.C., Crowley, J., Yanagisawa, M., et al. (2008). Effects of the gut microbiota on host adiposity are modulated by the short-chain fatty-acid binding G protein-coupled receptor, Gpr41. Proc. Natl. Acad. Sci. *105*, 16767–16772.

Sanz, E., Yang, L., Su, T., Morris, D.R., McKnight, G.S., and Amieux, P.S. (2009). Cell-type-specific isolation of ribosome-associated mRNA from complex tissues. Proc. Natl. Acad. Sci. U. S. A. *106*, 13939–13944.

Satoh, T., and Akira, S. (2016). Toll-Like Receptor Signaling and Its Inducible Proteins. Microbiol. Spectr. *4*, 1–7.

Savage, D.C., and McAllister, J.S. (1971). Cecal enlargement and microbial flora in suckling mice given antibacterial drugs. Infect. Immun. *3*, 342–349.

Scanzano, A., and Cosentino, M. (2015). Adrenergic regulation of innate immunity: a review. Front. Pharmacol. *6*, 171.

De Schepper, S., Verheijden, S., Aguilera-Lizarraga, J., Viola, M.F., Boesmans, W., Stakenborg, N., Voytyuk, I., Schmidt, I., Boeckx, B., Dierckx de Casterlé, I., et al. (2018). Self-Maintaining Gut Macrophages Are Essential for Intestinal Homeostasis. Cell *175*, 400-415.e13.

Schloss, P.D., Westcott, S.L., Ryabin, T., Hall, J.R., Hartmann, M., Hollister, E.B., Lesniewski, R.A., Oakley, B.B., Parks, D.H., Robinson, C.J., et al. (2009). Introducing mothur: Open-source, platform-independent, community-supported software for describing and comparing microbial communities. Appl. Environ. Microbiol. *75*, 7537–7541.

Schreiber, H.A., Loschko, J., Karssemeijer, R.A., Escolano, A., Meredith, M.M., Mucida, D., Guermonprez, P., and Nussenzweig, M.C. (2013). Intestinal monocytes and macrophages are required for T cell polarization in response to Citrobacter rodentium. J. Exp. Med. *210*, 2025–2039.

Schridde, A., Bain, C.C., Mayer, J.U., Montgomery, J., Pollet, E., Denecke, B., Milling, S.W.F., Jenkins, S.J., Dalod, M., Henri, S., et al. (2017). Tissue-specific differentiation of colonic macrophages requires TGFβ receptor-mediated signaling. Mucosal Immunol. 1–13.

Schulthess, J., Pandey, S., Capitani, M., Rue-Albrecht, K., Arnold, I., Franchini, F., Chomka, A., Ilott, N., Johnston, D., Pires, E., et al. (2019). The short chain fatty acid butyrate imprints an antimicrobial program in macrophages. Immunity 1–14.

Schuster, D.J., Dykstra, J.A., Riedl, M.S., Kitto, K.F., Belur, L.R., Scott McIvor, R., Elde, R.P., Fairbanks, C.A., and Vulchanova, L. (2014). Biodistribution of adeno-associated virus serotype 9 (AAV9) vector after intrathecal and intravenous delivery in mouse. Front. Neuroanat. *8*, 1–14.

Scott, M.M., Williams, K.W., Rossi, J., Lee, C.E., and Elmquist, J.K. (2011). Leptin receptor expression in hindbrain Glp-1 neurons regulates food intake and energy balance in mice. J. Clin. Invest. *121*, 2413–2421.

Scrocchi, L.A., Brown, T.J., MaClusky, N., Brubaker, P.L., Auerbach, A.B., Joyner, A.L., and Drucker, D.J. (1996). Glucose intolerance but normal satiety in mice with a null mutation in the glucagon-like peptide 1 receptor gene. Nat. Med. *2*, 1254–1258.

Selwyn, F.P., Csanaky, I.L., Zhang, Y., and Klaassen, C.D. (2015). Importance of Large Intestine in Regulating Bile Acids and Glucagon-Like Peptide-1 in Germ-Free Mice. Drug Metab. Dispos. *43*, 1544–1556.

Semba, T. (1954). Intestino-intestinal inhibitory reflexes. Jpn. J. Physiol. *4*, 241–245.
Sender, R., Fuchs, S., and Milo, R. (2016). Revised Estimates for the Number of Human and Bacteria Cells in the Body. PLoS Biol. *14*, e1002533.

Seo, S.U., Kamada, N., Muñoz-Planillo, R., Kim, Y.G., Kim, D., Koizumi, Y., Hasegawa, M., Himpsl, S.D., Browne, H.P., Lawley, T.D., et al. (2015). Distinct Commensals Induce Interleukin-1β via NLRP3 Inflammasome in Inflammatory Monocytes to Promote Intestinal Inflammation in Response to Injury. Immunity *42*, 744–755.

Serlin, H.K., and Fox, E.A. (2019). Abdominal vagotomy reveals majority of small intestinal mucosal afferents labeled in nav 1.8cre-rosa26tdTomato mice are vagal in origin. J. Comp. Neurol.

Sessenwein, J.L., Baker, C.C., Pradhananga, S., Maitland, M.E., Petrof, E.O., Allen-vercoe, E., Noordhof, C., Reed, D.E., Vanner, S.J., Lomax, A.E., et al. (2017a). Protease-mediated suppression of DRG neuron excitability by commensal bacteria
Protease-mediated suppression of DRG neuron excitability by commensal bacteria

Abbreviated title : Anti-nociceptive effects of commensal gut bacteria Gastrointestinal Disease R.

Sessenwein, J.L., Baker, C.C., Pradhananga, S., Maitland, M.E., Petrof, E.O., Allen-Vercoe, E., Noordhof, C., Reed, D.E., Vanner, S.J., and Lomax, A.E. (2017b). Protease-mediated suppression of DRG neuron excitability by commensal bacteria. J. Neurosci. *37*, 11758–11768.

Sharkey, K.A., Parr, E.J., and Keenan, C.M. (1999). Immediate-early gene expression in the inferior mesenteric ganglion and colonic myenteric plexus of the guinea pig. J. Neurosci. *19*, 2755–2764.

Shaw, T.N., Houston, S.A., Wemyss, K., Bridgeman, H.M., Barbera, T.A., Zangerle-Murray, T., Strangward, P., Ridley, A.J.L., Wang, P., Tamoutounour, S., et al. (2018). Tissue-resident macrophages in the intestine are long lived and defined by Tim-4 and CD4 expression. J. Exp. Med. *215*, 1507–1518.

Shcherbina, L., Edlund, A., Esguerra, J.L.S., Abels, M., Zhou, Y., Ottosson-Laakso, E., Wollheim, C.B., Hansson, O., Eliasson, L., and Wierup, N. (2017). Endogenous beta-cell CART regulates insulin secretion and transcription of beta-cell genes. Mol. Cell. Endocrinol. *447*, 52–60.

Silva, H.M., Báfica, A., Rodrigues-Luiz, G.F., Chi, J., D'Emery Alves Santos, P., Reis, B.S., Hoytema Van Konijnenburg, D.P., Crane, A., Arifa, R.D.N., Martin, P., et al. (2019). Vasculature-associated fat macrophages readily adapt to inflammatory and metabolic challenges. J. Exp. Med. *216*, 786–806.

Skatchkov, S.N., Bukauskas, F.F., Benedikt, J., Inyushin, M., and Kucheryavykh, Y. V. (2015). Intracellular spermine prevents acid-induced uncoupling of Cx43 gap junction channels. Neuroreport *26*, 528–532.

Sleigh, J.N., Weir, G.A., and Schiavo, G. (2016). A simple, step-by-step dissection protocol for the rapid isolation of mouse dorsal root ganglia. BMC Res. Notes *9*, 82.

Smith, S.M., and Vale, W.W. (2006). The role of the hypothalamic-pituitary-adrenal axis in neuroendocrine responses to stress. Dialogues Clin. Neurosci. *8*, 383–395.

Soda, K. (2018). Polyamine metabolism and gene methylation in conjunction with one-carbon metabolism. Int. J. Mol. Sci. *19*.

Solis, A.G., Bielecki, P., Steach, H.R., Sharma, L., Harman, C.C.D., Yun, S., de Zoete, M.R., Warnock, J.N., To, S.D.F., York, A.G., et al. (2019). Mechanosensation of cyclical force by PIEZO1 is essential for innate immunity. Nature *573*, 69–74.

Song, Y., Koehler, J.A., Baggio, L.L., Powers, A.C., Sandoval, D.A., and Drucker, D.J. (2019). Gut-Proglucagon-Derived Peptides Are Essential for Regulating Glucose Homeostasis in Mice. Cell Metab. 1–11.

Spencer, S.P., Fragiadakis, G.K., and Sonnenburg, J.L. (2019). Pursuing Human-Relevant Gut Microbiota-Immune Interactions. Immunity *51*, 225–239.

Spengler, R.N., Blenk, N., Chensue, S.W., Giacherio, D.A., and Kunkel, S.L. (1994). Endogenous norepinephrine regulates tumor necrosis factor-α production from macrophages in vitro. J. Immunol. *152*, 3024–3031.

Spit, M., Koo, B.K., and Maurice, M.M. (2018). Tales from the crypt: Intestinal niche signals in tissue renewal, plasticity and cancer. Open Biol. *8*.

Stirling, L.C., Forlani, G., Baker, M.D., Wood, J.N., Matthews, E.A., Dickenson, A.H., and Nassar, M.A. (2005). Nociceptor-specific gene deletion using heterozygous NaV1.8-Cre recombinase mice. Pain *113*, 27–36.

Strandwitz, P., Kim, K.H., Terekhova, D., Liu, J.K., Sharma, A., Levering, J., McDonald, D., Dietrich, D., Ramadhar, T.R., Lekbua, A., et al. (2019). GABA-modulating bacteria of the human gut microbiota. Nat. Microbiol. *4*, 396–403.

Straub, R.H., Wiest, R., Strauch, U.G., Harle, P., and Scholmerich, J. (2006). The role of the sympathetic nervous system in intestinal inflammation. Gut *55*, 1640–1649.

Strege, P.R., Mazzone, A., Bernard, C.E., Neshatian, L., Gibbons, S.J., Saito, Y.A., Tester, D.J., Calvert, M.L., Mayer, E.A., Chang, L., et al. (2018). Irritable bowel syndrome patients have SCN5A channelopathies that lead to decreased Na v 1.5 current and mechanosensitivity. Am. J. Physiol. - Gastrointest. Liver Physiol. *314*, G494–G503.

Sudo, N., Chida, Y., Aiba, Y., Sonoda, J., Oyama, N., Yu, X.N., Kubo, C., and Koga, Y. (2004). Postnatal microbial colonization programs the hypothalamic-pituitary-adrenal system for stress response in mice. J. Physiol. *558*, 263–275.

Swain, M.G., Blennerhassett, P.A., and Collins, S.M. (1991). Impaired sympathetic nerve function in the inflamed rat intestine. Gastroenterology *100*, 675–682.

Szentirmai, É., Millican, N.S., Massie, A.R., and Kapás, L. (2019). Butyrate, a metabolite of intestinal bacteria, enhances sleep. Sci. Rep. *9*, 1–9.

Szurszewski, J.H., Ermilov, L.G., and Miller, S.M. (2002). Prevertebral ganglia and intestinofugal afferent neurones. Gut *51 Suppl 1*, i6–i10.

Tack, J.F., and Wood, J.D. (1992). Actions of noradrenaline on myenteric neurons in the guinea pig gastric antrum. J. Auton. Nerv. Syst. *41*, 67–77.

Talbot, J., Hahn, P., Kroehling, L., Nguyen, H., Li, D., and Littman, D.R. (2019). VIP-producing enteric neurons interact with innate lymphoid cells to regulate feeding-dependent intestinal epithelial barrier functions. BioRxiv 721464.

Tansy, M.F., and Kendall, F.M. (1973). Experimental and clinical aspects of gastrocolic reflexes. Am. J. Dig. Dis. *18*, 521–531.

Tatemoto, K., Carlquist, M., and Mutt, V. (1982). Neuropeptide Y - A novel brain peptide with structural similarities to peptide YY and pancreatic polypeptide. Nature *296*, 659–660.

Teitelman, G., Alpert, S., Polak, J.M., Martinez, A., and Hanahan, D. (1993). Precursor cells of mouse endocrine pancreas coexpress insulin, glucagon and the neuronal proteins tyrosine hydroxylase and neuropeptide Y, but not pancreatic polypeptide. Development *118*, 1031–1039.

Terry, N., and Margolis, K.G. (2017). Serotonergic Mechanisms Regulating the GI Tract: Experimental Evidence and Therapeutic Relevance. Handb. Exp. Pharmacol. *239*, 319–342.

Tervo, D.G.R., Hwang, B.Y., Viswanathan, S., Gaj, T., Lavzin, M., Ritola, K.D., Lindo, S., Michael, S., Kuleshova, E., Ojala, D., et al. (2016). A Designer AAV Variant Permits Efficient Retrograde Access to Projection Neurons. Neuron *92*, 372–382.

Theodoropoulou, M., and Stalla, G.K. (2013). Somatostatin receptors: From signaling to clinical practice. Front. Neuroendocrinol. *34*, 228–252.

Thompson, K.J., Khajehali, E., Bradley, S.J., Navarrete, J.S., Huang, X.-P., Slocum, S., Jin, J., Liu, J., Xiong, Y., Olsen, R., et al. (2018). DREADD AGONIST 21 (C21) IS AN EFFECTIVE AGONIST FOR MUSCARNIC-BASED DREADDS IN VITRO AND IN VIVO. ACS Pharmacol. Transl. Sci.

Thorens, B. (2014). Neural regulation of pancreatic islet cell mass and function. Diabetes. Obes. Metab. *16 Suppl 1*, 87–95.

Thursby, E., and Juge, N. (2017). Introduction to the human gut microbiota. Biochem. J. *474*, 1823–1836.

Ting, H.-A., and von Moltke, J. (2019). The Immune Function of Tuft Cells at Gut Mucosal Surfaces and Beyond. J. Immunol. *202*, 1321–1329.

Tomuschat, C., Virbel, C.R., O'Donnell, A.M., and Puri, P. (2018). Reduced expression of the NLRP6 inflammasome in the colon of patients with Hirschsprung's disease. J. Pediatr. Surg. 6–10.

Tong, Q., Ye, C.-P., Jones, J.E., Elmquist, J.K., and Lowell, B.B. (2008). Synaptic release of GABA by AgRP neurons is required for normal regulation of energy balance. Nat. Neurosci. *11*, 998–1000.

Touré, A.M., Landry, M., Souchkova, O., Kembel, S.W., and Pilon, N. (2019). Gut microbiota-mediated Gene-Environment interaction in the TashT mouse model of Hirschsprung disease. Sci. Rep. *9*, 1–14.

Travagli, R.A., and Anselmi, L. (2016). Vagal neurocircuitry and its influence on gastric motility. Nat. Rev. Gastroenterol. Hepatol. *13*, 389–401.

Travagli, R.A., Hermann, G.E., Browning, K.N., and Rogers, R.C. (2006). Brainstem circuits regulating gastric function. Annu. Rev. Physiol. *68*, 279–305.

Tsolis, R.M., Townsend, S.M., Miao, E.A., Miller, S.I., Ficht, T.A., Adams, L.G., and Bäumler, A.J. (1999). Identification of a putative Salmonella enterica serotype typhimurium host range factor with homology to IpaH and YopM by signature-tagged mutagenesis. Infect. Immun. *67*, 6385–6393.

Tsuchiya, K., Nakajima, S., Hosojima, S., Thi Nguyen, D., Hattori, T., Manh Le, T., Hori, O., Mahib, M.R., Yamaguchi, Y., Miura, M., et al. (2019). Caspase-1 initiates apoptosis in the absence of gasdermin D. Nat. Commun. *10*.

Ueno, M., Ueno-Nakamura, Y., Niehaus, J., Popovich, P.G., and Yoshida, Y. (2016). Silencing spinal interneurons inhibits immune suppressive autonomic reflexes caused by spinal cord injury. Nat. Neurosci. *19*, 784–787.

Uesaka, T., Young, H.M., Pachnis, V., and Enomoto, H. (2016). Development of the intrinsic and extrinsic innervation of the gut. Dev. Biol. 1–10.

Usoskin, D., Furlan, A., Islam, S., Abdo, H., Lönnerberg, P., Lou, D., Hjerling-Leffler, J., Haeggström, J., Kharchenko, O., Kharchenko, P. V., et al. (2015). Unbiased classification of sensory neuron types by large-scale single-cell RNA sequencing. Nat. Neurosci. *18*, 145–153.

De Vadder, F., Kovatcheva-Datchary, P., Goncalves, D., Vinera, J., Zitoun, C., Duchampt, A., Bäckhed, F., and Mithieux, G. (2014). Microbiota-generated metabolites promote metabolic benefits via gut-brain neural circuits. Cell *156*, 84–96.

De Vadder, F., Grasset, E., Mannerås Holm, L., Karsenty, G., Macpherson, A.J.,

Olofsson, L.E., and Bäckhed, F. (2018). Gut microbiota regulates maturation of the adult enteric nervous system via enteric serotonin networks. Proc. Natl. Acad. Sci. U. S. A. *115*, 6458–6463.

Valles-Colomer, M., Falony, G., Darzi, Y., Tigchelaar, E.F., Wang, J., Tito, R.Y., Schiweck, C., Kurilshikov, A., Joossens, M., Wijmenga, C., et al. (2019). The neuroactive potential of the human gut microbiota in quality of life and depression. Nat. Microbiol. *4*, 623–632.

Vallon-Eberhard, A., Landsman, L., Yogev, N., Verrier, B., and Jung, S. (2006). Transepithelial Pathogen Uptake into the Small Intestinal Lamina Propria. J. Immunol. *176*, 2465–2469.

Varin, E.M., Mulvihill, E.E., Baggio, L.L., Koehler, J.A., Cao, X., Seeley, R.J., and Drucker, D.J. (2019). Distinct Neural Sites of GLP-1R Expression Mediate Physiological versus Pharmacological Control of Incretin Action. Cell Rep. *27*, 3371-3384.e3.
Veiga-Fernandes, H., and Mucida, D. (2016). Neuro-Immune Interactions at Barrier Surfaces. Cell *165*, 801–811.

Vertzoni, M., Augustijns, P., Grimm, M., Koziolek, M., Lemmens, G., Parrott, N., Pentafragka, C., Reppas, C., Rubbens, J., Van Den Abeele, J., et al. (2019). Impact of regional differences along the gastrointestinal tract of healthy adults on oral drug absorption: An UNGAP review. Eur. J. Pharm. Sci. *134*, 153–175.

Vivier, E., Artis, D., Colonna, M., Diefenbach, A., Di Santo, J.P., Eberl, G., Koyasu, S., Locksley, R.M., McKenzie, A.N.J., Mebius, R.E., et al. (2018). Innate Lymphoid Cells: 10 Years On. Cell *174*, 1054–1066.

Volk, J.K., Nyström, E.E.L., van der Post, S., Abad, B.M., Schroeder, B.O., Johansson, Å., Svensson, F., Jäverfelt, S., Johansson, M.E. V, Hansson, G.C., et al. (2019). The Nlrp6 inflammasome is not required for baseline colonic inner mucus layer formation or function. J. Exp. Med.

Wallrapp, A., Riesenfeld, S.J., Burkett, P.R., Abdulnour, R.-E.E., Nyman, J., Dionne, D., Hofree, M., Cuoco, M.S., Rodman, C., Farouq, D., et al. (2017). The neuropeptide NMU amplifies ILC2-driven allergic lung inflammation. Nature.

Wang, F., and Powley, T.L. (2007). Vagal innervation of intestines: afferent pathways mapped with new en bloc horseradish peroxidase adaptation. Cell Tissue Res. *329*, 221–230.

Wang, F.B., and Powley, T.L. (2000). Topographic inventories of vagal afferents in gastrointestinal muscle. J. Comp. Neurol. *421*, 302–324.

Wang, S., Miura, M., Jung, Y.K., Zhu, H., Li, E., and Yuan, J. (1998). Murine caspase-11, an ICE-interacting protease, is essential for the activation of ICE. Cell *92*, 501–509.

Waterson, M.J., and Horvath, T.L. (2015). Neuronal Regulation of Energy Homeostasis: Beyond the Hypothalamus and Feeding. Cell Metab. *22*, 962–970.

Wendeln, A., Degenhardt, K., Kaurani, L., Gertig, M., Ulas, T., Jain, G., Wagner, J., Häsler, L.M., Wild, K., Skodras, A., et al. (2018). Innate immune memory in the brain shapes neurological disease hallmarks. Nature *556*, 332–338.

Wichmann, A., Allahyar, A., Greiner, T.U., Plovier, H., Lundén, G.Ö., Larsson, T., Drucker, D.J., Delzenne, N.M., Cani, P.D., and Bäckhed, F. (2013). Microbial modulation of energy availability in the colon regulates intestinal transit. Cell Host Microbe *14*, 582–590.

Wilhelm, C.L., and Yarovinsky, F. (2014). Apicomplexan infections in the gut. Parasite Immunol. *36*, 409–420.

Williams, E.K., Chang, R.B., Strochlic, D.E., Umans, B.D., Lowell, B.B., and Liberles, S.D. (2016). Sensory Neurons that Detect Stretch and Nutrients in the Digestive System. Cell *166*, 209–221.

Wlodarska, M., Thaiss, C.A., Nowarski, R., Henao-Mejia, J., Zhang, J.P., Brown, E.M., Frankel, G., Levy, M., Katz, M.N., Philbrick, W.M., et al. (2014). NLRP6 inflammasome orchestrates the colonic host-microbial interface by regulating goblet cell mucus secretion. Cell *156*, 1045–1059.

Womack, W.A., Mailman, D., Kvietys, P.R., and Granger, D.N. (1988). Neurohumoral control of villous motility. Am. J. Physiol. *255*, G162-7.

Wood, J.D. (1972). Excitation of intestinal muscle by atropine, tetrodotoxin, and xylocaine. Am. J. Physiol. *222*, 118–125.

Wood, J.D. (2002). Neuropathophysiology of irritable bowel syndrome. J. Clin. Gastroenterol. *35*, S11-22.

Wood, J.D. (2007). Neuropathophysiology of functional gastrointestinal disorders. World J. Gastroenterol. *13*, 1313–1332.

Wood, J.D. (2011). Enteric Nervous System.

Woods, S.C., Lotter, E.C., McKay, L.D., and Porte, D. (1979). Chronic intracerebroventricular infusion of insulin reduces food intake and body weight of baboons. Nature *282*, 503–505.

Worthington, J.J., Reimann, F., and Gribble, F.M. (2017). Enteroendocrine cells-sensory sentinels of the intestinal environment and orchestrators of mucosal immunity. Nat. Publ. Gr.

Wu, Q., Whiddon, B.B., and Palmiter, R.D. (2012). Ablation of neurons expressing agouti-related protein, but not melanin concentrating hormone, in leptin-deficient mice restores metabolic functions and fertility. Proc. Natl. Acad. Sci. *109*, 3155–3160.

Xu, J., Bartolome, C.L., Low, C.S., Yi, X., Chien, C.H., Wang, P., and Kong, D. (2018). Genetic identification of leptin neural circuits in energy and glucose homeostases. Nature *556*, 505–509.

Yadav, V.K., Ryu, J.H., Suda, N., Tanaka, K.F., Gingrich, J.A., Schütz, G., Glorieux, F.H., Chiang, C.Y., Zajac, J.D., Insogna, K.L., et al. (2008). Lrp5 Controls Bone Formation by Inhibiting Serotonin Synthesis in the Duodenum. Cell *135*, 825–837.

Yang, B., Treweek, J.B., Kulkarni, R.P., Deverman, B.E., Chen, C.-K., Lubeck, E., Shah, S., Cai, L., and Gradinaru, V. (2014). Single-cell phenotyping within transparent intact tissue through whole-body clearing. Cell *158*, 945–958.

Yang, M., Fukui, H., Eda, H., Xu, X., Kitayama, Y., Hara, K., Kodani, M., Tomita, T., Oshima, T., Watari, J., et al. (2017). Involvement of gut microbiota in association between GLP-1/GLP-1 receptor expression and gastrointestinal motility. Am. J. Physiol. - Gastrointest. Liver Physiol. *312*, G367–G373.

Yano, J.M., Yu, K., Donaldson, G.P., Shastri, G.G., Ann, P., Ma, L., Nagler, C.R., Ismagilov, R.F., Mazmanian, S.K., and Hsiao, E.Y. (2015). Indigenous Bacteria from the Gut Microbiota Regulate Host Serotonin Biosynthesis. Cell *161*, 264–276.

Yavorska, I., and Wehr, M. (2016). Somatostatin-expressing inhibitory interneurons in cortical circuits. Front. Neural Circuits *10*, 1–18.

Ye, D.W., Liu, C., Tian, X.B., and Xiang, H.B. (2014). Identification of neuroanatomic circuits from spinal cord to stomach in mouse: Retrograde transneuronal viral tracing study. Int. J. Clin. Exp. Pathol.

Ye, L., Allen, W.E., Thompson, K.R., Tian, Q., Hsueh, B., Ramakrishnan, C., Wang, A.-C., Jennings, J.H., Adhikari, A., Halpern, C.H., et al. (2016). Wiring and Molecular Features of Prefrontal Ensembles Representing Distinct Experiences. Cell *165*, 1776–1788.

Yoo, B.B., and Mazmanian, S.K. (2017). The Enteric Network: Interactions between the Immune and Nervous Systems of the Gut. Immunity *46*, 910–926.

Young, A.A. (2012). Brainstem sensing of meal-related signals in energy homeostasis. Neuropharmacology *63*, 31–45.

Yuan, X., Huang, Y., Shah, S., Wu, H., and Gautron, L. (2016). Levels of Cocaine- and Amphetamine-Regulated Transcript in Vagal Afferents in the Mouse Are Unaltered in Response to Metabolic Challenges. ENeuro *3*.

Zaiss, M.M., Jones, R.M., Schett, G., and Pacifici, R. (2019). The gut-bone axis: how bacterial metabolites bridge the distance. J. Clin. Invest. *129*, 3018–3028.

Zariwala, H.A., Borghuis, B.G., Hoogland, T.M., Madisen, L., Tian, L., de Zeeuw, C.I., Zeng, H., Looger, L.L., Svoboda, K., and Chen, T.W. (2012). A Cre-dependent GCaMP3 reporter mouse for neuronal imaging in vivo. J. Neurosci. *32*, 3131–3141.

Zarrinpar, A., Chaix, A., Xu, Z.Z., Chang, M.W., Marotz, C.A., Saghatelian, A., Knight, R., and Panda, S. (2018). Antibiotic-induced microbiome depletion alters metabolic homeostasis by affecting gut signaling and colonic metabolism. Nat. Commun. *9*, 2872.

Zeisel, A., Hochgerner, H., Lönnerberg, P., Johnsson, A., Memic, F., van der Zwan, J., Häring, M., Braun, E., Borm, L.E., La Manno, G., et al. (2018). Molecular Architecture of the Mouse Nervous System. Cell *174*, 999-1014.e22.

Zeng, W.-Z., Marshall, K.L., Min, S., Daou, I., Chapleau, M.W., Abboud, F.M., Liberles, S.D., and Patapoutian, A. (2018). PIEZOs mediate neuronal sensing of blood pressure and the baroreceptor reflex. Science *362*, 464–467.

Zhang, J., Holdorf, A.D., and Walhout, A.J. (2017). C. elegans and its bacterial diet as a model for systems-level understanding of host–microbiota interactions. Curr. Opin. Biotechnol. *46*, 74–80.

Zhang, Y.-Q., Resta, S., Jung, B., Barrett, K.E., and Sarvetnick, N. (2009). Upregulation of activin signaling in experimental colitis. Am. J. Physiol. Gastrointest. Liver Physiol. *297*, G768-80.

Zhu, H., Aryal, D.K., Olsen, R.H.J., Urban, D.J., Swearingen, A., Forbes, S., Roth, B.L., and Hochgeschwender, U. (2016). Cre-dependent DREADD (Designer Receptors Exclusively Activated by Designer Drugs) mice. Genesis *54*, 439–446.

Zimmer, M.R., Fonseca, A.H.O., Iyilikci, O., Pra, R.D., and Dietrich, M.O. (2019). Functional Ontogeny of Hypothalamic Agrp Neurons in Neonatal Mouse Behaviors. Cell 1–16.

Zmora, N., Suez, J., and Elinav, E. (2019). You are what you eat: diet, health and the

gut microbiota. Nat. Rev. Gastroenterol. Hepatol. *16*, 35–56.

Zubcevic, J., Richards, E.M., Yang, T., Kim, S., Sumners, C., Pepine, C.J., and Raizada, M.K. (2019). Impaired Autonomic Nervous System-Microbiome Circuit in Hypertension. Circ. Res. *125*, 104–116.

Zwighaft, Z., Aviram, R., Shalev, M., Rousso-Noori, L., Kraut-Cohen, J., Golik, M., Brandis, A., Reinke, H., Aharoni, A., Kahana, C., et al. (2015). Circadian Clock Control by Polyamine Levels through a Mechanism that Declines with Age. Cell Metab. *22*, 874–885.